



HAL
open science

Study of the mechanisms of carbon enrichment in austenite in Q&P steels

Samy Aoued

► **To cite this version:**

Samy Aoued. Study of the mechanisms of carbon enrichment in austenite in Q&P steels. Material chemistry. Université de Bordeaux, 2019. English. NNT : 2019BORD0181 . tel-03372617

HAL Id: tel-03372617

<https://theses.hal.science/tel-03372617>

Submitted on 11 Oct 2021

HAL is a multi-disciplinary open access archive for the deposit and dissemination of scientific research documents, whether they are published or not. The documents may come from teaching and research institutions in France or abroad, or from public or private research centers.

L'archive ouverte pluridisciplinaire **HAL**, est destinée au dépôt et à la diffusion de documents scientifiques de niveau recherche, publiés ou non, émanant des établissements d'enseignement et de recherche français ou étrangers, des laboratoires publics ou privés.

THÈSE PRÉSENTÉE
POUR OBTENIR LE GRADE DE
DOCTEUR DE
L'UNIVERSITÉ DE BORDEAUX

ÉCOLE DOCTORALE DES SCIENCES CHIMIQUES

Physico-Chimie de la Matière Condensée

Par Samy AOUED

**Étude des mécanismes d'enrichissement en carbone de
l'austénite dans les aciers duplex Q&P à très haute résistance**

Sous la direction de : Mohamed GOUNÉ
(co-directeur : Frédéric DANOIX)

Soutenue le 10 octobre 2019

Membres du jury :

M. GODET Stéphane	Professeur à l'Université Libre de Bruxelles, Belgique	Président du jury
Mme. GOURGUES-LORENZON Anne-Françoise	Professeur au Centre des Matériaux MINES ParisTech, France	Rapporteur
M. MAUGIS Philippe	Professeur à l'IM2NP, Université d'AIX-Marseille, France	Rapporteur
M. ALLAIN Sébastien	Professeur à l'IJL, Université de Lorraine, France	Examineur
M. SOLER Michel	Ingénieur de recherche, ArcelorMittal Maizières Recherche, France	Examineur
M. HEINTZ Jean-Marc	Professeur à l'ICMCB, Université de Bordeaux, France	Examineur
M. DANOIX Frédéric	Chargé de Recherche au GPM, Université de Rouen, France	Examineur
M. GOUNÉ Mohamed	Professeur à l'ICMCB, Université de Bordeaux, France	Examineur
Mme. POULON-QUINTIN Angéline	Maître de conférence à l'ICMCB, Université de Bordeaux, France	Invité

The first principle is that you must not fool yourself and you are the easiest person to fool.

Richard P. Feynman

À ma mère,

REMERCIEMENTS

Je souhaite avant tout remercier mes deux directeurs de thèse, Mohamed GOUNÉ et Frédéric DANOIX, pour tout le temps consacré à l'encadrement de cette thèse, pour tous les conseils et nombreuses relectures. C'est grâce au haut niveau d'exigence, à l'implication et la disponibilité sans faille de mes encadrants que les travaux présentés dans ce manuscrit ont pu aboutir. Outre leur implication scientifique, c'est aussi la confiance et le soutien humain qu'ils ont pu m'apporter dans les moments importants et difficiles d'une thèse qui m'a permis de mener à bien cette étude. Je leur suis donc extrêmement reconnaissant et je suis fier d'avoir pu travailler à leurs côtés.

Je tiens aussi à remercier Mario MAGLIONE, Directeur de l'ICMCB, pour m'avoir accueilli au sein de son laboratoire.

Je remercie le Professeur Stéphane GODET pour m'avoir fait l'honneur de présider mon jury de thèse. Je remercie également les Professeurs Anne-Françoise GOURGUES-LORENZON et Philippe MAUGIS d'avoir accepté de juger et de rapporter mon travail. Enfin, je remercie le Professeur Jean-Marc HEINTZ pour avoir accepté de faire partie de mon jury de thèse.

Je remercie vivement les acteurs du projet ANR CapNano, c'est grâce à leur expertise dans des domaines de recherche à la pointe de la science des matériaux que cette thèse a pu voir le jour. Ce fut un privilège et une source d'inspiration que d'avoir pu effectuer ces années de doctorat entouré de personnes aussi passionnées par la métallurgie. Je remercie donc Sébastien ALLAIN, Guillaume GEANDIER et Steve GAUDEZ de l'IJL de Nancy pour avoir conduit les expériences de DRX aux hautes énergies, Frédéric DANOIX du GPM de Rouen pour les expériences de sonde atomique tomographique et Angéline QUINTIN-POULON pour les expériences de MET. Travaillant au centre de Recherche ArcelorMittal à Maizières-lès-Metz, je remercie Michel SOLER, Jean-Christophe HELL et Mathieu SALIB pour les conseils et discussions autour de la conduite des expériences de caractérisation MEB/FEG, EBSD et DRX. Je remercie également Magali BOUZAT, Aude NADLER, Laurent CHAPUIS et Patrick BARGES, pour leur précieux appui technique et leur sympathie.

Je remercie également les membres permanents du groupe Métallurgie et Matériaux Fonctionnels de l'ICMCB pour m'avoir accueilli dans leurs locaux : Jean-François SILVAIN, Sylvie BORDERE, Stéphane GORSSE, Jean-Marc HEINTZ, Amélie VEILLERE, Guillaume AUBERT, Guillaume LACOMBE, Sophie TENCÉ, Etienne GAUDIN, Jean-Louis BOBET.

Je tiens à remercier Carole MALBURET et Sandrine QUILLATEAU, agents administratifs de l'ICMCB, pour leur aide dans les démarches administratives mais surtout pour leur bienveillance.

Je remercie Stéphane TOULIN, bibliothécaire de l'ICMCB, pour l'aide concernant les aspects bibliographiques et l'édition de la version finale du manuscrit de thèse.

Je remercie aussi Sébastien FOURCADE, Cathy ELISSALDE, Eric LEBRAUD et Lionel TEULE-GAY pour les discussions agréables que nous avons pu avoir au détour d'un couloir.

Je remercie les membres du service informatique : Cyril DUFOUR, Bernard CLAVEL, Fabien PALENCIA et William DE ALMEIDA pour leur aide lorsque les outils informatiques ont pu poser problème.

Je tiens à remercier les doctorants que j'ai eu le réel plaisir de côtoyer tout au long de mes années à l'ICMCB et qui ont parfois eu la lourde tâche de supporter mes monologues sur le cyclisme :

- Clio et Tadhg, merci pour tous les repas agréables au CAES et pour les (peut-être moins agréables pour certains !) sorties de course à pied ! J'ai été chanceux de vous avoir eu à mes côtés et vous avoir vu brillamment soutenir votre thèse m'a clairement montré la voie pour réussir la mienne ! Bon vent à vous deux !
- Les habitants du A16 (autrement appelé « Quartararo Fan Club ») :
 - o Benji : roi de la bidouille et compagnon de rédaction/préparation de soutenance, c'est toujours agréable de pouvoir partager les hauts et les bas de ces étapes ardues de la thèse !
 - o Maël : le jeunot et roi de la communication scientifique, merci de ta bonne humeur et je te souhaite le meilleur pour la suite de ta thèse !
 - o Iñaki : le pur produit basque et le plus céramiste d'entre nous, merci de nous avoir poussé à sortir régulièrement boire « juste une bière » au Central,
 - o Loukass : le roi du sushi, cauchemar des douaniers et futur recordman du 10000m, merci pour les fous-rires et reste comme tu es !
 - o Les autres doctorants dont j'ai eu le plaisir de faire la connaissance : Jonathan, Maureen, Diaa, Vola, Zhengyan, Zouhair, Emilien et tous les doctorants des autres groupes de l'ICMCB.

Enfin je voudrais remercier ma famille et mes amis, les doctorants ont la fâcheuse habitude de disparaître des radars pendant la durée de la thèse, et je n'ai pas fait exception. Je vous remercie de votre patience et de votre soutien indéfectible !

Merci à toute la Team : Lionel aka « BERNARDAN », Luiiisss aka « Le Rick's », Jean aka « VortexGod », Mat aka « ShotMathieu », Guillaume aka « Le Bucheron » et rendez-vous à Lyon pour monter la start-up (#champagneencannette) !

Merci à Colette, Michel et Marine pour le soutien précieux pendant les moments difficiles et pour être venus assister à ma soutenance.

Merci à Mermoz qui, par le non verbal, a toujours réussi à me transmettre ses encouragements.

Merci à Beryl, qui m'a supporté (dans les deux sens du terme !) tous les jours et à qui je dois beaucoup de vacances et week-end loin de Pessac !

Merci à ma sœur, Bahia, qui malgré ses vadrouilles aux quatre coins du monde a toujours eu un mot pour me soutenir !

Enfin, je remercie ma mère, Brigitte, sans qui je ne serais pas où je suis et qui a réussi à m'inculquer des valeurs d'humanité et à faire preuve de persévérance dans tout ce que j'entreprends.

RÉSUMÉ SUBSTANTIEL EN FRANÇAIS

L'allègement dans le secteur de l'automobile revêt un enjeu important du fait de normes d'émission de CO₂ de plus en plus drastiques, de la nécessité de réduire la consommation en carburant des véhicules et d'une aspiration sociétale à une économie « plus verte ». Même si les alliages à faible densité comme ceux à base d'aluminium ou de magnésium semblent de bons candidats pour l'allègement des structures, l'acier reste le matériau de premier choix dans l'industrie. En effet, son faible coût et sa grande polyvalence en font un matériau idéal pour faire face aux nouveaux défis de conception. Les parties structurelles des véhicules (éléments de châssis avant et arrière, le pied milieu et les montants de pare-brise) doivent répondre à de nombreuses propriétés souvent antagonistes comme l'allègement, la formabilité, la résistance mécanique, la rigidité et le coût.

Les aciers conventionnels contiennent principalement des phases ferritiques monophasées conduisant à de très bonnes propriétés de formabilité grâce à la ductilité de la ferrite de structure cubique centrée (bcc) mais aussi à des propriétés de résistance mécanique amoindries. Les aciers conventionnels les plus communs sont les aciers IF (Interstitial Free), les aciers BH (Bake Hardening) et les aciers HSLA (High Strength Low Alloy Steel). L'augmentation de la résistance mécanique de ce type d'acier est difficile car les mécanismes classiques de durcissement (par solution solide, affinement des grains ou par précipitation) entraînent une réduction drastique des propriétés de ductilité et de formabilité.

Le projet ULSAB (Ultralight Steel Auto Body) a été lancé en 1994 pour stimuler la recherche en vue d'accroître la sécurité et l'efficacité énergétique par l'allègement des structures des véhicules. Cela marque le début du développement des aciers à très haute résistance (THR ou AHSS en anglais). Cette nouvelle génération d'aciers a permis de s'éloigner de la courbe traditionnelle de résistance/allongement et de produire des aciers avec un meilleur compromis entre ces propriétés, permettant la production de tôles plus minces capables de réduire le poids de la structure.

Le nouveau paradigme derrière les aciers THR nouvelle génération est la fabrication de microstructures constituées par assemblage de phases complexes obtenues par l'association d'une composition chimique et d'un traitement thermique judicieusement choisis.

Les deux aciers phares de la première génération d'aciers THR sont les aciers TRIP et les aciers DP. Ces derniers combinent de la ferrite et de la martensite de sorte que la résistance mécanique est ajustable via la fraction de martensite introduite dans la microstructure. Les aciers TRIP profitent d'une présence importante d'austénite résiduelle qui va permettre de bénéficier de bonnes propriétés d'écrouissage sur une large gamme d'allongement grâce à l'effet de plasticité induite par transformation (effet TRIP). Cet effet de composite dynamique est très dépendant de la teneur en carbone de l'austénite qui est enrichie via une transformation bainitique pendant un palier isotherme durant le traitement.

La seconde génération d'aciers THR reconnaît l'importance d'avoir de l'austénite comme phase principale de la microstructure pour augmenter les propriétés de ductilité et d'écrouissage. Les aciers TWIP profitent d'un ajout important de manganèse (entre 15 % et 30%) afin d'avoir une microstructure austénitique stable à température ambiante. Les propriétés de résistance mécanique sont ensuite obtenues grâce au mécanisme de déformation par maclage dans l'austénite sous l'effet des sollicitations extérieures. Cependant, la production d'aciers TWIP s'avère très coûteuse et exigeante en termes de contrôle de la chaîne de production.

La troisième génération d'aciers THR propose de combler le gap entre les aciers de 1^{ière} génération et les aciers TWIP. Les propriétés inédites des aciers THR 3^{ième} génération sont obtenues grâce à des microstructures encore plus complexes que les aciers des générations précédentes. En effet, elles sont au moins bi-phasées et souvent très fines. Elles sont constituées d'une matrice nanostructurée combinée à une importante quantité d'austénite résiduelle. Alors que la matrice offre de très bonnes propriétés de résistance et de ténacité, l'austénite résiduelle apporte les propriétés de ductilité et de formabilité via l'effet TRIP. Parmi ces aciers de 3^{ième}

génération, le traitement de « Quenching and Partitioning » (Q&P) proposé en 2003 par Speer est considéré comme étant le plus prometteur. Le traitement thermique Q&P consiste d'abord à chauffer l'acier jusqu'au domaine austénitique, puis de tremper l'acier jusqu'à atteindre la température QT (« quenching temperature ») située entre Ms et Mf afin de former une fraction contrôlée de martensite, ensuite une étape de remontée en température permet d'atteindre un palier isotherme à la température PT (« partitioning temperature » ou étape de partition), il est attendu que le carbone partitionne depuis la martensite sursaturée vers l'austénite, enfin une étape de trempe finale permet de redescendre à température ambiante. Bien que les mécanismes d'enrichissement en carbone de l'austénite résiduelle lors de l'étape de partition soient encore débattus dans la littérature, il existe des preuves tangibles qui attestent d'un phénomène de partition du carbone de la martensite vers l'austénite dont la force motrice est le gradient de potentiel chimique du carbone dans la martensite et dans l'austénite. Cependant, la formation de bainite et de carbures dans la martensite soulève la question de l'influence de ces réactions et de leurs interactions sur les mécanismes et les cinétiques d'enrichissement en carbone de l'austénite. Il s'agit clairement d'un sujet d'intérêt puisque les propriétés mécaniques de ces aciers reposent principalement sur la teneur en carbone des îlots d'austénite.

Cette thèse qui repose sur une approche expérimentale multi-échelle couplée à une approche théorique en champ moyen, apporte des éléments de réponse quant aux mécanismes de transformation de phases et d'enrichissement en carbone de l'austénite dans un aciers duplex Q&P à très haute résistance de composition Fe-0,3C-2,5Mn-1,5Si.

Les températures optimums de trempe et de partition ont été déterminées en combinant les techniques de dilatométrie et de diffraction des rayons X. Trois températures de trempe initiale différentes ont été choisies (200°C, 230°C et 260°C) afin d'effectuer l'étape de partition avec trois fractions de martensite différentes. L'étape de partition s'effectue à 400°C. L'étude dilatométrique a mis en évidence une dilatation pendant l'étape de partition qui peut être induite par la formation de bainite. Afin de confirmer cette hypothèse, une méthodologie d'analyse d'images a été menée sur différents traitements Q&P et sur un échantillon de référence ayant subi un traitement destiné à former de la bainite (traitement de Bainite Sans Carbures ou BSC). L'attaque chimique Nital/Picral préalable des échantillons a permis de discriminer les phases riches (austénite résiduelle et îlots martensite/austénite) et pauvres (martensite revenue et bainite) en carbone par MEB. L'austénite est présente sous la forme de fines petites et longues lattes ainsi qu'à la périphérie des îlots MA. La martensite revenue est facilement reconnaissable en raison de la présence importante de carbures intra-lattes. L'analyse d'images a permis de montrer que la bainite peut être morphologiquement caractérisée par de petites lattes sans carbures. L'évolution de la fraction de phase de bainite a été étudiée par une méthode de comptage manuel sur des micrographies d'échantillons trempés à différents temps pendant le palier de partition. L'augmentation continue de la fraction de bainite mesurée par analyse d'image présente une cinétique très similaire à celle mesurée par dilatométrie. Cette tendance est également observée lorsque la température de trempe initiale QT varie : comme observée par dilatométrie, plus la fraction d'austénite présente pour la partition est grande (c'est-à-dire que QT est haut), plus la fraction de bainite mesurée par analyse d'images est importante. Ceci confirme que le critère morphologique choisi pour la bainite (à savoir des petites lattes sans carbures) est pertinent. La présence de bainite a également été confirmée par des expériences in-situ de diffraction des rayons X aux hautes énergies. En effet, une augmentation significative et lente d'une nouvelle fraction de phase BCT au détriment de l'austénite se produit pendant la phase de remontée en température et se poursuit pendant le palier de partition. Les fractions volumiques de bainite mesurées sont en accord avec celles relevées par analyse d'images. En outre, il a été montré que la teneur maximale en carbone de l'austénite peut être située au-dessus de la ligne décrite par le modèle thermodynamique du CCE habituellement considéré comme une limite haute de l'enrichissement en carbone de l'austénite. Ceci a été attribué à un effet géométrique induit par la présence de bainite car la réduction du volume d'austénite entraîne mécaniquement une

augmentation de concentration en carbone. Toutes les analyses menées semblent donc confirmer la formation de bainite pendant le traitement Q&P étudié.

Contrairement à la bainite, la martensite revenue présente une large précipitation intra-latte. La composition en carbone de ces carbures a été mesurée par Sonde Atomique Tomographique (SAT) et présentent une concentration de 20,0%at à 27,7%at. La seule donnée de composition ne permet pas de statuer sur la nature des carbures qui peuvent être soit de nature transitoire (carbures ϵ ou η) ou bien d'équilibre (cémentite θ). Même si des expériences complémentaires par micro-diffraction en MET ont permis d'écarter la présence de cémentite, la distinction entre les carbures ϵ et η s'est avérée difficile. Les carbures présentant une morphologie de fines plaquettes ont été identifiés comme étant des carbures η alors que les précipités plus sphériques sont probablement des carbures ϵ .

Une quantité importante de carbone est aussi piégée sur les défauts de la martensite et plus spécifiquement sur les joints de lattes (ségrégation 2D). De façon surprenante, aucune ségrégation sur ce qui pourrait être identifié comme des dislocations (ségrégations 1D) n'a été observé. Les concentrations d'excès mesurées par SAT à plusieurs instants du traitement suggèrent qu'un phénomène de ségrégation du carbone sur les joints de lattes s'opèrent dans les premiers instants du traitement puis qu'une déségrégation s'effectue depuis les joints de lattes pendant le palier de partition.

L'utilisation de la diffraction des rayons X aux hautes énergies a permis d'avoir accès à des informations quantitatives in-situ et de façon extrêmement résolues en temps pendant le traitement Q&P. Trois différents traitement thermiques Q&P avec trois valeurs de QT (200, 230 et 260°C) ont été étudiés. L'évolution des fractions de phases est très similaire pour les trois conditions et peut être décomposée en quatre étapes :

- (1) La première partie de la trempe initiale depuis le domaine austénitique (900°C) jusqu'à une température correspondant à Ms durant laquelle aucune transformation de phases n'est observée,
- (2) La deuxième partie de la trempe initiale une fois passé Ms durant laquelle une augmentation importante de la fraction de martensite au dépend de la fraction d'austénite est notable. La cinétique de transformation est très grande dans les premiers temps puis devient plus faible en fin de transformation. Les fractions finales de martensite mesurées dépendent de la température du palier QT (85% à QT200, 76% à QT230 et 65% à QT260),
- (3) Une étape constante pendant le début de la remontée en température depuis QT vers PT où les fractions de phases sont inchangées,
- (4) Une lente mais néanmoins importante augmentation d'une nouvelle phase BCT au dépend de l'austénite s'effectue pendant la remontée en température puis continue pendant le palier de partition. Cette nouvelle phase BCT a été identifiée comme étant de la bainite. Le taux de transformation bainitique, qui est un meilleur indicateur que la fraction absolue de bainite formée, diminue avec la diminution de la température de trempe initiale QT (de 45% à QT260 à 20% à QT200). Pour les trois température QT étudiées, la majeure partie de la bainite est formée dans un temps très court : 75% de la fraction totale de bainite est formée en 28,2s, 24,6s et 30s pour respectivement QT200, QT230 et QT260.

L'analyse de l'évolution du paramètre de maille de l'austénite s'est avérée difficile car elle est le résultat de contributions thermiques, chimiques et mécaniques. Une tentative de découplage des différentes contributions a été menée et les contraintes internes formées dans l'austénite lors de la trempe à QT ont été déterminées. Un des résultats marquants est que l'austénite soit sujette à une

succession d'états de traction et de compression induits par la formation de martensite. La fraction critique de martensite pour laquelle l'austénite passe d'un état de traction à un état de compression a été mesurée pour les 3 QT : 56, 44 et 52% pour respectivement QT200, QT230 et QT260. D'un point de vue qualitatif, ces observations sont en accord avec les travaux théoriques d'Eshelby, de Mori-Tanaka et de Scherer.

De plus, il a aussi été montré que les variations de paramètre de maille de l'austénite une fois le palier de QT passé sont dues soit à un enrichissement en carbone de l'austénite ou bien à des phénomènes de relaxation des contraintes formées à QT. Il n'est pas exclu que ces deux phénomènes puissent opérer de manière simultanée. Cependant, il est extrêmement compliqué de quantifier et de découpler les phénomènes de relaxation de contraintes, étape pourtant nécessaire afin d'isoler la contribution de l'enrichissement en carbone de l'austénite. Dans le but de pallier cette difficulté, il a été proposé de définir deux limites pour l'évolution de la concentration en carbone de l'austénite en considérant deux cas extrêmes pour la relaxation des contraintes. Le premier cas considère qu'il n'y a aucun phénomène de relaxation pendant la remontée en température et l'étape de partition à PT. En d'autres termes, les phénomènes de relaxation de contraintes sont négligés et toute augmentation du paramètre de maille observée après le palier à QT est attribué à la contribution chimique, cette dernière étant de fait surestimée dans ce cas. Le second cas consiste à considérer que l'intégralité des contraintes formées sont relaxées immédiatement à la sortie du palier de QT. La véritable contribution chimique à l'augmentation du paramètre de maille de l'austénite évolue très probablement entre ces deux limites.

En suivant cette approche, l'évolution de la teneur en carbone de l'austénite pour les trois conditions de QT a été déterminée. La première conclusion est que l'influence de la relaxation des contraintes internes sur l'évolution de la teneur en carbone n'est pas significative. En effet, l'impact de la relaxation des contraintes représente tout au plus une réduction de la teneur en carbone calculée de 0.10%_m pour un enrichissement en carbone total de 0.7%_m à QT200. Comme attendu, l'influence de la relaxation des contraintes dépend de la température de trempe initiale QT, c'est-à-dire de la quantité initiale de martensite à QT. C'est lors du traitement à QT260 que l'impact de la relaxation s'est avéré le plus faible (0.05%_m pour un enrichissement total de 0.7%_m). L'explication de cette tendance est simple puisque plus la fraction de martensite à QT est basse, plus les contraintes internes induites par la formation de martensite sont faibles. Le résultat le plus surprenant de cette partie de l'étude est que l'enrichissement total en carbone de l'austénite ne dépend pas de la température de trempe initiale QT. De plus, l'enrichissement en carbone résulte de deux contributions : la partition du carbone depuis la martensite et la transformation bainitique. Cependant, du point de vue expérimental, il est très difficile de découpler la contribution de chaque mécanisme à l'enrichissement final.

Afin d'apporter des réponses aux questions soulevées et de rationaliser les résultats expérimentaux obtenus par diffraction des rayons X aux hautes énergies, une approche théorique originale a été développée. Elle couple numériquement la partition du carbone, la transformation bainitique et la précipitation des carbures dans la martensite. Les résultats obtenus et l'analyse effectuée apportent des clarifications quant aux mécanismes d'enrichissement en carbone de l'austénite pendant le traitement Q&P. Il a été clairement montré que l'enrichissement résulte à la fois de la contribution de la partition du carbone depuis la martensite et de la transformation bainitique. Leurs contributions respectives en fonction de la température de trempe initiale QT ont été déterminées, il a été montré que celle de la partition depuis la martensite est de plus en plus grande à mesure que la température QT est abaissée. Ce comportement peut être expliqué par un effet domino, en effet la quantité de carbone rejeté ainsi que la cinétique de rejet sont plus grands lorsque QT est bas, ce qui a ensuite pour effet d'inhiber la transformation bainitique.

De façon intéressante, il a été montré qu'en présence de bainite ; la teneur en carbone de l'austénite à la fin du palier de partition peut être situé au-dessus de la limite fixée par le modèle du CCE. Ce phénomène a été attribué à un phénomène géométrique : l'augmentation de la teneur en carbone de l'austénite est exacerbée par la réduction de volume de l'austénite induite par la

formation de bainite.

De façon surprenante et pouvant paraître, de prime abord, contre-intuitif, il a été montré que l'enrichissement en carbone maximal de l'austénite ne dépend pas de la température de trempe initiale QT. Cela a été expliqué par le fait que la transformation bainitique contrôle l'enrichissement final à 400°C. En effet, pour les trois températures QT étudiées, il a été montré que la transformation bainitique se poursuit alors que le processus de rejet de carbone depuis la martensite est fini. Dans ce cas, il a été mis en évidence que la transformation bainitique est le processus limitant de l'enrichissement puisque la teneur maximale en carbone de l'austénite correspond au stasis, c'est-à-dire à la teneur en carbone critique pour laquelle la transformation bainitique s'arrête.

Afin d'augmenter l'enrichissement en carbone de l'austénite, il est nécessaire de faire en sorte que la partition du carbone depuis la martensite devienne le processus limitant de l'enrichissement. Dans notre cas, cela requiert de rejeter plus de carbone depuis la martensite.

Il y a deux façons d'obtenir un tel résultat. La première consiste à réduire la cinétique de précipitation du carbone dans la martensite, la seconde étant d'augmenter la vitesse de rejet du carbone depuis la martensite en affinant la microstructure. La cinétique de précipitation du carbone dans la martensite par rapport à la vitesse de rejet depuis la martensite est donc un paramètre important à contrôler.

La partition des éléments d'alliages depuis la martensite vers l'austénite pendant le traitement de Q&P a été étudié en couplant les expériences de DRX aux hautes énergies et celles de sonde atomique tomographique. Dans les premiers temps de l'étape de partition, une rapide et significative partition du carbone depuis la martensite vers l'austénite sans aucune partition du Mn et du Si a été observé alors que l'interface est immobile. Après un temps relativement court à 400°C, une partition claire du Mn a été observée à proximité de l'interface α'/γ . L'analyse conduite a permis de montrer que le manganèse équilibre son potentiel chimique pendant l'étape de partition ce qui soulève des questions quant à l'application du modèle du CCE pendant l'étape de partition.

Pour conclure, ces travaux de thèse montrent clairement l'effet des interactions complexes entre la précipitation du carbone dans la martensite, le rejet de carbone depuis la martensite et la transformation bainitique sur l'enrichissement en carbone de l'austénite pendant un traitement Q&P à 400°C. Il y a cependant deux points qui n'ont pas été abordés dans cette thèse. Le premier concerne l'influence de la ségrégation de carbone sur les défauts dans la martensite sur l'enrichissement final de l'austénite. A priori, cela pourrait être considéré comme un processus limitant l'enrichissement de l'austénite. Cependant, des calculs que nous avons menés récemment montrent un effet inverse : la ségrégation favorise la partition depuis la martensite vers l'austénite car elle a pour effet de ralentir la précipitation de carbures dans la martensite. A notre connaissance, cette interaction n'a jamais été reportée dans la littérature. Le deuxième point concerne les propriétés thermodynamiques de la martensite. Dans ces travaux, la martensite est considérée se comporter comme de la ferrite. En l'absence de carbures, le potentiel d'enrichissement dû au rejet depuis la martensite semble être surestimé car le potentiel chimique du carbone dans la martensite est plus bas que dans la ferrite. Il n'est donc pas certain que l'absence de carbures dans la martensite entrainerait automatique une augmentation de l'enrichissement en carbone de l'austénite.

Table of contents

GENERAL INTRODUCTION	16
CONTEXT OF THE STUDY	16
OBJECTIVES OF THE STUDY	18
CHAPTER I : LITERATURE REVIEW	20
I.1 QUENCHING AND PARTITIONING TREATMENT	21
I.1.1 <i>Austenite carbon enrichment and process parameters</i>	21
I.1.1.1 Influence of quenching temperature on the austenite fraction and carbon content	21
I.1.1.2 Effect of partitioning temperature and time on austenite fraction and carbon content	25
I.2 MICROSTRUCTURAL ANALYSIS	27
I.2.1 <i>Austenite</i>	27
I.2.1.1 Morphology of retained austenite	27
I.2.2 <i>Carbon trapping in martensite</i>	30
I.2.2.1 Segregation on defects	30
I.2.2.2 Carbides precipitation	34
I.2.2.3 Carbon content of martensite	40
I.2.3 <i>Bainite transformation in Q&P steels</i>	46
I.2.3.1 Differentiate bainite from martensite	46
I.2.3.2 Effect of preexisting martensite on bainitic transformation	48
I.2.3.3 Effect of quenching and partitioning temperatures on the bainitic transformation	49
I.3 MECHANISMS OF CARBON ENRICHMENT	50
I.3.1 <i>Partitioning from martensite and interface mobility</i>	50
I.3.2 <i>Partitioning from a bainitic source</i>	53
I.4 MODELING INTERACTION BETWEEN CARBON PARTITIONING AND COMPETING MECHANISMS	54
I.4.1 <i>Models without interactions</i>	54
I.4.2 <i>Models with interactions</i>	59
I.5 PARTIAL CONCLUSION	63
CHAPTER II : MICROSTRUCTURAL EVOLUTION	64
II.1 MATERIALS AND TECHNICAL CONSIDERATIONS	65
II.1.1 <i>Standard Q&P heat treatment</i>	65
II.1.2 <i>Optimum treatment parameters</i>	66
II.2 DILATOMETRIC STUDY	71
II.3 PHASE IDENTIFICATION BY IMAGE ANALYSIS: MORPHOLOGY CRITERIONS	74
II.3.1 <i>Metallographic preparation of the samples</i>	74
II.3.2 <i>Morphological differences between phases</i>	74
II.3.2.1 Carbide Free Bainite microstructure	75
II.3.2.2 Q&P microstructure	81
II.4 CARBIDES CHARACTERIZATION: COMPOSITIONAL (APT) AND STRUCTURAL (TEM) MEASUREMENTS	91
II.4.1 <i>Carbide compositional study by means of atom probe tomography</i>	91
II.4.2 <i>Carbide structural study by means of Transmission Electron Diffraction</i>	96
II.5 CARBON SEGREGATED IN MARTENSITE: APT STUDY	99
II.5.1 <i>Segregation during the initial quench</i>	100
II.5.2 <i>Segregation evolution at martensite lath boundaries during partitioning</i>	101
II.6 PARTIAL CONCLUSION	108
CHAPTER III : IN-SITU INVESTIGATION OF QUENCHING AND PARTITIONING BY HIGH ENERGY X-RAY DIFFRACTION EXPERIMENTS	110
III.1 EXPERIMENTAL SETUP	111
III.2 HEAT TREATMENTS	111
III.3 METHODOLOGY	112
III.3.1 <i>Nature and volume fraction of phases</i>	112
III.3.2 <i>Austenite lattice parameter and internal stresses</i>	117
III.3.3 <i>Carbon composition of austenite</i>	122
III.4 EFFECTS OF QT ON THE EVOLUTION OF MICROSTRUCTURES DURING QUENCHING AND PARTITIONING	124
III.4.1 <i>Evolution of the volume fraction of phases</i>	124
III.4.2 <i>Kinetics of carbon enrichment in austenite</i>	126
III.4.2.1 Evolution of austenite lattice parameter with QT	126
III.4.2.2 Evolution of carbon content in austenite with QT	129
III.4.2.3 Origins of the C enrichment in austenite	131

III.5 PARTIAL CONCLUSION.....	134
CHAPTER IV : EFFECTS OF COMPETITIVE REACTIONS ON C ENRICHMENT IN AUSTENITE DURING QUENCHING AND PARTITIONING AT 400°C.....	136
IV.1 INDIVIDUAL KINETICS MODELS.....	137
IV.1.1 <i>Carbon partitioning from martensite to austenite</i>	137
IV.1.1.1 General equations.....	137
IV.1.1.2 Numerical method.....	138
IV.1.2 <i>Carbide precipitation in martensite</i>	139
IV.1.2.1 Nucleation rate.....	139
IV.1.2.2 Growth rate	139
IV.1.3 <i>Bainite transformation</i>	140
IV.1.3.1 Nucleation of bainite	141
IV.1.3.2 Growth process.....	141
IV.2 THERMODYNAMICS ASPECTS, REPRESENTATIVE VOLUME ELEMENT AND MODEL COUPLING	142
IV.2.1 <i>Determination of the chemical potentials</i>	142
IV.2.2 <i>Representative volume element</i>	143
IV.2.3 <i>Coupling</i>	144
IV.3 RESULTS AND DISCUSSIONS	145
IV.3.1 <i>Kinetics of physical phenomena</i>	145
IV.3.2 <i>Carbon enrichment in austenite</i>	149
IV.3.3 <i>Critical carbon content into austenite at the end of partitioning step</i>	152
IV.3.4 <i>Avenues for increasing C enrichment in austenite</i>	154
IV.3.5 <i>Complementary investigation: Mn partitioning at the α'/γ interface</i>	155
IV.4 PARTIAL CONCLUSION.....	160
GENERAL CONCLUSION.....	162
BIBLIOGRAPHY	165

GENERAL INTRODUCTION

Context of the study

The need to reduce the fuel consumption of vehicles, improve passenger safety and the new global standards for the tailpipes emissions that converge towards lower gas emission force the automotive industry to rapidly develop new materials [1]. Even though new candidates for vehicles design emerge with low-density metals (Al and Mg based alloys), steel largely remains the first choice of the industry to face the new challenge in conception due to its versatility and cost [2] [3]. In terms of properties, the Body in White (BIW) parts of a vehicle (i.e. the skeleton of the car), must meet numerous and often contradictory constraints such as lightness, high formability while maintaining high strength, sufficient stiffness and all of this at relatively low price [4]. The so-called “Banana curve” (see Figure 0-1) sums up the challenge of optimizing both tensile strength and total elongation, the latter decreasing typically with increasing strength. The main goal being to reduce the thickness of the products, the tradeoff between formability and high strength are the properties that researchers try to optimize through the development of successive generation of Advanced High-Strength Steels (AHSS).

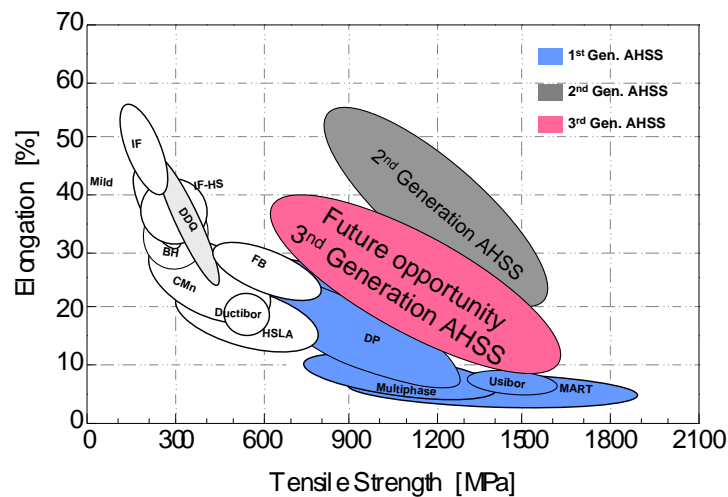


Figure 0-1 - Schematic representation of the different AHSS families.

Conventional High Strength Steels (HSS) mainly contain single-phase ferritic phases leading to pretty good formability properties thanks to the soft nature of the BCC-ferrite phase at room temperature but provide relatively low strength. Among them, we can cite Interstitial Free (IF), Bake Hardening (BH) or High Strength Low Alloy Steel (HSLA) [5]. Improving the strength of such steels is made difficult because the classical strengthening mechanisms such as solid solution, grain refinement and precipitation have generally a detrimental effect on both ductility and formability.

The Ultralight Steel Auto Body (ULSAB) project was launched in 1994 to boost the research towards increased safety, fuel efficiency through light-weighting of the vehicle structures [1]. It marks the beginning of the development of the so-called Advanced High-Strength Steels (AHSS). This new generation of steels allowed to break free from the traditional strength/formability curve and to produce steels with better balance between these proprieties [2], making it possible the production of thinner-gauged sheets capable of reducing the weight of the structure.

The new paradigm behind the AHSS generation is the tailoring of complex multi-phase microstructures obtained by the combination of carefully chosen chemical composition and heat treatments [1]. The two most important steels of AHSS's first generation are Dual Phase (DP) and Transformation Induced Plasticity (TRIP) steels. DP steels are a combination of a soft ferritic matrix with 10-40% of martensite or martensite-austenite present as islands. Such microstructures are obtained after a short annealing time in the intercritical domain in order to

form austenite that will transformed into martensite during the final cooling to RT. The strength of DP steels is tunable via the fraction of martensite. Their chemical composition is mainly low carbon (around 0.1wt.%) with manganese addition (approx. 1.5wt.%). This unique combination of ferrite and martensite allows to get continuous low yield strength (thanks to ferrite) while having high tensile strength (thanks to martensite) [2]. TRIP steels are also multiphased but combine ferrite, martensite and retained austenite. The presence of retained austenite at room temperature permits to attain really good uniform elongation. Indeed, as in DP steels, the dispersion of a hard second phase (martensite) creates a high work hardening rate. The retained austenite gradually transforms into martensite under stress, resulting in good work hardening rate at higher strain whereas hardening rate in DP drops at high strain values. Mainly composed of Carbon and Manganese, Silicon is also added (around 1.5wt.%) in TRIP grades in order to prevent any formation of carbides, an important source of carbon trapping. The carbon enrichment in austenite (and thus in retained austenite) is mainly done via bainite transformation. The level of carbon in austenite is a key parameter since it controls the strain level at which austenite begins to transform into martensite [1][4]. We can also cite Complex Phase (CP), Martensitic (MS) as a part of the 1st gen. of AHSS.

The second generation of AHSS acknowledge the importance of having austenite as one of the main phases in order to enhance the ductility and work hardening rate. TWinning Induced Plasticity (TWIP) steels use high amount of Manganese (15% to 30%) to obtain an austenitic structure stable at room temperature. Contrary to TRIP steels, the enhancement of strength properties comes from the deformation-nucleated twins formed in austenite during straining of the specimen. As a consequence, the dislocation mean free path is reduced leading to high strain-hardening effect. TWIP steels can combine both very high level of strength and ductility [2] (see Figure 0-1). However, the production of TWIP grade steels has proved to be very challenging due to their relatively high cost, the constraint on the purity of added species (phosphor and sulfur pollution/contamination can be very detrimental) or the rigorous control of the rolling and annealing temperatures [4].

It was within this overall context that third generation of AHSS was developed. They are certainly the most promising family of Advanced High Strength Steels (AHSS). They are considered by steelmakers as a breakthrough alternative to existing 1st generation high strength DP (Dual Phase) or TRIP (Transformation Induced Plasticity) steels as they could be used for manufacturing strategic parts of the body-in-white of cars with a significant lightweighting potential. It will permit to reduce their energy consumption and to comply with EU regulations regarding their CO₂ emission.

The viability of this scenario has for instance been demonstrated by the S-in motion initiative [6] and confirmed by Ron Krupziter, head of the AISI:

“... with the new third generation steels now under development, we expect to achieve more than 35 percent in structural mass reduction, which will significantly help automakers improve fuel efficiency and reduce greenhouse gas emissions.”

As its competitors, ArcelorMittal has a large part of its product development activity dedicated to 3rd Generation steel grades. Intensive discussions with car markers allowed establishing precise product targets and development timelines. The target is to develop a new steel grade family allowing 20% weight reduction compare to the present 1st generation AHSS commercialized solutions. Timelines are short meaning that a high efficiency in the development activity is needed. To do so, a strong need of knowledge is one of the keys of success.

Objectives of the study

As discussed previously, conventional DP or TRIP steels are actually produced on continuous annealing lines (including galvanizing lines). The microstructures of these steels are obtained from the decomposition of austenite during cooling from the intercritical range (so called soaking part of the annealing process) and are mainly composed of a ferritic matrix and bainite, martensite and retained austenite as second phases. In the particular case of TRIP steels, the thermal treatment includes also an isothermal bainitic holding in the range 400°C-500°C, which permits the stabilization of higher amount of retained austenite. The remarkable combination of high strength and formability of these steels is hence explained by a composite effect, between the soft ferrite and hard phases of the microstructures.

The ground-breaking properties of 3rd generation AHSS are achieved thanks to even more complex microstructures, which are at least duplex; i.e. made of a nanostructured matrix intricated with a large amount of retained austenite. The matrix provides the higher strength and toughness, while retained austenite explains the formability of the considered steels thanks to an efficient TRIP effect. These particular microstructures are also obtained from austenite decomposition during annealing but the temperature and the kinetics are incompatible for the time being with industrial practices. In 2003, a novel steel heat treatment termed “quenching and partitioning” (Q&P) has been proposed as an alternative way to obtain steels with a nanostructured martensitic matrix avoiding the bainitic transformation and permitting to retain also large amounts of austenite. The development of Q&P steels relies on a processing route, originally proposed by Speer et al [7], that involves quenching below the martensite start temperature (M_s) followed by a rapid heating and ageing above the initial quench temperature. The ageing step, usually performed between 300°C and 500°C, is also termed “partitioning step” since carbon enrichment in austenite is expected to occur during this stage. The benefits of such a treatment in terms of improved mechanical properties depends strongly on the austenite stability, and thus on the level of carbon enrichment in austenite during the partitioning step. Although the mechanisms of carbon enrichment in retained austenite during the partitioning step are still a matter of debate, strong evidences of carbon partitioning from martensite to austenite exist in the literature. The process of carbon enrichment is thus very original with respect to other AHSS such as TRIP steels. These steels have the potential to meet the weight reduction requirements needed to meet the new regulations for reduction of the CO₂ production in ground transportation, imposed by the European Commission by the year 2021. This new process, has been adopted by most of the main Asian steelmakers. The detailed industrial parameters have been derived from ‘end properties’ oriented investigations, with very limited basic knowledge.

This thesis work is a part of the ANR project ‘CapNano’, the goal of which is to provide a better fundamental understanding of the quenching and partitioning (Q&P) process, in the aim of optimizing the production of the next generation of AHSS. This project is conducted under the coordination of Sebastien Allain (Institut Jean Lamour, Nancy) with the partnership of two other public laboratories (Institut de Chimie de la Matière Condensée de Bordeaux, Bordeaux and Groupe de Physique des Matériaux, Rouen) and ArcelorMittal Maizières Research SA, Maizières-lès-Metz, as the industrial partner.

The combination of the multiple expertises in characterization technics developed by the different laboratories involved allowed to have a multiscale approach, providing a unique opportunity to give enlightments on the controversies related to the mechanisms involved in the Q&P treatment. More specifically, this thesis aims at developing a deeper understanding of the various mechanisms operating in the Q&P process, with a special attention paid to both kinetics aspects of carbon enrichment in austenite and microstructural evolutions. The multi-scale approach is based on both advanced technics (see Figure 0-2) and a mean-field modelling.

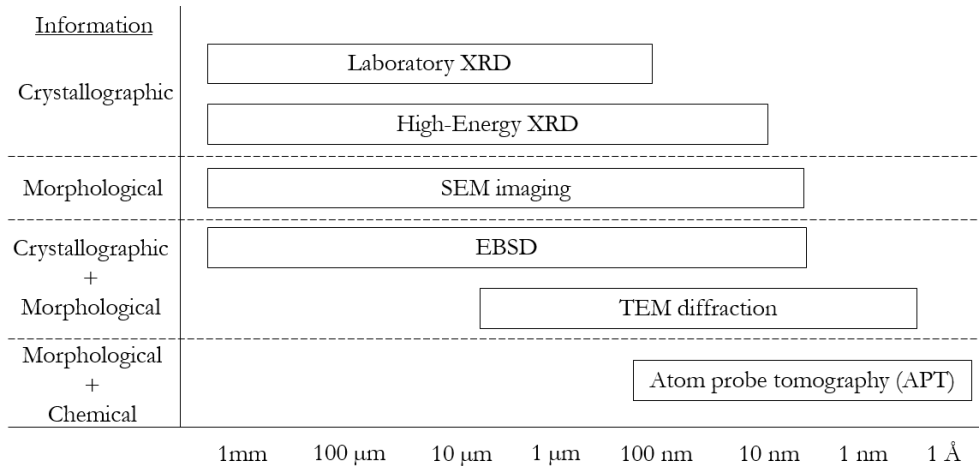


Figure 0-2 - Schematic representation of the multiscale approach adopted in this thesis. Redrawn from Burnett et al. [8]. The right-hand limit of each box indicates the highest resolution/slice thickness, and the left-hand limit the maximum sample size.

This thesis is divided into four chapters:

- The first chapter is a survey of the Q&P steels that gives an overview of the current knowledge on the impact of process parameters on the evolution of the microstructure, the microstructural characterization of Q&P steels as well as the competitive mechanisms behind the austenite carbon enrichment.
- The second chapter focusses on the microstructural characterization of a Q&P steel. Multiple experimental technics such as dilatometry, image analysis, electronic microscopies and atom probe tomography were coupled in order to obtain relevant informations on the microstructural evolution during a Q&P treatment. Particular attention will be drawn on the mechanisms taking place in martensite.
- The third chapter presents the contribution of in-situ High Energy X-Ray Diffraction (HEXRD) to the study, giving access to time-resolved precise quantitative information about phase transformations and lattice parameter evolutions. A particular emphasis will be drawn on the mechanisms of both austenite carbon enrichment and phase transformations.
- To rationalize the in situ High Energy X-Ray Diffraction experiments, an original theoretical approach was developed in chapter four. The results obtained and the analysis conducted give some clarifications regarding both the mechanisms of carbon enrichment into austenite and the effects of competitive reactions on the evolution of carbon enrichment into austenite during Q&P treatments.

Chapter I : LITERATURE REVIEW

Table of contents

I.1 QUENCHING AND PARTITIONING TREATMENT	21
I.1.1 AUSTENITE CARBON ENRICHMENT AND PROCESS PARAMETERS	21
I.1.1.1 <i>Influence of quenching temperature on the austenite fraction and carbon content</i>	21
I.1.1.2 <i>Effect of partitioning temperature and time on austenite fraction and carbon content</i>	25
I.2 MICROSTRUCTURAL ANALYSIS	27
I.2.1 AUSTENITE	27
I.2.1.1 <i>Morphology of retained austenite</i>	27
I.2.2 CARBON TRAPPING IN MARTENSITE	30
I.2.2.1 <i>Segregation on defects</i>	30
I.2.2.2 <i>Carbides precipitation</i>	34
I.2.2.3 <i>Carbon content of martensite</i>	40
I.2.3 BAINITE TRANSFORMATION IN Q&P STEELS	46
I.2.3.1 <i>Differentiate bainite from martensite</i>	46
I.2.3.2 <i>Effect of preexisting martensite on bainitic transformation</i>	48
I.2.3.3 <i>Effect of quenching and partitioning temperatures on the bainitic transformation</i>	49
I.3 MECHANISMS OF CARBON ENRICHMENT	50
I.3.1 PARTITIONING FROM MARTENSITE AND INTERFACE MOBILITY	50
I.3.2 PARTITIONING FROM A BAINITIC SOURCE	53
I.4 MODELING INTERACTION BETWEEN CARBON PARTITIONING AND COMPETING MECHANISMS	54
I.4.1 MODELS WITHOUT INTERACTIONS	54
I.4.2 MODELS WITH INTERACTIONS	59
I.5 PARTIAL CONCLUSION	63

I.1 Quenching and Partitioning treatment

The Quenching and Partitioning (Q&P) treatment was introduced by Speer in 2003 as an innovative approach to produce 3rd generation of Advanced High Strength Steels. The process, as illustrated in Figure I-1, is mainly composed of three steps [7]:

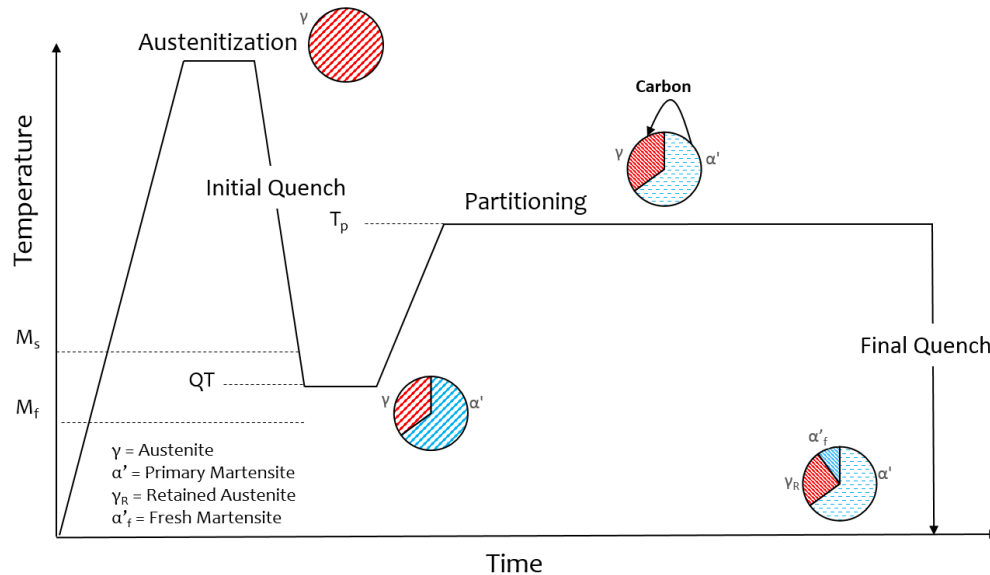


Figure I-1 - Thermal path and phases of a Q&P treatment

- an initial quench (IQ) from the austenitic domain or from the intercritical domain down to the Quenching Temperature (QT), between M_s and M_f respectively the martensite start and finish temperatures) in order to form a controlled amount of martensite (f_M^0). At this point, the microstructure consists of martensite and untransformed austenite (f_γ^0),
- a reheating to the Partitioning Temperature (PT) for a given duration (called Partitioning time, Pt)
- lastly, a final quench (FQ) down to Room Temperature (RT).

The final microstructure of a Q&P steel is expected to be composed of tempered martensite, fresh martensite and a significantly carbon-enriched retained austenite.

This multi-phase structure gives to the Q&P steels their outstanding mechanical properties. Indeed, the martensite brings high strength, whereas the retained austenite (RA), thanks to the TRansformed Induced Plasticity effect, brings ductility [9].

I.1.1 Austenite carbon enrichment and process parameters

The main goal of the Q&P process being the stabilization of austenite at RT through carbon enrichment, the impact of the different process parameters on the amount of RA and its carbon content are of primary concern.

I.1.1.1 Influence of quenching temperature on the austenite fraction and carbon content

I.1.1.1.1 Optimum Quenching Temperature

The amount of carbon that can be transferred from martensite towards austenite during the partitioning step depends on the martensite phase fraction at QT. As the amount of martensite formed at this point only depends on the undercooling degree at QT (i.e the ΔT between QT and M_s), it is possible to develop a simple model to find the optimum QT leading to the maximum enrichment of austenite.

The amount of martensite formed at QT can be calculated using the well-known Koistinen-Marburger (KM) relationship [10] :

$$f = 1 - \exp(-\alpha_m(M_s - QT)) \quad (I.1)$$

where f is the fraction of martensite formed at QT, α_m is a chemical-dependent coefficient and M_s is the martensite start temperature.

The K-M equation requires the knowledge of the values of M_s et α_m to derive f. VanBohemen conducted a study in order to reassess the equations for M_s and α_m as a function of temperature and steel concentration in order to better fit the experimental observations, especially for high-carbon steels (taken on 115 different steels with C content ranging from 0.17 to 1.8 wt%) [11]. As the final martensitic transformation in the Q&P process takes place in a carbon-enriched austenite, this reassessment is particularly important for Q&P steels. Based on their work, the following relation was established:

$$M_s(^{\circ}C) = 565 - \sum_i K_i x_i - 600[1 - \exp(-0.96x_c)] \quad (I.2)$$

where $\sum_i K_i x_i (^{\circ}C) = 31x_{Mn} + 13x_{Si} + 10x_{Cr} + 18x_{Ni} + 12x_{Mo}$

where x_x is the composition in wt% of the element X

As highlighted by Van Bohemen (see Figure I-2), the dependence of M_s on carbon content follows an exponential declining law, and not a linear one, as initially claimed by Andrews [12]. This new description of M_s is of significant importance for austenite with high carbon content (as austenite encountered in Q&P steels), a range of concentration that was poorly described with the prior linear relations.

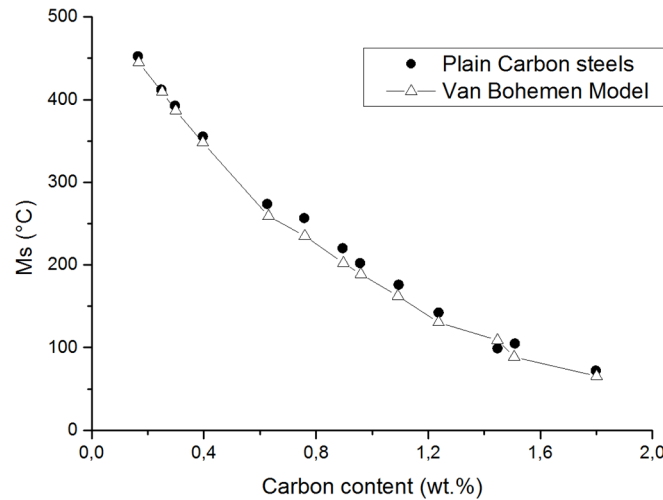


Figure I-2 - Evolution of the M_s temperature with carbon content for 14 plain carbon steels, together with the calculated values using Van Bohemen exponential model for M_s (redrawn from [11])

Later, Barbier compiled most of the classical relations linking M_s to steel's chemical composition and, from measurements by dilatometry, he proposed a new relation between M_s and alloying elements including W and Cu. This work does not question the one of Van Bohemen and al. Indeed, for Q&P steel (with pretty common alloying elements) it is shown that Van Bohemen relation remains very appropriate even if, as shown in Figure I-3, Barbier's relation gives a more narrow distribution around the experimental values of M_s [13].

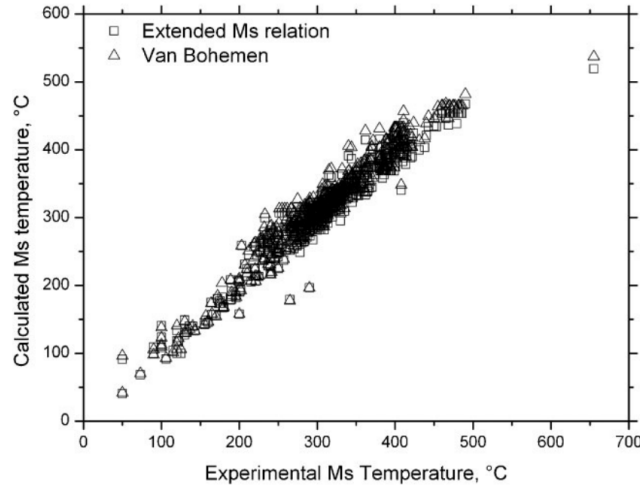


Figure I-3 - Comparison of the experimental Ms values with the ones predicted by Barbier's (named extended Ms relation) and Van Bohemen's relations (taken from Barbier et al. [13])

As an example, Van Bohemen relationship indicates that an hypothetical steel of composition 0.3C-2.5Mn.1.5Si (wt%), has a Ms temperature of 317°C. If after partitioning, the austenite carbon composition is raised to 1.5%, the Ms temperature drops below room temperature, potentially hindering any further martensite formation during the final quench.

Besides, Van Bohemen also reconsidered its own linear equation for the determination of α_m that was released in ref. [14] in 2009 (previously α_m was considered as an universal constant equal to 0.011). Indeed, as for Ms, an exponential dependence on x_c was introduced in the calculation of α_m and provides a better fit, particularly for the low and high carbon steels (cf Figure I-4).

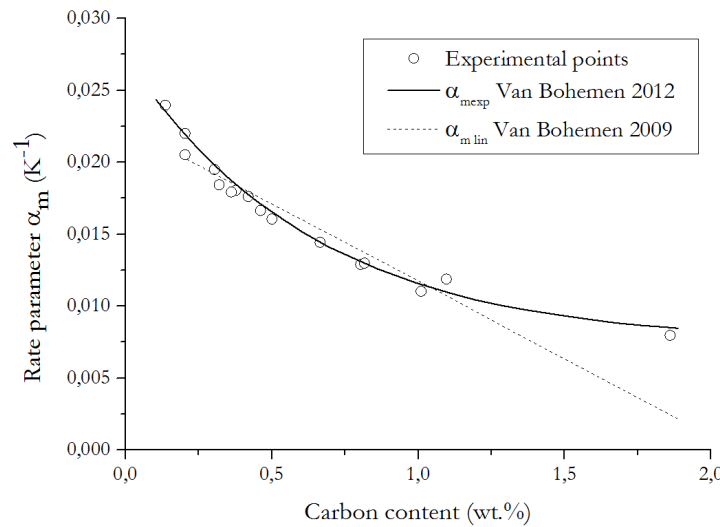


Figure I-4 - Comparison between the linear and exponential equation for the calculation of the rate parameter as a function of carbon concentration (open circles : values evaluated in [15])

The α_m coefficient obtained is given by:

$$\alpha_m (\times 10^{-3} K^{-1}) = 27.2 - \sum_i S_i x_i - 19.8 [1 - \exp(-1.56x_c)]$$

with

$$\sum_i S_i x_i = 0.14x_{Mn} + 0.21x_{Si} + 0.11x_{Cr} + 0.08x_{Ni} + 0.05x_{Mo}$$

As expected, the previous relationships indicate that lowering QT increases the fraction of initial martensite. For our hypothetical steel, the fraction of martensite formed would be 30%, 50% and 90% for respective QTs of 300°C, 280°C and 200°C.

Increasing the amount of martensite formed before partitioning (by a large undercooling under M_s for example) allows to increase the amount of carbon available to stabilize austenite. However, this is done at the expense of the amount of austenite remaining after QT, resulting in less residual austenite but potentially very rich in carbon. On the other way, an initial quench with QT closer to M_s results in more austenite available for the partitioning step, but in a smaller reservoir of carbon. The amount of martensite formed might not provide enough carbon to stabilize the austenite below room temperature. Consequently, a significant amount of residual austenite will transform into fresh martensite during the final quench, according to the K-M relationship (calculated with the new austenite carbon content after partitioning). Consequently, an optimum QT must exist, leading to the ideal balance between the amount of austenite and its carbon content leading to the higher retained austenite fraction after the final quench. Speer et al. proposed a simple approach to estimate the optimum QT, based on a theoretical approach [16]. Their approach is based on the following assumptions:

- all competing phase transformation mechanisms affecting the carbon mass balance are precluded (bainite transformation and carbide precipitation),
- all the carbon contained in martensite partitions towards austenite.

The evolution of the retained austenite fraction (γ_{final}) can thus be plotted as a function of QT (Figure I-5) after different steps that can be decomposed, for a given QT, in the following way:

- 1) calculation of the fraction of α' formed during the initial quench at QT (curves $M_{\text{initial quench}}$ and $\gamma_{\text{initial quench}}$ in the Figure I-5) using the K-M equation,
- 2) calculation of the carbon content in austenite assuming that all the carbon from α' partitions into retained γ (dashed curved % Carbon in the Figure I-5),
- 3) re-application of the K-M equation to C-enriched retained austenite to determine the fraction of martensite formed from residual austenite during the final quench,
- 4) subtraction of the amount of freshly formed martensite to $\gamma_{\text{initial quench}}$ to obtain the final amount of retained austenite at room temperature for any given original QT.

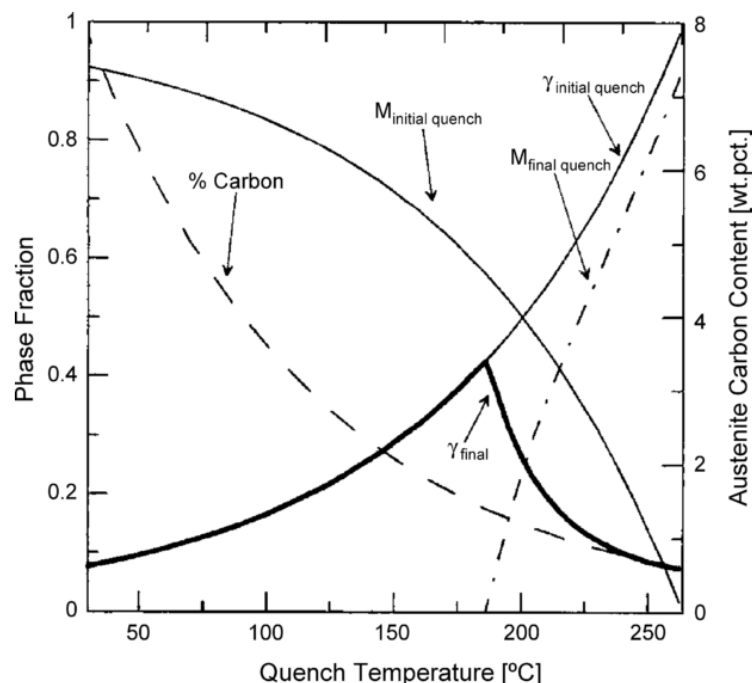


Figure I-5 - Graph of the different curves leading to the final fraction of retained austenite as a function of QT for a 9260 alloy steel (0.5C-0.9Mn-2.0Si in wt.%) (taken from Speer et al. [16])

The maximum of the γ_{final} curve defines the optimum QT, as the higher RA phase fraction is the goal of the Q&P treatment.

I.1.1.1.2 Experimental observations

QT is a key process parameter since it controls the phase fractions of martensite and austenite, and thus the amount of carbon available to partition from martensite to austenite. As QT decreases (high f_M^0 , low f_Y^0), a larger amount of carbon (from martensite) is available to enrich a smaller fraction of austenite during the partitioning step, leading to higher austenite carbon content (X_C^Y) after partitioning. This “downward” trend of X_C^Y with increasing QT was indeed reported in the literature [17][18]. However, some recent studies showed another evolution of X_C^Y with QT. For example, Santofimia et al. tested several QT (from 130°C to 316°C) before a partitioning step of 100s at 400°C on a low carbon steel (0.2C-2.5Mn-1.5Si in wt.%) [19]. Based on XRD measurements, the austenite carbon content at RT was identical for each QT condition. Contrary to the expected trend predicted by the Speer method (see section I.1.1.1.1). This behavior was later confirmed by Toji et al. on a higher carbon steel (1.07C-2.9Mn-2.2Si-0.048Al in wt.%) and by Liu et al. on a low carbon steel (0.3C-3.0Mn-1.5Si in wt.%) [20][21]. Toji et al. gave an explanation for this constant X_C^Y , based on cementite precipitation in martensite [20]. This point will be discussed in section I.4.2.

Regarding the amount of retained austenite after various Q&P cycles, as illustrated in Figure I-6, all the experimental studies reported in the literature showed the trend predicted by the Speer method, presented in section I.1.1.1.1) with an optimum QT value maximizing the retained austenite fraction.

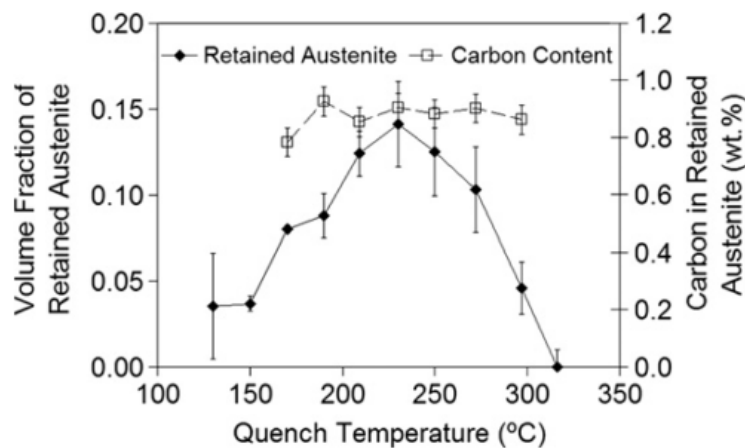


Figure I-6 - Volume fraction and carbon content of retained austenite with QT (PT/t=400°C/100s) (from Santofimia et al. [19])

I.1.1.2 Effect of partitioning temperature and time on austenite fraction and carbon content

The optimum quenching temperature being set, the two remaining Q&P treatment parameters, namely partitioning temperature (PT) and time (Pt), must be chosen. Numerous experimental studies dealt with this issue. Even though the chemical composition of the investigated steels varied, some general trends can be observed. Choosing the right temperature for the partitioning step is not obvious. Indeed, if PT is too low, the carbon atoms will not have enough mobility to rapidly diffuse into austenite. As showed in Figure I-7 a) (PT=400°C), the peak in RA (measured as ~14% of total iron Fe by Mössbauer spectrometry) is reached after 50s, leading to an austenite carbon content of ~5at% (Mössbauer measurement).

By increasing PT (as in Figure I-7 b)), the increase of carbon mobility results in an earlier and higher RA peak (18at% around 30s) for the approximately same X_C^Y . Thus a greater amount of carbon is partitioned at 450°C.

However, a higher PT leads to a steeper drop of f_Y for longer partitioning time due to the higher risk of austenite decomposition at such high temperature (lowering X_C^Y due to carbide formation

in the case of lower bainite transformation) [19] [22].

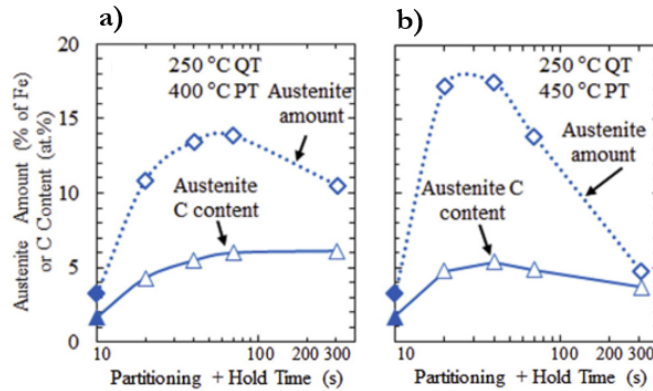


Figure I-7 – Evolution of austenite amount and carbon content for two different PT ($QT=constant$) (taken from Pierce et al. [22])

Once the PT is chosen, the effect of the partitioning time can be isolated. Generally, and as illustrated in Figure I-8, a peak in f_Y and X_C^Y is reached in the first 100s (the higher the PT, the sooner it appears, as discussed previously). However, with increasing Pt, austenite decomposition can occur and drops in f_Y and X_C^Y happen. This may be attributed, respectively, to bainite formation and carbide precipitation [23]. It is worth noting that, in some cases, for long partitioning times, a second peak of carbon enrichment can appear, due to possible dissolution of carbides formed in the early stage of partitioning, providing a new source for austenite stabilization [24][25].

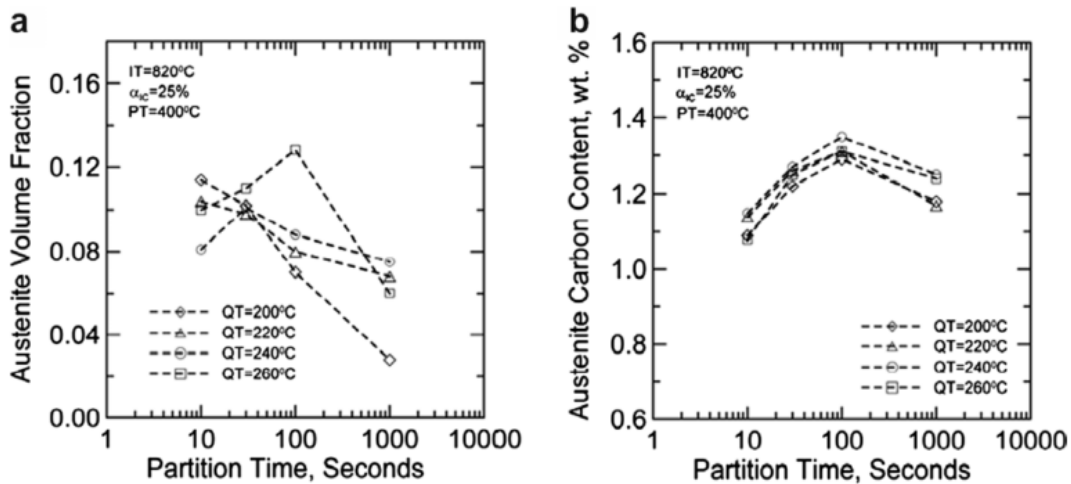


Figure I-8 – Impact of Pt on austenite volume fraction and carbon content (taken from Clarke et al. [23])

I.2 Microstructural analysis

Microstructural analysis of Q&P steels is particularly challenging, because of the many possible phases that can form during the process, and their morphological similarities. The resulting microstructure can be seen in Figure I-9 and proves to be very complex. Indeed, the resulting microstructure may include retained austenite, tempered martensite (either from the IQ or FQ), fresh martensite and bainite.

The QT, PT and Pt values will impact both fraction and morphology of the different phases. In order to characterize the final microstructure, it is thus necessary to find criteria to determine the nature of each phases, and allow their respective fractions to be estimated.

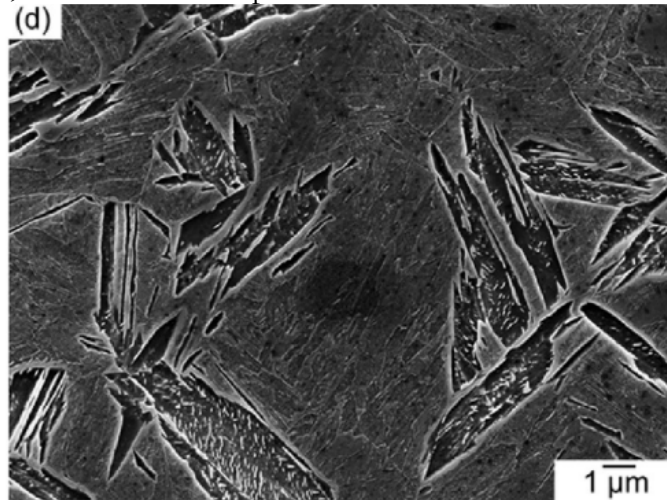


Figure I-9 - Q&P microstructure (taken from Hajyakbary et al. [26])

I.2.1 Austenite

The fact that austenite is the only FCC phase present in the final Q&P microstructure makes its identification and study pretty straightforward thanks to crystal structure discriminating technics such as XRD or EBSD.

I.2.1.1 Morphology of retained austenite

Austenite may be present in the final microstructure under different morphologies [17][21][27][28] :

- retained austenite films (approx. 50nm wide), located between martensite laths,
- blocky Martensite/Austenite islands (MA) of various sizes up to 500nm,
- ultra-fine retained austenite (20-30nm thick) distributed in the bainitic matrix.

In order to understand how these different morphologies are formed, it is necessary to study what is happening during the initial quench. Liu et al. studied how the martensitic formation at QT can refine austenite grain before the partitioning step [21]. Indeed, once the Ms temperature is reached, an initial martensitic transformation burst creates the first large laths of martensite that will grow across the austenite grains. Upon further undercooling under Ms, smaller laths will auto-catalytically grow between the previously formed larger laths, resulting in a refinement of the austenite blocks. It is thus unlikely to find large austenite islands at low QT, because of the high amount of small α' laths fractioning the parent austenite phase. This shows that the level of undercooling at QT controls the initial duplex γ/α' microstructure, and thus the morphology of the remaining austenite before the partitioning step. Liu et al. used EBSD to study the refinement of austenite after martensite formation. In Figure I-10, austenite is represented in blue and martensite in red. It appears that a lower QT leads to finer RA, while a higher QT results in more blocky RA islands.

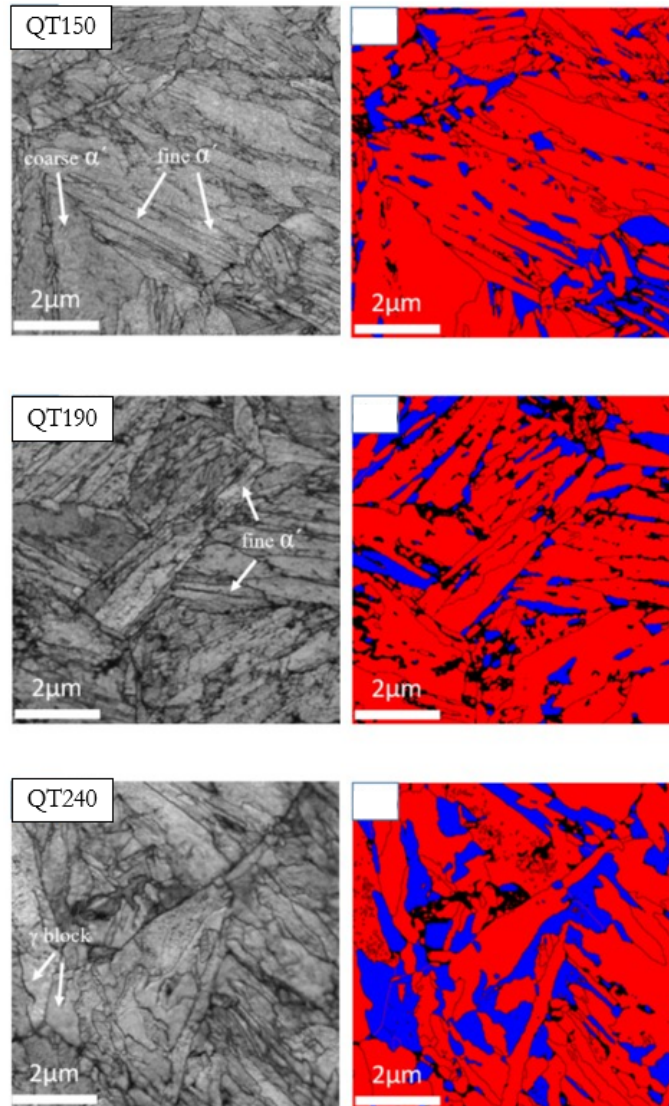


Figure I-10 - Austenite morphology at various QT (first column is band contrast, second column is phase maps blue: austenite red: martensite, adapted from Liu et al. [7])

In addition to its carbon content, the morphology of austenite will also play an essential role on its behavior during the final quench. Indeed, in order to attenuate the transformation strain induced by the martensitic transformation, martensite forms via a stratified structure (packets \rightarrow blocks \rightarrow laths) with multi-variants in the Prior Austenite Grain (PAG), leading to the minimization of the total strain energy. However, Takaki et al. showed that if the size of the PAG is reduced enough to be of the order of a martensite lath, multi-variant structure is then impossible to form, leading to a simplified structure as shown in Figure I-11 [29].

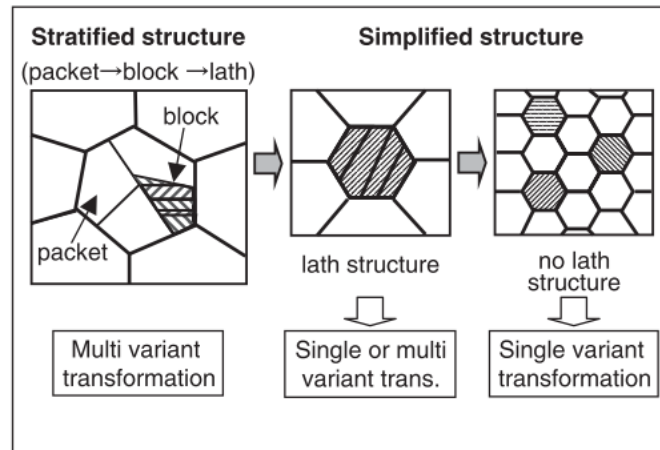


Figure I-11 - Schematic illustration showing the transition from multi to single variant transformation depending on the austenite grain size (taken from Takaki et al. [29])

Figure I-12 shows that once the PAG is smaller than $1\mu\text{m}$, a huge amount of elastic strain energy is needed to nucleate a martensite lath in a single variant mode. This energy barrier is enough to completely hinder martensitic transformation in very fine austenitic grains. Interestingly, this effect is only observed for athermal martensite formation and not for transformation-induced martensite. Indeed, during deformation, the lath already tends to form under the single variant mode in order to accommodate the anisotropic strain induced by the tensile strain applied on the phases.

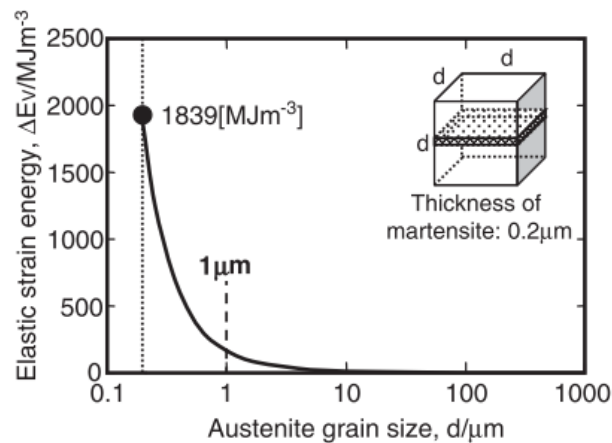


Figure I-12 – Relation between austenite grain size and elastic strain energy required for nucleation of thin plate-martensite (taken from Takaki et al. [29])

Using High-Energy Synchrotron X-Ray to study the stability of retained austenite in Q&P Steels, Xiong et al. showed that despite its lower carbon content, film-like RA is more stable than blocky RA during deformation [30]. This might be due to the fact that higher hydrostatic pressure can be exerted on the film-like austenite than on the blocky austenite, mechanically increasing the stability of austenite. Furthermore, the film like austenite was surrounded by lath martensite (the blocky one were surrounded by proeutectoid ferrite) thus providing a shielding effect that make the necessary volume expansion accompanying martensite formation impossible to be accommodated.

The benefit of having film-like RA in the microstructure was also recently highlighted by Liu et al. who demonstrated that steels with lower f_γ but with larger amount of film-like RA showed better mechanical properties than steels with higher f_γ (and similar X_C^γ) but more blocky RA [21]. Therefore, the thermal path for Q&P steels (including QT) must be chosen to provide enough volume fraction of austenite but with the appropriate balance between the different

morphologies of RA to obtain the best mechanical properties.

I.2.2 Carbon trapping in martensite

The benefits of Q&P treatments in terms of improved mechanical properties depend on the austenite stability and thus on the level of carbon enrichment in austenite during the partitioning step, which, in turn, relies on the carbon transferred from martensite to austenite. It is thus obvious that any carbon trapped in martensite cannot contribute to the austenite enrichment. Therefore, any competing mechanisms of carbon trapping within martensite can only be detrimental to the primary goal of the Q&P treatment.

This section aims at giving a large view on the different phenomena that can be a potential source of carbon trapping in martensite along the Q&P process.

I.2.2.1 Segregation on defects

Even before the aging and tempering steps, martensite formed at M_s starts to undergo internal carbon redistribution phenomena until QT, that is the auto-tempering effect [31]. McLean treated equilibrium solute segregation in term of the lattice distortion energy around solute atoms [32]. Grain boundaries, and more generally defects, provide regions that supply already distorted sites, and thus are preferential sites to relieve the strain energy generated by the carbon atoms in the octahedral site of the α' matrix. Carbon atmospheres around dislocations are commonly named Cottrell atmospheres [33]. Segregation is thus defined as a redistribution of solute atoms (mainly carbon in our study) between the bulk and a defect of the structure (being dislocations, grain/lath boundaries, vacancies). The equilibrium is reached when the carbon chemical potential is homogenous through the system. This translates into the following equation, known as the McLean equation, for the equilibrium of carbon atoms between the defect and the matrix:

$$\frac{X_c^d}{X_{C-max}^d - X_c^d} = \frac{X_c^b}{1 - X_c^b} \exp \frac{E_S}{RT} \quad (I.3)$$

where X_c^d is the atomic fraction of carbon on the defect, X_{C-max}^d is the maximum atomic fraction of carbon that the defect can accommodate, X_c^b is the atomic fraction of carbon in bulk far away from the defect, and E_S is the segregation energy on the defect.

The term X_{C-max}^d reflects the fact that in a distorted lattice, there are sites, so-called ‘‘forbidden sites’’, not available for carbon to segregate.

In order to calculate the interaction energy between a carbon atom and a dislocation, Cochardt et al. used the elastic theory approach [34]. This theory was largely used because of its capacity to estimate the interaction energy between interstitials and defects by using the calculation of the elastic field around a defect and the elastic distortion of the host lattice (often Fe cubic lattice) due to the interstitial (often carbon) [35][36]. The elastic theory is appropriate because martensite lattice parameter is a linear function of carbon content. In addition, martensite elastic constants can be assumed composition independent when $X_C^{a'} < 11\text{at.}\%$. [37][38].

Cochardt et al. first considered the strain tensor S_C of a iron unit cell containing one carbon atom by considering that the introduction of a carbon atom induces a tetragonal distortion of the lattice as [34]:

$$S_C = \begin{pmatrix} \delta_a & 0 & 0 \\ 0 & \delta_b & 0 \\ 0 & 0 & \delta_c \end{pmatrix} \quad (I.4)$$

where S_C is the strain tensor associated with the introduction of a carbon atom in the iron cell and where

$$\delta_a = \delta_b = -0.026, \quad \delta_c = 0.38$$

These coefficients represent the expansion concentration coefficient (in $\text{\AA}\cdot\text{wt.}\%$) and link the evolution of the a, b and c lattice parameters of the BCT martensite and the atomic fraction x_C of carbon atoms by the following relations:

$$\begin{aligned} a(x_c) &= b(x_c) = a_0(1 + \delta_a x_c) \\ c(x_c) &= a_0(1 + \delta_c x_c) \end{aligned} \quad (I.5)$$

The values of δ_a (or δ_b) and δ_c can be obtained either by experimental measurements (by linear fitting of XRD experiments for example [32][33]) or by simulation, Table I-1 sums up the values encountered in the literature.

Table I-1 - Values for δ_a and δ_c from the literature

	Method	δ_a or δ_b	δ_c
Cheng et al. [39]	Experimental	-0.094	0.85
Clouet et al. [41]	Atomistic simulation	-0.088	0.56
Chentouf et al. [38]	Ab-initio	-0.025	0.84
Douthwaite et al. [42]	Experimental	-0.07	0.83
Cochardt et al. [34]	Experimental	-0.052	0.76
Bacon et al. [43]	Experimental	-0.0977	0.862

The interaction energy is then calculated by tetragonally expanding a unit cell of the crystal near a dislocation (that possesses its own stress tensor). The interaction energy is equal to the work that is necessary to move each face of the crystal on a distance, d_i , against the force, F_i , that is exerted by the dislocation [34].

Cochardt et al. calculated that for both screw and edge dislocations, the maximum interaction energy of a carbon atom at a distance of one Burger vector is 0.75eV. The authors pointed out that applying elastic equations near the dislocation core might lead to an overestimation of this maximum interaction energy (Cottrell and Mott estimated that this value might be closer to 0.5eV) [44][45]. Clouet et al. later compared these elastic calculations with atomistic simulations and showed that for dislocations and octahedral sites situated at a distance larger than 2 Å, the binding energy is equal to 0.41eV for a screw dislocation and 0.66eV for an edge dislocation [41]. It is possible to represent the redistribution of carbon around a dislocation by a simple geometrical construction as shown by Kalish and Cohen, and presented in Figure I-13 [46]. The dislocation creates an interaction zone (for $r < r_i$) that is directly related to the maximum binding energy of the dislocation.

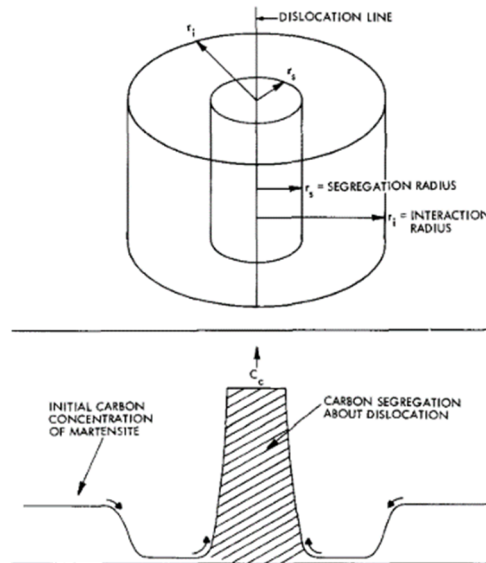


Figure I-13 - Representation of carbon-segregation distance (r_s) and interaction distance (r_i) and corresponding carbon-concentration gradients around a dislocation (from Kalish et al. [46])

Indeed, as suggested by Cochardt, carbon atoms are bounded to the dislocation only when U_{DC}

(interaction energy between the dislocation and carbon atoms) is larger than the thermal energy $k_B T$. The radius R of the region where carbon interacts with the defect is given by:

$$R = \frac{A}{k_B T} \quad (I.6)$$

with A , a constant given by :

$$A = \frac{\sqrt{2} b G a^3}{3\pi} (\delta_c - \delta_b) \quad (I.7)$$

where a is the lattice parameter, b is the Burgers vector as $\frac{1}{2}\sqrt{3}a$, δ_c is the c-direction part of the strain tensor in Eq. (I.4), δ_b is the b-direction part of the strain tensor in Eq. (I.4), G is the shear modulus of iron.

By using the relation between A and E_s (for $r=b$):

$$A = E_s b \quad (I.8)$$

With E_s , the interaction energy between dislocations and carbon atoms

We can calculate the maximum radius of interaction of a dislocation with an interaction energy E_s :

$$R = \frac{E_s b}{k_B T} \quad (I.9)$$

Such trapping phenomena on defects are strong enough to hinder the precipitation of transitional carbides during the first stage of tempering. Indeed Kalish et al. calculated that for a steel with less than 0.2 wt.%C, about 85% of the available carbon is trapped by dislocations and as the carbon/dislocation binding energy is higher than the one of carbon/ ϵ -carbide (0.27eV), carbon will not move away from dislocations to form precipitates [47]. Once the temperature is high enough to lower the radius of interaction, carbon will be released from dislocations, and available for precipitation.

Thomas et al. used Atom Probe Tomography (APT) to follow the carbon redistribution process at low temperature (<Ms) [48]. They were able to highlight pretty advanced segregation of carbon atoms in as-quenched sample (from the fully austenitic state) in the form of clusters in the α' laths (cf Figure I-14) and segregations within the martensitic structure. As-quenched sample of Q&P steels were also investigated by APT by Toji et al. (Figure I-15), fluctuations of the carbon concentration were noticeable (between 1.5%at and 4.5%at) with enriched zones of about 8-10 nm, thus comparable with Cottrell atmospheres already measured by Wilde et al. [49][50].

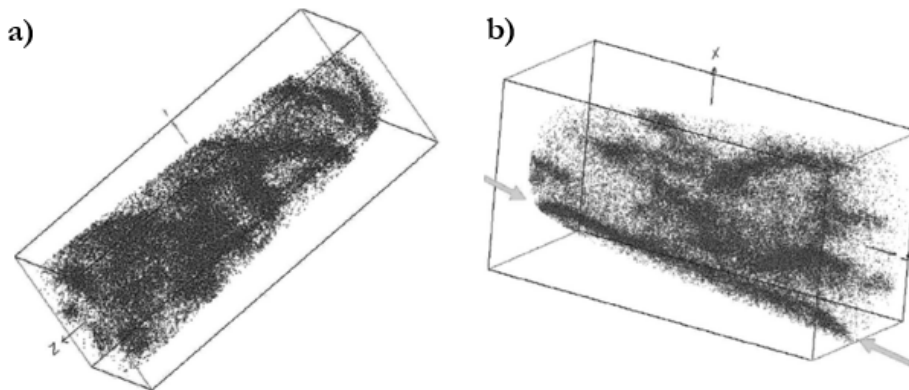


Figure I-14 - a) Carbon distribution of the as-quenched condition b) Carbon distribution of the as quenched condition with a carbon segregation on a martensite lath, indicated by the grey arrow (taken from Thomas et al. [48])

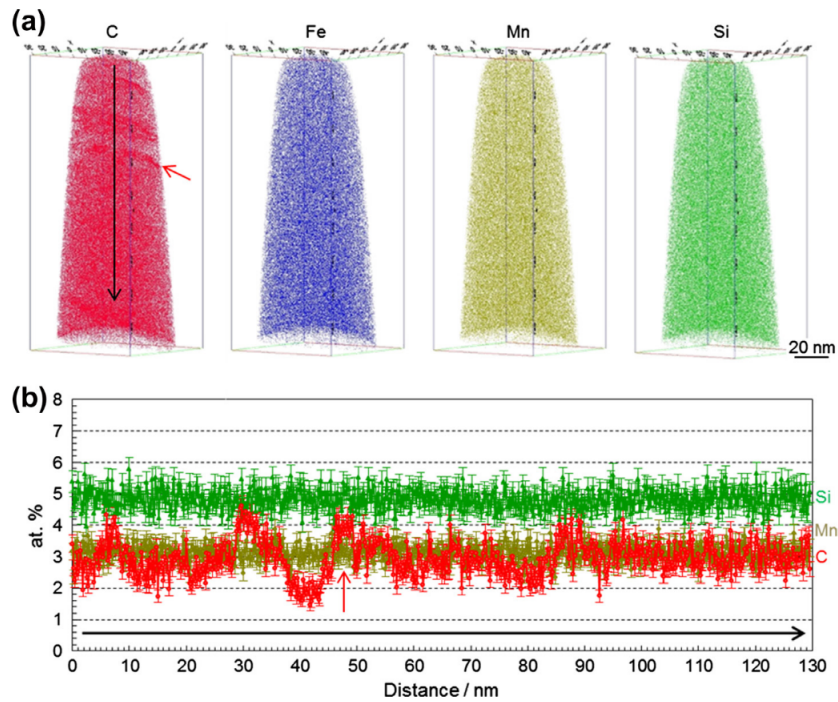


Figure I-15 - (a) Atom maps of C, Fe, Mn and Si of an as-quenched Q&P steel showing segregated zones of C - (b) C, Mn and Si concentration profiles along the black arrow direction indicated in (a) (Taken from Toji et al. [49])

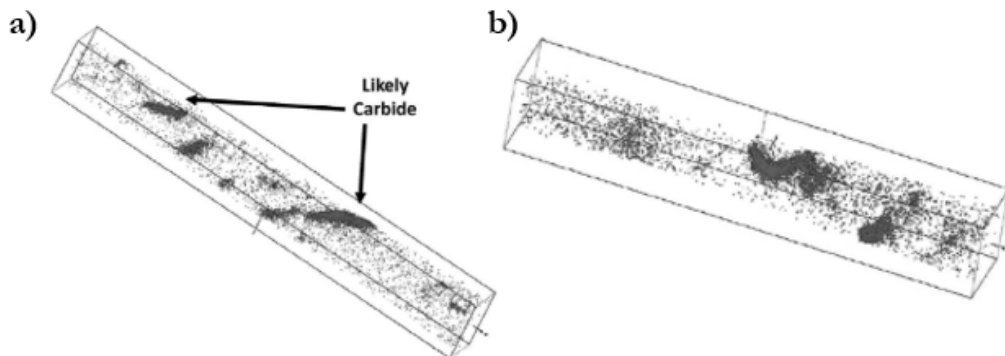


Figure I-16 - Carbon distribution in martensite after partitioning at PT/ $t=400^{\circ}\text{C}/100\text{s}$ (taken from Thomas et al. [48])

It is common during Q&P treatments to hold the sample a few seconds at QT before the reheating step in order to obtain a good temperature homogenization of the sample. Hence, it is likely that some ageing phenomena can occur during this step due to the fact that carbon is enough mobile to migrate on tens of nanometers (depending on the holding time). Indeed, Nagakura et al. noted the appearance of diffuse spikes around the fundamental martensite spots on an electron diffraction pattern of an as-quenched sample (1.1wt%C) [51]. These spikes would be due to the formation of interstitial carbon clusters (short range ordering). Indeed further studies on these diffuses spikes showed carbon clusters of about 10 Å spaced out by 6 to 8nm. After operating aging treatment (in the 0 – 90°C range), satellite spots starts to appear on the electron diffraction patterns which are caused by the arrangement of previous carbon clusters to form a modulated structure (“tweed like”) that consist of an arrangement of carbon rich (approx. 10at.%C) and poor regions which wavelength depends on the steel’s carbon content. However, above 1wt%C (4.7at.%C), the wavelength of this arrangement becomes constant (i.e is no longer function of the carbon content) and equal to 1nm [52]. Taylor et al. also showed that diffuse

scattering centered about the fundamentals reflection of martensite occurs and explained that this modulated structure develops through a spinodal mechanism [53][54].

Some recent APT studies bring enlightments on the formation kinetics of the modulated structure [55][56]. Indeed, early in the aging process, carbon segregates first on the dislocations to form Cottrell atmosphere (about 8 to 9 at.%C) on a radius of 7nm and with the increase of the temperature, clusters gradually forms (about 14at.%C) along the dislocations [50]. These clusters can be the onset of the incoming transitional carbides, as in Figure I-16, formed during the first stage of tempering (or during the hold at PT in Q&P steels for example). Indeed, even after partitioning at 400°C for 300s, carbon clusters of 5-50 nm in size and with a maximum level of carbon of 10 at.% are observed by APT in Pierce's study [57].

I.2.2.2 Carbides precipitation

The question of carbide precipitation during Q&P treatment is crucial because the carbon trapped in carbides is no longer available to enrich and stabilize the austenite. The first characterization of transitional carbides formed in tempered martensite was based on X-ray diffraction analysis by Jack et al. with diffraction data close to other hexagonal phases (such as Fe_3N and Fe_2N) [58]. Thus, the newly named "ε-carbide" was attributed a chemical composition between Fe_2C and Fe_3C . Later, TEM work of Nagakura et al. confirmed an hexagonal structure for this transitional carbide [59]. Ruhl and Cohen estimated the composition to be $\text{Fe}_{2.4}\text{C}$ by using the atomic volume per iron atom but, as pointed out by Jack, this is very sensitive to the unit-cell dimensions chosen and the stoichiometry might be closer to Fe_3C [60][61]. However, another electron diffraction study by Hirotsu and Nagakura showed the presence of a orthorhombic transitional carbide isomorphous to Co_2N and Co_2C [62]. Therefore, they named this transitional carbide "η-carbide" with a chemical composition of Fe_2C .

Even though silicon is added in Q&P steels to prevent cementite formation (and in a lesser extent transitional carbides), numerous studies point out the fact that a high density of carbides is present within the martensite laths. Indeed, the modulated structure of carbon atoms formed before the partitioning step would facilitate the formation of transitional carbides even if the way they form is still not clear. Indeed, Taylor et al. explained that carbides nucleate heterogeneously along the carbon rich zones induced by the spinodal decomposition (and not on the dislocations) whereas Génin showed that the modulated structure is in fact made of what he called « extended multiplet » which will then transform into carbides[53][56][57]. Some recent APT studies tend to confirm that the clusters gradually transform into transitional carbides with a stoichiometry close to ε and η carbides [55].

Concerning transitional carbide nature, Lu et al. studied the carbon redistribution in the martensitic phase of an as-quenched Fe-15Ni-1C (wt.%) alloy after 2-3 years of aging at RT [65]. They compared TEM Small Angle Diffraction (SAD) patterns obtained along three zone axes of martensite ($\langle 113 \rangle$, $\langle 111 \rangle$ and $\langle 100 \rangle$), with simulated SAD patterns of ferrite + four types of carbides (θ, ε, η and γ). The best match was obtained for the η- Fe_2C carbide.

It must be highlighted that the exact stoichiometry of ε (30at.%) and η (33at.%) is rarely found. Indeed, Vieweg et al. emphasized that even if the structure of ε-carbide is confirmed by electron diffraction, the stoichiometric 30at% is not found with APT measurement on tempered martensite [55]. Similarly, even if η- Fe_2C was identified by Lu et al. as stated above, APT measurements on the same samples gave a carbide carbon content of 26.8 ± 2.5 at.%. This difference in stoichiometry was attributed to APT artefact measurement (such as pile-up and local magnification effect).

I.2.2.2.1 Nature of carbides

Using Electron Diffraction and Mössbauer: Structural Information

The identification of the nature of transitional carbides is made difficult by the fact that even though ε and η carbides crystallize in two different systems, they are quite similar, in a structural point of view. As showed by Thompson, it is possible to switch between the HCP structure of ε-

carbides and the orthorhombic one of η carbides by slight modification of the occupancy site of carbon atoms such that the x axis expands and the y and z axes contract [66]. As a result, it is not surprising to see studies identifying the carbides as being ϵ (Edmonds et al [24], Hajyakbary et al. [26], Nayak et al. [67]) or η (Pierce et al. [41][57]).

The identification of martensite laths by TEM is based on the observation of highly dislocated laths separated by linear regions identified as being the laths boundaries. Moreover, in the case of tempering treatments, intra-laths carbides can be observed.

Thompson showed using Centered Dark Field (CDF) images that, for a 4340 steel isothermally treated at 200°C for 3600s, each linear feature found in martensite laths is composed of several small segments [66]. Many segments seem to possess almost equiaxed shapes and some even approximating spheres. Using SAD diffraction technique, magnetite O is found in Bain orientation relationship with martensite $(001)_O // (0 -1 1)_\alpha$ and $(010)_O // (0 -1 -1)_\alpha$. Low intensity spots are cementite θ and presumed to be the plate-like precipitates having the relationship with martensite consistent with that reported by Bargaryatsky: $(100)_\theta // (0 -1 1)_\alpha$ and $(011)_\theta // (011)_\alpha$ [69]. On Figure I-17, C could be considered as a plate of cementite associated with small precipitates of the transition iron carbide phase. Others un-indexed spots on the SAD diffraction pattern provide clear evidence of a transition iron-carbide phase such as ϵ (hexagonal unit cells) or η (orthorhombic unit cells). Thompson focusses on η and ϵ to compare their orientation relationships with martensite: $(001)_{\epsilon_0} // (011)_\alpha$ or $(1 -1 0)_{\epsilon_0} // (0 -1 1)_\alpha$ and $(100)_\eta // (011)_\alpha$ or $(-100)_\eta // (0 -1 1)_\alpha$ [66].

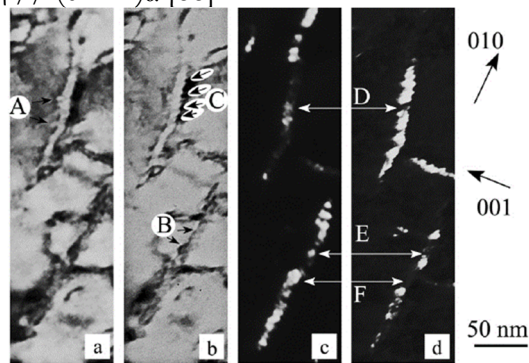


Figure I-17 - Transition-iron-carbide precipitates in a lath of tempered martensite. Bright-field ((a) and (b)) images and CDF TEM images ((c) and (d)) of the same region but from different diffraction spots. A = possibly spherical appendage (at arrows), B = black dark contrast features that show some curvature, C = arrows point a ragged interface between the precipitate and the martensite matrix, D, E and F = precipitate clusters aligned mostly along the $[010]$ martensite direction and illustrate the presence of sub-units not all of the same crystallographic direction. (taken from Thompson et al. [66])

Based on the same method to obtain diffraction patterns, Lu et al. have established the presence of θ - M_3C carbides (Figure I-18) in a Fe-0.3C-13Cr martensitic stainless steel after Q&P treatment (quenched at 220°C, then partitioned at 400°C for 30 min) [70]. They concluded that the orientation relationship between the carbides θ - M_3C and martensite α' is $[011]_\theta // [1 -2 -2]_{\alpha'}$.

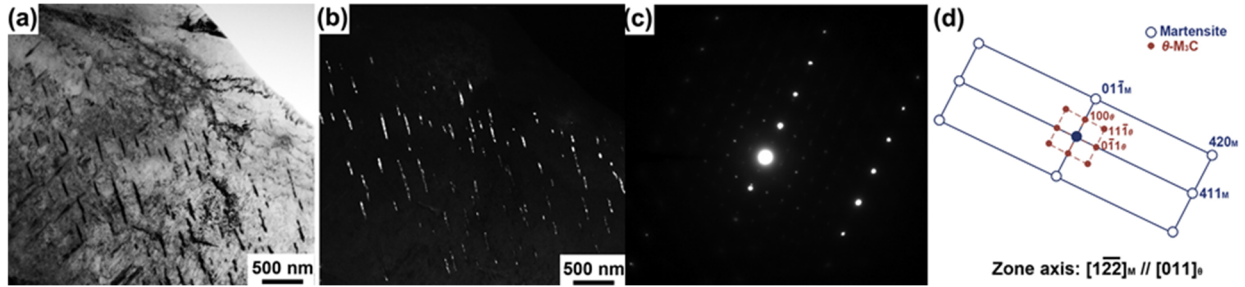


Figure I-18 - Transmission electron microscopy images of the θ - M_3C carbides in the QT 220-400-30min sample [4]: (a) bright-field image, (b) corresponding dark-field image illuminated by using $(11-1)\theta$ reflection, (c) the selected-area electron diffraction pattern, and (d) the corresponding analysis of (c). (taken from Lu et al. [70])

Pierce et al. studied several Q&P and Q&T (quenching at RT then reheating to a tempering stage) samples and showed that for classical partitioning temperatures (typically 400°C), the observed transitional carbide is η [68]. As showed in Figure I-19 on the SAD pattern along two ferritic axes, characteristics spot of several η -carbides (η , η_1 , η_2) appear.

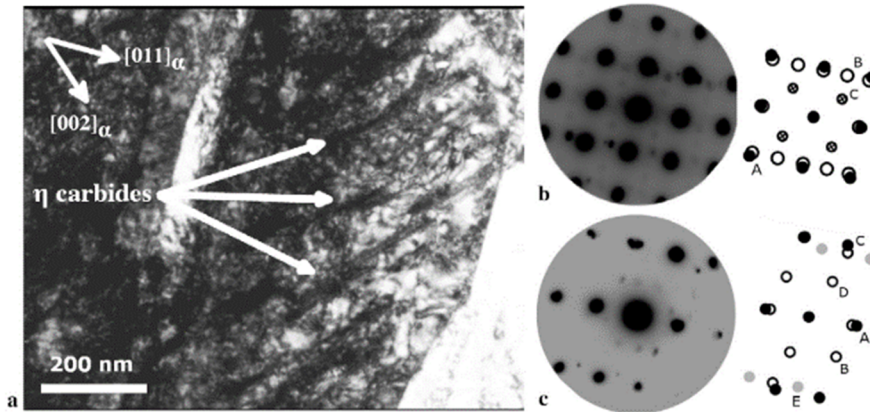


Figure I-19 – (a) $[-100]_\alpha$ zone axis BF TEM micrograph showing η -carbides within the martensitic matrix in a Q&P (QT=225°C, PT/t=400°C/10s) (b) $[-100]_\alpha$ SAD pattern corresponding to the image in (a) (filled circles = matrix, open circles = η , open circle with \times = η superlattice), where $A = (0-20)a$, $B = (210)\eta$, and $C = (110)\eta$ (c) $[-3-11]_\alpha$ SAD pattern (filled circles = matrix, grey and open circles = η) where $A = (011)a$, $B = (2-10)\eta_2$, $C = (-12-1)a$, $D = (-101)\eta_2$, and $E = (-301)\eta_1$ from the same variant as (b). (taken from Pierce et al. [68])

Moreover, the measured reticular distances shown in Table I-2 indicate that the closer match is with η carbides. Interestingly, Pierce et al coupled TEM and Mössbauer and found that approximately 33% of the total amount of η -carbide are in fact non-stoichiometric ($Fe_3C-\eta$). Despite being the same stoichiometry than $Fe_3C-\theta$, the difference in lattice parameter and atom locations makes the distinction between the two carbides possible.

For high partitioning temperatures and with increasing partitioning time, transitional carbides are replaced by cementite (θ - Fe_3C) as showed by Pierce with electron diffraction and Mössbauer [22].

Table I-2 - Comparison of η and ϵ carbides interreticular spacings, from Pierce et al. [68]

η -Carbide	$d_{(200)}$ (Å)	$d_{(210)}$ (Å)
Present work	2.33	2.05
Fe-1.22C wt.%, tempered at 120 °C	2.33	2.07
Fe-0.45C wt.%, tempered at 200 °C	2.341	2.058
ϵ -Carbide	$d_{(010)}$ (Å)	$d_{(011)}$ (Å)
Fe films carburized at <200 °C	2.383	2.091

Hajyakbary et al. reported the presence of epsilon (ϵ) carbides at the very early stage of the partitioning step in a Fe-0.3C-3.6Mn-1.6Si steel (in wt.%) [26]. They claimed that these transitional carbides appear during the quenching step. Based on the comparison of DF images of carbides with the same PT, they observed the decrease of the ϵ -carbides fraction when Pt (5 or 200 s) is increased. To identify the type of carbides, they used Selected Area Diffraction (SAD) and made the comparison between the calculated and the experimentally obtained interplanar spacing considering only ϵ -carbide and θ -cementite (cf Figure I-20). Thanks to measured interplanar spacing values closer to the values reported for ϵ -carbide, they have confirmed its presence in the specimen.

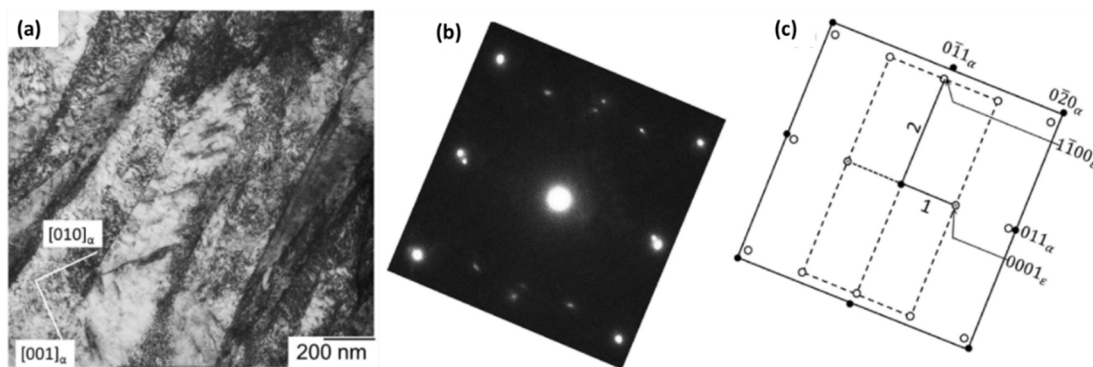


Figure I-20 - (a) BF micrograph of the QT180-400-200s specimen, (b) the corresponding SAD pattern and (c) the corresponding key diagram. Filled circles belong to ferrite reflections and open circles show carbide reflections and open circles with cross show forbidden carbide reflections and beam $\sim // [100]_{\alpha} \sim // [11-2 0]_{\epsilon}$. (taken from Hajyakbary et al. [26])

They explained the difference of carbides nature between their study and Pierce's by the difference in chemical composition of the steel (0.3C-3.5Mn-1.6Si) compared to Pierce's steel (0.38C-1.54Mn-1.48Si both in wt.%) resulting in different stability domains for the transitional carbides during partitioning at 400°C.

Even if the total carbide amount is quite small (in the order of 1 to 2.4 at. phase%), the fact that their carbon content is high may lead to a considerable carbon trapping effect [22]. Indeed, the amount of carbon in carbides can go up to 40% of the total carbon amount [68]. This can have tremendous limiting effects on the enrichment mechanism of austenite during partitioning. In order to estimate the amount of C trapped in carbides, it would be necessary to better estimate the transitional carbides carbon content.

Using Atom Probe Tomography: Compositional Information

For this purpose, APT was used to provide compositional information on precipitates observed on Q&P samples.

Studying carbides by APT is useful to compare their measured composition (often taken as the maximum carbon concentration in the core of the carbide) to the expected one ($\theta=25\text{at}\%$, $\epsilon=30\text{at}\%$, $\eta=33\text{at}\%$). As Table I-3 shows, the maximum concentration of the different carbides studied does not exceed 25at%.

Table I-3 - Comparison of the measured carbide composition by APT for different studies

	Carbides composition	Si/Mn distribution	Q&P treatment	Composition (wt%)
Pierce2018 [57]	~ 20%at (5.10 wt%) (identified as η by TEM)	Homogeneous	QT=210°C PT/t=400°C/300s	0.20C-1.54Mn-1.30Si-1.48Cr-0.07Ni
Kim2017 [71]	~ 25%at (6.69 wt%)	Homogeneous	QT=50°C PT/t=200°C/300s	1C-1Mn-2Si
Toji2014 [49]	~ 20%at (5.10 wt%)	Homogeneous	QT=RT PT/t=400°C/300s	0.59C-2.0Si-2.9 Mn
Ariza2018 [72]	~ 25%at (6.69 wt%)	Si rejection	QT=318°C PT/t=400°C/100s	0.23C-1.23Si-1.50Mn

While it can indicate that the observed carbides might be cementite, Pierce et al. clearly showed by coupling TEM and APT that η are present [57]. It clearly shows that the sole APT information is not sufficient to characterize the carbides as the crystallographic information is missing. To some extent, a sign of Si rejection (as shown by Ariza et al.) can be used to provide additional arguments for cementite precipitation but is rarely observed [72].

I.2.2.2.2 Kinetics of carbides precipitation

Despite being easily observable by SEM or TEM, carbides present a low volume fraction making their measurements by both standard and advanced techniques pretty difficult and challenging. Therefore, it is quite tedious to obtain a time evolution of the carbide volume fraction formed in α' during the Q&P process.

Based on SEM observation, Hajyakbary et al. argue that as partitioning time increases, carbide volume fraction seems to decrease [26]. Therefore, the dissolution of ϵ -carbides can allow a second enrichment peak for longer partitioning times, as observed by Edmonds et al. [24].

On the contrary, the Mössbauer spectroscopy study by Pierce et al. (allowing a fine follow-up of the amount of η -carbides during the partitioning) showed that the majority of carbides are formed during the initial quench to QT by auto-tempering and that η -carbides do not dissolve during the partitioning step [22].

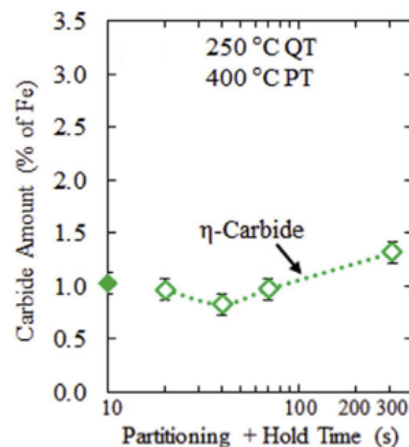


Figure I-21 - Evolution of η carbides amount during partitioning at 400°C (Pierce et al. [68])

After a stationary state during the first 60s of partitioning, the authors even highlighted a slight increase in carbide fraction for longer partitioning times (approx. 300s) as shown in Figure I-21. The main finding of Pierce's study is that the leading martensite carbon supersaturation release

mechanism is η -carbides precipitation during the initial quench to QT. Carbon partitioning towards austenite during the rest of the treatment only occurs after. This is a strong evidence that carbide will affect the amount of carbon available to enrich the austenite during partitioning.

I.2.2.2.3 Impact of Si addition on carbides precipitation

The various quenching, reheating, and isothermal steps can lead to the formation of unwanted phases and features that can hinder the carbon enrichment of austenite such as:

- carbide precipitation in α' ,
- decomposition of austenite into ferrite + carbides

By comparing the austenite volume fraction and carbon content of a high silicon (HSi) steel and a low one (LSi) after bainitic treatments at different temperatures from 350°C to 410°C, Jacques et al. showed that 1.5 wt% of silicon is enough to suppress cementite precipitation from austenite during its decomposition [73]. This is the basis of the Carbide Free Bainitic steels (CFB) whose microstructure is mainly composed of a bainitic matrix with retained austenite films between the bainitic ferrite laths and at the periphery of the martensite/austenite islands.

It is thus important to assess the impact of Si on the decomposition of austenite and carbide precipitation during a Q&P treatment [71][74]. While the formation of carbides seems inevitable between the initial quench and the first 10s of the partitioning, for larger partitioning time, the LSi steel showed an increasing amount of carbides while the HSi steel exhibited no further carbides formation [74]. Apart from reducing (but not totally suppressing) carbide precipitation, silicon has also proved to retard the austenite decomposition mechanisms during the partitioning step, leading to higher fractions of RA for long Pt [71].

The fact that silicon hinders cementite precipitation is generally explained by the low solubility of silicon in cementite and the need for cementite to reject Si in order to grow. This is only possible when the temperature is sufficiently high to give enough mobility to Si atoms to diffuse outside of cementite. Indeed, Caballero et al. proved by APT measurements that the Si concentration in cementite is function of the tempering temperature (cf Figure I-22) [75].

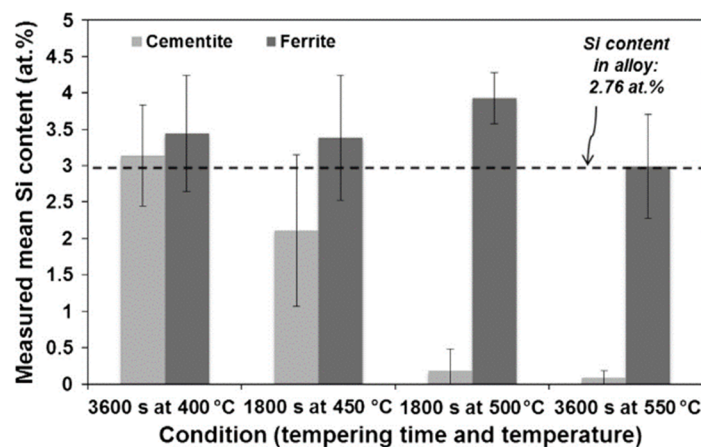


Figure I-22 - Silicon content in ferrite and cementite for different tempering condition (plotted by Kim et al. [76] from tabulated data of Caballero et al. [75])

However, the temperature range of isothermal steps in CFB or martensite tempering treatment is usually too low to allow silicon diffusion on large scales (classically 400°C) [77]. This is why cementite is often considered to nucleate in paraequilibrium conditions (see nucleation stage a) on Figure I-23) even though Miyamoto et al. demonstrated that at 450°C, the driving force for cementite nucleation under paraequilibrium was much lower than under local equilibrium with partitioning of Si between the two phases for a Fe-0.6C-2Si (wt.%) steel [78].

By considering paraequilibrium conditions during nucleation, Kim et al. demonstrated that the driving force for cementite nucleation was indeed decreasing with silicon content [76]. Once

cementite is nucleated and if the temperature and tempering time are high enough, Owen explained that a small amount of Si is rejected from the growing cementite particle leading to an increase in Si content around the particle [79]. However, this Si-rich layer tend to increase carbon activity leading to a reduction of the carbon flux from the matrix towards the particle (see b) precluding further growth of the particle. Hence, cementite growth is governed by silicon partitioning out of the particle.

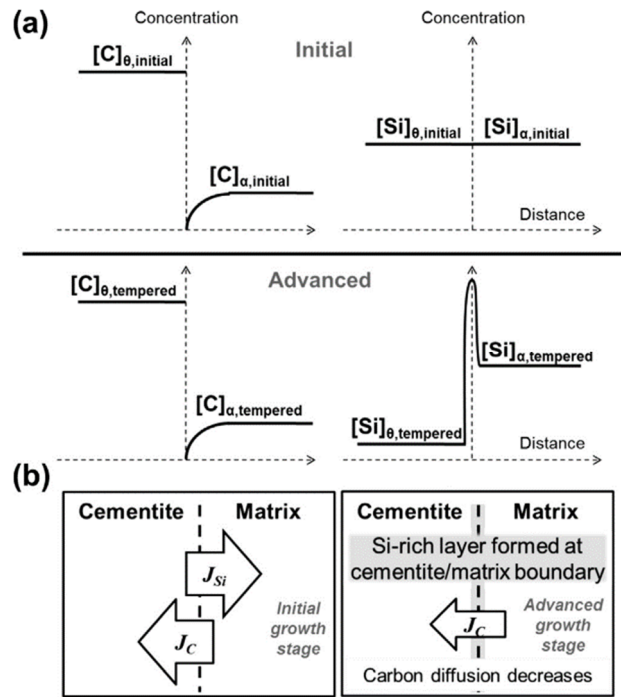


Figure I-23 - a) Possible growth mechanism after the paraequilibrium nucleation of cementite b) silicon and carbon content variation throughout (J_C and J_{Si} refer to the carbon and silicon flux across the interface) (taken from Kim et al. [76])

Silicon does not have a similar effect on transitional carbides, but it was shown that increasing the amount of Si tends to shift the TTT nose of ϵ -carbides to lower temperatures [67]. Furthermore, once formed, ϵ -carbides have a higher coherency with the matrix than cementite due to a contraction along the c-axis by 0.5%, delaying the transition from the precipitation of transitional carbides ϵ/η to θ formation as shown in Table I-4 [78].

Table I-4 - Effect of adding Si or Mn on the precipitation of carbides (taken from Miyamoto et al. [46])

Transition of carbides in the tempering of Fe-0.6C-M martensite						
Alloy	523 K		723 K			
	30 s	1.2 ks	30 s	120 s	300 s	1.2 ks
Fe-0.6C	ϵ	θ	θ	-	-	θ
Fe-0.6C-2Mn	ϵ	θ	θ	-	-	θ
Fe-0.6C-2Si	ϵ	ϵ	ϵ	ϵ/θ	θ	θ

I.2.2.3 Carbon content of martensite

The primary purpose of Q&P treatments is to stabilize the austenite by pushing carbon out of the martensite, and thus to reach a minimum carbon content in the α' matrix. As previously stated, carbon in α' can segregate or precipitate in various forms. In order to draw a complete picture of the carbon mass balance, and its distribution, in the steel, it is necessary to find a suitable method to measure carbon in solid solution within martensite.

I.2.2.3.1 APT measurements

Obtaining a value of the carbon in solid solution in martensite is quite difficult because standard techniques like XRD cannot separate the contributions of the different carbon rearrangement mechanisms. Indeed, the carbon clustering can cause a local increase in tetragonality, that will be wrongly attributed to an overall increase in the matrix tetragonality (and c/a ratio). Thereby, using classical formula to link the c/a ratio to the martensite carbon content will lead to an overestimation of carbon atoms remaining in the martensite lattice [80]. Atom probe tomography (APT) is particularly suitable for solid solution composition measurements due its high spatial resolution and its ability to detect carbon.

As Table I-5 shows, the measurement of carbon in SS in α' is often measured using average values on a concentration profile.

Table I-5 - APT carbon measurements of carbon in α' after partitioning in different studies

	Measurement method	Q&P treatment	Martensite carbon concentration	Composition (wt%)
Clarke2008 [23]	Average value on 2 profiles	QT=220°C PT/t=400°C/10s	0.50at% (0.10wt%)	0.19C-1.59Mn-1.63Si-0.036Al
Pierce2018 [57]	Excluding segregations	QT=210°C PT/t=400°C/300s	0.20at% (0.043wt%)	0.20C-1.54Mn-1.30Si-1.48Cr-0.07Ni
Seo2016 [18]	Average value on 1 profile	QT=170°C PT/t=450°C/300s	0.25at% (0.055wt%)	0.2C-4.0Mn-1.6Si-1.0Cr
Ariza2018 [72]	Average value on 1 profile	QT=318°C PT/t=400°C/100s	0.23at% (0.050wt%)	0.23C-1.23Si-1.50Mn

Figure I-24 (taken from Pierce et al.) presents an APT reconstruction of a low carbon region identified as martensite [57]. 3%at-C isosurfaces are shown and presented as being carbon segregation. Excluding those segregations in the measurement allows to be closer to the concentration of carbon in SS in α' (0.20at% in [57]).

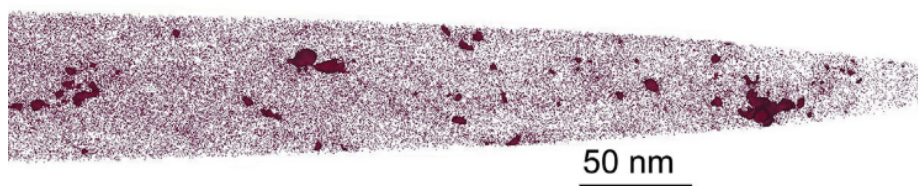


Figure I-24 - Martensite after partitioning showing segregations with 3at% C-isosurfaces (taken from Pierce et al. [57])

We can highlight the fact that, even by taking into account the measurements including segregations, for low-carbon steels (approx. 0.2wt%C), the martensite is depleted in carbon at the end of the partitioning (approx. 0.050wt%). The high value of carbon in α' from the study of Clarke et al. is probably due to the fact that the partitioning step is interrupted after 10s thus limiting the amount of carbon able to leave the α' laths [23].

I.2.2.3.2 Martensite tetragonality measurements

While being less suited than APT to obtain solid solution measurements, XRD is still largely used to measure the carbon content in martensite by using the c/a ratio of tetragonal martensite. The evidence of a tetragonality of martensite came from the observation of a split of (002) and (200) martensite peaks on XRD diffractograms. Increasing α' carbon content led to a break of the cubic nature of the lattice (BCC) towards a more tetragonal symmetry (BCT) [81][82].

Martensite tetragonality is commonly attributed to two phenomena:

- carbon's preferential occupancy of the c octahedral sub-lattice inherited from the Bain's deformation, as shown in Figure I-25. Tetragonality would be thus a direct consequence of the displacive character of the martensite transformation [83],

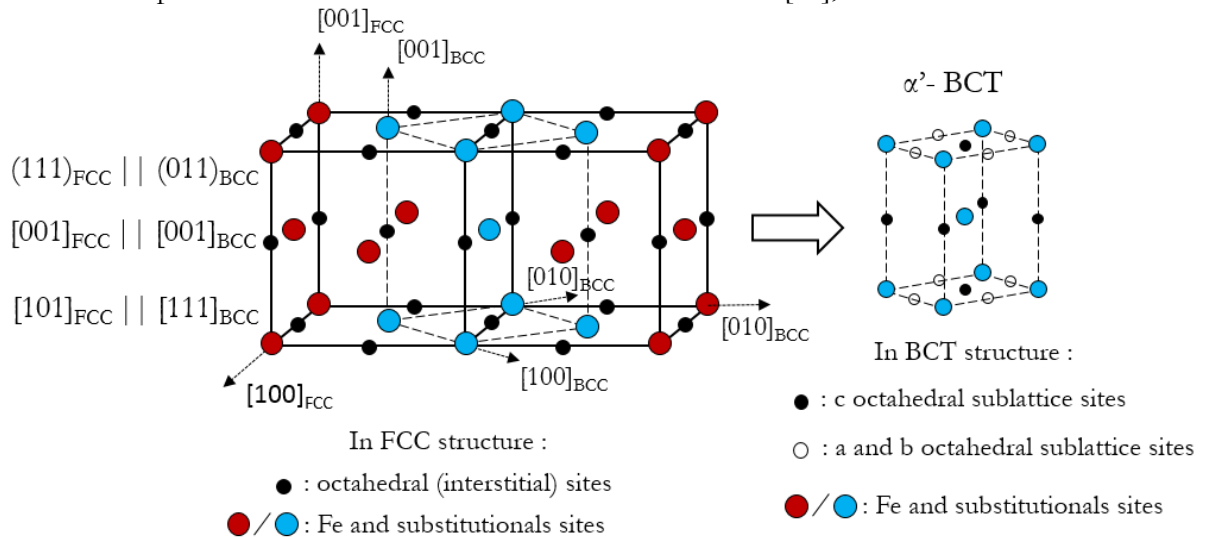


Figure I-25 - Bain Transformation and inheritance of octahedral sites between FCC austenite and BCT martensite

- as Zener claimed in his original paper, carbon ordering along the c -axis would be a consequence of the elastic interactions between carbon atoms [84]. Indeed, for a given carbon content, under a critical temperature (T_C) carbon atoms are arranged in a ordered structure (Zener ordering) in order to minimize the Gibbs energy of the system (mainly coming from the interaction of the elastics fields of every carbon atoms) [85]. There is a constant balance between the configurational entropy that leads to a tendency for the carbon atoms to redistribute onto the three octahedral site sublattices and the elastic energy minimization that lead to an ordering on one of the three octahedral site sublattices (and thus leading to tetragonality).

The monitoring of a and c lattice parameters of martensite is often done via X-ray measurement at RT after quenching from the austenite domain. As Figure I-26 shows, the early X-ray experiments on the determination of the evolution of c and a with carbon content showed that tetragonality only appears when $X_C^{\alpha'} > 0.6\text{wt.}\%$. This value is now contested and attributed to the fact that XRD technics were not precise enough to detect the tetragonality split on the diffractograms at low carbon contents due to stress-induced peak broadening [86][87]. The generalized assumption was that the experimental data at high carbon contents could be extrapolated at low contents, and a was equal to c when the carbon content of martensite is equal to zero.

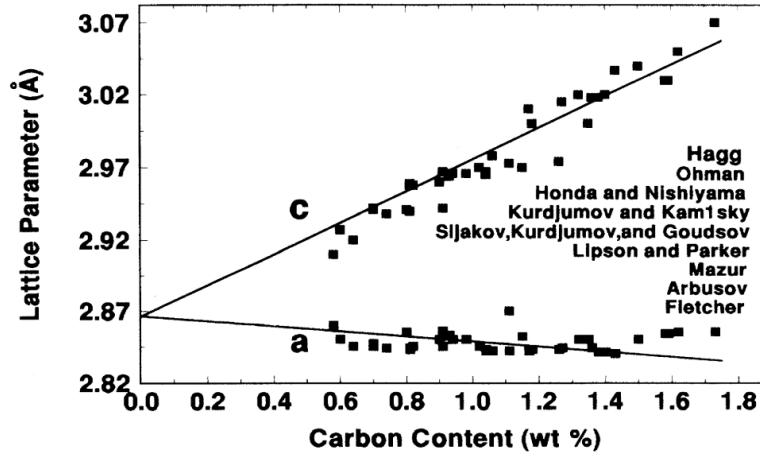


Figure I-26 - Summary of lattice parameter evolution of martensite of early studies (taken from Roberts [88])

In parallel, Zener's view of tetragonality was used by Khachatryan et al. to define a critical temperature T_C where there is a transition between the disordered form of martensite (BCC) to the ordered one (BCT) by using mean field theory and microscopic elastic theory (MET) as [89]:

$$T_C = 0.361 \frac{\lambda_0}{k_B} u_C \quad (I.10)$$

Where T_C is the critical temperature of carbon ordering, u_C is the u-fraction of carbon and λ_0 is the strain interaction parameter.

Equivalently, if the temperature is fixed, one can determine the critical carbon content at which the disorder/order transition occurs as:

$$u_C = \frac{T k_B}{0.361 \lambda_0} \quad (I.11)$$

Where T is the temperature where the critical carbon content has to be determined.

Thus, using data found in the literature on c and a measurements, and observing that no tetragonality was measured for $X_C^{a'} < 0.6\text{wt}\%$ (cf Figure I-26), Sherby et al. stated that at RT the critical carbon content was equal to 0.6wt%, and that the extrapolation previously done wasn't relevant [90].

The number of studies on the tetragonality of the martensite lattice when $X_C^{a'} < 0.6\text{wt}\%$ is very limited. Two of them can however be cited and gave enlightments on the carbon order-disorder transition in martensite. First, Liu et al. found that at low carbon contents, the structure is BCC, thus, in agreement with Sherby et al., refuting the fact that the c and a evolution at high carbon content can be extrapolated to 0 wt.%C [86]. Moreover, they highlighted the fact that tetragonality is detected as soon as $X_C^{a'} = 0.18\text{wt}\%$. The authors mentioned that when carbon content is low (between 0.18wt.% and 0.55wt.%), even if the experimentally observed peaks have not yet splitted, apparent lattice parameter noted a' and c' can be calculated and are a proof of the start of the disorder-order transition. The split between the martensite peaks is noticeable when $X_C^{a'} > 0.55\text{wt}\%$ as already highlighted by the earlier studies (cf Figure I-26). The second study was very recently published by Lu et al. using a High-resolution X-ray diffractometer and Rietveld refinement procedure, to analyze steels with carbon content ranging from 0.124 wt.% to 1.24wt.% [91]. They deconvoluted martensite peaks (002) and (200) with precision to show that martensite is BCT even at carbon content as low as 0.124wt.%. Indeed, tetragonality was observed on the whole range of steels studied.

We summarize the experimental values measured by X-ray diffraction obtained by Honda et al. (representative of the early studies on martensite tetragonality), Liu et al. and Lu et al. in Figure I-27 [86][91][92]. The previously mentioned limits in carbon content above which martensite tetragonality is detected (i.e a/c ratio measured different from 1) is clearly shown.

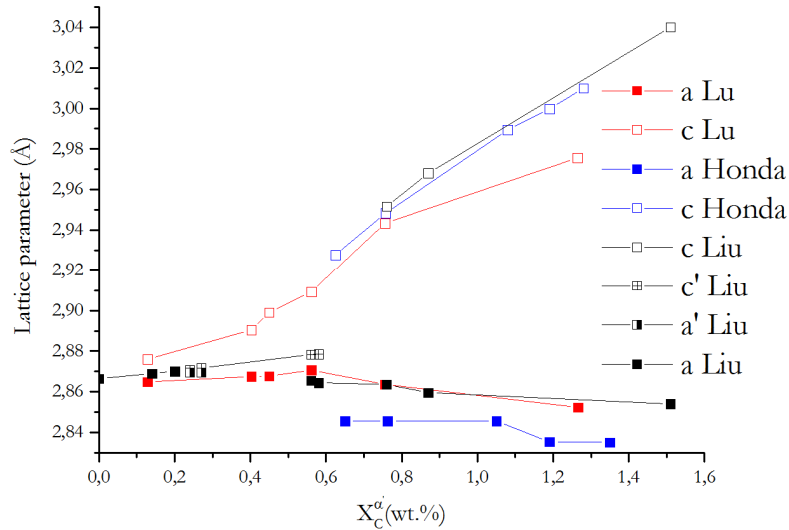


Figure I-27 - Selected experimental values of martensite lattice parameter a and c obtained by X-ray diffraction

As the XRD measurements are conducted at RT, we can use eq.(I.5) to find the theoretical critical carbon content for which martensite becomes tetragonal ($X_C^{\alpha' crit}$). However, because the value of λ_0 is still the matter of much debate and of primary importance, different values will lead to different critical carbon values for which the tetragonal lattice is stable at RT. Khachaturyan proposed several values for λ_0 , before reporting a final value of 2.73 eV/atom [89][93]. Later, Udyansky et al., using first principles calculations, proposed the value of 6.38 eV/atom [94]. Finally, Chirkov et al. using two different methods of simulation, (Molecular Dynamics (MS) and Molecular Static (MS)), found 4.95 eV/atom and 5.63 eV/atom respectively [95]. We plotted the c/a ratio resulting from the c and a lattice parameter presented in Figure I-27 together with the values for the critical carbon content calculated for the four values of λ_0 presented above (vertical dashed lines).

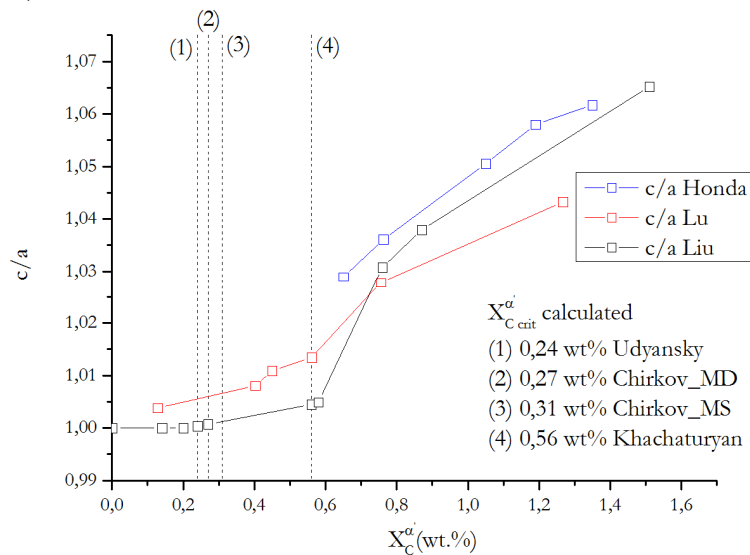


Figure I-28 - c/a ratio versus carbon content at RT for three studies together with the calculated values for $X_C^{\alpha' crit}$ with four different values of λ_0

Regarding the c/a ratio presented Figure I-28, only the study from Liu et al. considers that no tetragonality is observed for low carbon content ($X_C^{\alpha'} < 0.18\text{wt.}\%$) [86]. For Honda et al., tetragonality has only been observed for $X_C^{\alpha'} > 0.6\text{wt.}\%$ (but was considered to exist down to $0\text{wt.}\%$), while for Lu et al. tetragonality is observed for $X_C^{\alpha'}$ as small as $0.124\text{wt.}\%$. The critical concentration calculated from the Khachaturyan's value of λ_0 is very close to what was

previously considered as the experimental limit for martensite tetragonality (approx.. 0.6wt.%). However, recent measurement shows that martensite exhibits tetragonality for much lower $X_C^{\alpha'}$. The values of λ_0 from both Udyansky and Chirkov predicted quite accurately the carbon content value of transition from disordered to ordered measured by Liu et al. (black line on Figure I-28). Lu data sets present tetragonality down to 0.124wt.%, it is almost half of the critical carbon content values calculated. This behavior might be explained by higher internal and/or external stresses in martensite (generated during quenching) that are expected to modify the order/disorder transition. Indeed, Maugis et al. showed that stressed supersaturated iron is never cubic because of the tendency to carbon ordering under stress [96]. Figure I-29 shows how the order parameter (η) and c and a values (presented here unit-less) can vary under stress. When the stress in martensite exceeds a critical value of stress (Σ_k) the order parameter and lattice parameter change continuously (contrary to the discontinuous change observed for $\Sigma < \Sigma_k$). Liu et al. deeply chemically etched their samples after mechanical polishing and before XRD measurements in order to reduce surface macro-stress whereas Lu et al. did not indicate any stress relieving technic before XRD measurement. As the XRD sources in both studies are not high energy ones, the volume probed is relatively small and surface effects are not negligible. This might explain the observed tetragonality even at low carbon content of Lu et al. study. A possible difference in stress-state in martensite between the studies in Figure I-28 can also explain the fact that the jump in c/a ratio observed for the three data sets in the 0.5wt.%-0.8wt.% range vary in degree similarly to the curve in Figure I-29 b).

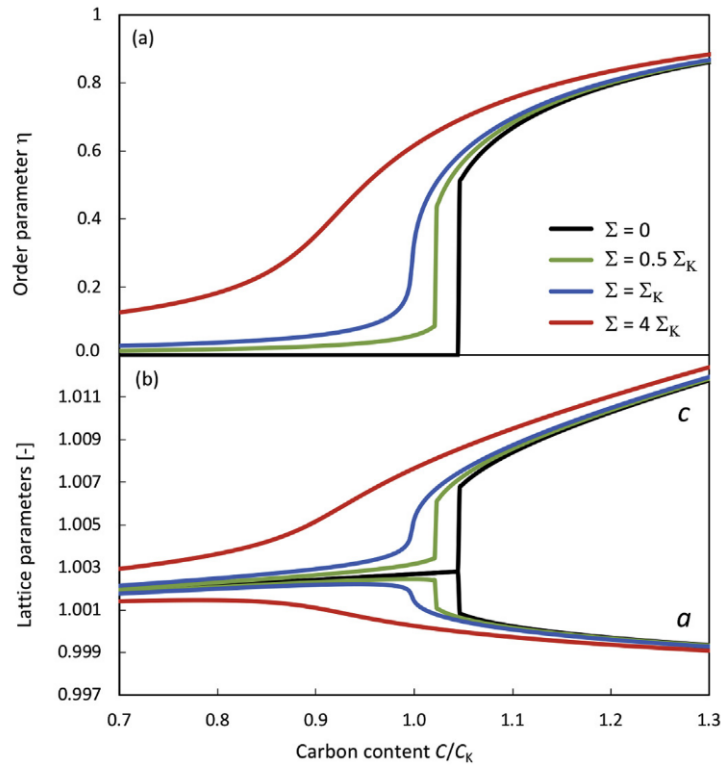


Figure I-29 - a) Order parameter b) unit-less lattice parameter a and c as function of reduced carbon content, at a given temperature, for different values of stress (Σ_k being a critical stress value) (taken from Maugis et al. [96])

In view of all this considerations, we choose to use the newly proposed relation proposed by Lu et al. in order to link the c/a ratio to the carbon content of martensite as [91]:

$$\frac{c}{a} = 1 + 0.031X_C^{\alpha'} (\text{wt}\%) \quad (I.12)$$

Moreover, this new relation seems to be in good agreement with the atomistic modeling of Becquart et al. [97].

However, it must be highlighted that following the changes in tetragonality of martensite is experimentally very challenging due to the many other concurrent mechanisms such as segregations on defects or carbides precipitation (see previous sections). Particularly, when measuring the c/a ratio of bainitic laths by means of XRD and comparing it to APT measurements of the matrix carbon content, Rementeria et al. suggested that the development of carbon clusters locally increases the tetragonality “viewed” by the XRD [80]. Indeed, as XRD is measuring an average value of the carbon clusters and non-carbon clusters regions, it gives biased values for what is often interpreted as representative of the martensite intrinsic tetragonality. As Lu et al. pointed out for steels with less than 1.5wt.%, the large majority of martensite cells does not even contain one carbon atom, in fact the c/a ratio is the average of expression of more than 40 iron atoms and 1 or 2 carbon atoms [98]. This indicates that martensite tetragonality can somewhat be viewed as small carbon clustering into martensite.

I.2.3 Bainite transformation in Q&P steels

Apart from carbide precipitation, the main competitive reaction in the considered temperature domain is austenite decomposition into bainite. As the partitioning step is typically conducted in temperature ranges favorable to the bainitic transformation, it is thus essential to understand how this can impact the Q&P treatment, in particular the carbon redistribution.

I.2.3.1 Differentiate bainite from martensite

The main challenge in the identification of bainite in Q&P microstructure is to be able to discriminate the possible phases, which could form during the Q&P process: tempered martensite formed during the first quench, bainite and/or isothermal martensite formed during the partitioning step, and fresh martensite formed during the final quench.

Since the majority of these products are formed by displacive mechanisms, they might have some similarity in morphology, dislocation density and internal structure (packets/block structure).

In order to differentiate bainite from martensite, isothermal treatments above M_s (where no martensite is expected to form) and below M_s (after the formation of small amount of martensite) were conducted by Kim et al. and Navarro-Lopez et al. and led to the following conclusions [99][100][101].

Bainite was identified both above and below M_s . Indeed, as Figure I-30 shows, bainite formed above M_s is present both as thin acicular features with interlaths retained austenite and as larger laths with irregular shapes. The main characteristic is the absence of carbides within the laths, as shown in Figure I-31.

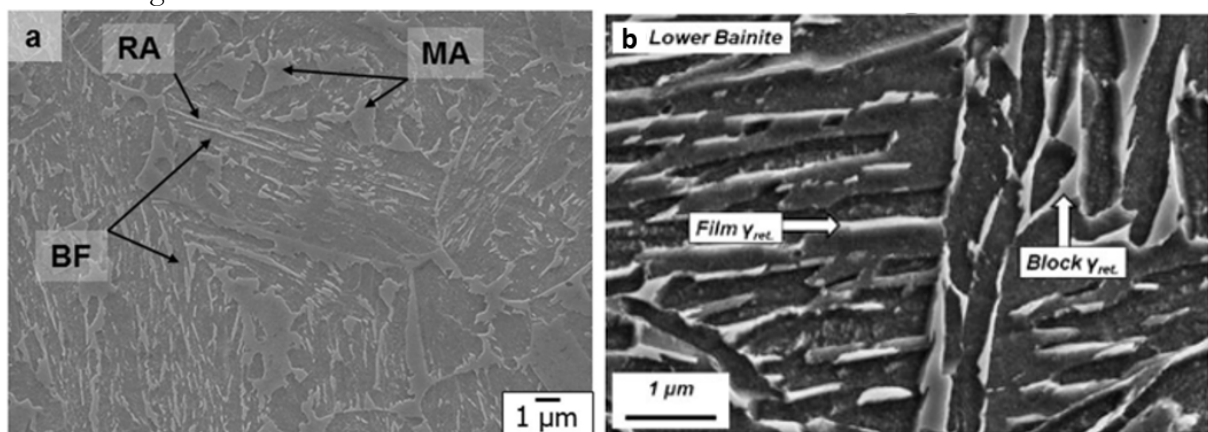


Figure I-30 - Microstructure obtained in a specimen isothermally treated above M_s for the steels studied by Kim et al. in a) and Navarro-Lopez et al. in b).

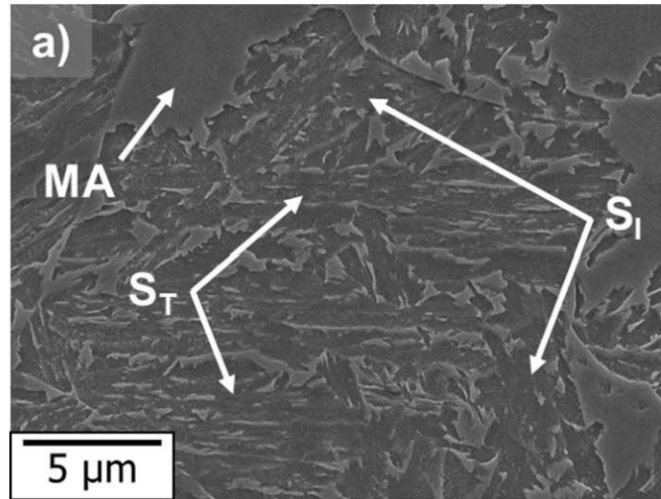


Figure I-31 - SEM image of a isothermally treated sample at 340°C (above M_s) in the study of Navarro-Lopez et al. [101] showing the lack of carbides in the bainitic features (S_T : thin bainite structure, S_I : irregular bainite structure)

Once isothermal treatments are conducted below M_s , in addition to the previous bainitic structures (also present under M_s as irregular shaped and thin carbide-free laths) new carbide-filled laths start to appear. Figure I-32 shows that these laths can be found as either laths with a sharp tip at an edge (called S_{TK} in [101]) and often surrounded by bainite laths or as larger and wider lath with wavy boundaries (called S_E in [101]) caused by the ledge-like protrusions that are probably bainite. As these features were only appearing under M_s , they were identified as martensite by Navarro-Lopez et al. [101].

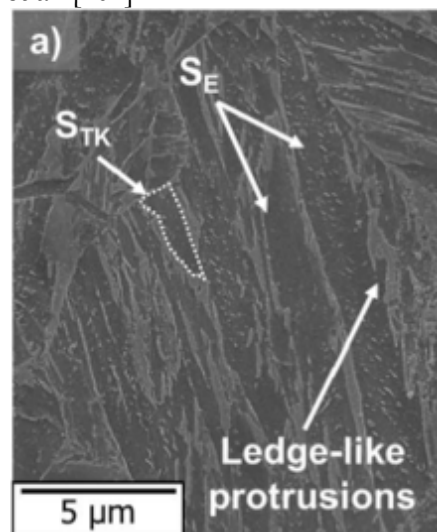


Figure I-32 – SEM micrograph after isothermal holding below M_s (270°C) showing the martensitic features (S_E : elongated martensitic structure, S_{TK} : thick martensitic structure) (taken from Navarro-Lopez et al. [101])

The distribution and morphology of RA can also be an indicator of the nature of product phases. By using EBSD phase distribution maps, Navarro-Lopez et al. demonstrated that RA tend to appear with two different morphologies: in between the bainite features as thin films or small blocks and in the form of elongated blocks between martensitic laths [101].

Carbides that precipitated in the tempered α' laths are multivariant as shown in Figure I-33.

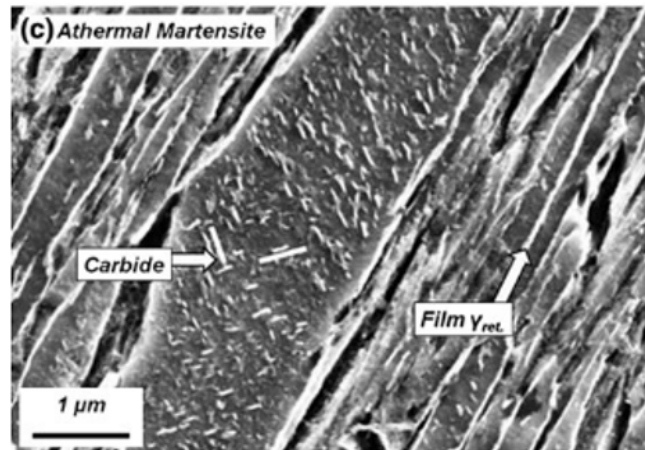


Figure I-33 - SEM micrograph of the typical morphology of the blocks in athermal martensite with multivariants carbides (taken from Kim et al. [99])

In high-Si Q&P steels, Santofimia et al. noted that lower bainite (lath with carbide precipitation) was formed during the initial quench and in the first 10 seconds of the partitioning step [74]. During the rest of the treatment only carbide-free bainite was formed. The same treatments were also conducted on low-Si Q&P steels, which showed that in the absence of sufficient Si to inhibit carbide precipitation, only lower bainite form through the whole treatment. In both cases, the increase of bainite volume fraction observed in the microstructures during the partitioning step matches the expansion measured by dilatometry (assuming that the dilatation observed during partitioning results from bainite formation).

I.2.3.2 Effect of preexisting martensite on bainitic transformation

Bainite formation in Q&P is different from treatments that are specifically designed to produce bainite. Indeed, whereas in Carbide Free Bainite treatments (CFB), bainite is formed from a 100% austenitic structure by isothermal holding, in Q&P steels, bainite forms in an austenite which is surrounded by a martensitic matrix [102]. The effect of pre-existing martensite on the bainite transformation was shown to reduce the incubation time for the bainite transformation [103][104][105]. Indeed, Samanta et al. studied isothermal holding under M_s and showed by SEM image analysis that bainite forms [105]. By applying a displacive kinetic model, they were able to compare the number density of nucleation sites between bainite formed with or without pre-existing martensite. A difference of one order of magnitude was found showing that martensite provides additional nucleation site for bainite formation. Navarro-Lopez et al. also showed that the initial nucleation rate (taken 0.5s after the start of the bainitic transformation) raises from $1.0 \cdot 10^{14}$ to $1.0 \cdot 10^{16} \text{ m}^{-3} \text{ s}^{-1}$ once some martensite is formed (cf Figure I-34) [100].

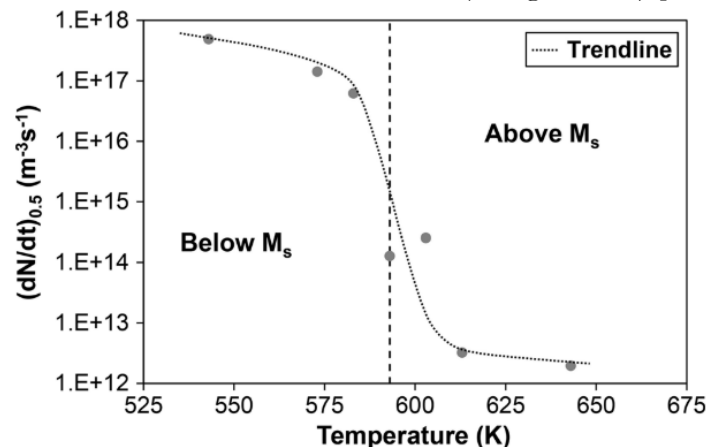


Figure I-34 - The initial nucleation rate as a function of the isothermal temperature at 0.5s after the start of the isothermal transformations (taken from Navarro-Lopez et al. [100])

Toji et al. conducted similar experiments by introducing 30% α' ($M_s=32^\circ\text{C}$) prior to an isothermal treatment at 300°C and also noted an accelerating effect of martensite on bainite transformation (cf Figure I-35 a)), they gave some possible mechanisms to explain this results [103]:

- the strain and dislocations induced by the martensite formation in austenite provides additional nucleation sites for bainite,
- carbides that form at the α'/γ interfaces reduce locally the carbon concentration and thus increase the driving force for bainitic transformation (cf Figure I-35 b))

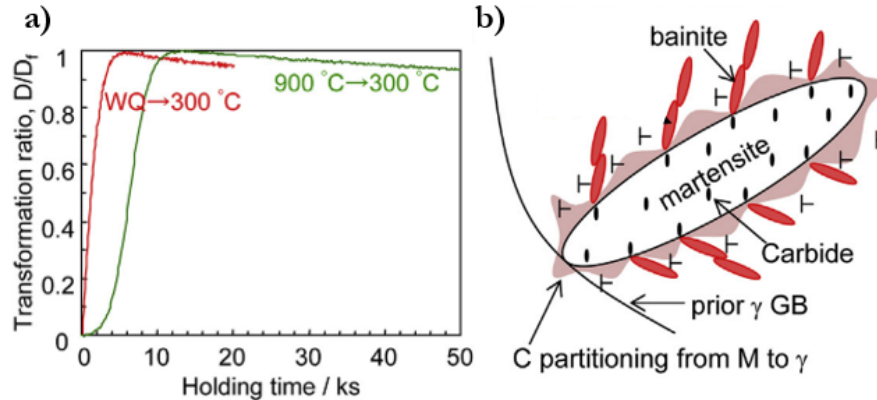


Figure I-35 - (a) Dilatation during holding at 300°C after a direct quench from 900°C to 300°C (martensite-free - green curve) and a direct quench at RT followed by a reheating to 300°C (resulting in 30% of martensite - red curve) (b) Schematic diagram showing the preferential nucleation sites of bainite on a martensite lath (taken from Toji et al. [103])

I.2.3.3 Effect of quenching and partitioning temperatures on the bainitic transformation

Traces of an expansion during the partitioning step, due to a change in specific volume between the austenite lattice and bainite lattice, is one of the first evidences of a decomposition of austenite into bainite.

The impact of PT and QT on the changes in volume (dilatation) during the partitioning step was studied by Somani et al. using dilatometry [106]. The experiments showed that for a given QT, increasing PT leads to an increase in length change attributed to the kinetics of bainite transformation. These trends can be explained by the fact that PT is located in the lower part of the bainite nose. The opposite situation was observed by Santofimia et al. where, as PT increase (for the same QT), the change in length measured during the partitioning step decreased, indicating that the temperatures chosen for partitioning were on the upper part of the bainite nose [19]. The rate of transformation presented in these studies are very similar to those observed for bainitic transformation (a rapid initial increase followed by a more sluggish transformation rate). This further support the fact that the partitioning temperature must be carefully chosen in order to allow sufficient carbon diffusion but at the same time limit the bainite transformation.

In order to understand the role of QT on the bainite transformation kinetics, Somani et al. also conducted treatments with a given PT but different QT [106]. In this case, the dilatometric curves during the partitioning steps showed a larger expansion with increasing QT. Such a behavior was also observed by Hajyakbary et al. [26]. Quenching to a high QT leads to a higher austenite volume fractions before the partitioning step, so if the same percentage of austenite transforms into bainite, it will mechanically lead to higher fraction of bainite than for low QT. However, unlike in classical CFB treatment, there is also carbon that diffuses from the surrounding martensite into the austenite, affecting the bainitic transformation kinetics during the Q&P treatment. Considering this, it might be incorrect to directly link the amount of austenite available for decomposition to the amount of bainite formed.

I.3 Mechanisms of carbon enrichment

Now that the different phases formed during the Q&P treatment have been presented, the focus shift to the carbon enrichment of austenite. Two different sources, and the related mechanisms of carbon enrichment, will be presented:

- carbon partitioning from martensite to austenite resulting from the chemical potential difference of carbon between the two phases,
- carbon rejection from bainite to austenite.

I.3.1 Partitioning from martensite and interface mobility

Traditionally, carbon diffusion in martensite is considered in the context of tempering process such as carbide precipitation or segregation on defects. Although the mechanisms of carbon enrichment in retained austenite during the partitioning step are still a matter of debate, strong evidences of carbon partitioning from martensite to austenite exist [16][100]–[102]. In order to describe carbon partitioning process, a Constrained Carbon Equilibrium (CCE) model was proposed [110]–[112]. It relies on the following hypothesis: the mobility of iron and the substitutional elements can be neglected, the competitive reactions, such as carbides precipitation and decomposition of austenite, are ignored, and the martensite/austenite interface is immobile or stationary. In that case, only carbon equilibrates its chemical potential, similarly to the ParaEquilibrium condition introduced by Hultgren [113].

It is worth noting that the CCE model does not describe the kinetic path related to the carbon partitioning from martensite to austenite but allows to access to the endpoint of the partitioning in terms of carbon content in austenite. The CCE final state is reached once the chemical potential of carbon through the system is homogenized. Carbon is then expected to diffuse from martensite, where the carbon chemical potential is higher, toward austenite, where it is lower.

This metastable equilibrium between the two phases can be illustrated, using graphical representation of the Gibbs free energy versus carbon content.

At full equilibrium conditions, in the binary Fe-C system, the chemical potentials of both carbon and iron can equilibrate themselves between martensite and austenite. The full equilibrium condition is defined by the common tangent as illustrated in Figure I-36.

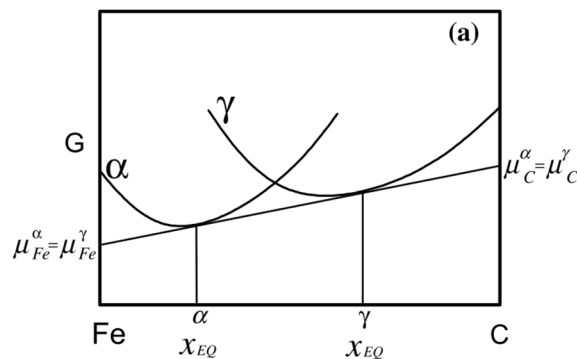


Figure I-36- Schematic Gibbs free energy versus carbon content showing the common-tangent construction for full equilibrium between martensite and austenite (taken from Speer et al. [7])

In the CCE condition, the only relation between chemical potentials is the following:

$$\mu_{CCE}^{\alpha'} = \mu_{CCE}^{\gamma} \quad (I.13)$$

where μ_{CCE}^{φ} is the chemical potential of carbon in the phase φ .

Figure I-37 presents a similar Gibbs free energy construction satisfying the CCE conditions, with two situations where the chemical potential of carbon is equal in α' and γ but with different values of chemical potential for iron. Indeed, it exists an infinity sets of austenite/martensite

compositions satisfying the CCE condition of equal carbon potential in α' and γ .

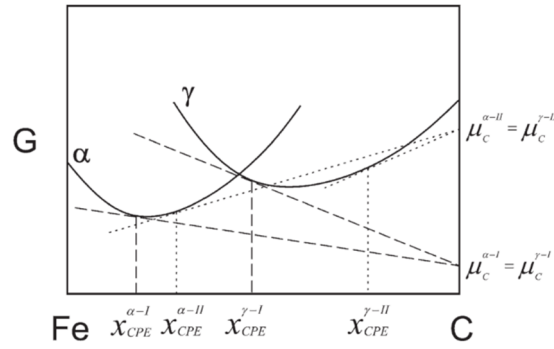


Figure I-37 - Schematic Gibbs free energy versus carbon content showing the common-tangent construction for the CCE condition between martensite and austenite (taken from Speer et al. [7]). The μ_c appearing in this graph are $\mu_{C\ CCE}$

The condition given in eq.(I.13) is not sufficient to define equilibrium, therefore an additional supplementary constraint is needed to define the equilibrium. This constraint is mass balance for both iron and carbon, which can be written as follow:

For iron:

$$f_Y^{CCE}(1 - X_{C_{CCE}}^Y) = f_Y^0(1 - X_C^0) \quad (I.14)$$

Where f_Y^{CCE} and $X_{C_{CCE}}^Y$ are the austenite fraction and carbon content at constrained carbon equilibrium when carbon partitioning is completed, and f_Y^0 and X_C^0 are the initial austenite fraction (taken at the end of QT) and nominal carbon content of the alloy. The iron concentration is always given as $X_{Fe}^Y = 1 - X_C^Y$

For carbon:

$$f_M^{CCE} X_{C_{CCE}}^{\alpha'} + f_Y^{CCE} X_{C_{CCE}}^Y = X_C^0 \quad (I.15)$$

Where f_M^{CCE} and $X_{C_{CCE}}^{\alpha'}$ are the martensite fraction and carbon content at constrained carbon equilibrium when carbon partitioning is completed.

Lastly the relation between the phase fractions is:

$$f_M^{CCE} + f_Y^{CCE} = 1 \quad (I.16)$$

Thus the CCE condition is represented by the solution of the previous four equations (I.13), (I.14), (I.15), (I.16) with four unknowns. This model allows the determination of the final carbon concentration in austenite and martensite after partitioning. The value determined this way can be seen as an upper boundary since the assumptions that competitive reactions are fully suppressed is unreliable.

Partitioning of substitutional elements

In the original CCE model, the equalization of the carbon chemical potential between martensite and austenite was made under the assumption that only carbon have enough mobility in the Q&P temperature range to diffuse through the α'/γ interface.

Furthermore, as very recently reported in the literature, nanoscale partitioning of small amounts of manganese was highlighted at low temperature and relatively short tempering time [42][107]. Indeed, Mn appears to be depleted on the martensite side of the interface, and enriched on the austenite side (see Figure I-38). This is an important point for many reasons. First, it raises the question of the CCE condition, which ignores the partitioning of iron and substitutional alloying elements during the partitioning stage. Second, it could be the marker of the motion of the α'/γ

interface, since it is well known that Mn can interact with a moving interface in steels [115]. Last, but not least, interfacial partitioning of substitutional elements is expected to play a key role on both the kinetics and the total carbon enrichment in austenite.

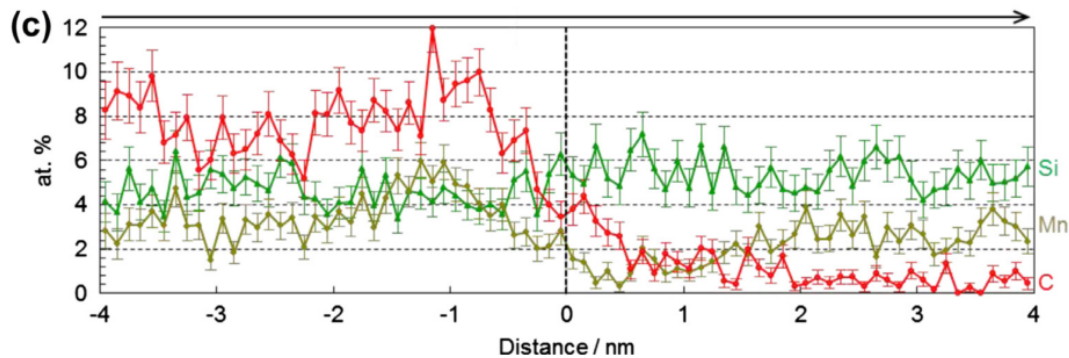


Figure I-38 - Average compositions of C, Si and Mn through a γ/a' interface obtained by APT (Q&P conditions : PT=400°C/300s) (taken from Toji et al. [49])

Interface migration

The only fact that carbon can diffuse from martensite to austenite without any motion of the α'/γ interface is questionable and led to a controversy in the Q&P literature. When the CCE model was proposed, one of the main assumptions was that the martensite/austenite interface is immobile [7]. Only carbon atoms were considered to diffuse over significant distances to allow austenite enrichment whereas iron and substitutional atoms are less mobile. However, there are some experimental evidences of the α'/γ interface motion during Q&P treatment. Zhong et al. first showed through TEM experiments, that the α'/γ interface might migrate based on a change of shape of the interface: from initially straight, to curved at the end of the partitioning step [116]. Later, Thomas et al. used EBSD and XRD to measure the evolution of phase fractions during partitioning [117]. They showed that austenite fraction increased and thus concluded that the interface migrates from martensite towards austenite. STEM was also used by De Knijf et al. to follow the change in width of an austenite film indicating that there is a bilateral (movement of interface towards one phase then towards the other phase) movement of the interface [118]. Indeed, as shown in Figure I-39, a fast increase of the austenite film width is first noted during the first 360s of partitioning, further partitioning leads to a slow decrease of the lath width to a final state where the lath is approximately 12% larger than at the beginning of the partitioning.

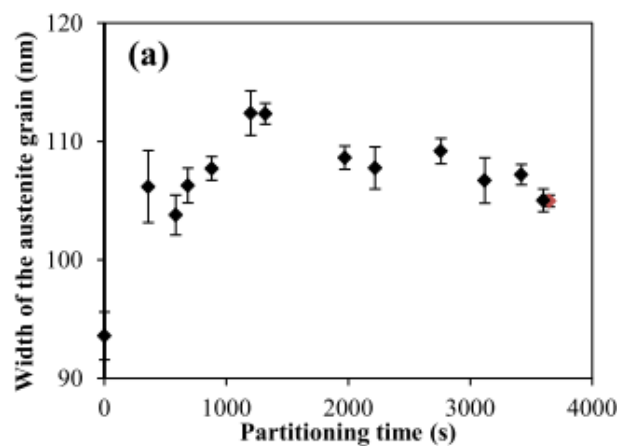


Figure I-39 - Change in austenite lath width during partitioning measured by TEM during in-situ annealing (taken from DeKnijf et al. [118])

Local Equilibrium models in Q&P Treatments

The previous part showed that the CCE conditions (no diffusion of substitutional elements, no interface migration) are not strictly respected during the process. Thus, some investigations were conducted to find other interface conditions that can better describe the Q&P process. Dai et al. conducted a study where the interface condition is assumed to be Local Equilibrium (LE) in order to assess the impact of interfacial Mn partitioning on interface migration and carbon partitioning [112][113].

At the beginning of the partitioning, the diffusivity of carbon in martensite being larger than in austenite, the diffusion flux of carbon on the α' side ($J^{\alpha'/\gamma}$) will be greater than on the γ side ($J^{\gamma/\alpha'}$). Thus, the interface will tend to go the opposite way, and migrate rapidly towards martensite. The isothermal section of a Fe-C-Mn ternary system indicates that the transformation is in the NPLE ($\alpha' \rightarrow \gamma$) mode (No Partitioning Local Equilibrium) and an inverse spike of Mn is formed at the α' side. At the end of the NPLE ($\alpha' \rightarrow \gamma$), $J^{\alpha'/\gamma}$ decreases and tend to be equal to $J^{\gamma/\alpha'}$. The interface velocity will then drop and leads to a PLE- ($\alpha' \rightarrow \gamma$) stage where the interface motion is accompanied by Mn diffusion, and a spike of Mn is formed ahead of the interface in austenite.

The carbon gradient on the α' side of the interface will be eliminated much faster than on the austenite side (in about 1s), leading to the case where $J^{\gamma/\alpha'} > J^{\alpha'/\gamma}$. The interface will start to migrate the opposite way; from martensite towards austenite: this is the NPLE- ($\gamma \rightarrow \alpha'$) mode. Once austenite homogenizes its carbon content, the interface movement becomes very sluggish and is made in the PLE- ($\gamma \rightarrow \alpha'$) mode where interface migration is controlled by Mn diffusion across the interface (cf Figure I-40 a).

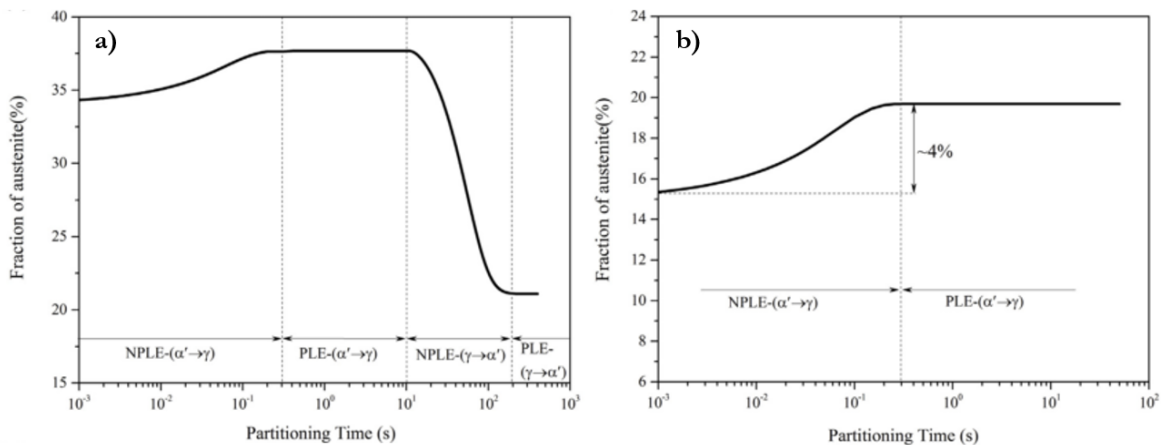


Figure I-40 - Evolution of austenite fraction for the different interface modes during partitioning predicted by the QP-LE model a) for $QT=290^\circ C$ b) for $QT=230^\circ C$ (taken from Dai et al. [119])

While this sequence of interfacial conditions is observed at $QT = 260^\circ C$ and $290^\circ C$, for lower QT the higher fraction of martensite leads to finer austenite films. Therefore, the homogenization of carbon in austenite is occurring much faster, indeed carbon gradient in austenite disappears after 20s of partitioning (versus 200s for $QT 290^\circ C$). Hence, for low QT there are only two modes: NPLE- ($\alpha' \rightarrow \gamma$) and PLE- ($\alpha' \rightarrow \gamma$) (cf Figure I-40 b)).

I.3.2 Partitioning from a bainitic source

Even though the bainitic transformation reduces the amount of austenite available for stabilization during the partitioning step, it can also have a stabilizing effect on surrounding austenite. Indeed, in the displacive view of bainitic transformation, nucleated sub-units of bainite grow up so rapidly that carbon atoms do not have enough time to diffuse away, and stay trapped by the advancing interface in the bainitic laths. Unlike martensitic transformation that is also displacive and diffusionless during the growth stage, bainite forms at temperatures that allow carbon to diffuse after the formation of each sub-unit. While high temperatures will promote

carbon escaping out of the plates to enrich surrounding austenite (leading to upper bainite), lower transformation temperatures (and thus lower carbon mobility) will lead to carbon precipitation into the laths (lower bainite) [121]. As stated before, sufficient silicon addition (above 1.5wt%Si) can prevent cementite precipitation in the laths and promote carbon diffusion towards austenite [73]. Even though it was showed that the bainitic transformation occurring during the partitioning cannot solely explain the levels of enrichment of austenite, it remains that it might be a non-negligible source of carbon [23].

The displacive approach states that the limiting factor for further nucleation of bainitic sub-units is the carbon content of austenite. Indeed, as bainite forms by a displacive mechanism, the free energy of the newly formed sub-units needs to be lower than the one of the parent austenite. By successive nucleation/growth mechanisms of bainite sub-units followed by rejection of the supersaturated carbon to the nearby austenite, it gets more and more difficult to nucleate new bainite sub-units in the remaining austenite, which gets richer carbon-wise thorough the transformation. For a given temperature, the point where the free energy of the parent austenite and the free energy of bainite are equal (and thus the driving force for nucleation of bainite is zero) is called T_0 [121]. It gives the maximum carbon enrichment of austenite during the bainitic transformation.

I.4 Modeling interaction between carbon partitioning and competing mechanisms

So far, the successive sections of this literature survey showed that the CCE model, initially adopted as a suitable model to describe the redistribution of carbon between martensite and austenite, is gradually being challenged by experimental evidences (carbide precipitation, bainite formation, interface migration). Indeed, as the understanding of the mechanisms involved in the partitioning process has advanced, it become clear that new models are needed in order to better describe the evolution of carbon distribution.

These models were first developed without taking into account the interactions between the different enrichment mechanisms but progressively, models dealing with multiples sources of enrichments or carbon trapping have arised.

I.4.1 Models without interactions

Interface Migration

The carbon partitioning kinetics will be impacted by the migration of the α'/γ interface.

Interface migration can be treated with three different approaches (taking the $\gamma \rightarrow \alpha$ phase transformation as example):

- the diffusion controlled model, where the interface mobility is assumed to be infinite. Thus, the volume diffusivity of carbon is the limiting factor for the interface mobility, and a gradient of carbon is established at the interfaces,
- the interface controlled model, in which the interface mobility controls the rate of transformation,
- a mixed-mode approach, situated between the two extreme situations described above [122][123][124].

During the carbon partitioning between γ and α' , the local carbon concentration at the interface on the γ side will deviate from the equilibrium value x_C^{fcc-eq} so that a driving pressure is created, that can be expressed as follows [125][126]:

$$\Delta G = \sum_{i=1}^N x_i^g (\mu_i^{fcc} - \mu_i^{bcc}) \quad (I.17)$$

where ΔG is the driving pressure, N is the number of components in the system (Fe or C), x_i^g is the concentration of component i in the growing phase, μ_i^{fcc} is the chemical potential of the component i in FCC, μ_i^{bcc} is the chemical potential of the component i in BCC.

For a binary Fe-C system, and assuming local equilibrium for C at the interface ($\mu_C^{fcc} = \mu_C^{bcc}$), the driving pressure solely results from the difference in chemical potentials of Fe between the FCC and the BCC phases. The driving pressure can also be expressed in terms of a difference between the carbon concentration at the interface at the austenite side and the equilibrium value as follow:

$$\Delta G = \chi(x_C^{fcc-eq} - x_C^{fcc-bcc}) \quad (I.18)$$

where ΔG is the driving pressure, χ is a proportionality factor that is temperature-dependent, x_C^{fcc-eq} is the interface carbon concentration in austenite at equilibrium, $x_C^{fcc-bcc}$ is the interface carbon concentration in austenite.

Hence, it is possible to have either a positive or a negative driving pressure. It is schematically represented in Figure I-41, always considering $\mu_C^{bcc} = \mu_C^{fcc}$:

- carbon at the interface is higher than the equilibrium value, then $\mu_{Fe}^{bcc} > \mu_{Fe}^{fcc}$ thus promoting interface migration towards martensite ($\alpha' \rightarrow \gamma$ transformation),
- carbon at the interface is lower than the equilibrium value, then $\mu_{Fe}^{bcc} < \mu_{Fe}^{fcc}$ thus promoting interface migration towards austenite ($\gamma \rightarrow \alpha'$ transformation).

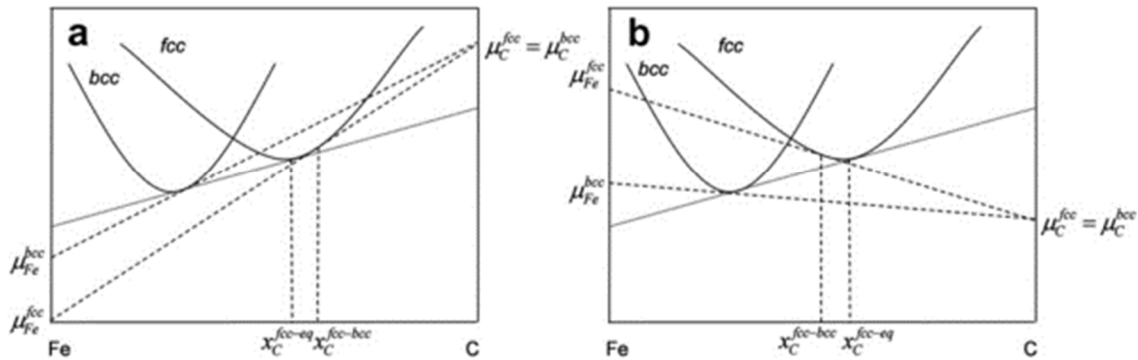


Figure I-41 – Austenite interface composition under CCE condition (dashed lines) and under equilibrium (solid lines) (a) Carbon concentration in the austenite at the interface is higher than the equilibrium concentration (b) Carbon concentration in the austenite at the interface is lower than equilibrium concentration (taken from Santofimia et al. [127])

Santofimia et al. used the mixed-mode approach to describe the velocity of the interface which is proportional to the driving pressure experienced by the interface as [127]:

$$v = M\Delta G \quad (I.19)$$

where v is the interface velocity, M is the interface mobility, ΔG is the driving pressure as defined in Eq. (I.18)

The mobility of the interface M is temperature depended and is expressed as a product of a pre-exponential factor, M_0 , and an exponential term that contains the interface migration activation energy term:

$$M = M_0 \exp\left(-\frac{Q_M}{RT}\right) \text{ with } M_0 = \frac{d^4 \nu_D}{k_B T} \quad (I.20)$$

where M is the mobility of the interface, Q_M is the activation energy for iron motion at the interface ($\text{kJ}\cdot\text{mol}^{-1}$), d is the average atomic spacing in the two phases separated by the interface in question, ν_D is the Debye frequency.

Assuming three different interface activation energies, Q_M , corresponding to different interface coherencies (and thus abilities to facilitate or not iron atom migration) under paraequilibrium conditions, Santofimia et al. were able to prove that the interface can have either a mono-directional motion towards austenite for an activation energy of about $180 \text{ kJ}\cdot\text{mol}^{-1}$, or a bidirectional motion for lower activation energies ($140 \text{ kJ}\cdot\text{mol}^{-1}$). Indeed, because of the huge difference between the carbon content at the interface in the early stages of partitioning and carbon equilibrium content, interface migration towards martensite occurs simultaneously with the carbon partitioning. Once carbon diffuses away from the interface, the carbon content is lower than the equilibrium value, so that interface reverses its migration direction and goes towards austenite (see Figure I-42). It is interesting to note that the in-situ TEM observation study led by study Knijf et al. has indeed evidenced such a bidirectional movement [118]. By applying the model described by Santofimia et al., they estimated an interface activation energy between 165 and $170 \text{ kJ}\cdot\text{mol}^{-1}$ concluding that the interface is more likely semi-coherent with a reduced mobility compared to the interfaces in austenite \rightarrow ferrite transformations.

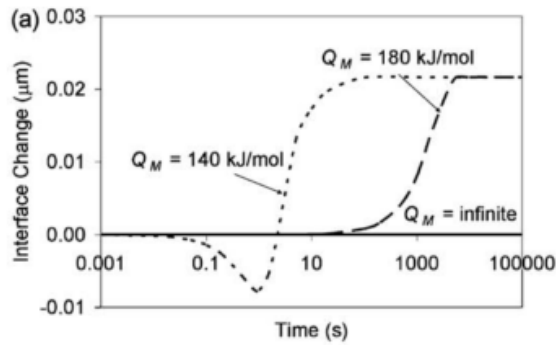


Figure I-42 - Interface migration direction changes during partitioning (positive meaning austenite to martensite) (taken from Santofimia et al. [127])

In Santofimia's model, because of the paraequilibrium condition chosen for the interface, the system adjusts the austenite fraction to attain the equilibrium value for carbon content (around $3.4 \text{ wt}\% \text{C}$ in that case). In the case of a low activation energy ($140 \text{ kJ}\cdot\text{mol}^{-1}$) and as shown in Figure I-43, the interface is mobile enough to allow carbon to reach its equilibrium value in the same timeframe (around 10 s) that for a fixed interface (CCE model or infinite activation energy). For intermediate interface mobilities, the interface starts to migrate at the 10 s mark and it takes more than 2000 s to reach the equilibrium state.

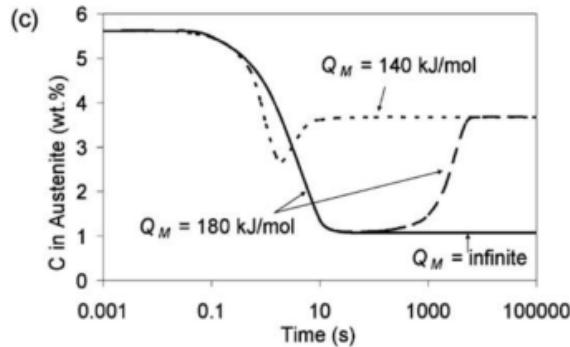


Figure I-43 - Evolution of carbon content at the austenite interface during partitioning (taken from Santofimia et al. [127])

Phase field modeling

QT sets the initial phase fraction but, as importantly, also sets the morphology of the remaining austenite for the partitioning step (cf I.2.1.1). Thermodynamic and 1D kinetic models help to understand the mechanisms of carbon diffusion between α' and γ , but fail to take into account both the morphological and topological aspects. In order to better capture and model how the morphology of austenite islands impacts the kinetics of partitioning and carbon redistribution, a phase field modeling approach was used by Takahama et al. and Mecozzi et al. [128][129]. In similar studies, they generated multi-phase structures that model the Q&P microstructures to study the carbon redistribution between α' and γ .

Phase field models describe the system using a so-called “order parameter” often noted ϕ . In a multiphase field method, each grain i is identified by its own order parameter $\phi_i(\vec{r}, t)$ such as:

$$\begin{cases} \phi_i(\vec{r}, t) = 1 & \text{if grain is present at location } \vec{r} \text{ and time } t \\ \phi_i(\vec{r}, t) = 0 & \text{if grain is not present at location } \vec{r} \text{ and time } t \end{cases}$$

In this modelling approach, the interfaces are considered as being diffuse (contrary to the sharp interface models). Indeed, between two different grains, there is a gradual change (cf Figure I-44) of the two order parameter (one for each grain) such that at each position r , $\sum_i^N \phi_i(r, t) = 1$ for a domain with a total number of N grains [130]. The interface thickness is then noted η .

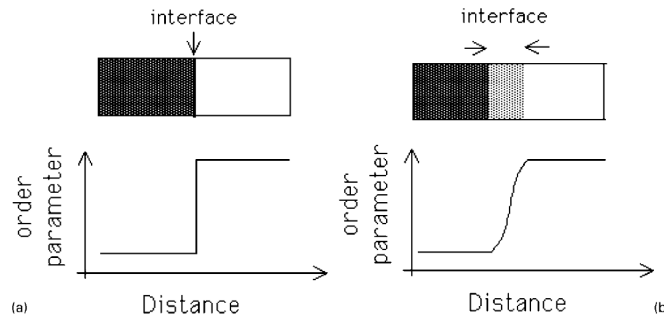


Figure I-44 - Schematic representation of the variation of the value of the order parameter through a) a sharp interface b) a diffuse interface (taken from [131])

Each grain was given a set of two attributes: its nature (FCC-austenite or BCC-martensite) and its lattice orientation. Then a concentration vector $\vec{x}(\vec{r}, t)$ (with components $x^{k=1\dots\xi}$ denoting the molar fraction of the solutes and x^0 the molar fraction of Fe) is introduced to describe the local composition of each phase. The evolution of the microstructure is then described by the evolution of the order parameter [132].

During the partitioning step, the interface was set immobile and any nucleation of bainite was excluded.

Both studies showed that in the early stage of partitioning, a peak of carbon is attained on the austenite side of the interface, due to the very fast escape of carbon from martensite laths. If the treatment is stopped in the early times of the partitioning, only the periphery of the austenite islands are enriched enough to be stable at RT as shown on Figure I-45. By increasing the partitioning time, the carbon atoms piled-up at the interface and have time to diffuse deeper into the austenite islands. The morphology of the austenite islands will play an important role as the smaller the grain is, the faster it is for the whole grain to reach the critical carbon concentration value (named x_c) that allow stabilization at RT. On the contrary, in large islands, the carbon has a larger austenite volume to enrich to x_c , thus as carbon diffuses away from the interface towards the center of the island, the carbon fraction falls to values lower than x_c . (see Figure I-45)

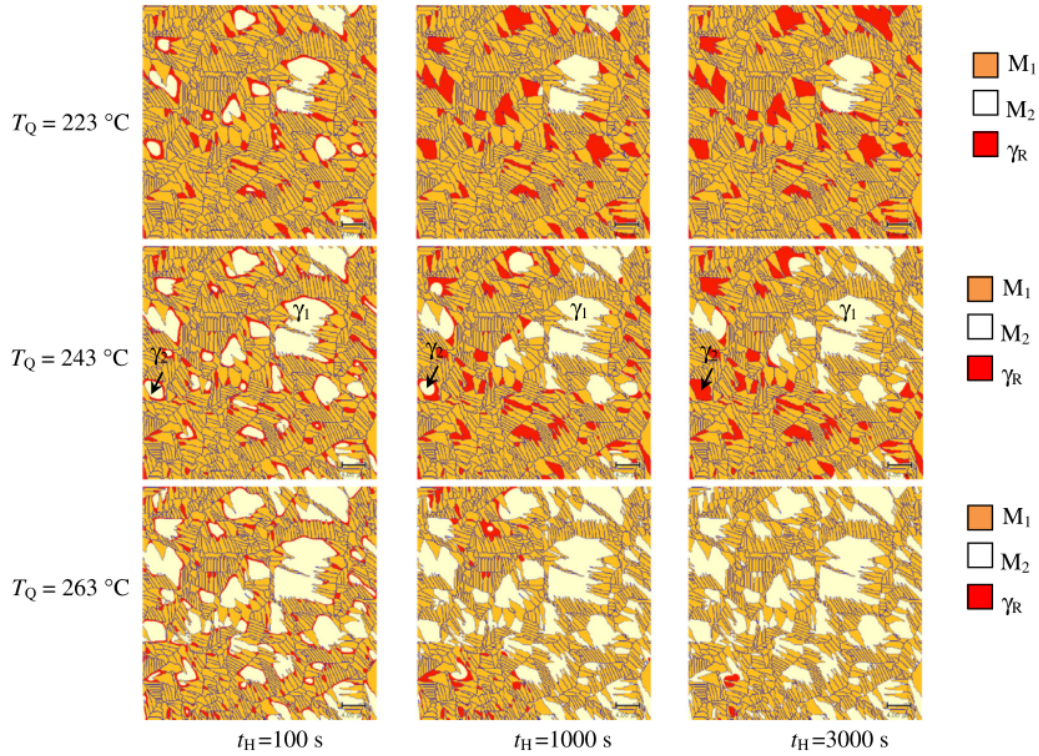


Figure I-45 - Final microstructures for different partitioning times and different QT. M1: Martensite from the initial quench, M2: martensite from the final quench, γ_R : Retained austenite (taken from Mecozzi et al. [129])

This behavior is clearly demonstrated by the graph representing retained austenite vs partitioning time Figure I-46. For microstructures with finer austenite islands (Low QT), the retained austenite fraction is increasing with partitioning time. The austenite grain marked “ γ_2 ” in Figure I-45 is a good example of a small grain that gets more and more stabilized with increasing Pt. For the microstructure with larger austenite islands (High QT), after a peak in retained austenite fraction for short partitioning times, the retained austenite fraction linearly decreases with Pt, and tends to zero. This is the consequence of carbon homogenization in large islands reducing the number of austenite regions locally reaching x_c . The grain marked “ γ_1 ” in Figure I-45 is an example of a large grain with a smaller fraction stabilized at the end of the treatment as Pt increases due to homogenization of carbon in the island.

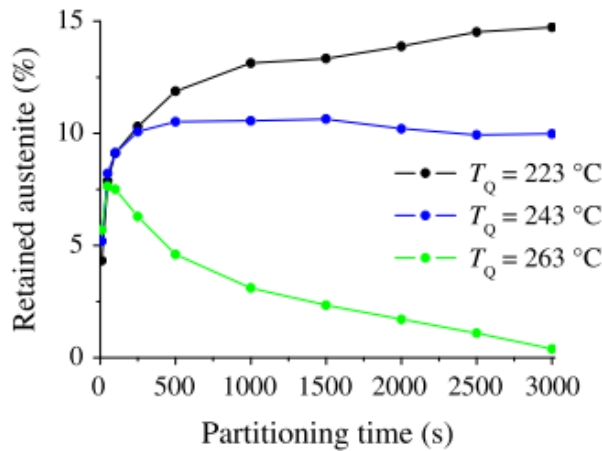


Figure I-46 - Fraction of retained austenite as function of partitioning time at 400°C for different QT's (taken from Mecozzi et al. [65])

As well as the austenite island morphology, surrounding martensite laths will affect the carbon

partitioning mechanism. Indeed, austenite islands that are small compared to the surrounding martensite laths will experience a sharper carbon peak at the interface for short partitioning time as the amount of carbon available for austenite enrichment will be high. Large austenite islands with respect to the surrounding martensite will experience a more gradual increase in carbon content [128].

I.4.2 Models with interactions

Interactions with carbide precipitation

Q&P investigations tend to study more and more the interactions between the different mechanisms occurring during partitioning. Indeed, as the variation of the measured carbon enrichment in austenite tends to exhibit different behaviors than the ones predicted by the CCE model, it is necessary to incorporate the effects of competing mechanisms. As pointed out in section I.1.1.1, it was observed that in some cases, the final enrichment level of austenite is independent of the QT [19][20]. Based on these observations, Toji et al. presented a modified CCE model (named CCE- θ) based on the interaction between carbon partitioning from α' to γ and cementite precipitation in α' [20]. Indeed, Toji et al. characterized the carbides precipitated in α' by APT as being Fe_3C - θ carbides (despite the fact that the steel contained 2.0 to 2.2 wt%Si). Then, they incorporated an extra term in the original CCE model equations accounting for the Fe_3C precipitation in α' as follow:

$$3\mu_{Fe_{CCE\theta}}^{\alpha'} + \mu_{C_{CCE\theta}}^{\alpha'} = G(Fe_3C) \quad (I.21)$$

$$\mu_{C_{CCE\theta}}^{\alpha} = \mu_{C_{CCE\theta}}^{\gamma} \quad (I.22)$$

$$f_{CCE\theta}^{\gamma} (1 - X_{C_{CCE\theta}}^{\gamma}) = f_i^{\gamma} (1 - X_C^{alloy}) \quad (I.23)$$

$$f_{CCE\theta}^{\alpha} X_{C_{CCE\theta}}^{\alpha} + f_{CCE\theta}^{\gamma} X_{C_{CCE\theta}}^{\gamma} + f_{CCE\theta}^{\theta} X_{C_{CCE\theta}}^{\theta} = X_C^{alloy} \quad (I.24)$$

$$f_{CCE\theta}^{\alpha} + f_{CCE\theta}^{\gamma} + f_{CCE\theta}^{\theta} = 1 \quad (I.25)$$

This CCE- θ is schematically drawn in comparison to the original CCE model in Figure I-47. The CCE- θ model states that the θ -carbides and martensite are under para-equilibrium, the value of equal potential of carbon in θ and α' is given by the intersection of the line passing through the free energy of θ (represented as a dot) and the free energy curve of α' and the right-Y axis. Martensite and austenite are under CCE conditions, meaning that carbon potential must be the same in the two phases, but as the chemical potential of carbon in α' is fixed by the presence of θ , the carbon concentration in austenite is given by the line linking the free energy curve of γ to the value of carbon potential in α' . Therefore, this model state that the final carbon concentration of austenite is indirectly linked to the thermodynamically equilibrium between α' and the θ -carbides and not by the original phase fraction or carbon content of the alloy.

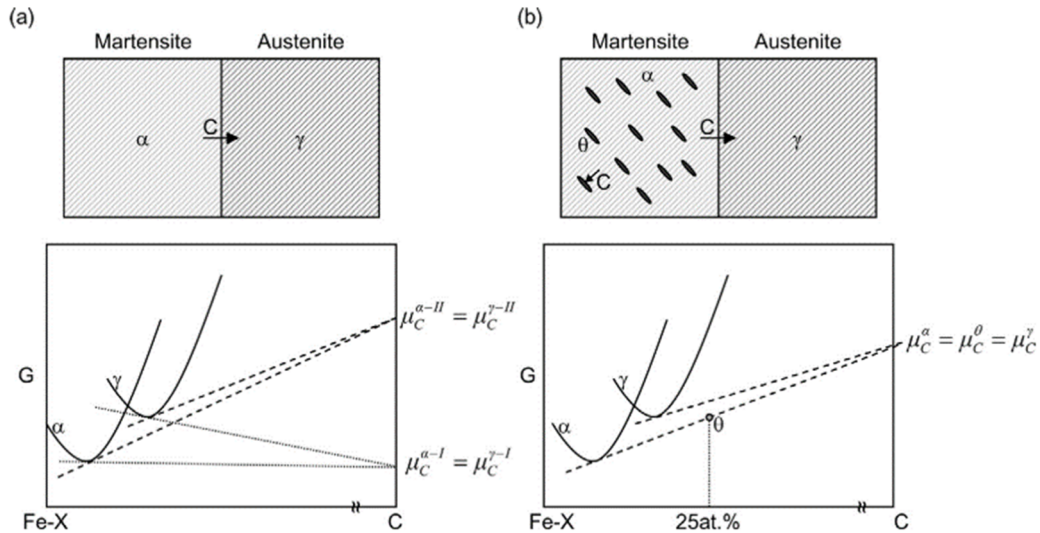


Figure I-47 - Comparison between (a) original CCE model with two (I and II) possible configuration satisfying the model and (b) modified CCE model (taken from Toji et al. [20])

Interactions with bainite formation

Recently, Nishikawa et al. published a study on the influence of bainite transformation on carbon enrichment in austenite during a Q&P treatment [133].

Two steels were studied, a low carbon one (0.25 wt.%C) and a high carbon one (0.8 wt.%C), giving two different martensite-austenite morphologies. The impact of alloying elements on the calculations was considered as negligible. For the low-C steel, the martensite is film-like and based on previous microstructure studies in [127]. Accordingly, the starting morphology chosen for the simulation of the low-C steel is as presented in Figure I-48.

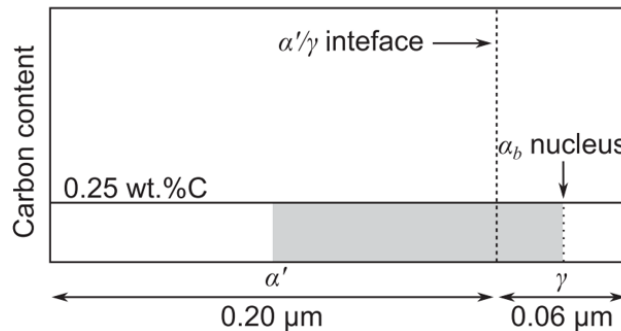


Figure I-48 - Schematic illustration of the morphologies considered in the simulations for a 0.25wt.%C steel alloy with one initial nucleus of α_b (grey zone : calculation domain)

In order to model the carbon partitioning with bainite formation, CCE conditions were used for the α'/γ interface (thus immobile) (cf section 3.1) and a bainite plate was assumed to nucleate in the middle of the austenite film.

The mixed-mode approach was used and the thermodynamic limit proposed for the bainitic reaction by Hillert et al. was chosen [134]. This so-called WBs (for Widmanstätten and bainitic ferrite) limit line was determined from three experimental data points of the measurement of carbon content in Fe-C. Then by using the thermodynamic data on Fe-C from Gustafson, the authors determined that the additional energies for bainite formation were 107, 1283, 2329 J.mol⁻¹ at 700°C, 450°C and 300°C [135]. These results were then interpolated with a spline in order to have a relationship linking the extra energy for bainite transformation with temperature.

The chemical potential of carbon and iron at the partitioning temperature in the different phases were calculated using TCFE8 database with Thermo-Calc. According to the relation described above, an extra energy for the bainitic reaction at 350°C of 1965 J.mol⁻¹ was added to the chemical potential of bainite. Consequently, at the metastable equilibrium between bainite and austenite, the carbon content of austenite reaches 1.75wt.% (cf Figure I-49)

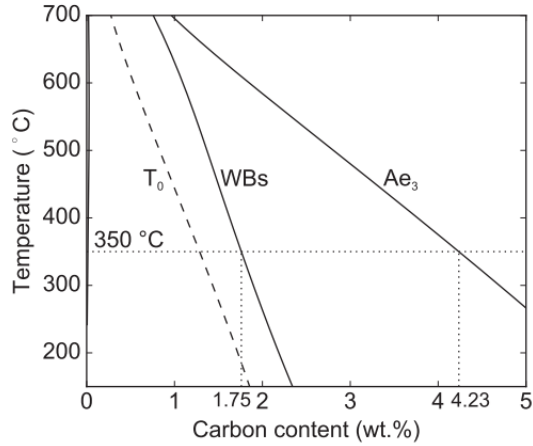


Figure I-49 - Fe-C phase diagram showing the lines proposed to be the critical limits for bainite growth (taken from Nishikawa et al. [133])

The configurations where partitioning occurs with (coupled model) and without (α'/γ model) growth of bainitic plates during the partitioning are then compared in term of kinetics of carbon enrichment in Figure I-50.

In either cases, on the martensite side of the α'/γ interface, carbon is depleted at the same rate because the escape of carbon is mainly controlled by diffusion in martensite. As shown in Figure I-50, for the first 0.3s, carbon content in austenite follows the same trend for the α'/γ model and the coupled model. However, once bainite transformation takes place, the carbon rejected from the bainitic laths leads to an acceleration of the austenite enrichment kinetics. Indeed, the CCE point (1.12wt%) is attained faster and as the interface γ/α_b is free to move, the austenite carbon content at equilibrium becomes the one imposed by the equilibrium between bainite and austenite. This equilibrium value is WBs (1.75 wt%) and is attained after approx. 10s.

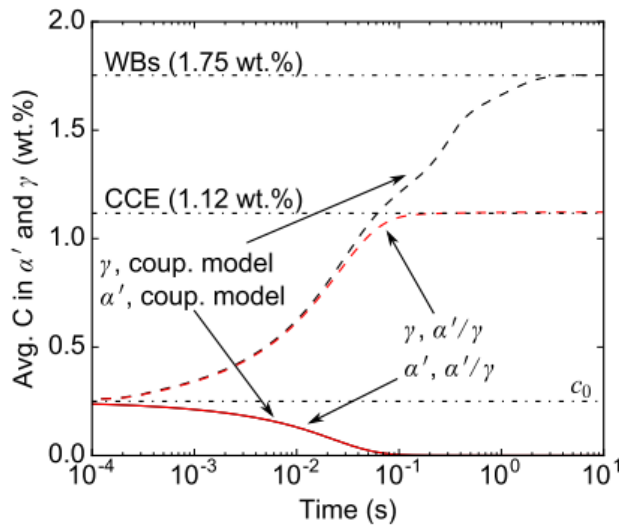


Figure I-50 -Comparison of the evolution of the average composition of α' and γ in the coupled model (black lines) and in the α'/γ model (red lines). (taken from Nishikawa et al. [66])

The free energy curves in Figure I-51 represent the state of the system once the equilibrium is

reached. A metastable equilibrium is reached between bainite and austenite, and a CCE equilibrium (with the austenite carbon content determined by the WBs limit) is reached between martensite and austenite so that the chemical potential of carbon is equal in all three phases.

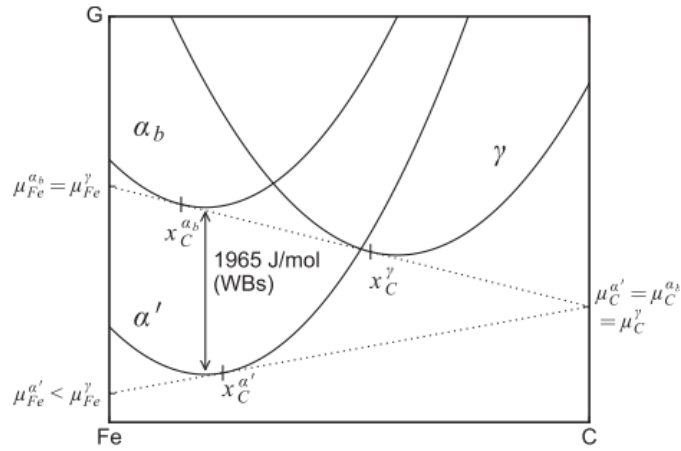


Figure I-51 - Free energies and compositions of the phases in the coupled model once the stationary state is reached (taken from Nishikawa et al. [133])

I.5 Partial conclusion

The Q&P treatment has proven to be a prime contender to lead the third generation of advanced high-strength steels. Theorized in 2003 by J.Speer, the treatment has since been largely studied, especially the relation between the process parameter (QT, PT and Pt) and the retained austenite amount, its morphology and carbon content.

As the experimentally obtained RA fraction and carbon content differed from the CCE framework of Speer, the scientific community started to study the hypothetical mechanisms that can interfere with the optimum austenite carbon enrichment. Very quickly, austenite decomposition, explaining the reduction in retained austenite fraction, was suspected to happen. The strongest argument in favor of austenite decomposition into bainite was the observed expansion by dilatometry during partitioning. However, the complexity of Q&P microstructures made bainite identification by SEM difficult. Apart from austenite decomposition, carbon trapping at defects and carbide precipitation were also suspected to be the two main explanations for the discrepancy between theory and experiments. Studies on carbide precipitation showed that these precipitates were most likely transitional (expected for high partitioning temperatures) but their nature (either η or ϵ) is still uncertain. Few studies focus on carbon atom segregations at defects while it might be a huge source of carbon trapping.

The main challenge in the Q&P field is still to assess the impact of each contribution to austenite enrichment as well as the interactions between them.

Chapter II : MICROSTRUCTURAL EVOLUTION

Table of contents

II.1 MATERIALS AND TECHNICAL CONSIDERATIONS	65
II.1.1 STANDARD Q&P HEAT TREATMENT	65
II.1.2 OPTIMUM TREATMENT PARAMETERS	66
II.2 DILATOMETRIC STUDY	71
II.3 PHASE IDENTIFICATION BY IMAGE ANALYSIS: MORPHOLOGY CRITERIONS	74
II.3.1 METALLOGRAPHIC PREPARATION OF THE SAMPLES	74
II.3.2 MORPHOLOGICAL DIFFERENCES BETWEEN PHASES	74
II.3.2.1 <i>Carbide Free Bainite microstructure</i>	75
II.3.2.2 <i>Q&P microstructure</i>	81
II.4 CARBIDES CHARACTERIZATION: COMPOSITIONAL (APT) AND STRUCTURAL (TEM) MEASUREMENTS	91
II.4.1 CARBIDE COMPOSITIONAL STUDY BY MEANS OF ATOM PROBE TOMOGRAPHY	91
II.4.2 CARBIDE STRUCTURAL STUDY BY MEANS OF TRANSMISSION ELECTRON DIFFRACTION	96
II.5 CARBON SEGREGATED IN MARTENSITE: APT STUDY	99
II.5.1 SEGREGATION DURING THE INITIAL QUENCH	100
II.5.2 SEGREGATION EVOLUTION AT MARTENSITE LATH BOUNDARIES DURING PARTITIONING	101
II.6 PARTIAL CONCLUSION	108

II.1 Materials and technical considerations

The composition of the studied steel grade is given in Table II-1.

Table II-1 - Aimed and measured chemical composition of the studied Q&P steel

	C (wt%)	Mn (wt%)	Si (wt%)	Fe (wt%)
Aimed	0.3	2.5	1.5	Bal.
Measured	0.313	2.44	1.52	Bal.
Castaing segregation ratio	1.6-1.7	1.1-1.3	1.1	

The alloy was first melted in an induction furnace and then cast into ingots. Next, the ingots were homogenized at 1250°C during 16h before a hot rolling step in order to obtain sheets of 10mm thick. Finally, the obtained sheets were machined into $\Phi 4$ standard (cylinder of diameter 4mm, 10mm in length) to fit the requirement of the dilatometer in which the heat treatment were conducted. The alloy was checked for micro-segregation by Castaing probe measurements with a step of 20 μ m. The ratio of the maximum over the minimum value (segregation ratio) was presented in Table II-1.

The dilatometer used is a Bahr DIL805D, the $\Phi 4$ sample is placed between two silica tubes and heated via induction (with a copper coil) as shown in Figure II-1. The cooling is provided by either nitrogen or helium flow. The treatment temperature is controlled via a type K thermocouple welded on the surface of the $\Phi 4$ sample. This setup allows the measurements of the change in length of the sample with a precision of 0.05 μ m during the whole Q&P treatment.

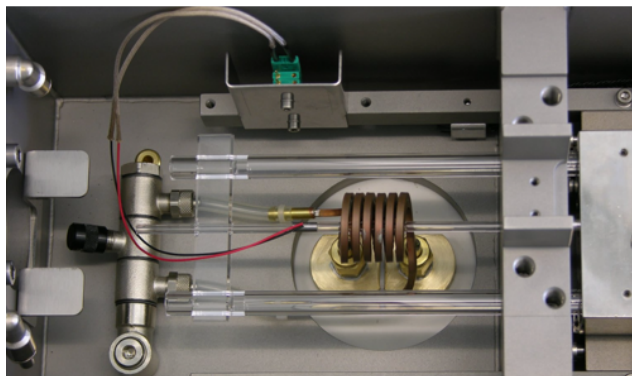


Figure II-1 - Sample between silica tubes, connected to a TC and in front of the copper coil induction device

II.1.1 Standard Q&P heat treatment

The general heat treatment for a Q&P steel is presented Figure II-2. The heating rate was set to 5°C/s and the austenitization was done at 900°C for 5 min to attain a fully austenitic microstructure, and to prevent any excessive growth of austenite grains. A cooling rate of 50°C/s from 900°C to quenching temperature was chosen to preclude any ferrite formation before Ms. The QT temperature is held during 5s for sake of temperature homogeneity of the sample. The heating rate to the partitioning temperature was 30°C/s and the final quench was done at the maximum cooling rate until RT. However, the quenching speed cannot be considered constant from 400°C to RT. Indeed, the maximum speed was attained in the first moments of the quench (average of 173°C/s from 400°C to 300°C), and decrease with temperature (average of 71°C/s from 200°C to 100°C and 10°C/s from 100°C to 20°C).

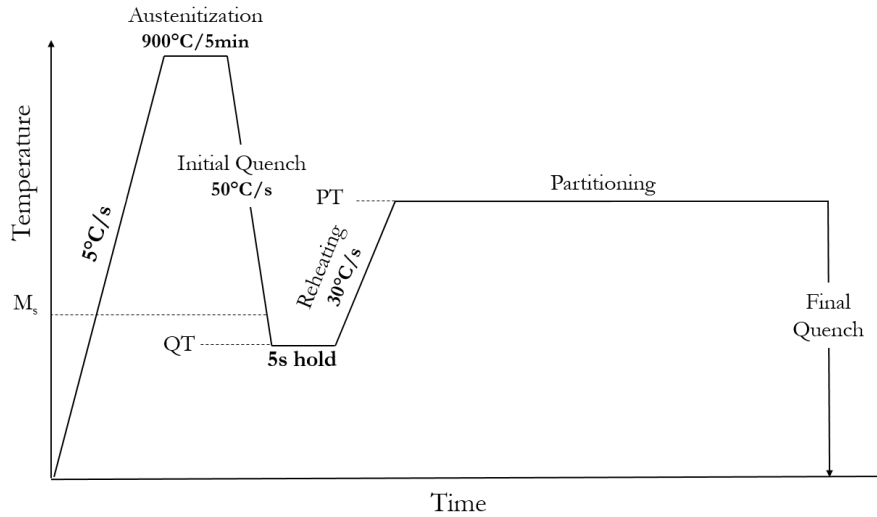


Figure II-2 - Standard Q&P treatment

II.1.2 Optimum treatment parameters

As shown in chapter 1, QT and PT are two key parameters that must be carefully chosen in order to efficiently reach the optimum amount of RA.

QT selection:

The choice of QT was mainly based on the value of Ms.

The martensitic start (Ms) temperature was evaluated using the dilatometric curves. As α' has a larger molar volume than γ , the martensitic transformation is accompanied by a change in volume of the sample, traditionally assumed to be isotropic. Thus, by recording the change in length of the sample during a quench from the austenitic domain, it is possible to estimate the Ms temperature. Figure II-3 is the dilatometric curve of a sample heated to a temperature of 900°C for 5min and then quenched at 50°C/s to RT. The increase of dilatation observed at 290°C is an indicator of martensite formation. The amount of martensite formed at a given temperature can be obtained by the classical lever rule, assuming that the amount of phase formed is proportional to the change in length. The following relation can thus be obtained:

$$f_M = \frac{\Delta L - \Delta L_\gamma}{\Delta L_{\alpha'} - \Delta L_\gamma} \quad (II.1)$$

The Ms value was defined as the temperature at which 5% of α' was formed.

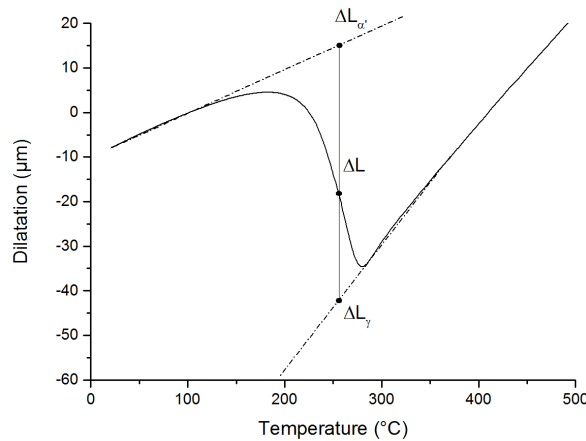


Figure II-3 - Dilatometric curve during a quench from austenitic state to RT

By averaging the measured value on 30 different samples treated by dilatometry, the following

value of M_s was obtained:

$$M_s = 285^\circ\text{C} (\sigma = 12^\circ\text{C})$$

This measured value was compared to the ones calculated from different empirical equations proposed in the literature. The result of the calculations as well as the alloying elements taken into account in the relations are indicated in Table II-2.

Table II-2 - Comparison between the different M_s values taken from equations published

Authors	M_s	Alloying elements in formula	Comment
Van Bohemen [11]	313,9°C	C, Mn, Si, Cr, Ni, Mo	Exponential dependence on %C
Barbier [13]	297,2°C	C, Mn, Si, Cr, Ni, Mo, V, Co, Al, Cu, Nb, Ti, B	Exponential dependence on %C
Carapella [136]	294,5°C	C, Mn, Si, Cr, Ni, Mo, Co, W	Non linear equation

All the M_s values calculated were in relatively good agreement with our measurements. The slight discrepancies highlighted can be explained from the fact that the equations proposed for M_s temperature do not depend on austenite grain size. It is well known that a difference in austenite grain size from $50\mu\text{m}$ to $5\mu\text{m}$ can lead to deviations of about 15°C , as Van Bohemen pointed out in [11].

The measured kinetics of martensitic transformation was compared to the ones predicted by Van Bohemen and Lee and Van Tyne relations [11][137]. Both equations have the form of the classical Koistinen and Marburger equation that can be expressed as:

$$f_M = 1 - \exp[-\alpha_m(M_s - T)^\beta] \quad (II.2)$$

where f_M is the volume fraction of martensite, α_m and β are two parameters that are function of the steel composition and T is the temperature.

While both relations give the same value for α_m (0.019), only the Lee and Van Tyne model uses the β parameter. The comparison between the experimental values and calculated ones is given in Figure II-4.

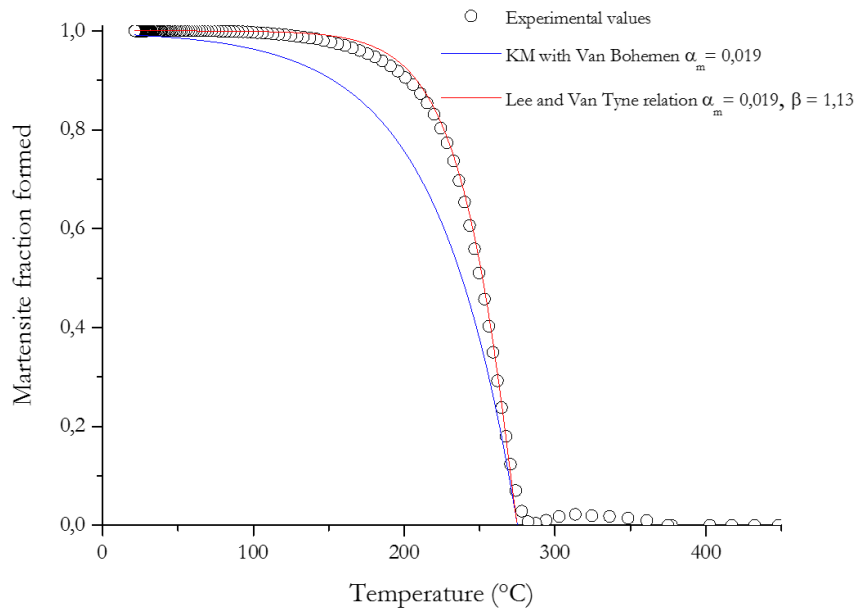


Figure II-4 - Comparison of the experimental α' formation kinetics with Van Bohemen and Lee Van Tyne relations [11][137]

The equation proposed by Lee and Van Tyne (LV Model) gives the best agreement with

experimental data and will be used to determine the optimum Retained Austenite (RA) fraction at the end of the Q&P treatment [137]. The Ms temperature used is the one extracted from experimental measurements (285°C). The model developed by Speer et al. was applied (see section I.1.1.3) in order to obtain the amount of martensite and retained austenite after carbon redistribution [16]. The results obtained are summarized in Figure II-5, that describes the evolution of both martensite and austenite fractions with QT. It is worth noting that the maximum amount of retained austenite is obtained for a critical temperature close to 240°C. When QT is high, the austenite is not stable enough, since its carbon content has not increased enough during the Q&P process.

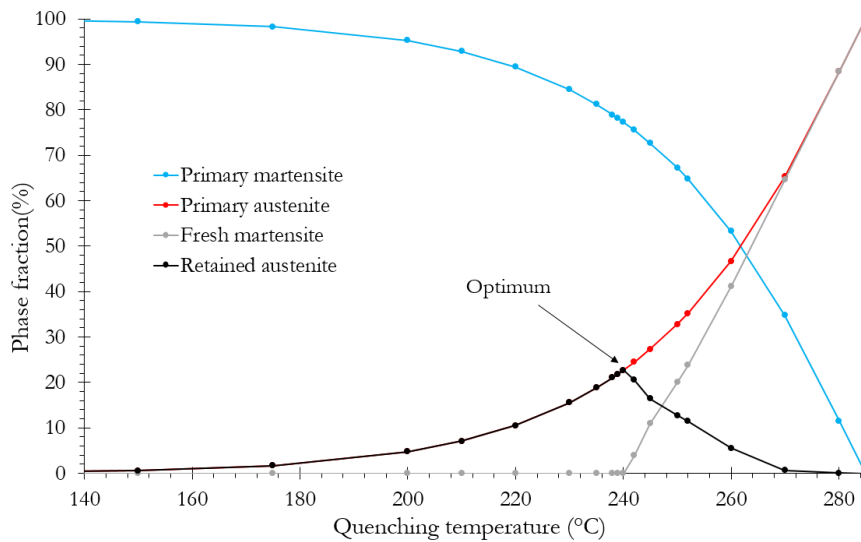


Figure II-5 - Evolution of the phase fractions for different QT according to Speer Model

As our study aims to improve our knowledge of the mechanisms of austenite carbon enrichment, as highlighted in the first chapter, it is necessary to compare different starting microstructures before the partitioning step. The CCE model states that the final redistribution of carbon is solely dependent on the initial fraction of martensite formed at QT (if the nominal composition is constant). Therefore, different QT's (200°C, 230°C and 260°C) around the optimum one were chosen, leading to different thermal paths (cf. Figure II-6) and to different martensite fractions before partitioning (cf Figure II-6).

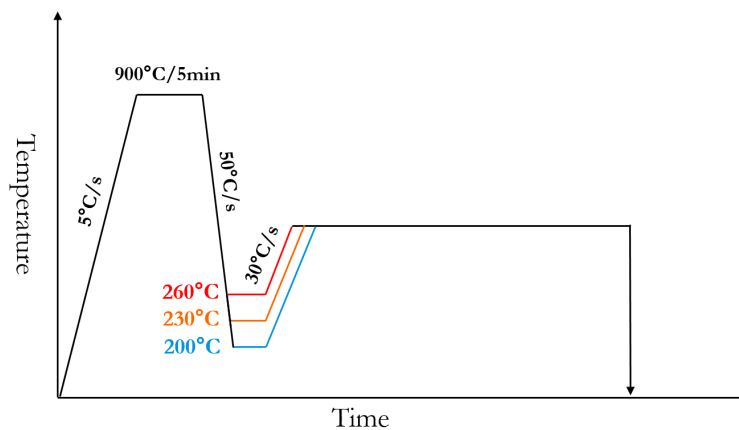


Figure II-6 - The three different Q&P thermal path with varying QT used in this study

Now that the different QTs are set, a choice for PT has to be made. PT was selected in order to allow carbon atom redistribution, while avoiding competing mechanisms. Speer et al. tested multiple PT on a 0.6%C-0.95%Mn-1.96%Si (wt.%) to maximize the retained austenite fraction.

Low PT values (250°C) yielded to the lowest retained austenite fraction (RA fraction) while increasing PT to 400°C led to the highest RA fraction. Based on qualitative TEM observations, Speer explained this effect by stating that more transitional carbides are formed at low PT, trapping more carbon in martensite. Thomas et al. also compared the enrichment kinetics of austenite for several PT and observed that it was more pronounced and faster at 400°C compared to 200°C and 300°C [48]. However, excessive PT (above 400°C) led to the formation of cementite, as Pierce’s Mössbauer study’s showed [68]. Based on this literature review, the time evolutions of retained austenite were compared at two different partitioning temperatures: 370°C and 400°C. It is worth noting that 400°C is a widely used PT in the Q&P literature [19][14][19][57][114][119][138][139][140][141].

X-ray diffraction (XRD) diffractograms were obtained using a Bruker D8-Advance (Bruker, Karlsruhe, Germany) with Cobalt K α radiation (1.78897Å) operated at 35kV and 40mA at the ArcelorMittal R&D Center in Maizières-les-Metz. The 2 θ ranges from 47° to 128° with a step size of 0.017°/1.77s and two rotations along the phi (1080°/min) and chi (60°/min) axis to reduce the impact of texture.

The use of a Co X-Ray sources gives the following theoretical 2 θ for the austenite and martensite main peaks:

Table II-3 - Theoretical peak positions in 2 θ for austenite and martensite with a Co radiation

Phase \ 2 θ (°)	50.940	52.377	59.595	77.235	89.549	99.705	111.366
Austenite	(111)		(200)		(220)		(311)
Martensite		(110)		(200)		(211)	

Figure II-7 below gives a typical diffractogram obtained after a Q&P treatment with QT=230°C and PT/t=400°C/200s. The different peaks for austenite and martensite are indexed.

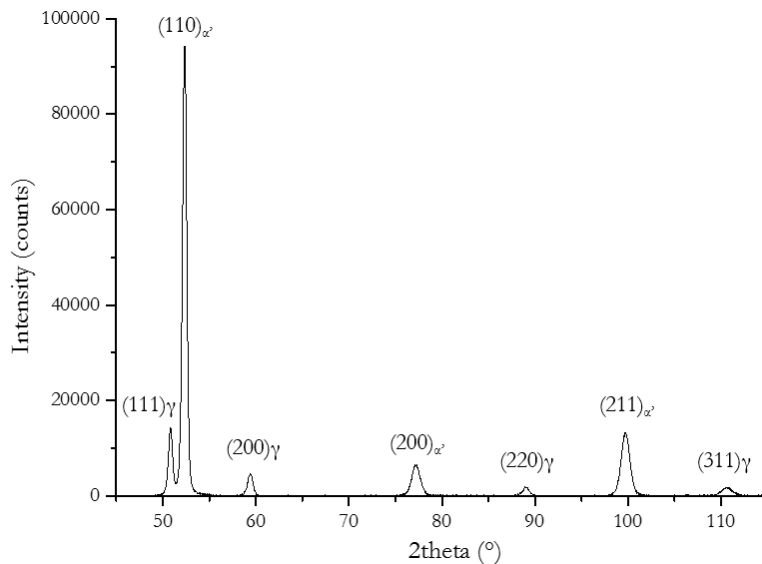


Figure II-7 - Diffractogram obtained with a Co radiation source on a Q&P treated specimen (QT=230°C PT/t=400°C/200s)

The determination of the amount of retained austenite was done following the ASTM E975-13. This standard uses the experimental integrated intensities (area under peak above background)

and compares them to the theoretical ones to determine the phase quantities of both martensite and austenite. This practice can be considered as valid for near random crystallographic orientations of both martensite and austenite and for retained austenite level above 1% [142].

The first two peaks of austenite and martensite, respectively $(111)_\gamma$ and $(110)_\alpha$, are very close and overlap with each other, becoming hard to resolve. Therefore, other peaks must be chosen for the calculation of integrated intensities. We chose the four peaks represented Figure II-8 because of the absence of overlap with other peaks and their good resolution.

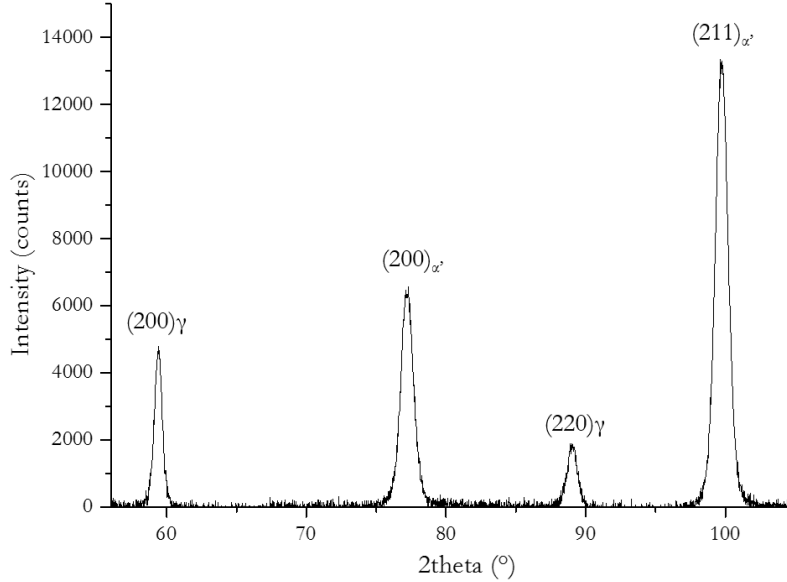


Figure II-8 - The four peaks of austenite and martensite used to apply the ASTM E975 method (zoom of Figure II-7) with background correction

The volume fraction of austenite (f_γ) derived from the measured intensities of the four austenite and martensite peaks is given by:

$$f_\gamma = \frac{\frac{1}{2} \left(\frac{I_{(200)\gamma}}{R_{(200)\gamma}} + \frac{I_{(220)\gamma}}{R_{(220)\gamma}} \right)}{\frac{1}{2} \left(\frac{I_{(200)\alpha'}}{R_{(200)\alpha'}} + \frac{I_{(211)\alpha'}}{R_{(211)\alpha'}} \right) + \frac{1}{2} \left(\frac{I_{(200)\gamma}}{R_{(200)\gamma}} + \frac{I_{(220)\gamma}}{R_{(220)\gamma}} \right)} \quad (II.3)$$

Where $I_{(hkl)\varphi}$ is the integrated intensity of the (hkl) plane of the phase φ , $R_{(hkl)\varphi}$ is the theoretical intensity values for the same (hkl) planes of the phase φ (taken from SAE Technical Paper 800426 for a cobalt radiation [143]).

The resulting austenite volume fractions determined for the two Q&P treatments characterized by the same QT of 230°C and two different PT (370°C and 400°C) are shown Figure II-9.

The question of the relative accuracy on retained austenite measurements is often subject of debates in the literature and multiples interlaboratory blind round robin tests [144][145]. Jacques's study in particular showed that while a general good agreement is obtain with the XRD technique, some important variability still exists. However, a pretty recent work of Gnäupel-Herold et al., mainly on TRIP steels with a similar chemical composition as our Q&P steels, showed that when XRD measurements are done with specimen orientation averaging (as in our study), a minimum of 10% of relative precision can be attain [146]. Therefore, the error bars presented in Figure II-9 are taking this value for each experimental point. The two curves exhibit the same trend: a sharp increase of RA during the beginning of the partitioning with a maximum at 50s followed by a slow decrease.

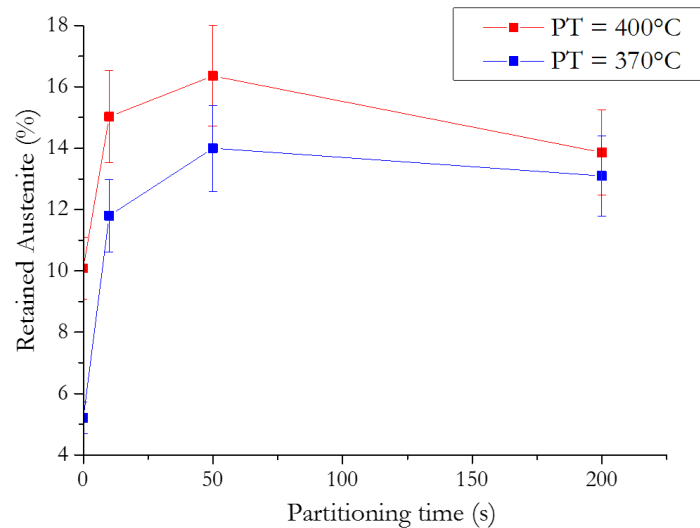


Figure II-9 - Evolution of retained austenite volume fraction with partitioning time for two different partitioning temperatures

An increase of PT from 370°C to 400°C leads to a faster austenite stabilization kinetics, characterized by a higher RA peak. This is consistent with the literature (section I.1.1.2) which points out that higher PT provides much more mobility for carbon, that can faster enrich the austenite islands (which is the most obvious for short partitioning times).

The fact that the RA fraction diminishes with time is questionable. This is largely interpreted in the literature as an indication of austenite decomposition (i.e bainite formation). However, as already presented in section I.4.1, Mecozzi et al. provided an additional explanation by phase field modeling [129]. Indeed, when Pt increases, austenite regions that were previously stabilized at shorter Pt becomes unstable due to the carbon homogenization in the whole austenite island. This effect is more pronounced at PT=400°C than at 370°C, because of faster diffusion at higher temperature of partitioning.

At last, it is interesting to note that some austenite islands are already stabilized at 0s of partitioning (i.e when the sample is quenched just after reaching PT). As samples directly quenched after the 5s QT hold showed no amount of RA, this highly suggests that austenite stabilization begins during the reheating to PT.

II.2 Dilatometric study

The study of dilatometric curves is useful to provide information related to the phase transformations occurring during the Q&P treatment. The dilatometric curve of dilatation versus temperature presented Figure II-10 is extracted from a Q&P treatment with QT=230°C and PT/t=400°C/200s. The steps of the treatment were drawn using different colors.

The austenization (dash/dot line) and initial quench to QT (first black line) steps are pretty conventional and present the classical Ac1, Ac3 and Ms points where a significant change in the rate of dilatation is observed marking phase transformation. The first interesting phenomenon is observed during the 5s hold (green segment) at QT just before the reheating step to PT (red segment). Indeed, a dilatation of 6.73 μm (or 0.067% of relative dilatation) is observed. It can be attributed to the temperature homogenization in the sample and the late martensitic transformation of some austenite of the sample reaching the QT temperature. However, it is not excluded that some isothermal martensite may form during the isothermal holding below Ms, as suggested by Kim et al. [147].

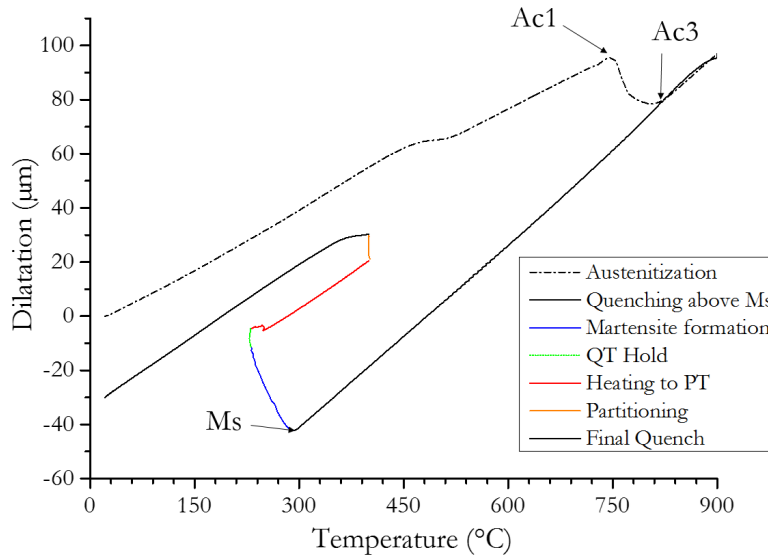


Figure II-10 - Dilatometer signal during a Q&P treatment ($QT=230^{\circ}C$, $PT/t=400^{\circ}C/200s$)

The heating step to PT is represented in red and, excepted at the very beginning, is quasi-linear. The change in length during the partitioning step is represented in orange, and the dilatation kinetics during this stage is presented Figure II-11 (relative dilatation vs partitioning time). During partitioning, the sample undergoes a relative dilatation of $8.60\mu m$ (or 0.086% of its total length).

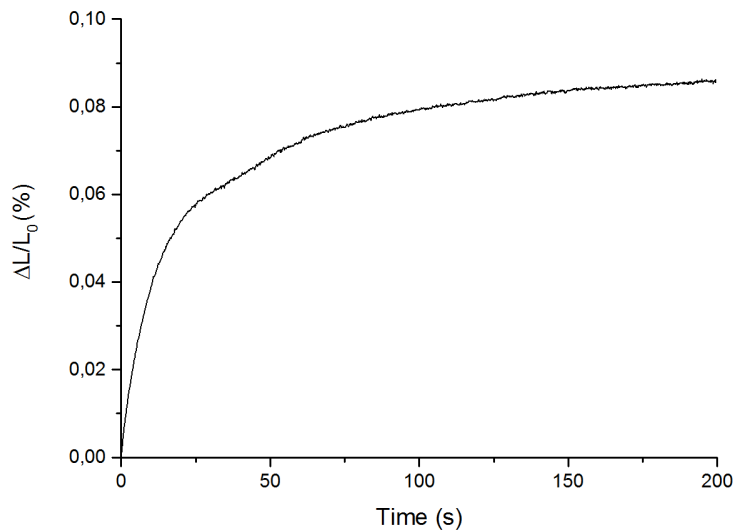


Figure II-11 - Relative dilatation of the sample during partitioning ($QT=230^{\circ}C$ $PT/t=400^{\circ}C/200s$)

In order to explain this expansion, we can start by determining the volume change associated to the redistribution of carbon atoms during partitioning by following the same approach as Santofimia et al. [140].

The calculations are based on the fact that the volume of the sample, V , during partitioning is linked to the specific volume of both martensite and austenite as:

$$V = f_M v_M + f_Y v_Y \quad (II.4)$$

where f_M and f_Y are the volume fraction, v_M is the specific volume of the martensite and v_Y is the specific volume of the austenite.

As the dilatation of the sample is assumed isotropic, we can write the relative length change as:

$$\frac{\Delta L}{L_0} = \frac{1}{3} \frac{(V - V_0)}{V_0} \quad (II.5)$$

where L_0 and V_0 are the sample length and volume at the beginning of the partitioning, ΔL is the change in length of the sample, V is the volume of the sample calculated at any time step

The change in austenite and martensite lattice parameters due to thermal expansion can be both calculated using the general equation for the variation in lattice parameters with temperature [148]:

$$a_\varphi = a_\varphi^0 \cdot [1 + \alpha_\varphi \cdot (PT - 300)] \quad (II.6)$$

Where a_φ is the lattice parameter of the phase φ at 300K (room temperature), a_φ^0 is the lattice parameter of the phase φ at the partitioning temperature PT (in K) and α_φ is the thermal expansion coefficient of the phase φ .

Once the effect of the thermal expansion is taken into account with eq.(II.6), the effect of carbon partitioning on both martensite lattice (escape of carbon leading to a contraction) and austenite lattice (insertion of carbon leading to dilatation) can be calculated in order to obtain the new specific volumes of each phase. The relations linking a and c with with carbon content (cf Table II-4) were obtained using a linear fit of the values presented in the newly published Lu et al. study [91]. The value for martensite lattice parameters when $X_C^{\alpha'}$ is equal to zero were taken as the iron lattice parameter (2.8664 Å from Babu et al.) [149]. The evolution of austenite lattice parameter was taken from from Toji et al. (a combination of the Dyson and Holmes and Ruhl et al. equations) [49][60][150].

The relations used to obtain the specific volumes of martensite and austenite are presented in Table II-4.

Table II-4 - Relations used to model the dilatation of the sample during partitioning

	Lattice parameter evolution with %C	Thermal Expansion Coefficient (K ⁻¹)	Specific volume
Austenite	$a_\gamma = 3.572 + 0.033 \cdot X_C^\gamma$ [49]	$2,07 \times 10^{-5}$ [151]	$v_\gamma = 0.25 a_\gamma^3$
Martensite	$a_M = 2.8664 - 0.00128 \cdot X_C^{\alpha'}$ [91]	$1,24 \times 10^{-5}$ [151]	$v_M = 0.5 c_{\alpha'} a_{\alpha'}^2$
	$c_M = 2.8664 + 0.0191 \cdot X_C^{\alpha'}$ [91]		

where $a_{\alpha'}$ and $c_{\alpha'}$ are the lattice parameters of the tetragonal martensite in Å, $X_C^{\alpha'}$ is the carbon concentration of martensite in at.%, a_γ is the lattice parameters of austenite in Å and x_γ is the carbon concentration of austenite in wt.%

Then, using Eq.(II.4) at the beginning (V_0) and at the end (V) of the partitioning step, Eq.(II.5) gives the specimen relative change in length during partitioning due to the carbon redistribution process (assuming no changes in volume fractions).

The next step is to estimate the carbon content of both austenite and martensite at the end of the Q&P treatment (QT=230°C and PT/t=400°C/200s). The XRD diffractogram presented Figure II-7 and Figure II-8 was used to calculate the austenite lattice parameter with the 2θ values of the (200) γ , (220) γ and (311) γ peaks. At the end of the treatment, the austenite lattice parameter was 3.6096 Å. Then, the equation from Toji et al. was used to calculate the carbon content of austenite as [49]:

$$X_C^\gamma = \frac{3.6096 - a_{\gamma 0} - b_0}{0.033} = 1.12 \text{ wt. \% C} \quad (II.7)$$

Where $a_{\gamma 0}$ is the austenite lattice parameter when $X_C^\gamma = 0$ (3.572 Å) and b_0 is a parameter that takes into account the effect of alloying elements on the austenite lattice as $b_0 = 0.0012\% \text{ Mn} - 0.00157\% \text{ Si}$.

The measured austenite carbon content is much lower than the one predicted by the CCE model (2.12 wt.%). This would be most likely due to carbon trapping in martensite.

Figure II-9 gives the retained austenite phase fraction at RT ($f_{\gamma} = 0.14$). Therefore we also get the martensite phase fraction ($f_M = 1 - 0.14 = 0.86$). A simple mass balance on carbon gives the martensite carbon content ($X_C^{\alpha'} = 0.17\text{wt}\%$). The values taken for the calculation as well as the resulting theoretical relative dilatation due to carbon partitioning are presented Table II-5.

Table II-5 - Relative dilatation resulting from the partitioning of carbon to austenite

	Austenite		Martensite		$\frac{\Delta L}{L_0}$
	f_{γ}	X_C^{γ} (wt%)	f_M	$X_C^{\alpha'}$ (wt%)	
QT=230°C PT/t=400°C/200s $X_C^0=0.3\text{wt}\%$	0.14	1.12	0.86	0.17	0.0058 %

Compared to the experimental value of relative dilatation (0.086%, see Figure II-11) the dilatation due to carbon partitioning is lower and cannot be the only explanation of the observed change in length. A possible explanation is the formation of bainite, that cannot be excluded and may explain the large dilatation observed because of its larger specific volume. We will come back later on this specific point.

II.3 Phase identification by image analysis: Morphology criterions

Even though the main purpose of the Q&P treatment is to obtain a duplex martensite/stabilized austenite microstructure, the complexity of the thermal path can promote the formation of other phases.

The dilatometry experiment presented in the previous section showed that it is possible that bainite forms during the partitioning step. As dilatometry is not able to discriminate between martensite and bainite, microstructural investigations using SEM image analysis can provide further elements to support this hypothesis, drawn from the inconclusive dilatometric study.

The combination of quenching, reheating and isothermal steps during the Q&P treatments results in a very complicated microstructure. Being able to distinguish and localize the different phases that are present in the final microstructure can help to understand the mechanisms of austenite stabilization.

In this section, a microstructural analysis method to discriminate the phases in Q&P steels based on morphological criterions is presented.

II.3.1 Metallographic preparation of the samples

First of all, and prior to any microstructural analysis, it is necessary to find the appropriate metallographic preparation that will effectively highlight the differences between phases. The purpose of the Q&P treatment being the redistribution of carbon between phases, it is thus logic to use a carbon-discriminating etchant. Nital etching (a mixture of nitric acid HNO_3 and ethanol) is largely used to reveal ferrite grains boundaries in steels and is very effective to reveal martensite lath structure. A good contrast between martensite and austenite is obtained, the latter appears with a bright contrast on SEM images. In addition, Picral etchant (a mixture of picric acid $\text{C}_6\text{H}_3\text{N}_3\text{O}_7$ and ethanol) is also used for its ability to obtain a better definition of the carbide structure in martensite/bainite.

The etching sequence consists of a Picral etch of a few seconds followed by a very quick Nital 1% etch (so-called “flash” etching).

II.3.2 Morphological differences between phases

By using SEM techniques in secondary electron mode (SE), the main information obtained is a

topological one. The etching step was selected in order to highlight the difference in carbon concentration between the different phases. In other words, a phase presenting a low carbon content will be more easily etched and will appear “dug”, in contrast to a high carbon content phase that will appear in relief. Moreover, due to their high carbon content, carbides will appear in an even higher relief contrast.

II.3.2.1 Carbide Free Bainite microstructure

In order to have a reference for the bainite morphology, a ‘Carbide-Free Bainite’ (CFB) type heat treatment was conducted. The thermal path applied is given in Figure II-12.

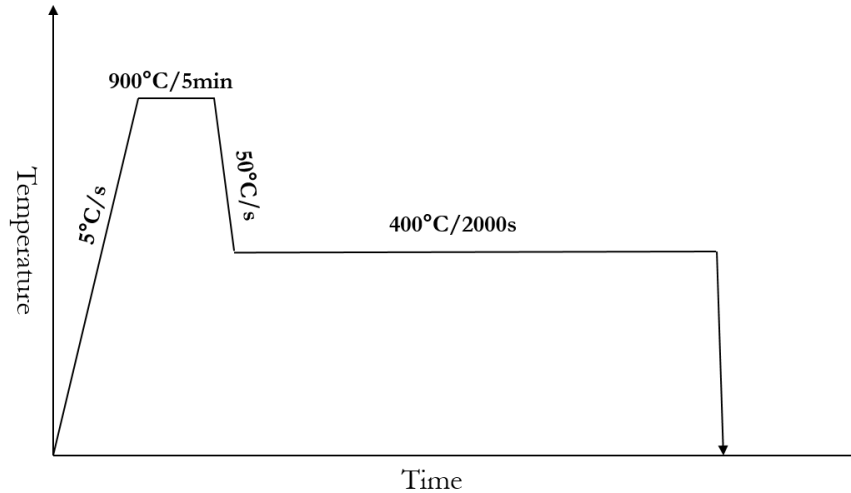


Figure II-12 - CFB treatment at 400°C during 2000s

The resulting microstructure is shown in Figure II-13. Two categories of phases, based on their relief aspect after etching, can be distinguished.

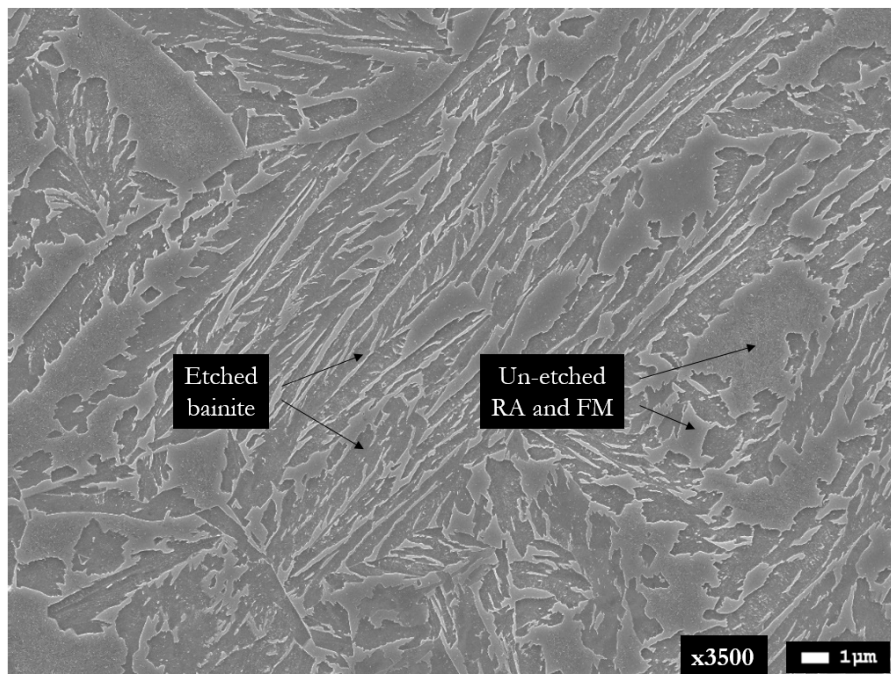


Figure II-13 - SEM image of a CFB microstructure (400°C/2000s)

Retained Austenite (RA) and Fresh Martensite (FM) are rich in carbon, and appear un-etched. Together, they constitute what is commonly called Martensite/Austenite islands (MA). On the contrary, bainite appears in low relief due to its carbon-depleted structure.

Figure II-14 schematically represents the phases appearing in the CFB microstructure and their relative height due to etching.

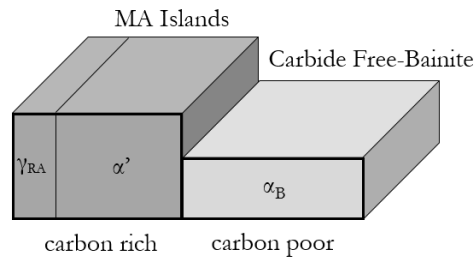


Figure II-14 - Schematic representation of relief between phases with different carbon content after etching

The use of automatic selection tools based on difference in pixels brightness in our case is difficult, thus every MA island was contoured manually as shown in Figure II-15.

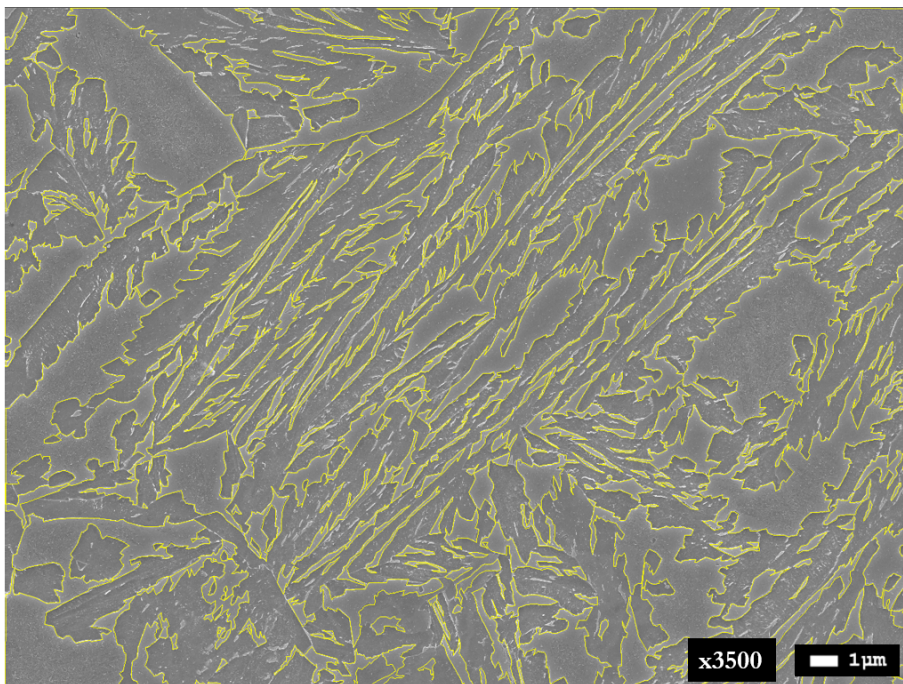
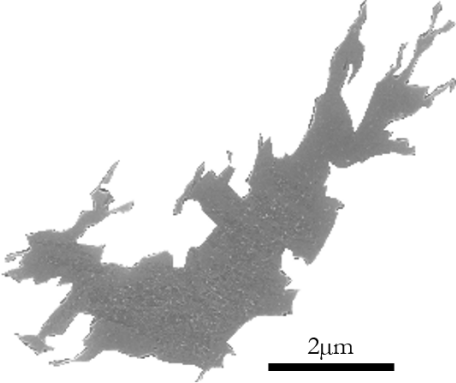
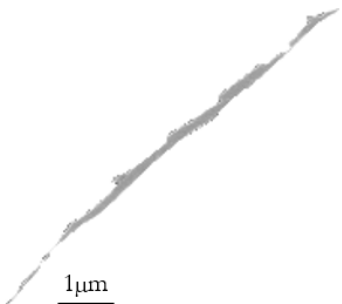
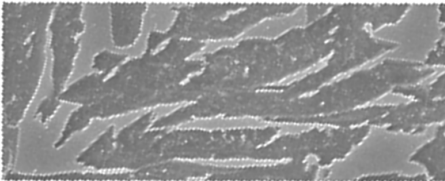


Figure II-15 - Contouring of the MA Islands in the CFB microstructure

Amongst the MA Islands, we can distinguish some main features and classify them based on morphology characteristics as shown in Table II-6.

Table II-6 - Classification and characteristics of the "relief" features in the CFB microstructure

Feature	Characteristics
<p style="text-align: center;">Large MA Islands</p>  <p>A micrograph showing several large, dark, irregularly shaped islands. A scale bar at the bottom right indicates 2 μm.</p>	<ul style="list-style-type: none"> - Large Islands - Internal structure (FM laths) - Phases : Fresh Martensite + Retained Austenite - Length : ~ 1 - 8 μm
<p style="text-align: center;">Fine elongated laths</p>  <p>A micrograph showing a single, long, thin, dark lath oriented diagonally. A scale bar at the bottom left indicates 1 μm.</p>	<ul style="list-style-type: none"> - Long laths - High contrast - Phase : Retained Austenite - Size : 1 – 5 μm
<p style="text-align: center;">Small grouped laths</p>  <p>A micrograph showing a dense group of small, dark, lath-like structures. A scale bar at the bottom right indicates 1 μm.</p>	<ul style="list-style-type: none"> - Small laths - Phase : Retained Austenite + Fresh Martensite - Length : 200nm – 1.5 μm

By filling all the MA islands selected in black, it is possible to have a view of the bainite formed during the treatment (Figure II-16). As expected, carbides are lacking thanks to the addition of large amount of Si in the steel. Some unselected fine RA laths (appearing in bright contrast) are still noticeable but they will have a negligible impact on the final phase fraction measurement.

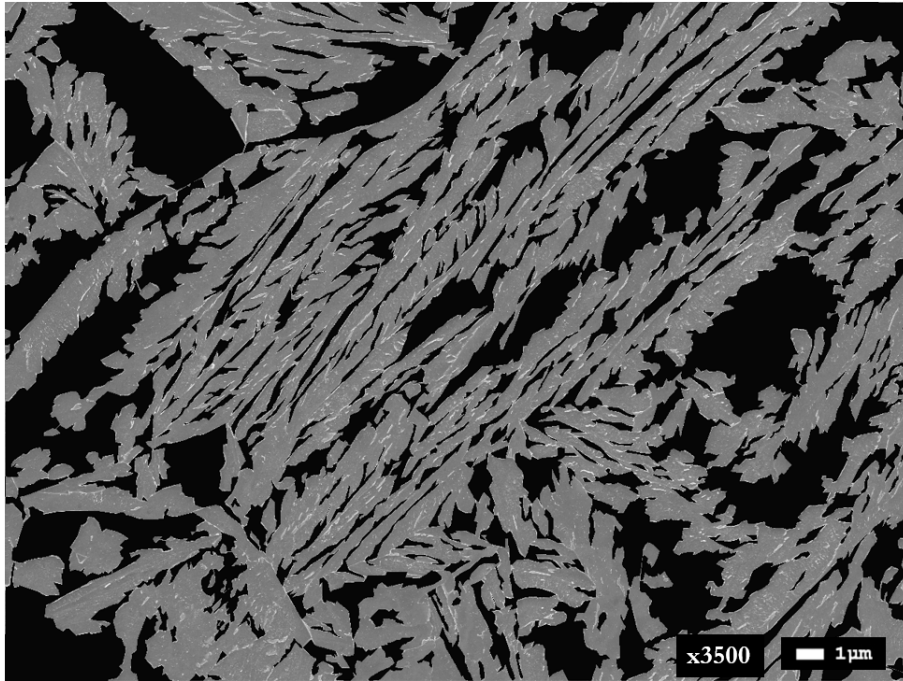
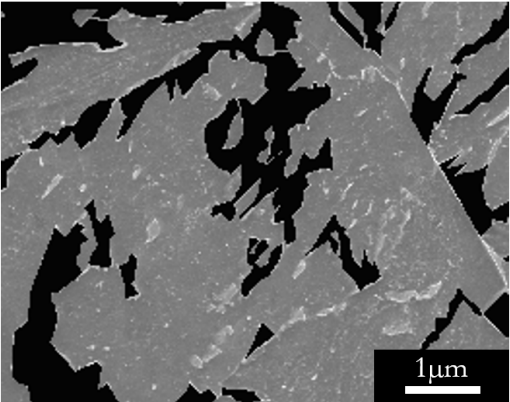
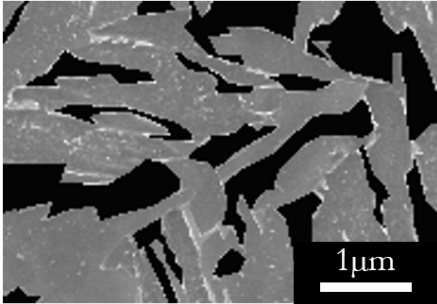
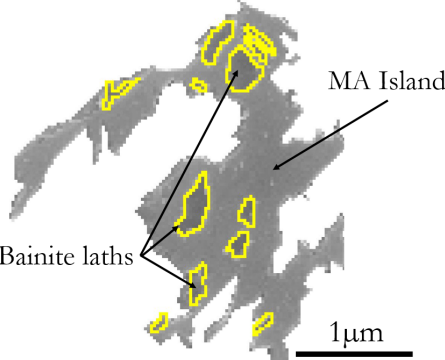


Figure II-16 - SEM image of the CFB sample after having filled in black all the MA Islands phases

Different morphologies of bainite can be observed, and are shown in Table II-7.

Table II-7 - Characteristics of the bainite observed in the CFB microstructure

Feature	Characteristics
<p data-bbox="347 1137 612 1171">Large bainite areas</p> 	<ul style="list-style-type: none"> - Coarse plates with irregular boundaries - Phases : Granular Bainite - Size : 2 – 9 μm

<p style="text-align: center;">Small bainite laths</p> 	<ul style="list-style-type: none"> - Individual laths more defined - Phase : Lath-like Bainite - Length : 250 nm -1.5 μm
<p style="text-align: center;">Small laths embedded in MA Islands</p> 	<ul style="list-style-type: none"> - Isolated lath (yellow contouring) into large MA (in light grey) - Phase : Bainite

While being interesting in order to study the morphology of phases, the manual delineation of phases is not very appropriate to tackle the large set of fields necessary to obtain volume fraction data with an acceptable repeatability.

Therefore, the fractions were also measured by using manual point counting (following ASTM E562) on 9 fields (4 fields at x3500 and 2 fields at x5000) on two samples that followed a CFB treatment [152]. The grid size (P_T) was 100 points per field (see Figure II-17), giving a sufficient relative accuracy considering the number of fields studied and the expected volume fraction of bainite.

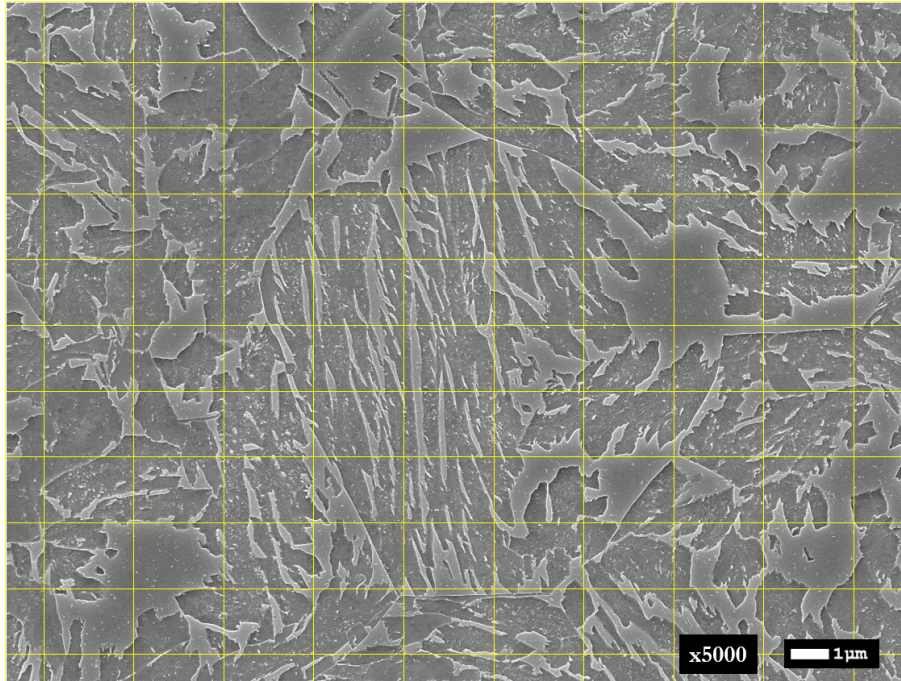


Figure II-17 – SEM image after a CFB treatment (400°C/2000s) with the 100 point grid used for manual point counting

All the following formulas used to obtain the phase fractions and relative accuracy values are also taken from the ASTM E562 norm.

The percentage of nodes falling within bainite in the i^{th} field $P_p(i)$ was calculated (if a point falls on the boundary, it was counted as one half) as follow :

$$P_p(i) = \frac{P_i}{P_T} \times 100 \quad (II.8)$$

where P_i is the point count for bainite on the i^{th} field and P_T is the total number of points in the test grid

Then the arithmetic average of $P_p(i)$ is calculated as :

$$\bar{P}_p = \frac{1}{n} \sum_{i=1}^n P_p(i) \quad (II.9)$$

where n is the total number of fields.

The standard deviation estimator, s , is given by:

$$s = \left[\frac{1}{n-1} \sum_{i=1}^n (P_p(i) - \bar{P}_p)^2 \right]^{1/2} \quad (II.10)$$

The standard deviation with a 95% σ can be calculated with:

$$\sigma_{95\%} = t \times \frac{s}{\sqrt{n}} \quad (II.11)$$

where t is a multiplier related to the number of fields studied

Finally the relative accuracy obtained can be calculated with:

$$\%Rel. Acc. = \frac{95\%CI}{\bar{P}_p} \times 100 \quad (II.12)$$

The results obtained are given in Table II-8 together with the values of n and t .

Table II-8 - Volume fraction of bainite and MA islands in the CFB microstructure measured by the manual point counting method

n=6 t=2.571	Volume fraction (%) ($\overline{P_P}$)	$\sigma_{95\%}$	%Rel. Acc.
Bainite	66.2	5.4	8.2
MA Islands	33.8	5.4	16.1

We can now compare the results from image analysis to the volume fraction obtained via XRD and dilatometry measurements. Figure II-18 presents the evolution of dilatation with temperature during the CFB treatment at 400°C. During the final quench, a deviation from linearity is observed. Indeed, the dashed black lines represent the linear change in length in case of the absence of a final martensitic transformation. The transformation of austenite into martensite leads to a net dilatation of 0.036% (represented in red in the plot). Preliminary experiments on fully martensitic treatments allowed us to determine that the formation of 99% volume fraction of martensite leads to a net dilatation of 0.93%. Therefore, a quick cross multiplication shows that 3.8% of fresh martensite is formed during the final quench of the CFB treatment. Finally, XRD measurements showed that the volume fraction of retained austenite is 20.3%. Consequently, the rest which is equal to 75.9% of the volume is considered as bainite.

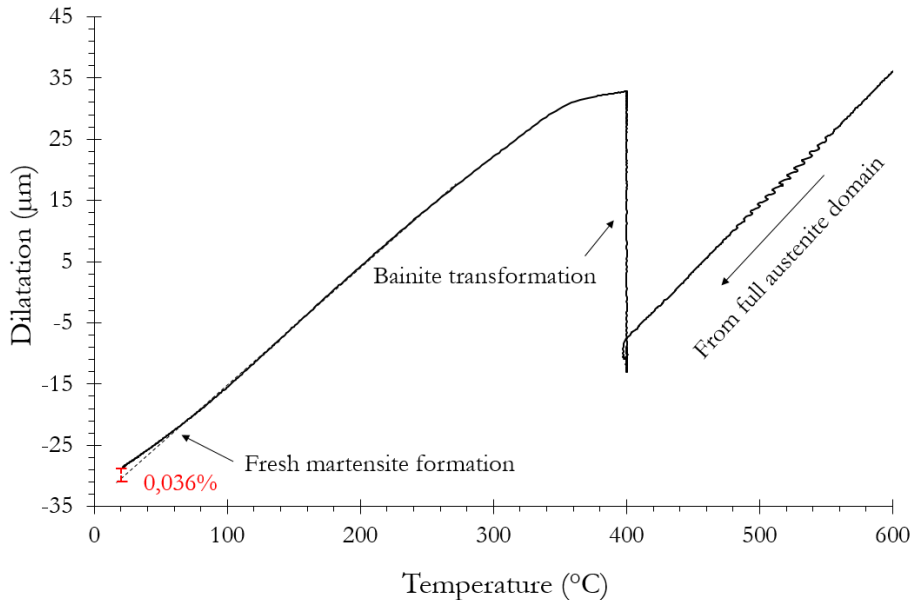


Figure II-18 - Dilatometer signal of the CFB sample treated at 400°C during 2000s. In red the change in length resulting from the fresh martensite formation during the final quench to RT.

The volume fraction of bainite determined by image analysis (66.2%) and dilatometry (75.9%) are pretty close considering the relative accuracy provided by the experimental technics used.

II.3.2.2 Q&P microstructure

The SEM image presented Figure II-19 corresponds to a sample that underwent a Q&P treatment with QT=230°C and PT/t=400°C/0s. The time spent at PT is very brief but as XRD showed, some carbon appears to redistribute during reheating to austenite, thus some microstructural changes (as compared to CFB treatment) should be noticeable.

At first sight, we can distinguish the phases that appear in relief and the other ones.

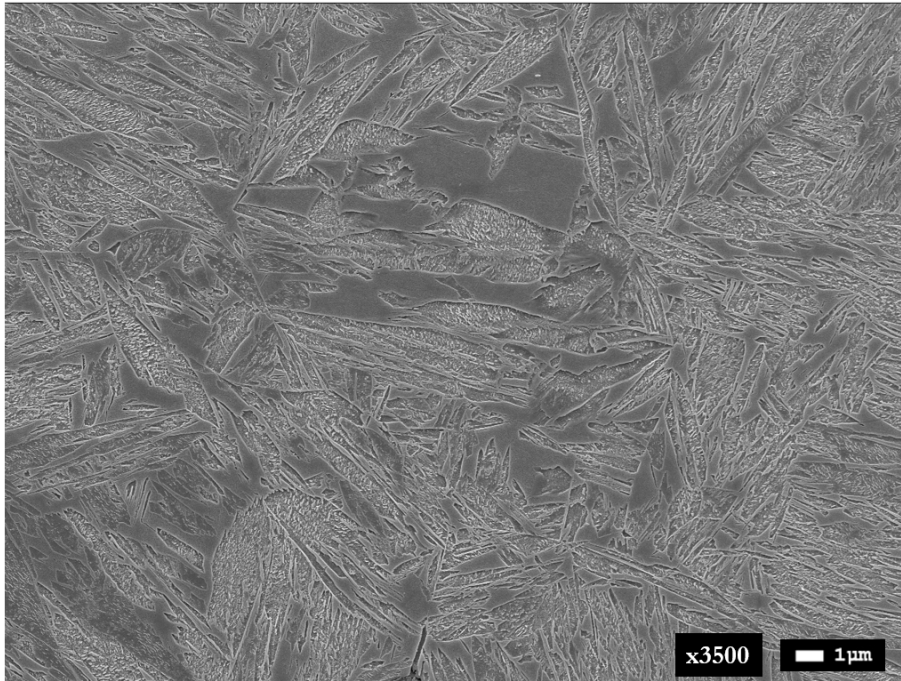


Figure II-19 - SEM image of a Q&P sample ($QT=230^{\circ}C$ PT/ $t=400^{\circ}C/0s$)

The phases that were enriched enough to appear un-etched are the following:

- retained austenite (γ_{RA})
- fresh martensite (α'_{FM}), formed during the final quench and resulting from the transformation of the non-sufficiently enriched austenite,

On the contrary, carbon-depleted (“dug” appearance) phases (other BCC or BCT phases) are:

- tempered martensite (α'_{TM}), formed at QT and that underwent tempering (can sometimes be called partitioned martensite),
- bainite (α_B) resulting from the decomposition of austenite during the partitioning step.

Figure II-20 schematically represents the phases appearing in the Q&P microstructure and their relative height due to etching.

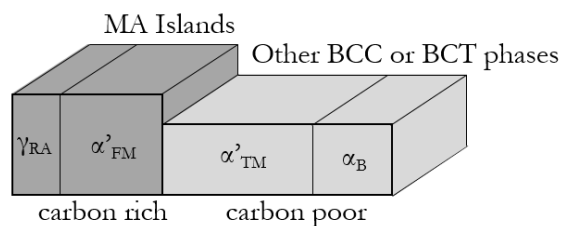


Figure II-20 - Schematic representation of relief between phases with different carbon contents after etching

Similarly to the procedure presented for CFB, the topological aspect of phases is the first discriminating criterion used to sort out our Q&P microstructure. The image analysis software used in this study is ImageJ.

Once again, the use of automatic selection tools based on difference in pixels brightness was made difficult, thus every MA was delineated manually as shown in Figure II-21.

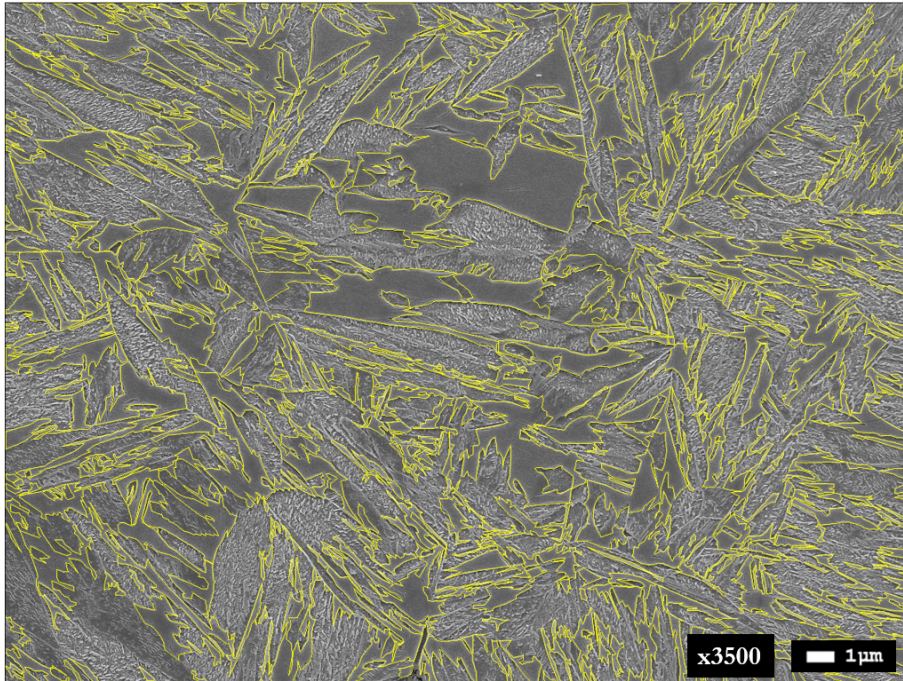


Figure II-21 - Delineation of the MA island features on the SEM image of the Q&P sample (QT=230°C PT/t=400°C/0s)

It is now possible to have the fraction of etched and un-etched (respectively carbon-poor and carbon-rich phases):

	MA Island	Other BCC or BCT phases
Volume fraction	34%	66%

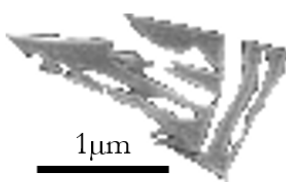
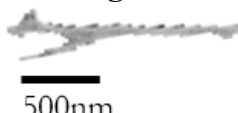
So for now a two phase-group classification was obtained, and some characteristics can be extracted from the image analysis.

MA Islands:

These features present a quite smooth surface aspect (even though some internal structure can be observed) and are mainly present as large islands, even though some present a finer lath-like morphology (see Table II-9).

Table II-9 - The different features and characteristics of MA islands in the Q&P microstructure

Feature	Characteristics
<p>Large Islands</p>	<ul style="list-style-type: none"> - Large block of MA - Smooth surface - Length : 400nm to 6μm - May present internal structure - Phase : Fresh martensite + RA

<p style="text-align: center;">Packets of small laths</p> 	<ul style="list-style-type: none"> - Groups of thin laths - Length of individual laths: 200 to 900 nm - Phase : Retained Austenite
<p style="text-align: center;">Long laths</p> 	<ul style="list-style-type: none"> - Long thin laths surrounded by other BCC or BCT phases - Appears pretty bright - Length : 1 – 2.5µm - Very high aspect ratio - Phase : Retained Austenite

Other BCC or BCT phases:

By filling in black all the identified MA phases (see Figure II-22), the remaining phases are the one we previously called “other BCC or BCT phases”.

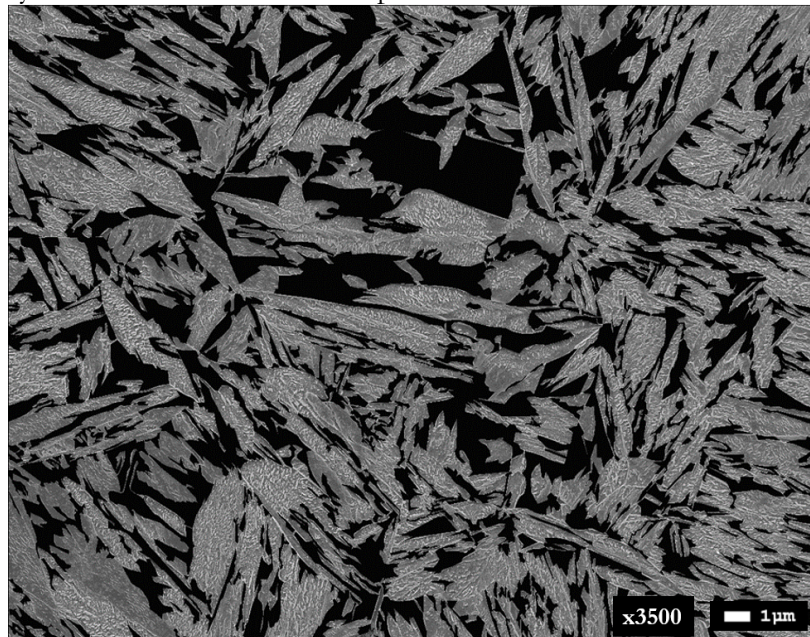
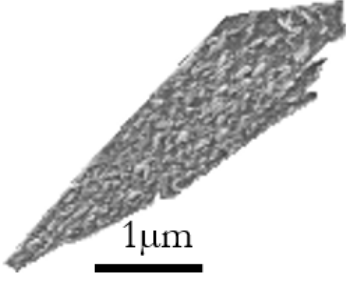
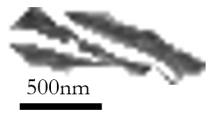
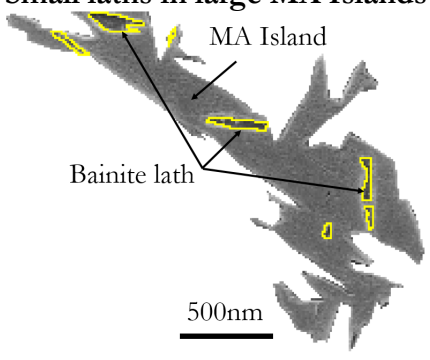


Figure II-22 - SEM image of the Q&P sample ($QT=230^{\circ}C$ PT/ $t=400^{\circ}C/0s$) after having filled in black all the MA Islands phases

Once again, we can extract two main features based on their morphological characteristics : large laths with carbides and small laths without carbides

The most striking characteristic of this microstructure is the presence of numerous carbides that are contained in large elongated laths. These laths are often surrounded by several similar parallel laths.

Table II-10 - The different features and characteristics of the others BCC or BCT phases in the Q&P microstructure

Feature	Characteristics
<p style="text-align: center;">Large laths with carbides</p> 	<ul style="list-style-type: none"> - Long laths - Contain carbides - Length: 1 – 5μm - Phase : Tempered Martensite
<p style="text-align: center;">Small carbide-free laths</p> 	<ul style="list-style-type: none"> - Thin acicular shaped laths - Carbide free - Length : 200-800nm - Phase : Bainite
<p style="text-align: center;">Small laths in large MA Islands</p> 	<ul style="list-style-type: none"> - MA Islands (in grey) with embedded bainite (yellow contouring) - Length: 200-800nm - Phase : Bainite

The small carbide-free laths present the same characteristics as the small bainitic laths observed in the CFB microstructure. Moreover, it is interesting to note that we also observed some bainitic lath growing in the large MA Islands. The microstructural study of Navarro-Lopez et al. above and under Ms led to the same conclusion, that is, bainitic features are presents as either thin units with no carbides or larges laths with irregular shape (identified as granular bainite in our study for the CFB microstructure but absent in the Q&P microstructure) [101]. Martensitic features only appeared either with carbides in it, like the long laths we observed in our Q&P structure or in the internal structure of the MA islands as fresh martensite (the latter being hardly etched due to its high carbon content).

Moreover, in addition to the ‘lack of carbides’ criterion, a second ‘size’ criterion is introduced for the bainitic laths. Indeed, some martensitic laths seem to have experienced a lesser extent of tempering and carbide precipitation is less obvious on the SEM images. It can also be due to a variation in the reaction to the chemical etching with some martensite laths exhibiting clear carbide contrast while other (due to a difference in carbide orientation and variants). Therefore, they might be etched more lightly and will not appear as defined and numerous as the carbide-filled martensite lath presented Table II-10. Figure II-23 is an example of a martensitic lath with

poorly defined carbides together with a carbide free bainitic lath. The bainitic lath is in the size range previously stated (200-800nm) while the martensite lath is way larger.

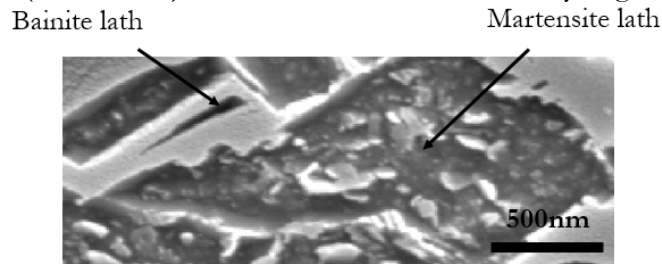


Figure II-23 - SEM image of a bainite lath together with a martensite lath with poorly defined carbides

Retained austenite location and morphology

The localization of retained austenite in the microstructure can give precious informations regarding the nature of the surrounding phases. Thus, EBSD was coupled with SEM on the same zone of a sample in order to combine morphological and crystallographic information. After a classical mechanical polishing step (from 320 grad to 1 μ m cloth on automatic polishing machine), a combination of automatic then manual OPU dry polishing allowed to reach a sufficiently clean surface for EBSD observation. Then, an EBSD map acquisition was done on a SEM JEOL FEG7001F equipped with Bruker Crystal align B400, the sample was tilted at 70°, the working distance was set to 12mm with a probe current parameter of 13 (u.a). The magnification was set at x1500 and the step size used was 100nm (giving map of 822 points on the X axis and 616 points on the Y axis). Once the EBSD map was done, a Nital etching is applied to reveal the mapped zone. Indeed, due to probe pollution during EBSD mapping, the mapped zone will appear unetched. This area was then marked by hardness points in order to be easily located. Then, the sample was quickly polished with dry OPU in order to remove the polluted surface but with taking care of not removing too much matter in order to have the same microstructure than the one observed with EBSD. Finally, the sample was chemical etched with Picral and Nital flash for SEM observations of the previously marked area.

The sample studied followed a Q&P treatment at QT=230°C and PT/t=400°C/200s.

Figure II-24 shows the IPF-Z EBSD map, the structure is mainly composed of lath like features and the structure of packets and block of martensite formed at QT is revealed.

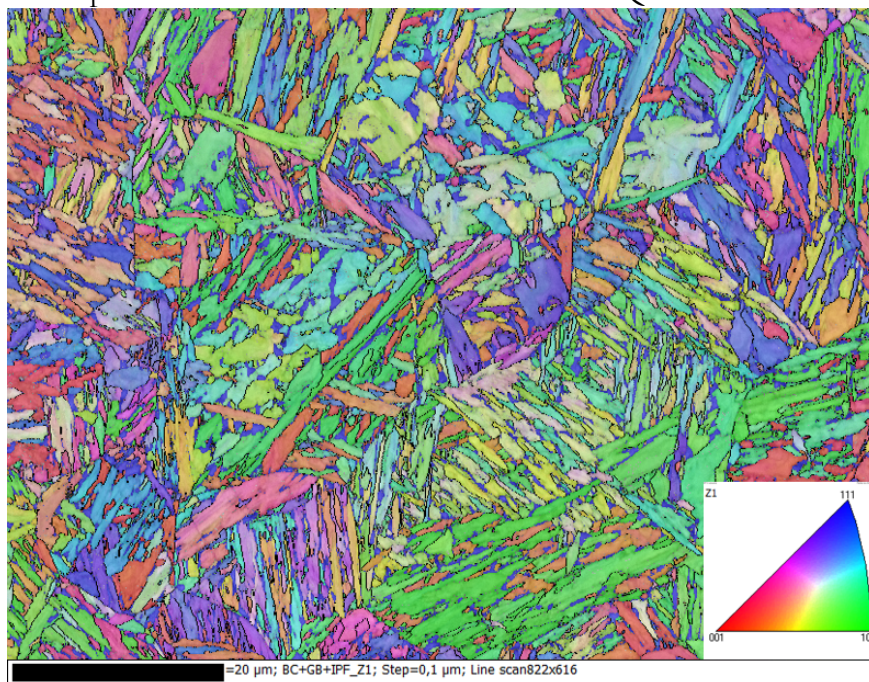


Figure II-24 - IPF-Z map of a sample after Q&P treatment (QT=230°C and PT/t=400°C/200s)

Figure II-25 shows a combination of band contrast image with the gamma phase represented in red and the grain boundary 10° as black lines. We superimposed the prior austenite grain boundary (PAGB) determined with MERENGUE 3 with yellow lines.

As the only two phases given to the EBSD software to index were FCC and BCC, all the microconstituents that are not red are either martensite (tempered or fresh) or bainite (carbides were too small to be probed with the current mapping settings).

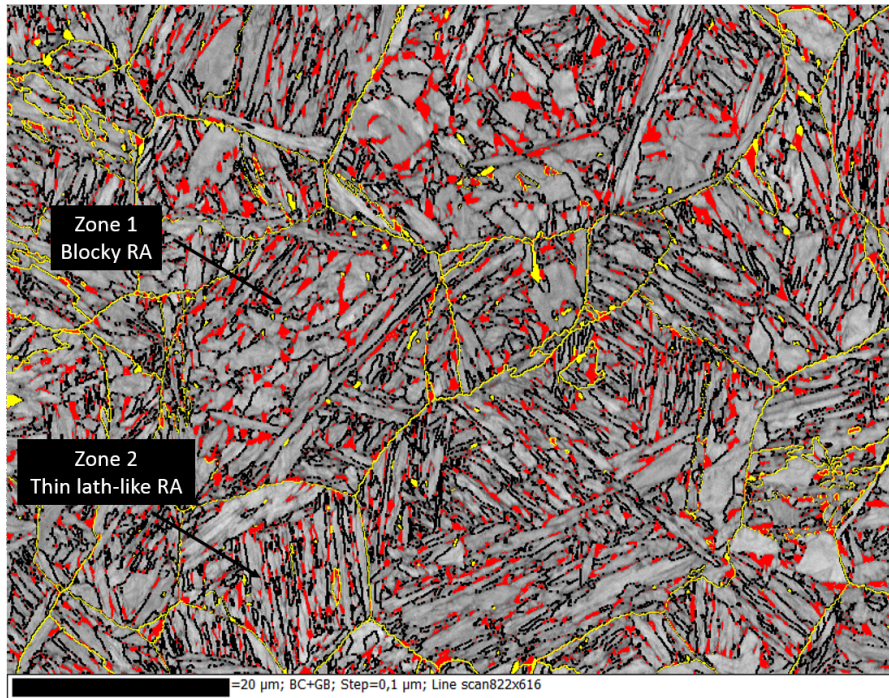


Figure II-25 - Band contrast and 10° grain boundaries (in black) together with retained austenite (in red) and PAGB (in yellow). Two zones presenting different retained austenite morphologies are also represented.

Retained austenite is present in two different morphologies. Either as blocky RA like in Zone 1 on Figure II-25 or as thin lath-like RA as in Zone 2 (see Figure II-27 and Figure II-28 for closer view of these zones). The band contrast and grain boundaries information shows that microconstituents surrounding the blocky RA are larger and with a lower aspect ratio than the microconstituent around the thin lath-like RA. Figure II-26 presents a SEM image of the same zones than in Figure II-25. The PAGB for the two prior austenite grain (PAG) with different RA morphologies presented Figure II-25 were also reported. The main difference between the two zones is that Zone 1 is mainly composed of irregular MA islands while Zone 2 is composed of finer MA.

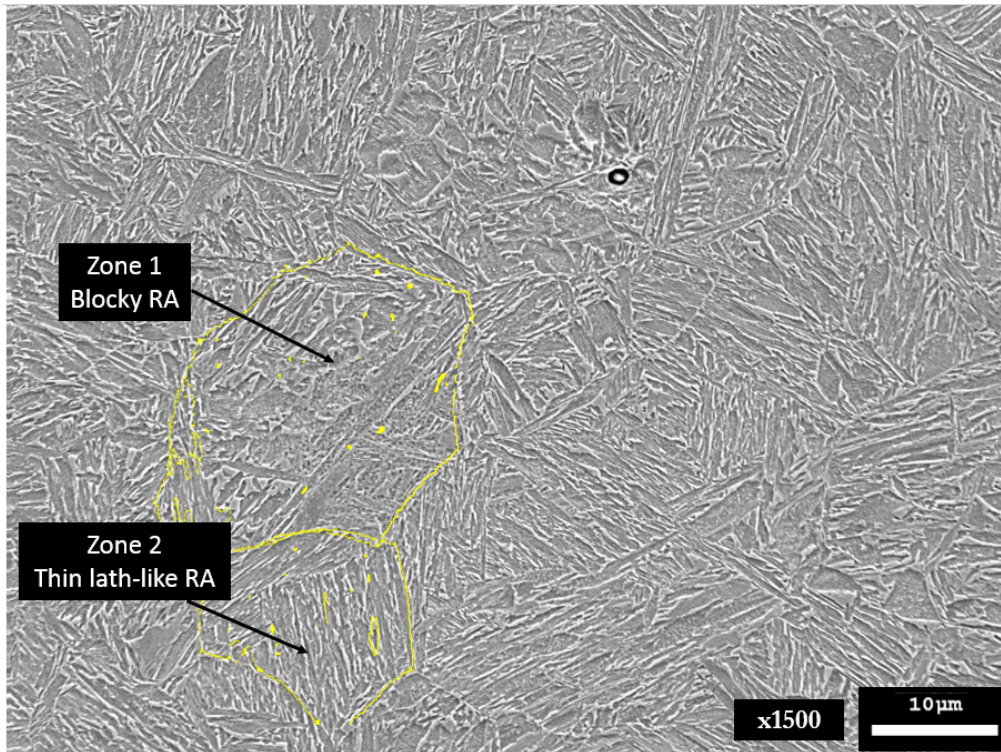


Figure II-26 - SEM image of the zone studied by EBSD in Figure II-24 and Figure II-25

In zone 1, RA is blocky and some MA islands that appear in relief on the SEM image (contoured in yellow on Figure II-27) are actually very poor in retained austenite and mainly made of fresh martensite. In zone 2, RA is refined due to the embedding in a very thin network of martensitic laths and bainite. Contrary to the MA islands in zone 1, the majority of what appears in relief on the SEM image is indexed as RA by EBSD (i.e. fine MA islands are mainly made of retained austenite). It is interesting to note that ultra-fine RA laths (yellow arrow in Figure II-28) are not detected via EBSD. This leads to an underestimation of the amount of RA (9.7% via EBSD, 14% via XRD).

Bainite is present in both zones as small carbide-free laths (green arrows on Figure II-27 and Figure II-28) and is very often surrounded by retained austenite.

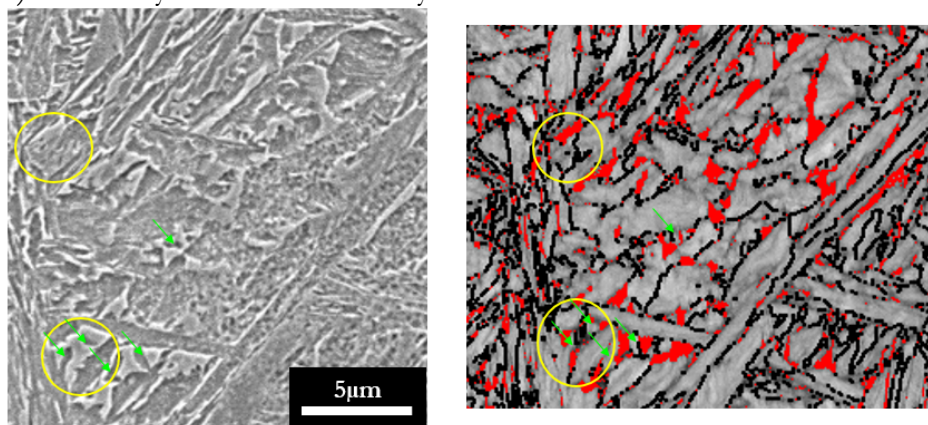


Figure II-27 - Zoom of Zone 1 in Figure II-26. Yellow circles: MA Islands. Green arrows: Bainite

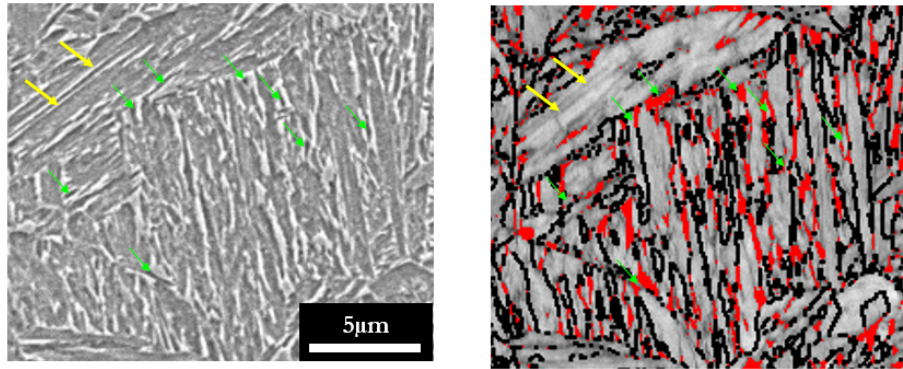


Figure II-28 - Zoom of Zone 2 in Figure II-26. Yellow arrows: ultra fine RA. Green arrows : Bainite

Navarro-Lopez et al. highlighted the fact that martensite is often surrounded by bainite laths, creating ledge-like protrusions [101]. Such features are indeed observed and showed in Figure II-29 by green arrows (taken on the same sample but from another area than the previous images). This further supports the study of Toji et al. who showed that martensite laths provide preferential nucleation site for bainite [20].

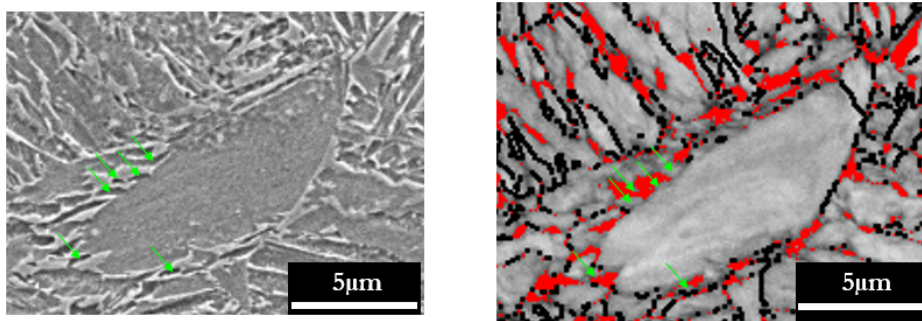


Figure II-29 - Large martensite lath with surrounding bainite lath (green arrows)

Bainite formation during the partitioning step is, like in CFB treatment, the result of austenite decomposition. Thus, the amount of small carbide-free laths identified as bainite must be increasing through the course of the partitioning. To verify if our visual criterion for bainite makes sense, the manual counting methodology was applied at three different times during the partitioning: 0s, 10s, 50s and 200s. Figure II-30 shows the evolution of bainite volume fraction obtained with image analysis. As expected, bainite volume fraction increases with time during PT.

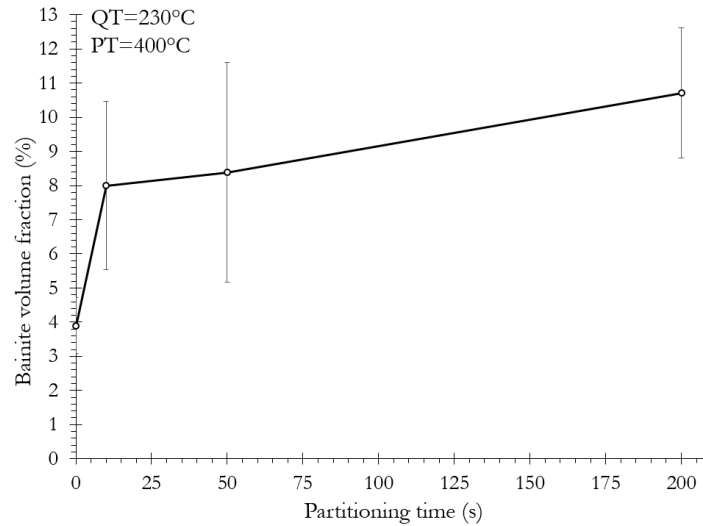


Figure II-30 - Bainite volume fraction evolution during the partitioning step from image analysis ($QT=230^{\circ}C$, $PT=400^{\circ}C$)

As the bainite fraction formed depends on the amount of austenite available, a higher volume fraction of bainite is expected to form at higher QT. Figure II-31 shows the relative change in length during partitioning at $400^{\circ}C$ for 200s for three different QT ($200^{\circ}C$, $230^{\circ}C$ and $260^{\circ}C$). On the QT200 curve (and to a lesser extent on the QT230), an inflexion point is noticeable after 25s of partitioning. However, after investigating possible causes for this behavior (different mechanisms operating at two moments of the partitioning for example), we conclude, based on other experiments done on a similar dilatometer, that this inflexion was an equipment induced artefact.

The higher the QT is, the larger the dilatation is during partitioning. This can support the fact that bainite forms, however as carbon partitioning also leads to dilatation of the sample it is hard to definitively conclude about bainite formation based only on dilatometry data. Further informations about carbon partitioning and kinetics are needed and will be presented in Chapter III.

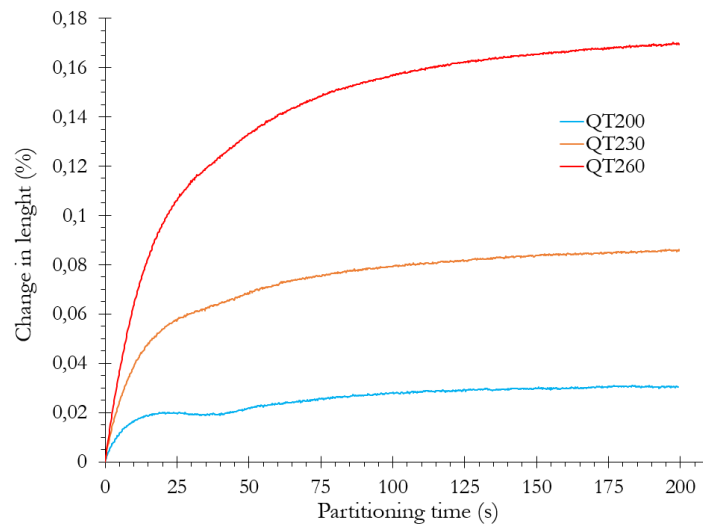


Figure II-31 - Change in length during partitioning for 3 QT ($200^{\circ}C$, $230^{\circ}C$ and $260^{\circ}C$)

Once again, the manual point count methodology was applied on these three QT after a partitioning step of 200s at $400^{\circ}C$. It led to the bainite fraction showed in Figure II-32. Bainite fraction is increasing with QT. Indeed, when reasoning in absolute fraction, a higher austenite fraction before partitioning (i.e higher QT) provides a greater potential for bainite formation and

thus higher absolute bainite fraction (as supported by the increase in change in length when QT increases).

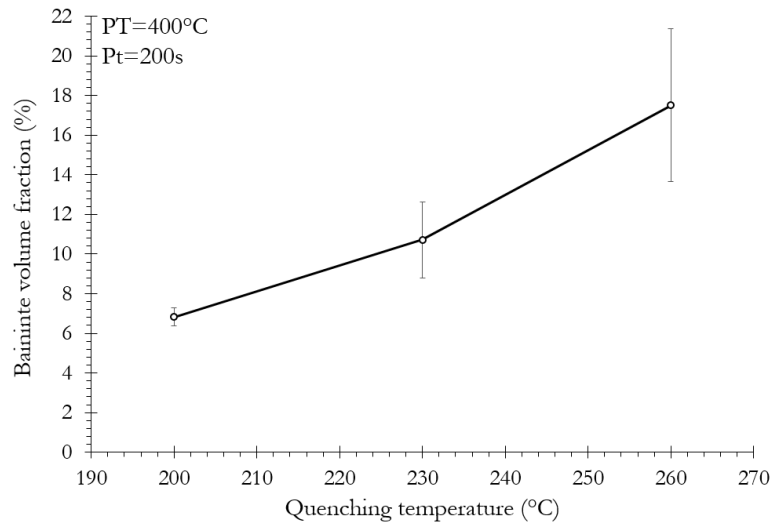


Figure II-32 - Bainite volume fraction for three different QT after a partitioning step of 200s at 400°C by image analysis

All the observations made support the bainite formation as a likely explanation for a part of the dilatation measured during the partitioning step.

II.4 Carbides characterization: Compositional (APT) and Structural (TEM) measurements

The image analysis study showed that martensite undergoes tempering during the Q&P treatment and presents a significant amount of carbides. As the main goal of Q&P treatments is to transfer atoms from martensite towards austenite, any carbon trapping mechanism into martensite is detrimental. Therefore, the following part aims at studying one of the main sources of carbon trapping, carbides. The first part is focused on the determination of carbides composition by atom probe tomography (APT), while the second part reports the use of transmission electron microscopy (TEM) to determine the structure and the nature of the observed carbides.

II.4.1 Carbide compositional study by means of atom probe tomography

The main advantage of atom probe tomography is its quantitativity and ability to probe interstitials at the sub-nanometer scale. Indeed, as this technic allows the detection of about 50% of the atoms of the tip specimen with equal sensitivity (whatever their chemical nature), and the subsequent determination of their nature and position, the composition measurements are pretty straightforward and precise as compared to others technics (such as SIMS or EDS). This section will be focused on the carbides precipitated in α' laths.

As the crystallographic nature of the phases is not directly given by APT, the identification of the phases observed is made based on compositional arguments. Thus, regions with a relatively low carbon concentration (as compared to the nominal carbon content) and presenting features with high carbon contents are identified as tempered martensitic phase with carbides.

APT measurement related to carbides were mainly conducted on the Q&P treatment with the highest martensitic volume fraction, i.e with the lowest QT in order to increase the probability to probe carbides.

Specimen must be prepared as fine needle, with end radius of curvature around lower than 50 nm. Dilatometer samples were first sectioned into matches with a square cross-section of approximately 300x300 μm^2 using a rotating diamond disk saw. Then, the electropolishing step consists of two stages: a first electrolyte mixture of 75% acetic acid and 25% perchloric acid, a

second mixture of 98% 2-Butoxyethanol and 2% perchloric acid. The prepared tips were analysed using a CAMECA LEAP® 4000 HR, under the following conditions: 0.3% average detection rate, 200 kHz pulse repetition rate, 50 K temperature and 20% pulse fraction.

In term of carbides, we can expect transitional carbides formation as the effect of adding Si has not proven to be very efficient to preclude their formation. Additionally, in some partitioning temperature ranges, cementite was shown to form [26][68]. Hence, carbides that might be expected in a Q&P martensitic phase are presented in Table II-11.

Table II-11 - Stoichiometry of the expected carbides in a Q&P structure

Carbide	Type	Carbon content	Ref.
Cementite- θ Fe_3C	Equilibrium	25at%	Wood et al. [153]
Epsilon- ϵ $\text{Fe}_{2.4}\text{C}$	Transitional	30 at%	Nagakura et al. [59]
Eta- η Fe_2C	Transitional	33 at%	Hirotsu et al. [62]

The Q&P conditions studied are presented in Figure II-33.

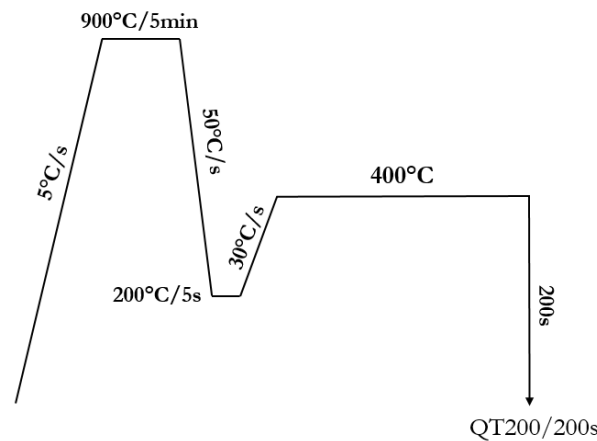
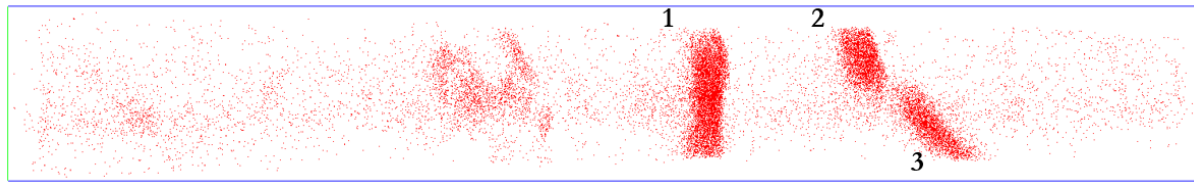


Figure II-33 - Q&P treatment conditions used for the APT study on carbides

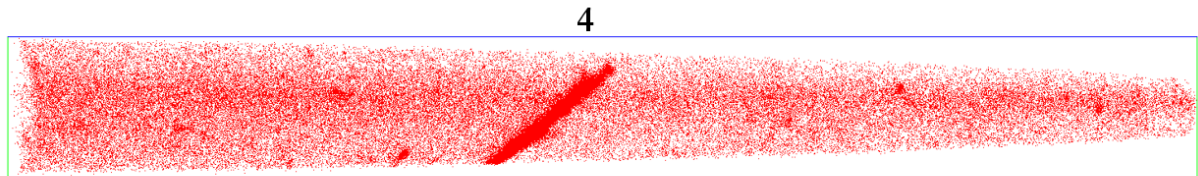
A sample presenting a low carbon content with discrete features of high carbon concentration is shown Figure II-34. The phase observed is considered to be tempered martensite (due to its low carbon content) and the three high concentration features are likely to be carbides. Similar microstructure is also presented in Figure II-35 with a carbide in a martensitic matrix.

A common method to represent carbon concentration in a precipitate (carbide) is the so-called proxigrams (for Proximity Histograms). Indeed, rather than plotting a concentration profile along a line or an axis of a region of interest (ROI), proxigrams calculate a profile with respect to the distance from a predefined interface (usually a user-defined isosurface of concentration)[154]. This method is particularly suited to study curved interfaces (encountered in most realistic cases). By using proxigrams, it is possible to avoid common measurement bias introduced by the use of 1D concentration profile measurements such as artificial widening of interfacial regions.



20nm

Figure II-34 – Carbon distribution map in martensite with three carbides (QT200/200s). Total volume analyzed was $30 \times 30 \times 140 \text{ nm}^3$ containing 20×10^5 ions. Each red dot is one individual carbon atom detected.



50nm

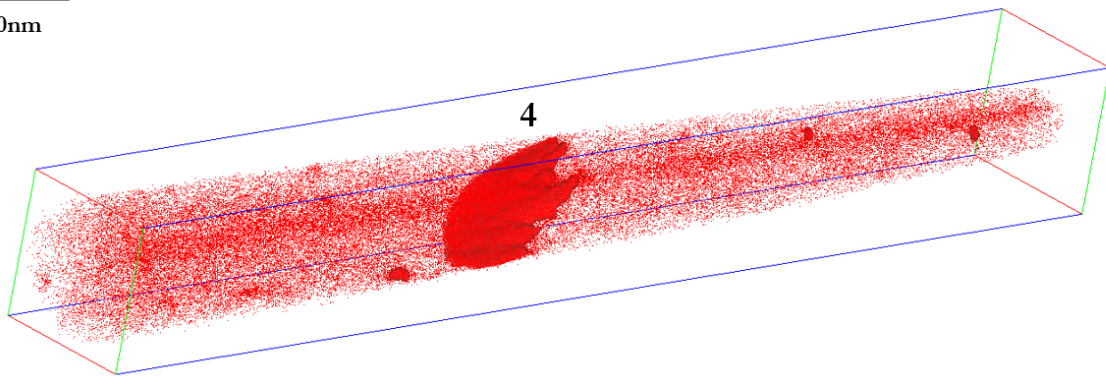


Figure II-35 – Carbon distribution map in martensite with one carbide (QT200/200s). Total volume analyzed was $60 \times 60 \times 500 \text{ nm}^3$ containing 37×10^6 ions. A 5at.%C isosurface is also represented in red to highlight the carbide

The proxigrams corresponding to the four carbides observed in Figure II-34 and Figure II-35 are presented Figure II-36.

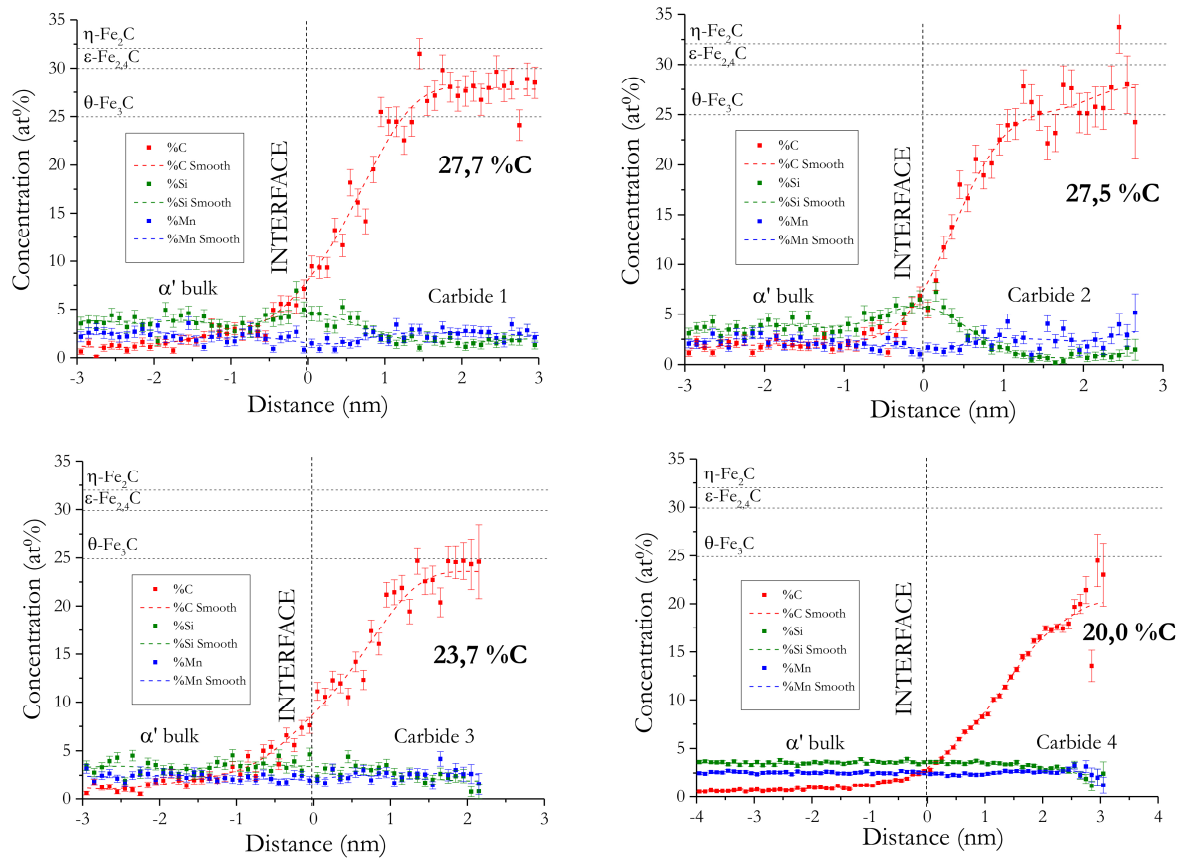


Figure II-36 - Proxigrams corresponding to the carbides in Figure II-34 and Figure II-35 (QT200/200s)

The goal of this section being to give informations on the nature of the observed carbides through compositional measurements, the stoichiometry of the three possible carbides (θ , ϵ and η) are reported in the proxigrams in the form of horizontal dashed lines for sake of comparison. Carbide carbon concentrations are determined by taking the average value on the last 5% of the proxigram (0% being the concentration value at 0nm and 100% being the last concentration value at the right end of the proxigram), this zone can be considered as the most representative of the carbide core composition.

While carbides 1 and 2 show similar carbon compositions (approx.. 27.5%C), situating them in between θ and ϵ carbides, carbide 3 and to a larger extent carbide 4 present a lower carbon content (respectively 23.7%C and 20.0 %C). These values indicate that carbides encountered in Q&P microstructures might not be of the same nature or/and at the same stage of formation (transition from a η/ϵ to a θ for example). Indeed, as our literature study suggested (see section I.2.2.2), non-stoichiometric transitional carbides (Fe_3C η -carbides for example) can be found.

Another possible explanation for the spread in carbides carbon content is the local magnification effect taking place during the APT measurements as already showed by Lu et al [65]. Indeed, as the matrix (martensite) and the carbide require different electric fields to evaporate, atoms located near the interface can be mis-positionned. In the case of a low-field precipitate (such as iron carbides), the preferential flattening of the carbide surface will result in a lower field region that will deviate the atoms inwards, causing an apparent increase in density of the impacts. For a high-field precipitate, the opposite mechanisms takes place as shown in

Figure II-37. As the carbides studied are very thin (their thickness is in the order of 5nm), this interface effect is remarkably high.

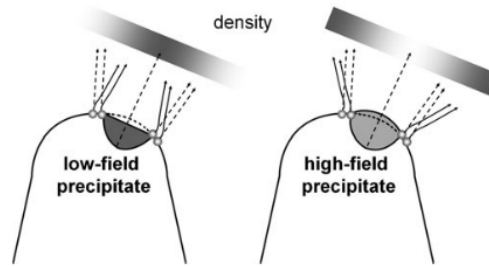


Figure II-37 – Deviation of the atoms near the carbide/matrix interface due to a change in the surface curvature in the case of a low- and high-field precipitate (taken from Gault et al. [155])

This effect has proven to be negligible when the carbide is perpendicular to the analysis direction (inclination angle = 0°) and increases with the inclination angle. We measured the inclination angle with respect to the analysis axis on the carbides probed by APT, and plotted carbide carbon concentration as a function of inclination angle in Figure II-38. The range of angles covered by the four studied carbides is 0° - 50° . As carbide 1 exhibits a 0° inclination angle, this makes its carbon concentration (27.7at.%C) less prone to be altered by the local magnification effect. Thus, the difference in carbide concentration can come from this measurement artefact.

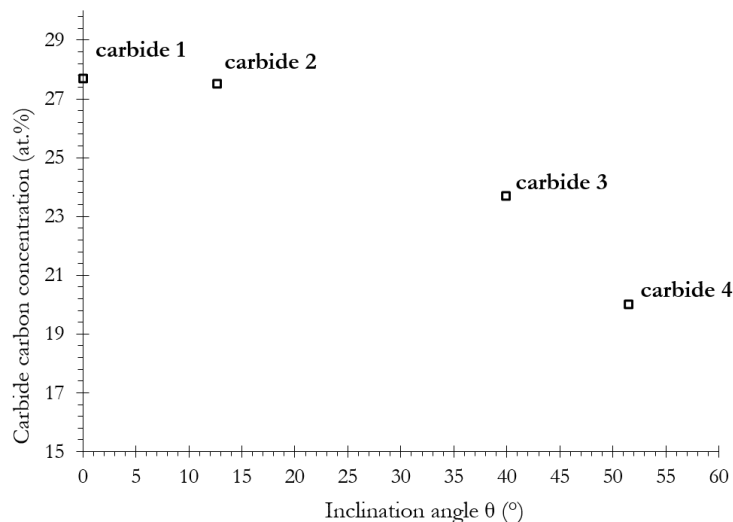


Figure II-38 - Impact of the inclination angle on the measurements of carbon concentration of carbides during APT experiments

Another indication about carbides nature can be found by analyzing the matrix/carbide distribution of substitutional elements. It is usually considered that cementite cannot precipitate under paraequilibrium condition and that Si must diffuse away from the carbide. Such a redistribution of Si is indeed significantly noticeable in carbides 1 and 2. Interestingly, the carbides presenting the highest carbon content (and thus more likely to be transitional carbides due to their stoichiometry) are the ones with the more advanced silicon redistribution (and thus closest to the characteristics of cementite). It is worth pointing that no significant Mn redistribution is noticeable as shown in Figure II-36.

It becomes quite clear that the APT compositional study must be coupled with others technics to determine the crystallographic nature of carbides.

II.4.2 Carbide structural study by means of Transmission Electron Diffraction

As previously mentioned in the bibliography chapter, the identification of the carbide precipitate (hexagonal ϵ , orthorhombic θ , orthorhombic η) in martensite α' is essential. Indeed, carbides reduce the carbon available to stabilize the retained austenite by trapping carbon in martensite, and thus blocking the potential enrichment of carbon in austenite.

However, the identification of the nature of carbides in the studied steel after a Q&P heat treatment (with QT=230°C and PT/t=400°C/200s) requires specific TEM analyses. Thin foils were prepared at low temperature using an EM-09100 JEOL cryo-ion slicer system (with a liquid nitrogen tank, JEOL, Tokyo, Japan). This allowed avoiding further tempering of martensite and altering the carbide structure. Moreover, no attenuated spot corresponding to iron oxide is observable on diffraction patterns, as when electropolishing is used. TEM observations were carried out on a JEOL 2100 (JEOL, Tokyo, Japan) operated at 200 kV.

Figure II-39 a), presents a martensite laths who underwent tempering, as shown by the large presence of carbides. Figure II-39 b) is a closer view on those carbides, showing an elongated shape as already observed via APT (for example on Figure II-35). The diffraction pattern of the matrix is presented Figure II-39 c). This shows that the observed carbides are aligned with the $[\bar{2}\bar{1}1]_{\alpha'}$ when the zone axis of the martensite grain is $[210]_{\alpha'}$ (cf Figure II-39 d)).

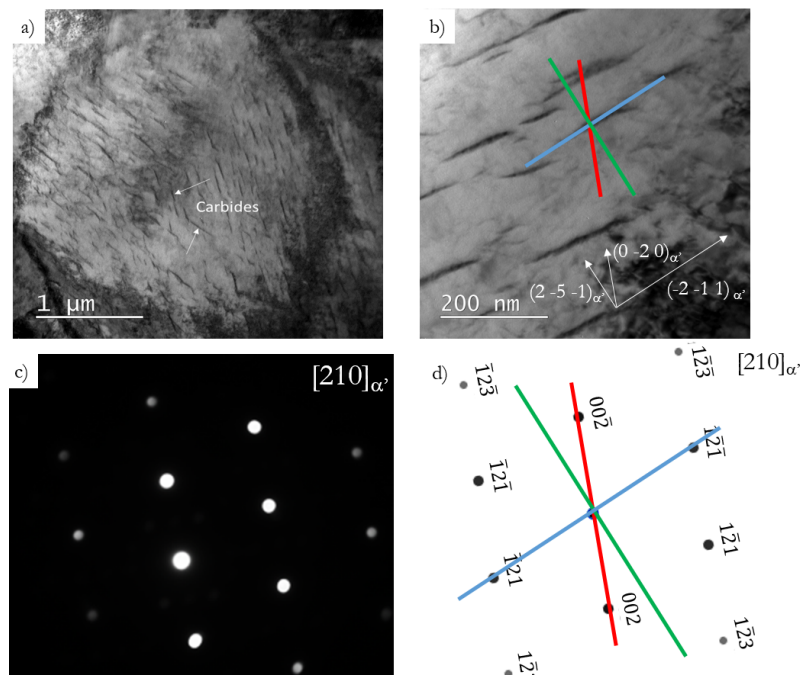


Figure II-39 – a) BF-TEM micrographs of a martensite lath presenting carbide precipitation: arrows highlight the presence of two variants of carbides (in dark contrast) in the tempered martensitic matrix (wide block) b) Studied carbides aligned along martensite $[-2 -1 1]_{\alpha'}$ in blue color (martensite diffraction pattern in $[210]_{\alpha'}$ zone axis) c) Diffraction pattern of the martensitic matrix $[210]_{\alpha'}$ zone axis d) simulation of the diffraction pattern for $[210]_{\alpha'}$ zone axis

To identify the carbides, we could have chosen the SAD method with martensite as calibration reference but the microdiffraction technique is preferred. In this case, as can be observed Figure II-40, only the diffraction pattern of the carbide is obtained. JEMS software is used to index the diffraction pattern with the possibility to choose as phases α' , ϵ , θ and η . These carbides, with a needle-shape morphology, are identified to be η thanks to its identification on the same carbide for three different zone axes.

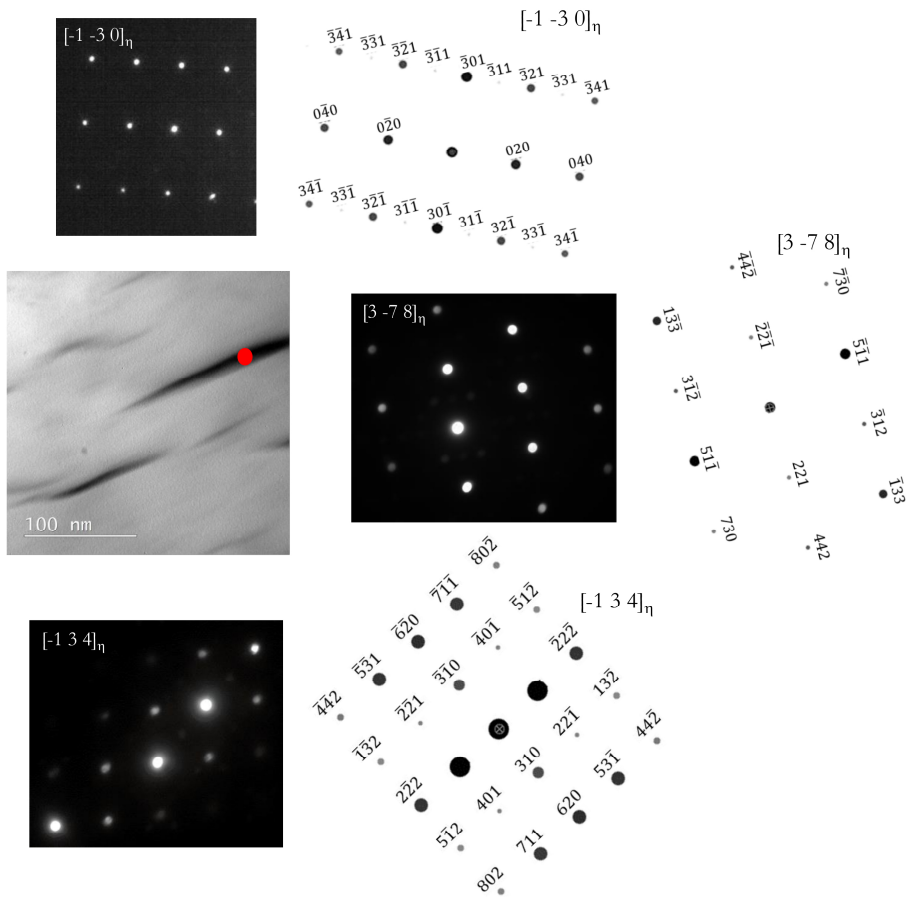


Figure II-40 - Diffraction patterns in three different z one axes for the carbide localized with a red point on the BF-TEM picture. Indexation indicates it can be identified as η carbide

Some precipitates are also identified to be ϵ carbides. Fortunately, they have a difference of morphology with η carbides as noticed on Figure II-41. ϵ carbides are larger and circular in shape. Their diameter varies from 20 nm to 50 nm. For η carbides, they are few hundred nanometers long and less than 20 nm in width. No quantification of the ratio between ϵ and η carbide fractions is possible with this technique.

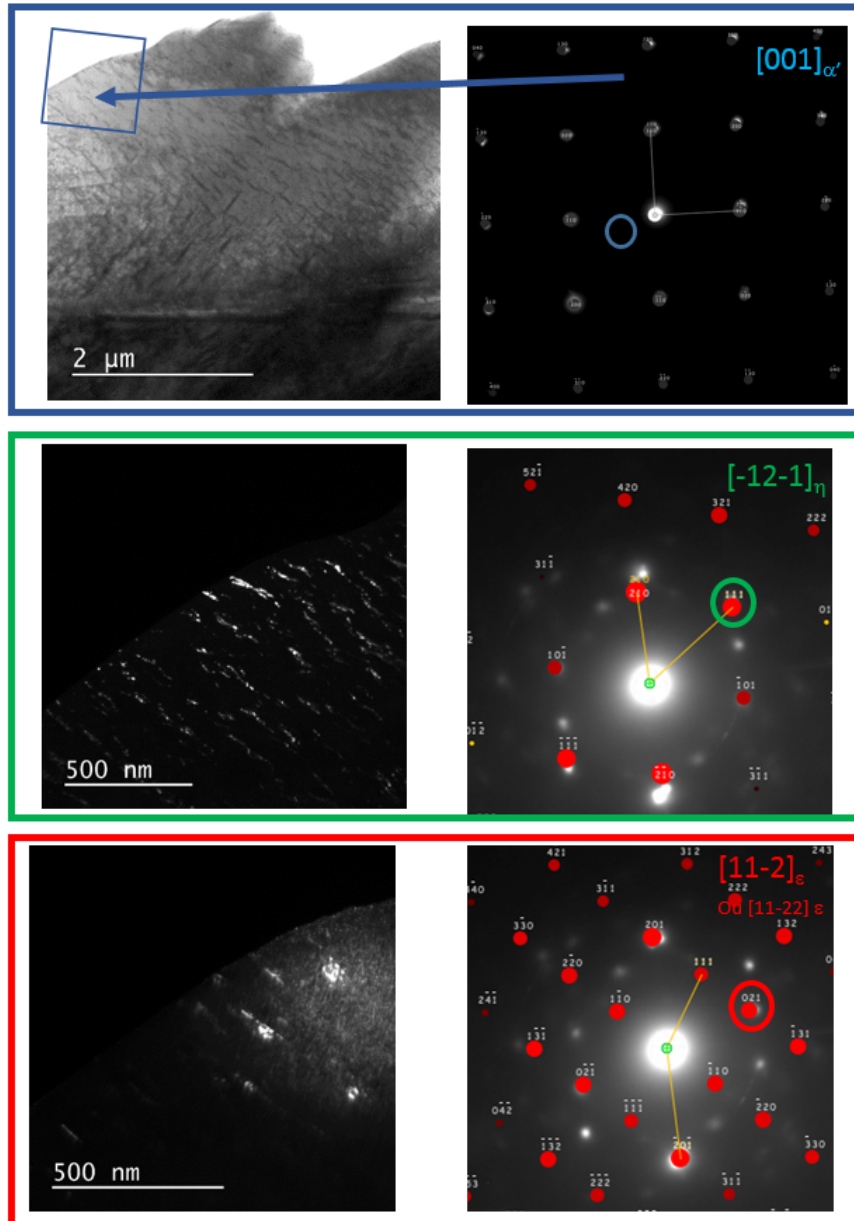


Figure II-41 - Three different diffraction patterns in zone axis for the carbide identified to be η localized with a red point on the BF-TEM picture.

Figure II-42 shows that the correlation of different characterization techniques allows to state the carbides presents a plate-like morphology. Indeed, the observation of a APT tip after eletropolishing (Figure II-42 a)) showed a non-etched carbide at the surface of the tip. Moreover, traces of pulled out carbides at the surface of the tip are also noticeable. Figure II-42 b) shows carbides precipitation inside a martensite lath, the plate-like nature of the carbide is clearly shown. Finally, Figure II-42 c) present a schematic 3D representation of the carbides.

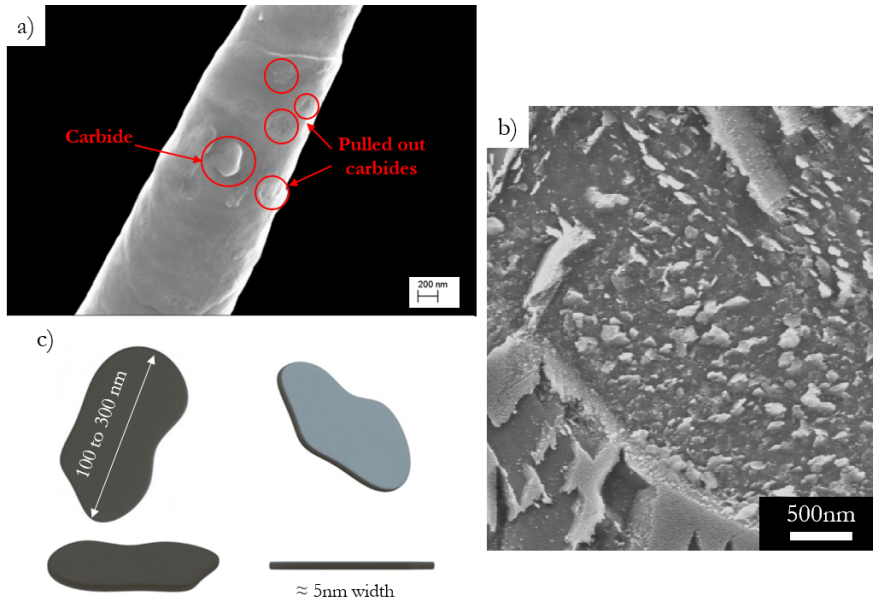


Figure II-42 - Correlation of characterization techniques to state on the plate-like carbide morphology a) APT tip observed via SEM after the electropolishing step showing a carbide and traces of pulled out carbides b) SEM image of a tempered martensite lath with intra-lath carbides c) 3D representation of the carbides morphology

II.5 Carbon segregated in martensite: APT study

Carbide precipitation is not the only carbon trapping mechanism during the Q&P treatment. Indeed, our literature survey suggested that carbon clustering before carbide formation is very likely to occur in martensitic microstructure undergoing tempering.

Carbon segregations observed in Q&P samples can be divided into two categories:

- Carbon segregated at martensite boundaries (laths, block, packets)
- Carbon segregated on others defects, such as dislocations

The APT study was conducted on three Q&P conditions with two different QT as presented in Figure II-43 and Table II-12.

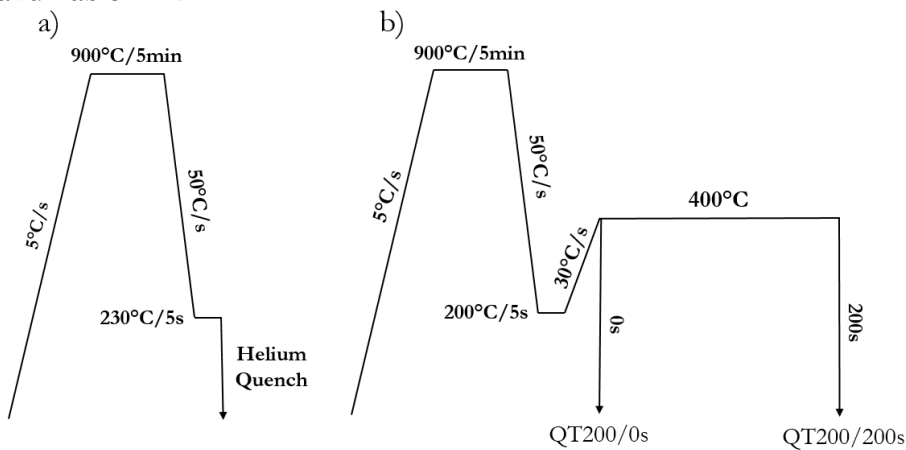


Figure II-43 - Q&P treatment used for the APT study on carbon segregation in martensite : a) Quench from the austenite domain with a 5s hold at QT230 before quenching to RT and b) two different Pt (0s and 200s) at PT = 400°C and after a quench at QT=200°C

Table II-12 - Q&P treatment conditions used for the APT study on carbon segregation

Name	Quenching Temperature	Partitioning Temperature	Partitioning time
QT230/HeQ	230°C		
QT200/0s	200°C	400°C	0s
QT200/200s	200°C	400°C	200s

II.5.1 Segregation during the initial quench

The first investigated treatment is a quench to RT after a hold of 5s at QT. Badinier used APT to study a high-Si alloy with medium carbon content (0.4wt.%) and with similar M_s than our samples (282°C) [156]. He studied the effect of a fast quench (water-quenched at 90°C/s) compared to a slower quench (helium-quench at 50°C/s) in term of carbon distribution at RT. Whereas the fast-quenched sample presented a relatively good carbon homogeneity, the sample that underwent a slower quench presented significant carbon redistribution. Indeed, carbon was already segregated on defects of the microstructure such as lath boundaries or dislocations. Some equiaxed features were even identified as being transitional carbides. As our Q&P treatment corresponds to what Badinier qualified as a “slow” quench rate, the distribution of carbon at QT is likely to be inhomogeneous, and must be characterized. A tip taken from the QT230/HeQ condition was analysed, the carbon distribution map is given in Figure II-44 with two different orientations.

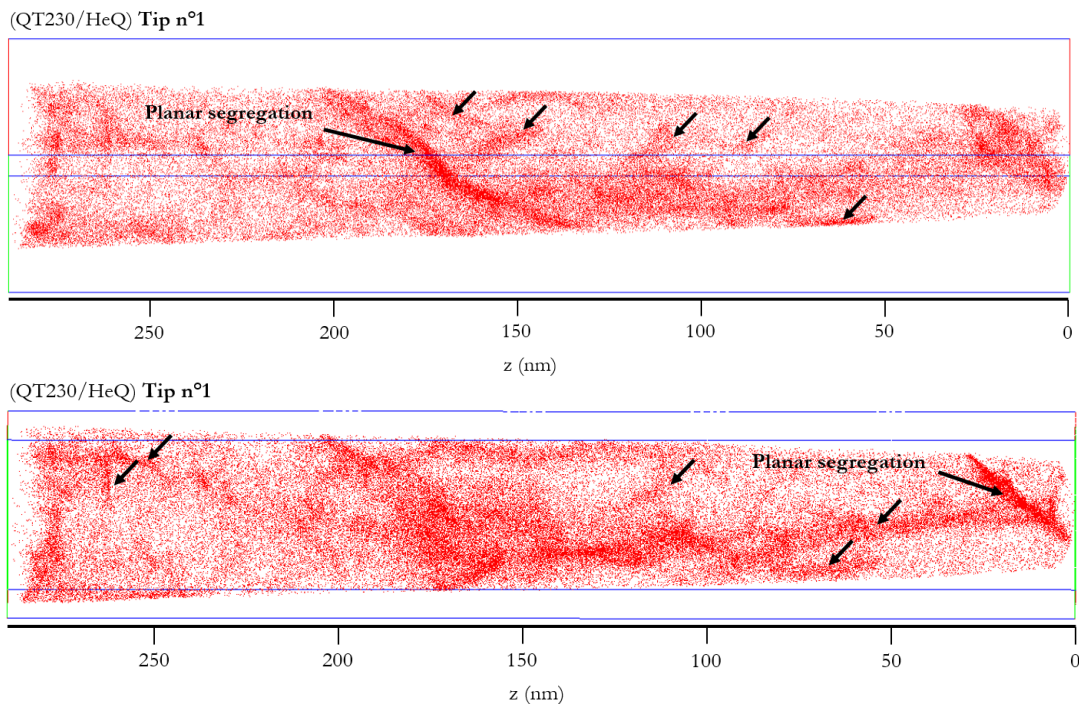


Figure II-44 - Carbon distribution map of a tip taken from the QT230/HeQ condition showing advanced redistribution of carbon on planar features and on other defects (black arrows)

At first sight, we can notice an important carbon redistribution. Indeed, two planar segregations that appear on each orientation of the tip are clearly noticeable. The disorientation between the two images is relatively small, the two planar segregations are quasi-parallel and separated by 150nm, this can correspond to a fine martensitic lath formed during the initial quench. In between these two lath boundaries, several carbon segregations with carbon content ranging from 3at.% to 6at.% are also present (black arrows on Figure II-44). However, it is very difficult

to state on the origin of these segregations even if we can confidently say that no carbide was present in this tip as the segregation carbon contents are far from the stoichiometry of transition carbides. Hutchinson et al. also observed carbon segregation in such low carbon alloys in between lath boundaries and concluded that they were probably Cottrell atmosphere around dislocations [157]. Furthermore, it must be highlighted that in our study, the initial quench is interrupted at QT for 5s, providing additional time for carbon to diffuse on defects. Even if martensitic structures might present high dislocation density (from 10^{13} to 10^{16} m^{-2}) and thus high potential for carbon trapping, segregation onto lath boundaries might be the main source of carbon trapping in our study (together with carbide precipitation). Indeed, Xiao et al. showed that when martensite tempering temperature is increased (above 170°C), carbon atoms gain greater energy to migrate towards lath boundaries [158]. As in Q&P the partitioning step is conducted at 400°C , change in segregation sites (from dislocations to lath boundaries) is thus expected.

II.5.2 Segregation evolution at martensite lath boundaries during partitioning

From simple visual inspection, it can be quite tedious to differentiate a martensite lath boundary and a carbide. As presented in the previous section, observed carbides are very thin and long, thus if a carbide goes through an entire tip, it can be misinterpreted as a separation between two martensite laths. Difference in thickness and carbon content can be used to discriminate lath boundaries and carbides.

Several features that can qualify as being martensite lath boundaries were selected for three key moments of the Q&P process. For the QT230/HeQ condition, the two lath boundaries are taken on the same tip whereas for the two other conditions (at 0s and 200s of partitioning at QT200) respectively, tens of tips were probed, but only two or three typical will be shown here.

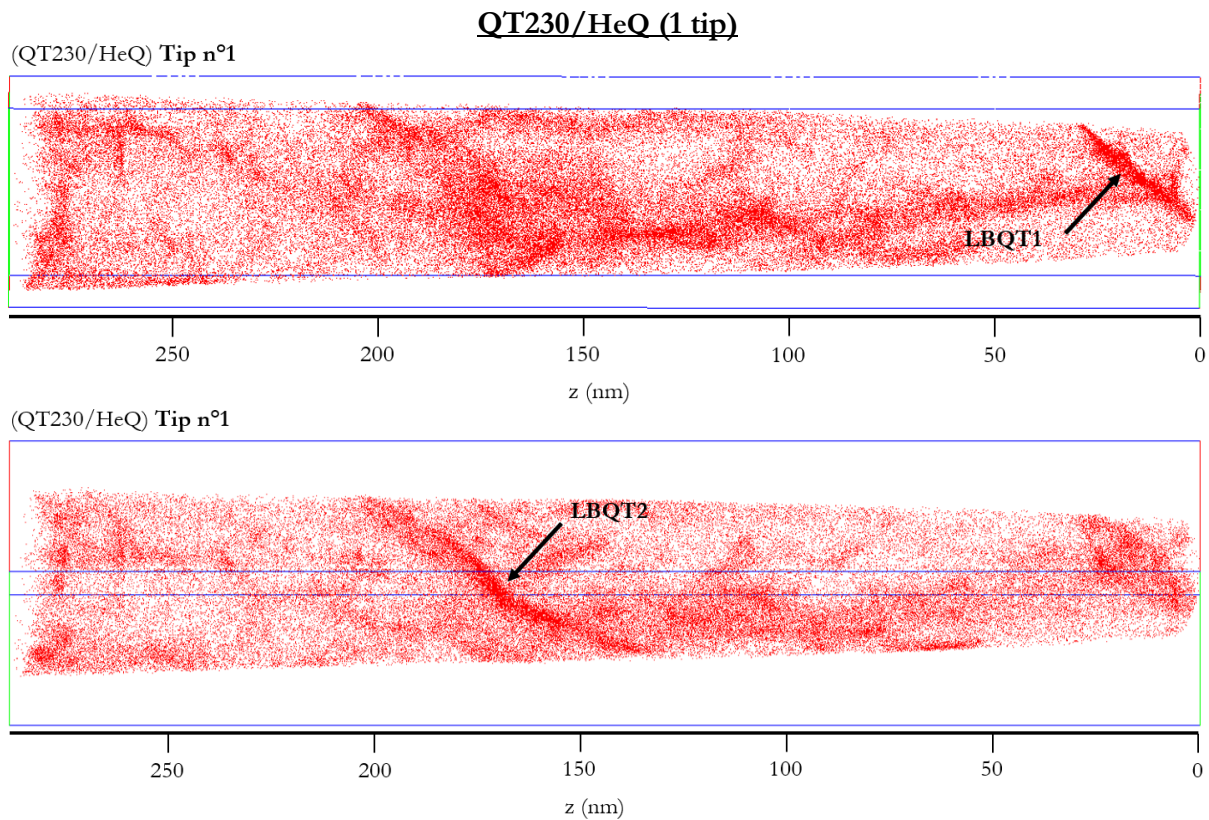
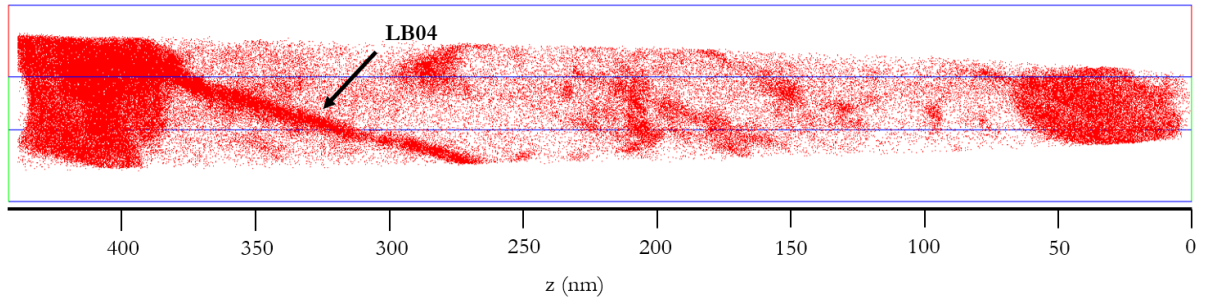


Figure II-45 – Carbon distribution map in martensite showing two carbon segregations at lath boundaries in tip n°1 (JDLQT1 and JDLQT2) (QT230/HeQ)

QT200 400/0s (2 tips)

(QT200/0s) Tip n°2



(QT200/0s) Tip n°3

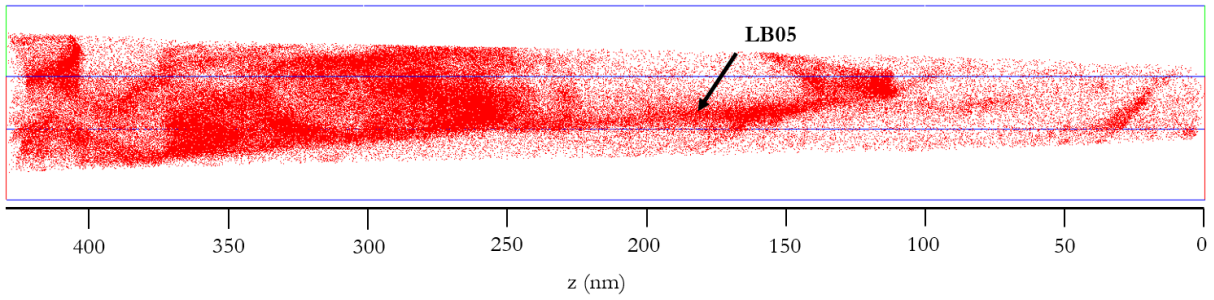
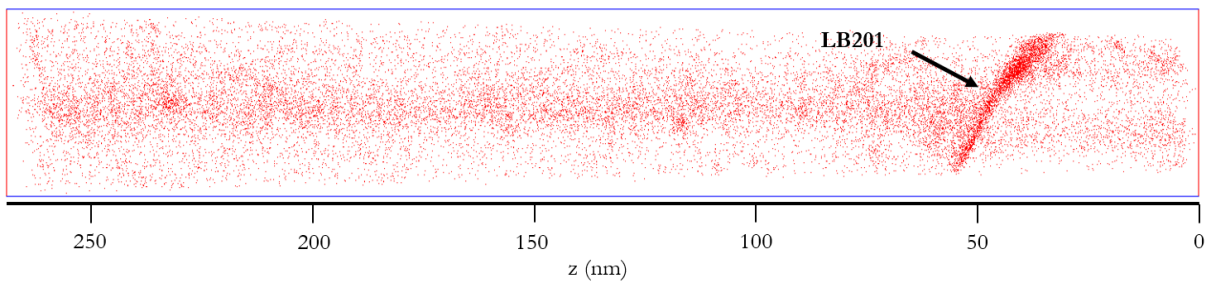


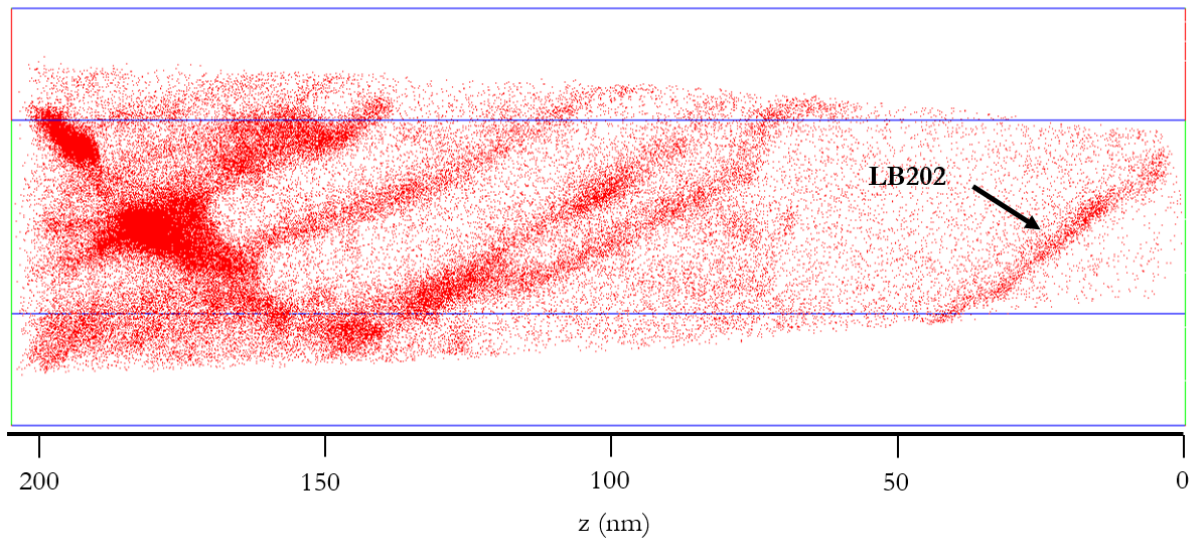
Figure II-46 - Carbon distribution maps in martensite showing two carbon segregations on lath boundaries in tip n°2 and tip n°3 (JDL04 and JDL05) (QT200 PT/t = 400°C/0s)

QT200 400/200s (3 tips)

(QT200/200s) Tip n°4



(QT200/200s) Tip n°5



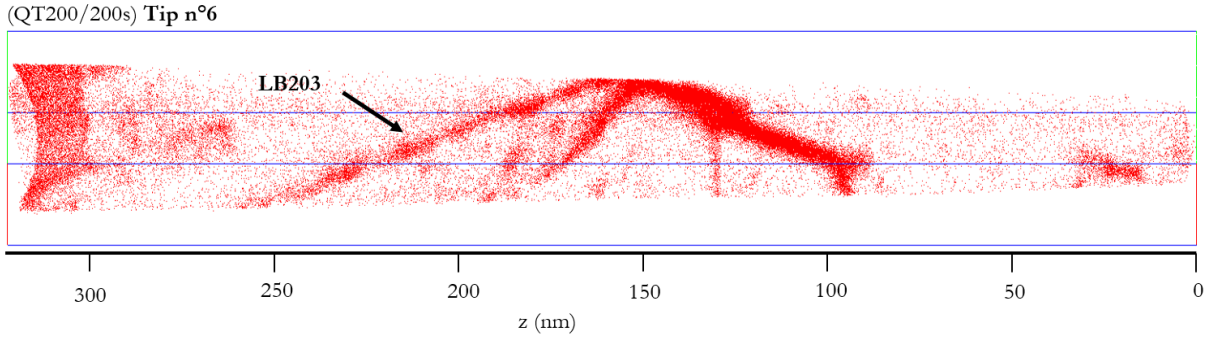


Figure II-47 - Carbon distribution maps in martensite showing three carbon segregations on lath boundaries in tip n°4, tip n°5 and tip n°6 (JDL201, JDL202 and JDL203) (QT200 PT/ $t = 400^{\circ}\text{C}/200\text{s}$)

Figure II-45, Figure II-46 and Figure II-47 present the different laths boundaries where significant carbon segregations occurred chosen on three Q&P key points of the treatment. The fact that these features are separating two low carbon regions, are planar and that they go through the whole width of the tips strongly suggest that they are martensite lath boundaries. Cylindrical regions of interest (ROI) were placed so that their axes are perpendicular to the boundary planes. Traditionally, the amount of segregation is measured by plotting a concentration profile along the axis of the cylinder and by taking the maximum of the plot as representative of the segregation level of the studied species. However, as Maugis et al. pointed out, the maximum concentration of the segregated element (in particular at lath boundaries (LB)) is not a thermodynamical variable in addition to being extremely sensitive to the measurement methods [159]. Indeed, different orientations of the ROI relative to the LB will lead to different maximum in concentration. Consequently, Maugis et al., extending the work of Krakauer et al., proposed the use of the concept of interfacial excess of solute [159][160]. Concentration profiles collected through a ROI are still used, but instead of measuring a peak concentration, we measure the total amount of solute in surplus in the vicinity of the interface. This excess interfacial concentration is resolution-independent, and is often expressed in $\text{at}\cdot\text{nm}^2$. When using atomic fraction as the measurement unit, X^{ex} , the excess fraction in length unit is the integral of the concentration profile over a distance L that encompasses the whole boundary as follows:

$$X^{ex} = \int_{-L/2}^{+L/2} (X(z) - X^{\infty}) dz \quad (II.13)$$

where X^{ex} is the excess fraction of solute in $\% \cdot \text{nm}$, $X(z)$ is the concentration of solute at the distance z in at%, X^{∞} is the concentration of solute far from the interface in at%

Figure II-48 presents a theoretical concentration profile (black solid line) together with its integral form (red dashed line). Graphically, X^{ex} is the area between the concentration profile and the horizontal line at $X = X^{\infty}$. The excess fraction is the asymptotic value of the integral concentration curve.

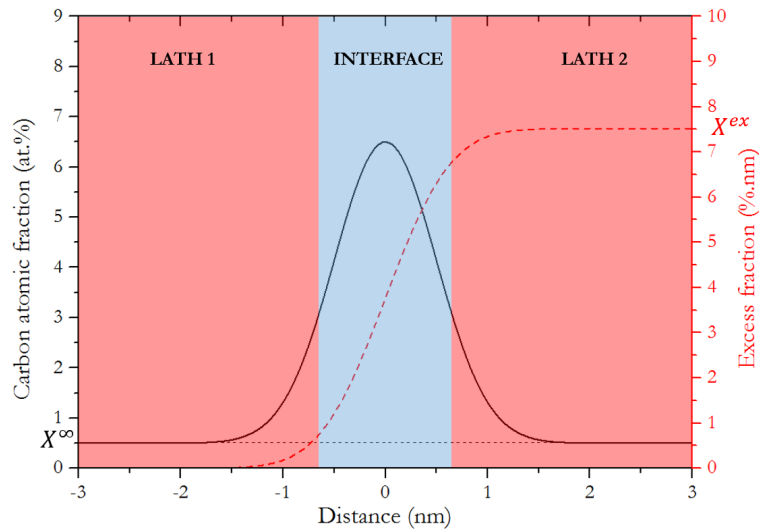


Figure II-48 - Schematic representation of the excess fraction methodology. Solid black line is the measured concentration profile. Dashed red line is the excess fraction calculated from the integration of the concentration profile with eq. (II.13)

The concentration profiles were measured along the z-axis of cylinders that encompass the LBs and with bin widths of 0.05nm. Figure II-49 presents the concentration profiles (black solid lines) along the three LB of the QT200/200s condition. The excess fraction is represented by a dashed red line. The value of X^∞ is indicated by a horizontal dashed black line on each graph. The integration of the profile with eq.(II.13) is represented on each graph as a red dashed line. The asymptotical value of X^{ex} is indicated in red.

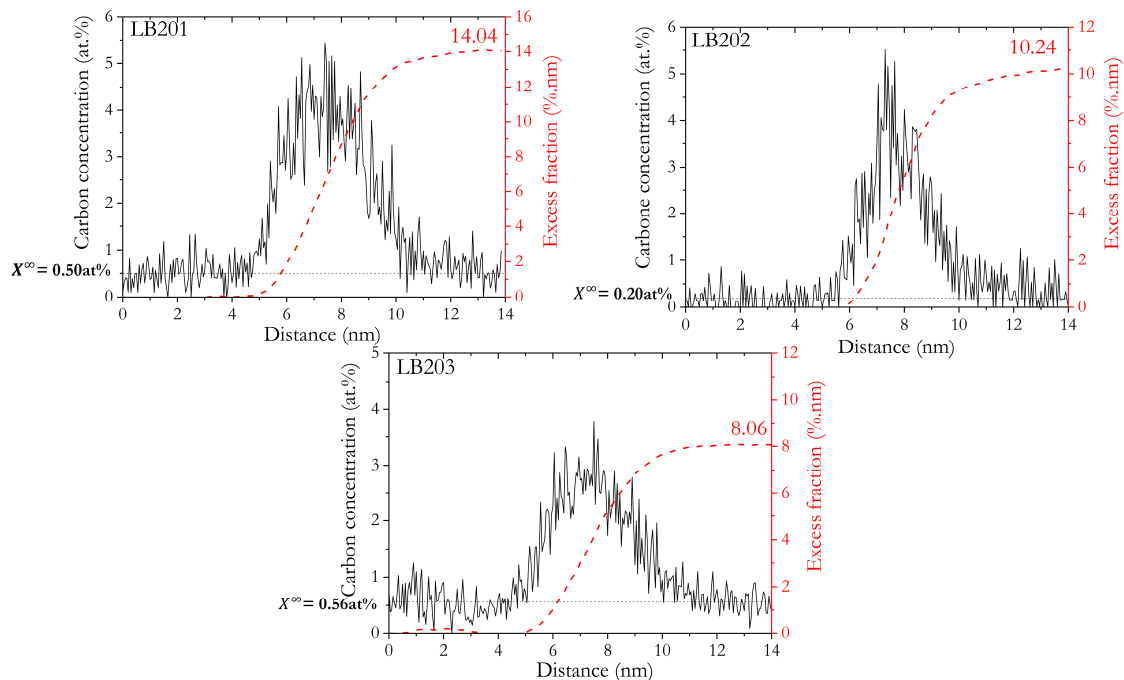


Figure II-49 – Concentration profiles (black solid line) of the LBs presented in Figure II-47 along with the integral (dashed red line) representing the excess fraction (QT200 PT/ $t = 400^\circ\text{C}/200\text{s}$).

If we take a more classical approach in order to assess the segregation potential of the LBs by comparing the peak concentration on each profile and the concentration of the matrix, LB202 presents the highest segregation energy with $X^\infty = 0.20\text{at.}\%$ and a peak concentration of approx..5.5at.%. This is largely due to the fact that the matrix is more depleted in carbon nearby

LB202 (0.20at.%C) compared to LB201 (0.50at.%C) while the two peak concentrations are similar.

However, by taking an excess fraction measurement approach, the integral allows to disregard the matrix depletion level, instead the distance over which segregation happens is taken into account. While their peak concentration is practically the same the carbon segregation occurs on a larger distance for LB201 (approx. 6nm) than for LB202 (approx. 4nm). This leads to a higher excess fraction for LB201 than for LB202. Unsurprisingly, the lower excess fraction is for LB203 because of a smaller concentration peak even though the segregation occurs on a large scale (just over 6nm).

We can now apply a MacLean approach to calculate the segregation energy of each LB. In his thesis, Da Rosa showed that the McLean equation describing the segregation of a solute atom on a defect can be rewritten with the excess concentration as [161]:

$$\frac{\Gamma}{\Gamma_{max} - \Gamma} = \frac{X^{\infty}}{1 - X^{\infty}} \exp\left(\frac{-Es}{RT}\right) \quad (II.14)$$

where Γ is the excess concentration of solute measured in at.nm^{-2} , Γ_{max} is the maximum excess of solute in at.nm^{-2} , X^{∞} is the concentration of solute far from the interface in %at and Es the Gibbs free energy of segregation in J.mol^{-1}

The excess concentration of solute in at.nm^{-2} is linked to X^{ex} by V_{at} , the average volume occupied by an atom in the crystal structure as:

$$\Gamma = \frac{X^{ex}}{V_{at}} \quad (II.15)$$

where Γ is the excess concentration of solute in at.nm^{-2} , X^{ex} is the excess fraction of solute in %at and V_{at} is the average volume occupied by an atom in the crystal structure in at.nm^{-3} .

For a ferritic structure containing 5.9at% C (in the range of the carbon values measured in our LB), Jang et al. calculated that the atomic volume of ferrite was 12.43 \AA^3 [162].

In order to assess the maximum excess concentration, an hypothesis regarding where carbon atoms segregate must be made. Indeed, the excess concentration must be ‘‘concentrated’’ on a chosen distance in order to translate the results in more classical quantities such as segregation energies or solute concentrations. Thus, we assume that the carbon atoms segregated on two (100) ferrite planes. Figure II-50 presents the (100) plane with all the octahedrals sites filled with a carbon atom. The surface density of Fe atoms on such planes is equal to:

$$C_{Fe}^S = \frac{\text{nb of Fe atom in the plane}}{\text{plane area}} = \frac{4 \times (1/4 \text{ Fe})}{a_{BCC}^2} = \frac{1}{0.2886^2} = 12.00 \text{ at.nm}^{-2} \quad (II.16)$$

where a_{BCC} is the lattice parameter of pure iron in nm.

The surface density of C atoms if all the octahedrals sites are occupied is:

$$C_C^S = \frac{\text{nb of C atom in the plane}}{\text{plane area}} = \frac{1C + 4 \times (1/2 C)}{a_{BCC}^2} = \frac{3}{0.2886^2} = 36.01 \text{ at.nm}^{-2} \quad (II.17)$$

where a_{BCC} is the lattice parameter of pure iron in nm.

If we consider the hypothesis of segregation on two (100) plane, the maximum excess concentration for carbon Γ_{max} (every site available for carbon segregation is occupied) is equal to $2C_C^S$ or 72.02 at.nm^{-2} .

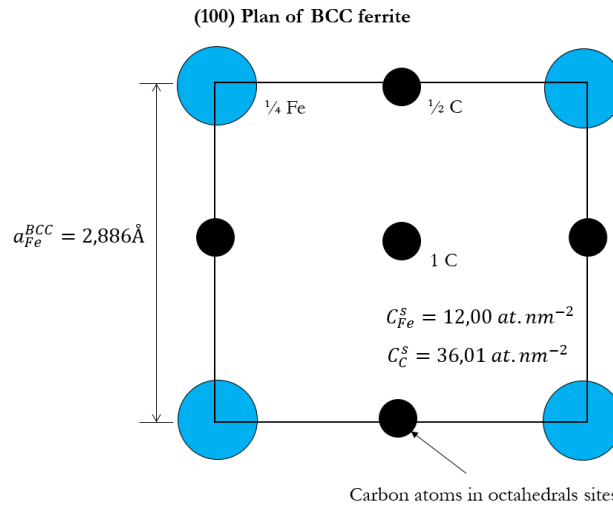


Figure II-50 - Schematic representation of one (100) iron plane with Fe atoms (in blue) and all the octahedral sites occupied with carbon atoms (in black)

Consequently, we can now use the measured values (X^{ex} and X^∞) and the calculated one (Γ_{max}) in order to determine the segregation energy using eq.(II.14). Another meaningful quantity is the occupancy ratio Γ/Γ_{max} that translates the percentage of segregation sites occupied (i.e if the LB is far from being saturated or not). Moreover, by using the hypothesis of carbon segregation on two (100) planes, it becomes possible to calculate the ratio of C to Fe atoms on these planes in order to estimate the stoichiometry in the case where a defined compound forms in the LB as:

$$\%C = \frac{\xi}{1 + \xi} \times 100 \quad (II.18)$$

$$\text{with } \xi = \frac{\Gamma}{2C_{Fe}^s}$$

where %C is the carbon concentration of the defined compound (in at%) and ξ is the ratio of experimentally measured carbon atoms Γ to the theoretical surface density of iron in (100) planes

When carbon atoms fill all the octahedral sites on both planes (i.e $\Gamma = \Gamma_{max} = 72.02 \text{ at.nm}^{-2}$), %C is equal to 74.9 at.%.

The same method was applied for the four others LB taken from the QT230/HQ and QT230/0s tips. Table II-13 summarizes the calculated values obtained with Maugis's approach for each LB studied.

These data must be interpreted with caution because of the relatively low number of LB probed, however we can extract some general trends. First, if we compare the excess fraction on each LB, the sample that was directly quenched after the five seconds QT step presents the largest level of carbon segregation with an average of 11.57 at.nm^{-2} . Then, as soon as PT is reach, the segregation level seems to have decreased a little (8.24 at.nm^{-2}) on the two LB studied. Finally, after a partitioning step of 200s, the excess concentration is furthermore reduced to reach 7.36 at.nm^{-2} . Consequently, the occupancy ratio Γ/Γ_{max} decreases along the Q&P treatment. This trend suggests that some possible segregation/desegregation scenario on the laths boundaries might take place during the Q&P treatment.

Table II-13 - Results of the measurements of carbon segregation on lath boundaries for different Q&P conditions

		X^{ex} (%.nm)	Γ (at.nm ⁻²)	X^{∞} (at%)	Γ/Γ_{max} (%)	Es (eV)	%C (%at)
QT230°C/HeQ	LBQT1 (tip n°1)	12.52	10.07	0.85	18.13	0.123	35.05
	LBQT2 (tip n°1)	16.23	13.06	1.30	13.98	0.118	29.39
	Average	14.38	11.57	1.08	16.06	0.120	32.22
QT200_400/0s	LB04 (tip n°2)	10.25	8.24	0.52	11.45	0.179	25.41
	LB05 (tip n°3)	10.25	8.24	0.90	11.45	0.149	25.41
	Average	10.25	8.24	0.71	11.45	0.164	25.41
QT200_400/200s	LB201 (tip n°4)	14.04	11.30	0.50	15.68	0.202	31.82
	LB202 (tip n°5)	10.24	8.24	0.20	11.44	0.233	25.40
	LB203 (tip n°6)	8.06	6.48	0.56	9.00	0.160	21.13
	Average	9.15	7.36	0.38	10.22	0.197	23.26

Moreover, the fact that the amount of carbon segregation in between the laths seems to decrease the further the partitioning advances, tends to confirm this hypothesis. However, some carbon clusters (between 5 and 35 nm with concentration lower than 10at.%) still remains in martensite even at the end of partitioning. These clusters can be present as small two-dimensional plate or as spherical features but do not reach the carbon concentration of LB or carbides. This kind of clusters have already been observed by Pierce et al. in martensite [57]. It is difficult to unambiguously rule on the nature of these clusters but it might be the onset of carbides that did not developed into near-stoichiometric η or ϵ during the treatment.

If we now turn to the evolution of X^{∞} , the carbon concentration of the matrix, a large decrease in carbon content of martensite (from 1.08 at.% to 0.38 at.%) is observed throughout the treatment. This is the result of the partitioning of carbon atoms towards austenite during the partitioning step, the precipitation of carbides and the segregations on others defects, depleting the matrix.

The segregation energy (Es) was calculated at these three key points of the treatment and gives different values. Indeed, Es seems to increase as the treatment progresses. However, if we assume that all LB presents the same characteristics, i.e the same structure and thermodynamic properties; their segregation energy should then be viewed as an intrinsic quantity, and not vary over the course of the treatment. It is important to bear in mind that when eq.(II.14) is used, the thermodynamical equilibrium is calculated in a closed system made of two subsets: the lath boundary and the matrix. Carbon atoms can either segregate on the LB or stay in solid solution in the matrix. However, when eq.(II.14) is used during the partitioning step, the system must be expanded to take into account the escape of carbon from martensite to austenite as well as carbide formation. Thus, the stage in the treatment that is closer to the closed system with two subset as used in eq.(II.14) is at QT. Therefore, the LB's segregation energy is likely closer to the value calculated for the two LB at the condition QT230°C/HeQ i.e approx. 0.12eV.

II.6 Partial conclusion

A model Q&P steel grade was designed in order to study the microstructural evolution during the treatment. The optimum quenching and partitioning parameters were determined by the combination of dilatometry and XRD technics with modeling. The dilatometry study showed that an expansion not due to carbon redistribution occurs during the partitioning and considering the temperature range of the partitioning (400°C), bainite was suspected to induce this dilatation.

In order to confirm the presence of bainite in the microstructure, an image analysis study on SEM images was carried out. The prior chemical etching of the samples allowed to discriminate the carbon rich (retained austenite and MA Islands) and poor phases (tempered martensite and bainite). Austenite was present as small and fine long laths as well as in the periphery of the MA islands. Tempered martensite was easily recognizable due to the large presence of intra-lath carbide precipitation. Prior image analysis on a CFB sample highlighted that bainite shows no evidence of carbide precipitation. As the Q&P microstructure also presented small carbide free laths, we identified those as bainite. The phase fraction evolution of these features were studied by a manual counting method on samples that were quenched at various time during the partitioning step. A continuous increase in bainite fraction is observed by image analysis accordingly to the expansion observed by dilatometry. This trend is also observed when the QT varies: as in dilatometry, the more austenite is present for partitioning, the more bainite is observed by image analysis. This confirms that the morphological criterion for bainite (small laths with no carbides) is relevant.

Contrary to bainite, tempered martensite laths present a large amount of carbides. As carbide precipitation, and more widely carbon trapping, is detrimental to austenite carbon enrichment, these phenomena must be quantified. Atom probe tomography (APT) was used to obtain compositional information on probed carbides. Carbon composition ranging from 20.0 at.% to 27.7 at.%C were obtained, however such variation in carbon content can be attributed to measurement artefacts. Therefore, it is difficult to rule out on the nature of those carbides that is either transitional (ϵ or η) or equilibrium carbide (θ). That is why, complementary TEM diffraction experiments were conducted. While the presence of cementite was easily excluded, the literature review showed that the distinction between ϵ and η carbides can be tedious. However, the analysis of three different zone axis on the same carbide showed that η carbide are present in the microstructure as thin plate. However, some precipitates presenting a more spherical shape have also been observed and identified as being ϵ -carbides. Apart from carbide precipitation, APT measurements showed strong martensite laths boundaries carbon segregations. An analysis of the evolution of the excess concentration of carbon at the lath boundaries suggested that carbon strongly segregate at the beginning of the process. However, as the occupancy ratio decreases after partitioning, desegregation of carbon away from lath boundaries likely occurs during the partitioning step.

Even though SEM, APT and TEM allows to have access to crucial information on the carbon redistribution process, such as local carbon concentration in phases, obtaining a complete description of the carbon diffusion mechanism require additional technics. Thus, High Energy X-Ray Diffraction was particularly well suited to fill the knowledge gaps in our study such as the kinetics of phase transformation or time resolved chemical evolution of austenite carbon content.

Chapter III : IN-SITU INVESTIGATION OF QUENCHING AND PARTITIONING BY HIGH ENERGY X-RAY DIFFRACTION EXPERIMENTS

Table of contents

III.1 EXPERIMENTAL SETUP	111
III.2 HEAT TREATMENTS	111
III.3 METHODOLOGY	112
III.3.1 NATURE AND VOLUME FRACTION OF PHASES	112
III.3.2 AUSTENITE LATTICE PARAMETER AND INTERNAL STRESSES	117
III.3.3 CARBON COMPOSITION OF AUSTENITE	122
III.4 EFFECTS OF QT ON THE EVOLUTION OF MICROSTRUCTURES DURING QUENCHING AND PARTITIONING	124
III.4.1 EVOLUTION OF THE VOLUME FRACTION OF PHASES	124
III.4.2 KINETICS OF CARBON ENRICHMENT IN AUSTENITE	126
III.4.2.1 <i>Evolution of austenite lattice parameter with QT</i>	126
III.4.2.2 <i>Evolution of carbon content in austenite with QT</i>	129
III.4.2.3 <i>Origins of the C enrichment in austenite</i>	131
III.5 PARTIAL CONCLUSION	134

Advances in instrumentation and data processing technologies made the use of High Energy X-Ray Diffraction (HEXRD) experiments one of the most powerful in-situ material characterization technics available. Compared to traditional laboratory X-Ray experiments, the HEXRD two main advantages are:

- the high energy of the generated photons (in the range of 10-120KeV) allows to penetrate deeper into the materials and even to work in transmission mode. This lets the users to analyze the volume of the sample contrary to traditional X-ray sources where the low energies provided by the cathodes only allow for surface analysis. This leads to better statistical representation of the probed sample. This also leads to higher diffracted energies that results in a very good signal/noise ratio. Finally, the small wavelength of the ray also permits the studying of little features down to the nanometer,
- the high brilliance of the photon beam (that can be viewed as a measure of the concentration of photons per volume unit) allows very short acquisition times (multiples diffractograms acquired per second) contrary to traditional X-rays where the acquisition of a diffractogram takes approximately one hour. This permits to have access to highly time resolved in-situ experiments and is very useful when phase transformation occurs during rapid temperature changes such as quenches or fast reheating.

III.1 Experimental setup

High Energy X-Ray Diffraction (HEXRD) experiments were conducted at the Deutsches Elektronen-Synchrotron DESY in Hamburg, Germany, on beamline Petra P-07. The $\Phi 4$ samples were placed into a commercial Bähr dilatometer (DIL805D) available on the line in order to reproduce the chosen Q&P treatments and to obtain dilatometry curves. A schematic representation of the experimental setup is shown on Figure III-1 below. The high energy monochromatic beam (100 keV) permits to work in transmission, and the association with a fast 2D detector enables high acquisition rates (10 Hz) suitable to study “real time” process on bulk sample. The detector was placed 1 m away from the sample, giving access to full Debye-Scherer rings with a maximum 2θ angle of 12° .

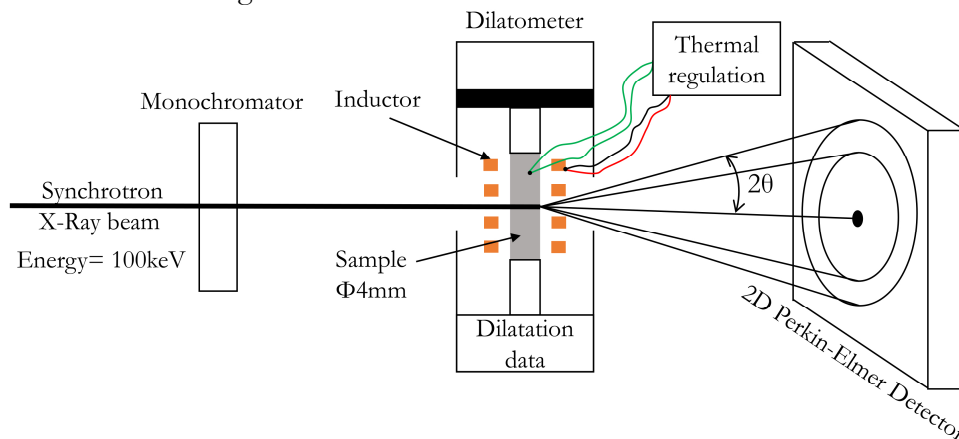


Figure III-1 - Schematic representation of the experimental setup as used at the DESY beamline P07.

III.2 Heat treatments

The following Q&P heat treatment was performed :

- heating rate at 5°C/s to reach the austenitic domain and to dissolve any cementite previously formed,
- austenitization at 900°C for 5 min to attain a fully austenitic microstructure without an excessive growth of grains,
- cooling at 50°C/s to quenching temperature (QT) to prevent any ferrite formation before M_s followed by an homogenization temperature step of 5s at QT,

- heating to partitioning temperature (PT) at 30°C/s
- and, a final quench at the maximum cooling rate until RT.

Three different QT temperatures were considered: 200°C, 230°C, 260°C as indicated in Figure III-2.

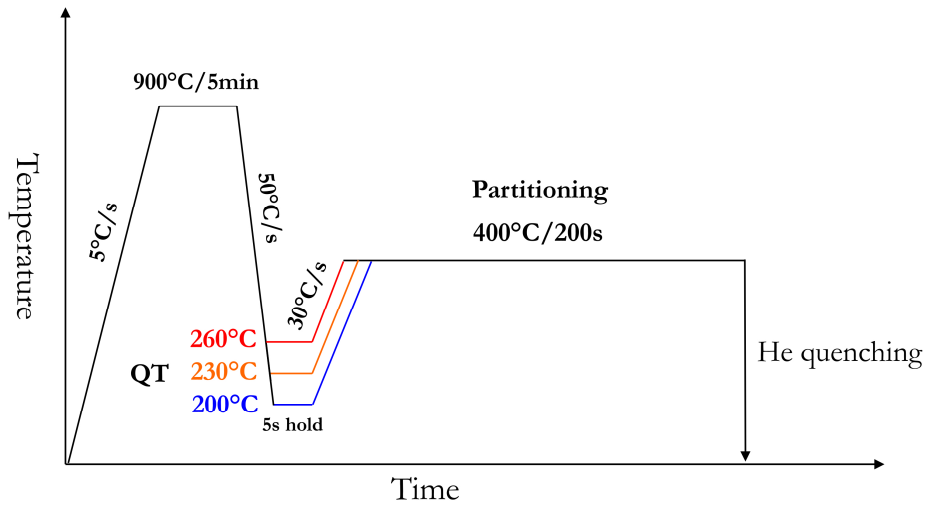


Figure III-2 - The three Q&P conditions studied by HEXRD.

III.3 Methodology

This section aims at giving the methodology used to treat the data collected with HEXRD. The Q&P condition at QT200 will often be used as an example to clarify our approach.

III.3.1 Nature and volume fraction of phases

The 2D diffraction patterns obtained with the detector were integrated circularly using the Fit2D software to obtain 1D diffractograms. Key times during the Q&P treatment were chosen as shown in Figure III-3 and the diffractograms corresponding to these points are shown in Figure III-4.

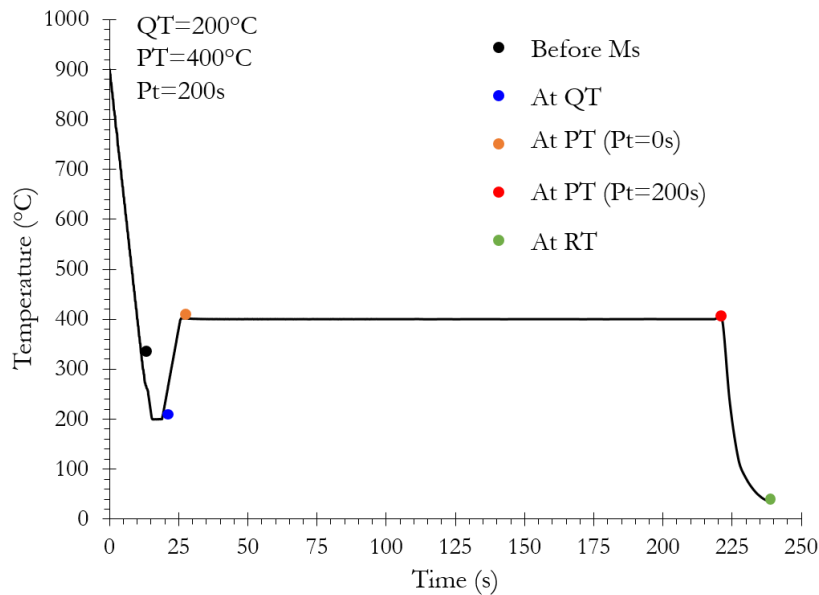


Figure III-3 – Critical times selected in the thermal treatment corresponding to (QT=200°C PT/Pt=400°C/200s)

The first diffractogram taken just before Ms (black dot on Figure III-3 and black line on Figure III-4) shows peaks characteristics of an FCC phase. Then, once under Ms and when QT is reached, the FCC peaks weakens and peaks that can be characteristics of a BCC or a BCT phase are observed. In order to rule on the nature of this second phase and to extract the phase fractions and lattice parameters, the diffractograms were analyzed with a full Rietveld refinement procedure [163]. Diffraction peaks were modeled using pseudo-Voigt functions using FullProf software with 20 degrees of freedom for each record (background, phase fraction, lattice parameters, shape of peaks, and temperature effects). The lattice parameters were obtained with the positions of the peaks while the phase fractions are extracted from the peak intensities. The uncertainty on both phase fractions and lattice parameters were estimated to be roughly $\pm 1\%$ and 0.005\AA respectively.

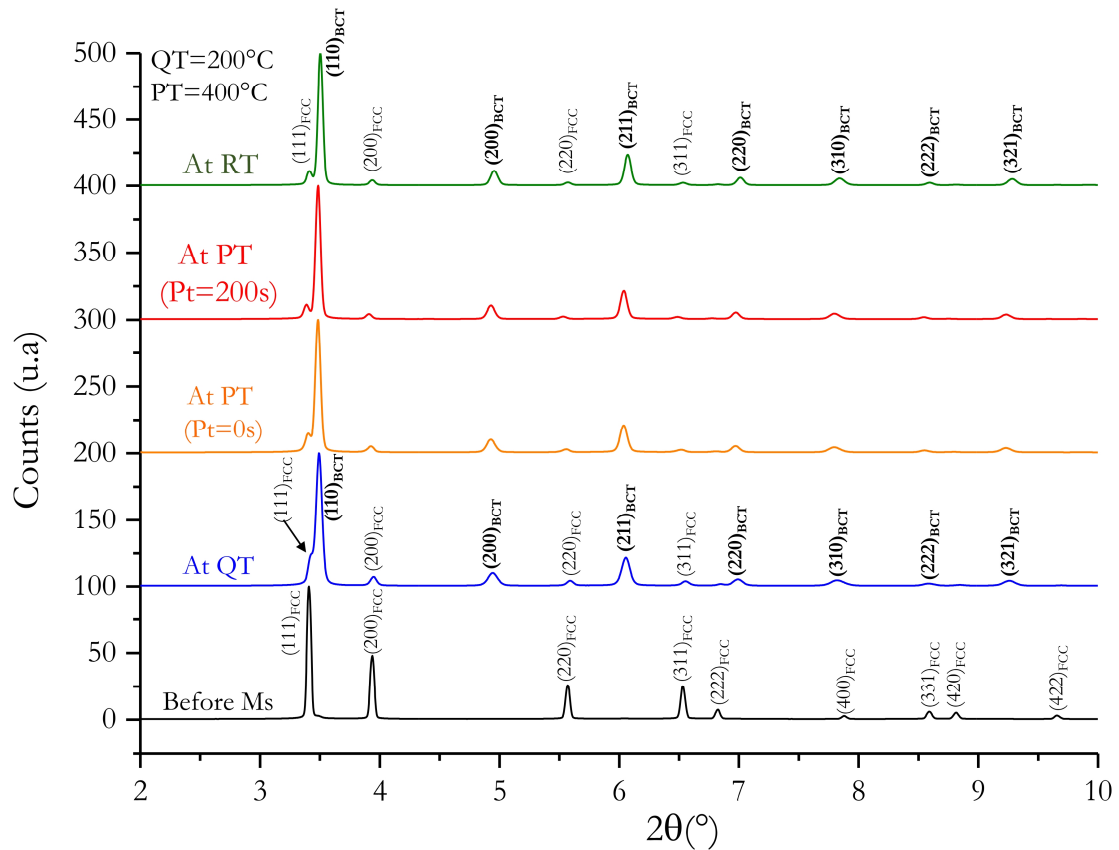


Figure III-4 - Diffractograms corresponding to the critical times selected in Figure III-3.

Two phases were considered in the refinement: austenite and ferrite. While the symmetry used to describe austenite is straightforward (FCC, $Fm\bar{3}m$), two different symmetries were tested to fit the ferritic phase: a body-centered cubic ($Im\bar{3}m$) and a body-centered tetragonal ($I4/mmm$). The weighted profile R factor (or Rwp) is largely used in Rietveld refinement procedure as a discrepancy index between the experimental and the calculated profiles and is expressed as [164]:

$$R_{wp} = \left[\frac{\sum_i w_i (y_i - y_{ci})^2}{\sum_i w_i (y_i)^2} \right]^{\frac{1}{2}} \quad (III.1)$$

Where w_i is the weight of the different reflexions, y_i and y_{ci} are the observed and calculated intensities and i is the 2θ angle.

The evolution of Rwp for the two considered symmetries for ferrite is plotted on Figure III-5 ($t=0s$ correspond to the start of the reheating step towards PT). As a lower Rwp means a better fit, the BCT structure seems to better describe the observed peaks.

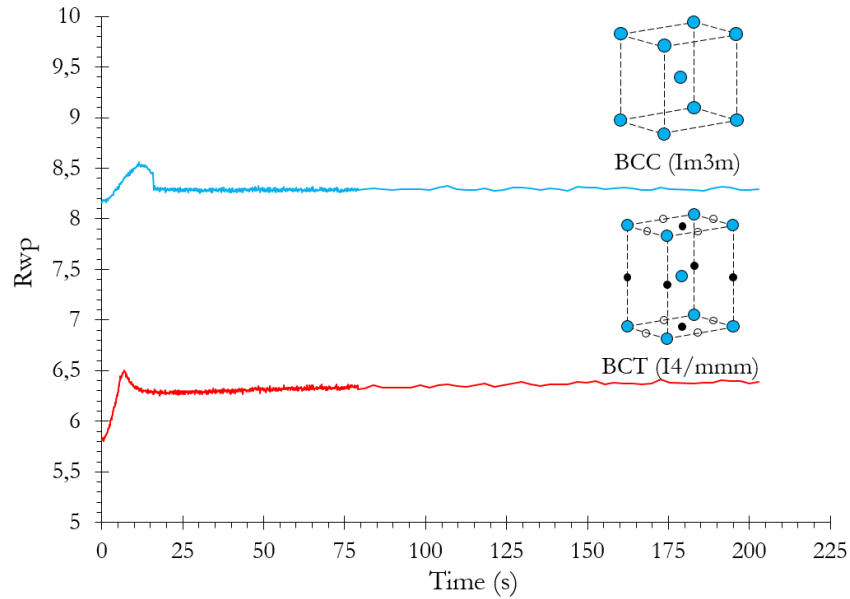


Figure III-5 - Rwp factors of the Rietveld procedure on ferritic peaks for the BCC and BCT structure ($t=0s$ correspond to the start of the reheating step from QT towards PT) at QT=200°C and PT/ $t=400^{\circ}C/200s$ (courtesy of S.Gaudez)

Figure III-6 presents the time evolution of the phase fractions determined from the Rietveld refinement together with the thermal path during the Q&P treatment. The QT=230°C condition is used as an example because of its larger amount of bainite formed than at QT=200°C, giving a better view of the phase transformation occurring during the treatment. The evolution of phase fraction can be decomposed into 5 stages:

- (1) a quenching from the fully austenitic domain (900°C) to a temperature of 301°C during which no phase transformation occurs,
- (2) a temperature decrease from 301°C to 230°C during which a significant increase in BCT-phase at the expense of austenite occurs (76.3% of BCT phase formed). The rate of this transformation is very fast in the first stages and becomes more sluggish at the final stage. It can be highly suspected that the BCT-phase corresponds to α' -martensite. At this stage of the study, the reason put forward for this is that the BCT-phase start temperature, evaluated from Figure III-7 is about 301°C.
- (3) A stagnant stage during reheating from 230°C to 369°C in which the microstructural state remains globally unchanged (even if a slight increase in austenite and a decrease in martensite is observed)
- (4) A significant and slow increase in a new-BCT phase fraction at the expense of austenite occurs from 369 to 400°C and during the whole partitioning step
- (5) Finally, a slight increase in BCT phase at the expense of austenite during final quenching that corresponds to the formation of fresh martensite.

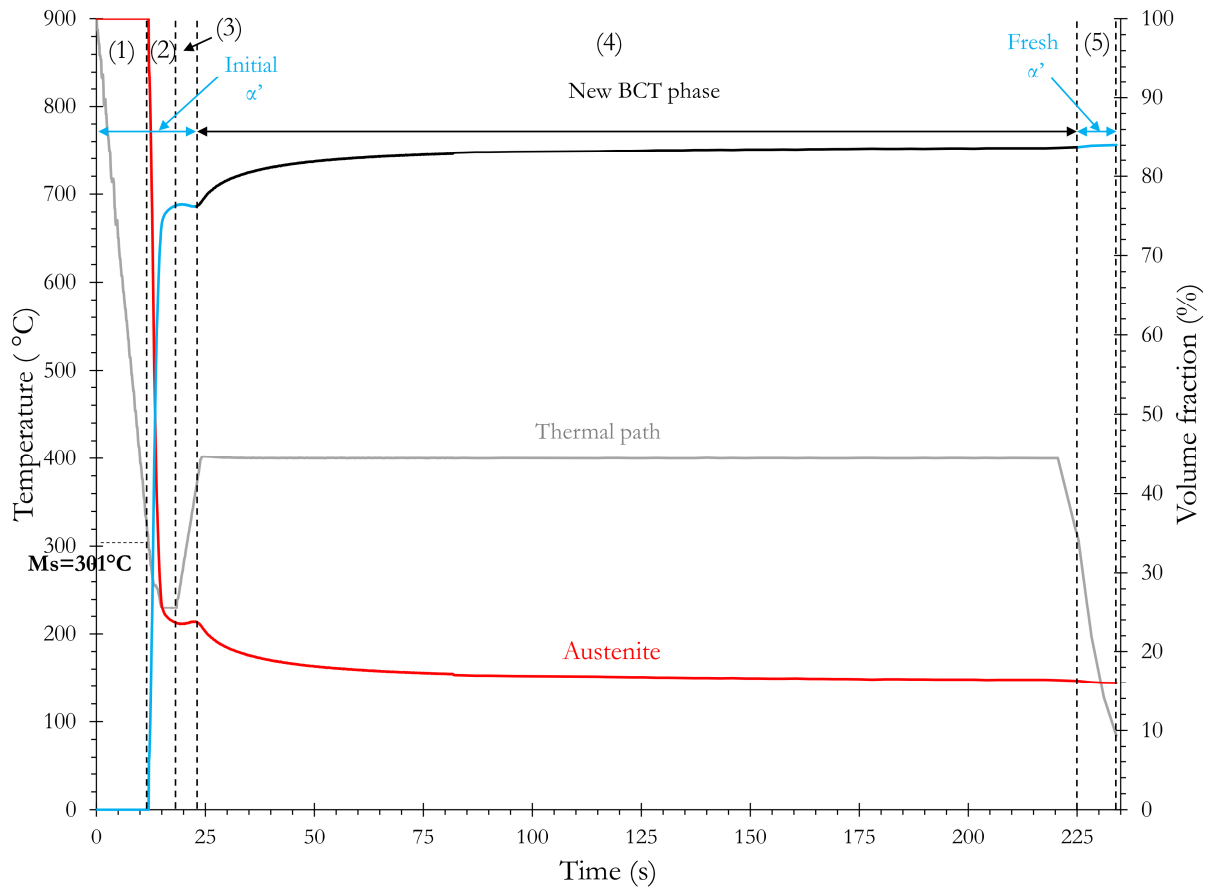


Figure III-6 - Time evolution of the phase fractions together with the thermal path of the QT230 sample during HEXRD experiment (QT230 PT/ $t=400^{\circ}\text{C}/200\text{s}$).

It is pretty clear that the FCC phase is austenite and that the BCT phase that form during the initial and final quench is α' -martensite. However, the nature of the new-BCT phase that forms during the reheating and partitioning step remains to be determined.

At QT230, the new BCT phase starts to form during the reheating step (above 369°C) and thus above M_s (301°C). The nature of this phase is subject to much debate as it can be either bainite or isothermal martensite. However, Navarro-Lopez showed via multiple isothermal treatment above, at and under M_s that in the temperature range above 320°C , no martensitic products is observed [101]. Moreover, the section on image analysis of the previous chapter showed some small carbide free laths that were identified as bainite (see the features presented Chapter 2, Table II-10). It can thus be highly suspected that the new BCT phase corresponds to bainite.

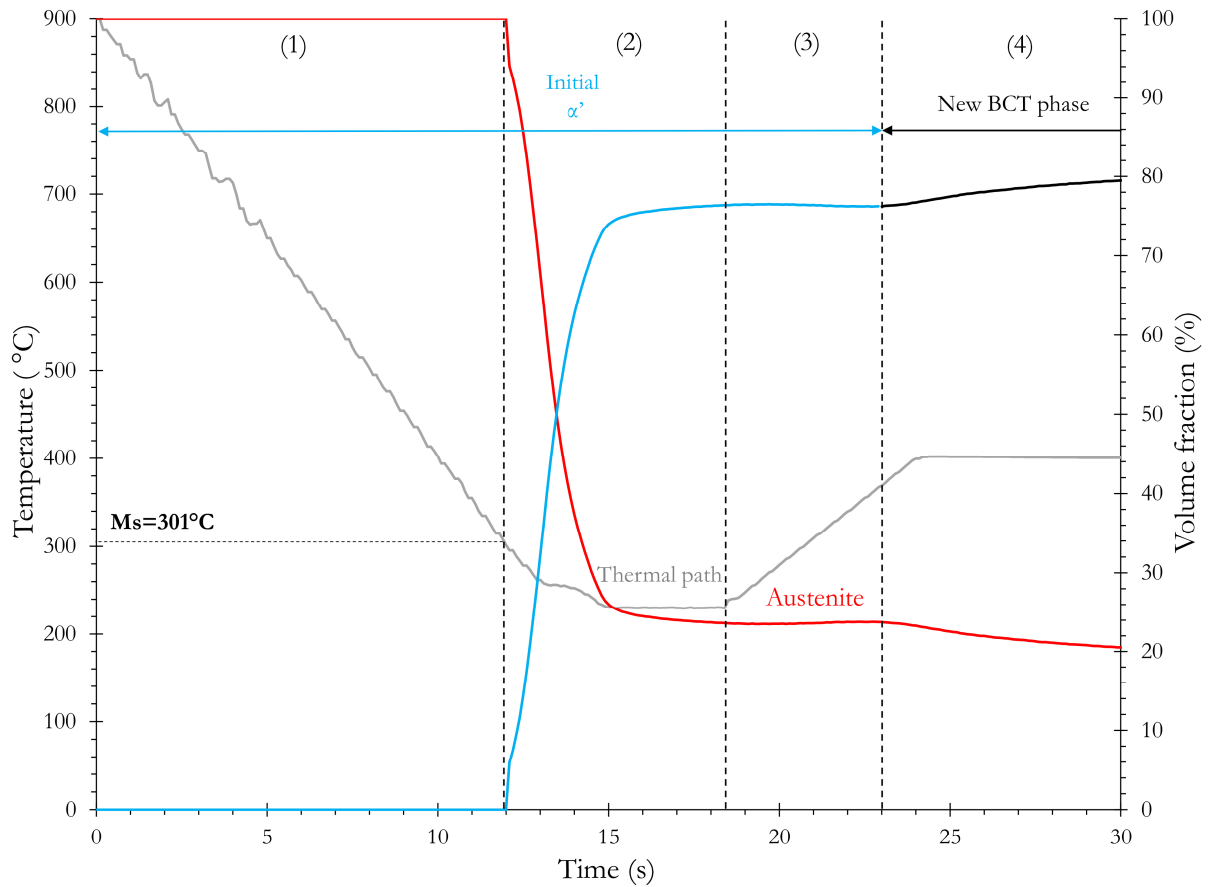


Figure III-7 - Magnification of the first 30s corresponding to (QT230 PT/ $t=400^{\circ}\text{C}/200\text{s}$).

In order to go further, the evolutions of the volume fraction of the product identified as bainite by image analysis was compared with those of the new BCT phase measured by HEXRD. The results corresponding are given on Figure III-8.

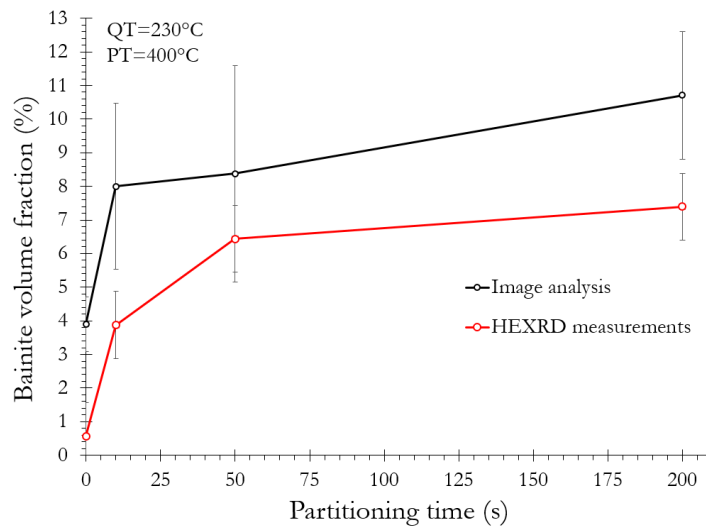


Figure III-8 – Comparison of the evolution of the bainite fraction measured by both image analysis and HEXRD (QT=230°C PT/ $t=400^{\circ}\text{C}$).

The two curves follow the same tendency with a rapid increase in the first moments of the BCT phase formation and with a more sluggish increase during the rest of the partitioning step. The error on phase fraction measurement by HEXRD is estimated to be 1%. The final bainite volume fraction is almost the same with the two methods: $(10.7 \pm 1.9) \%$ by image analysis and (7.4 ± 1)

% by HEXRD. Furthermore, the evolutions of the volume fraction of the new BCT phase measured by HEXRD at the end of the partitioning step were compared with those measured by image analysis for the three QT studied. The results obtained on Figure III-9 show clearly that the two curves follow the same trend with an increasing BCT phase fraction with increasing QT. Taking into account the measurement errors, the volume fractions at a given QT are very close. In general terms, it is worth noting that the measurements by image analysis tends to overestimate bainite fraction. All of these observations strongly suggest that the new BCT phase observed correspond to bainite.

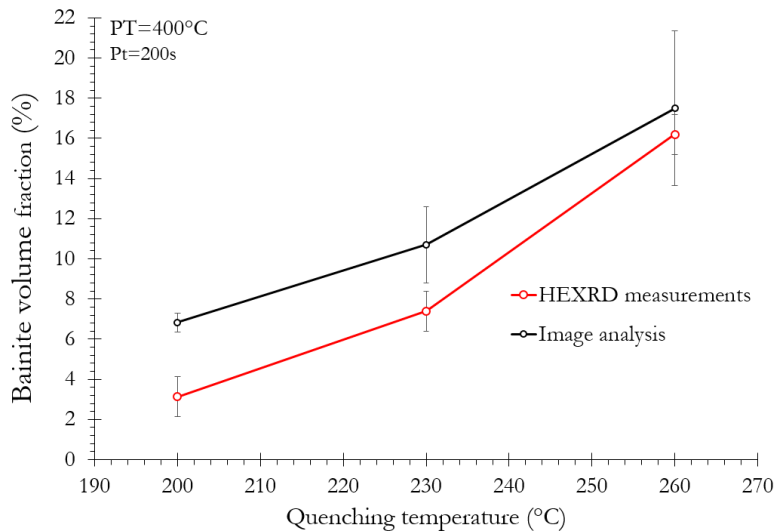


Figure III-9 - Comparison of bainite fraction measured by both image analysis and HEXRD at the end of the partitioning step for the three QT

III.3.2 Austenite lattice parameter and internal stresses

The in-situ synchrotron HEXRD is probably the most powerful technic available to follow the lattice parameter evolution during a heat treatment. Indeed, the Rietveld procedure allows us to extract the lattice parameter evolution of FCC and BCT phases at a high rate (10Hz) through the whole Q&P process. This section aims at interpreting the evolution in austenite lattice parameter in terms of change in chemical composition and stress state.

Figure III-10 presents the as-measured evolution of a_γ with temperature during the QT200 treatment starting at 900°C right before the quench to QT. This change in lattice parameter is the result of three contributions:

- a thermal contribution resulting from the pure change in volume of the lattice due to the thermal expansion,
- a chemical contribution due to the volume change of the lattice induced by sites occupation of atoms,
- a mechanical contribution resulting mainly from internal stresses due to phase transformations,

The evolution of the austenite lattice parameter with temperature for the QT200 condition is given Figure III-10. The austenite lattice parameter evolution can be divided into three main stages: the stress free contraction to M_s (black line in Figure III-10), below M_s during martensite formation (blue line in Figure III-10) and at the exit of QT for the rest of the treatment (red, orange and green lines in Figure III-10).

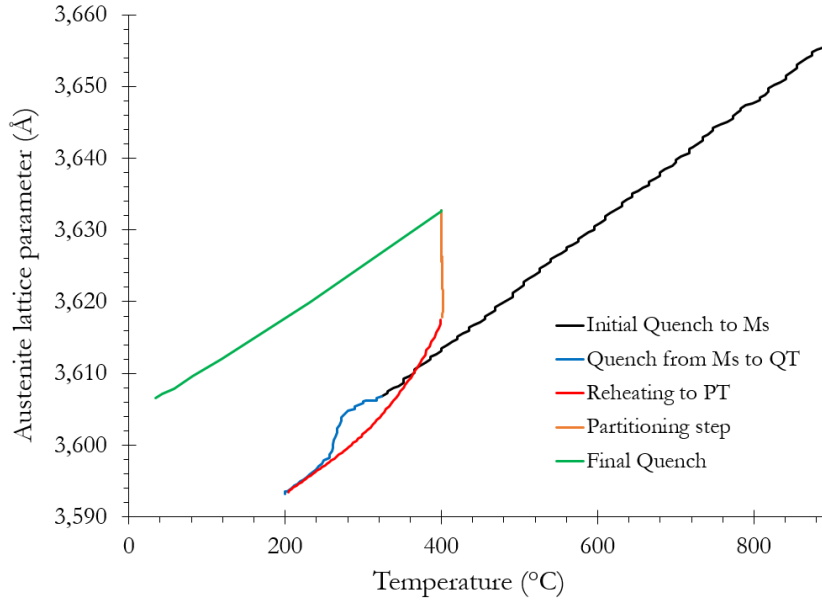


Figure III-10 – Evolution of the austenite lattice parameter during the QT200 treatment (QT200 PT/ $t=400^{\circ}\text{C}/200\text{s}$)

This evolution includes a thermal contribution that must be subtracted. To that end, it is thus a prime of necessity to estimate the Coefficient of Thermal Expansion (CTE) of austenite that depends on the microstructural state at a given temperature.

Stress free contraction of austenite (above Ms)

Van Bohemen showed that austenite's CTE, $\alpha_{\gamma}(T)$, can be modeled with a temperature dependency as [165]:

$$\alpha_{\gamma}(T) = B_{\gamma} \left[1 - \exp\left(-\frac{T}{\theta_{\gamma}}\right) \right] \quad (III.2)$$

Where B_{γ} is the CTE of austenite at high temperature and θ_{γ} is a critical temperature expressing the fact that in the high temperature domain (or $T \gg \theta_{\gamma}$), austenite's CTE tends to a constant value (B_{γ}). Van Bohemen highlighted the fact that because of the strong correlation between thermal expansion and heat capacity, θ_{γ} is probably best denoted as the Debye temperature of austenite (in the range of 400-470K)[165].

Moreover, the evolution of the austenite lattice parameter can be calculated as:

$$a_{\gamma}^{calc}(T_2) = a_{\gamma}^{calc}(T_1) [1 + \alpha_{\gamma}(T_2) \cdot \Delta T] \quad (III.3)$$

Where $a_{\gamma}^{calc}(T)$ is the value of the austenite lattice parameter at the temperature T and $\alpha_{\gamma}(T)$ is the CTE of austenite calculated at the temperature T.

In order to obtain B_{γ} and θ_{γ} , the calculated austenite lattice parameter (a_{γ}^{calc}) evolution obtained with eq. (III.3) was fitted to the experimentally measured a_{γ} with a least square method. By taking the value of a_{γ} at 800°C as initial condition, the following values were then obtained:

$$B_{\gamma} = 2.50 \times 10^{-5} \text{ K}^{-1} \quad \theta_{\gamma} = 250\text{K}$$

The fit of the calculated austenite lattice parameter to the measured one is shown Figure III-11 below.

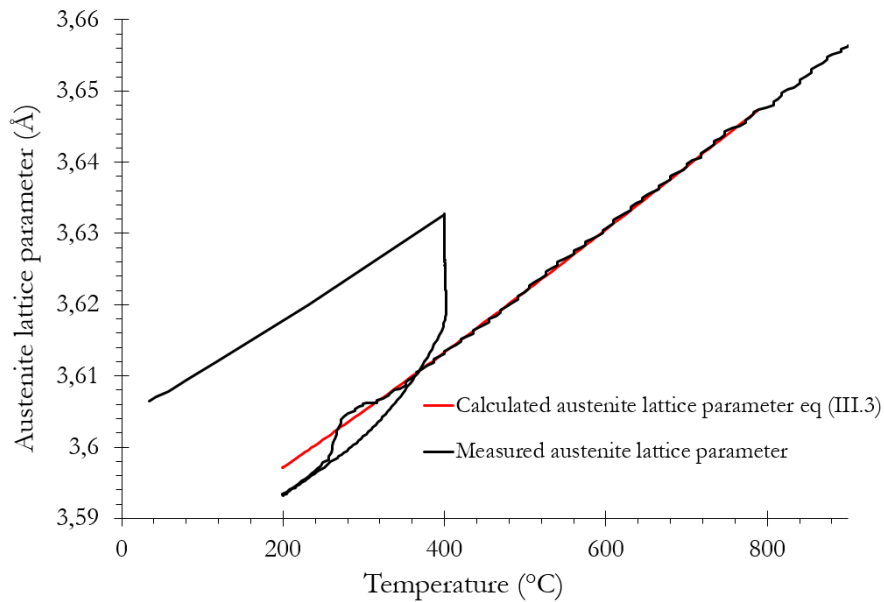


Figure III-11 - Fit of the stress free thermal contraction of austenite after equation III.3 (red) on the experimental curve (black) (QT200 PT/ $t=400^{\circ}\text{C}/200\text{s}$).

The use of VB model to calculate the stress free contraction of austenite during the quench gives a good fit but significant deviation from the model is observed starting at the M_s temperature (323°C). This point is addressed below.

Below M_s during martensite formation

Figure III-12 gives a better view of the zone where the experimental curve (black curve) deviates from pure thermal expansion linearity (red curve).

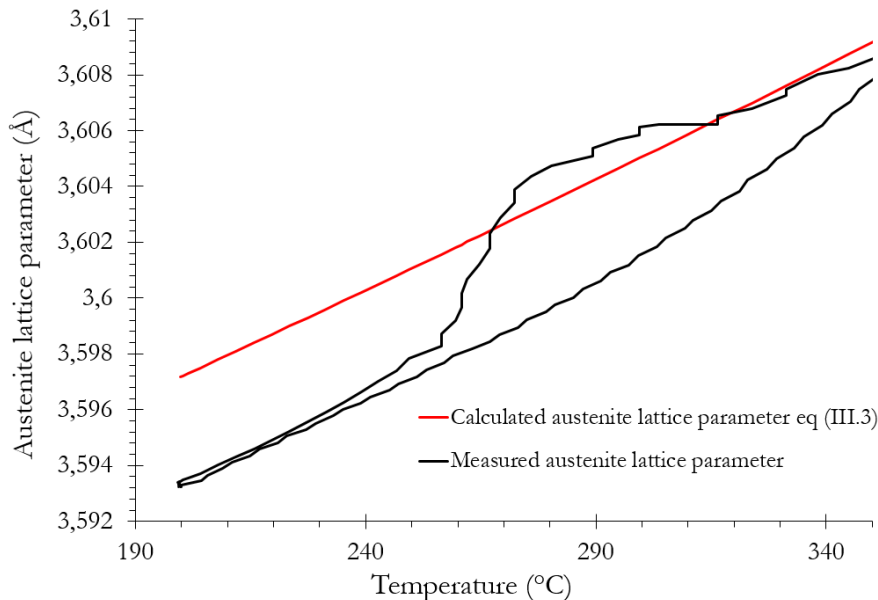


Figure III-12 - Closer view of the zone where experimental austenite lattice parameter deviates from the modeled stress free contraction (QT200 PT/ $t=400^{\circ}\text{C}/200\text{s}$).

At first and once M_s was reached (323°C), the experimental austenite lattice parameter becomes larger than the modeled one (red curve in Figure III-12) and, at 266°C , it becomes smaller. At QT, the experimental austenite lattice parameter is 0.0038 \AA smaller than the modeled one. As martensite forms via a diffusionless mechanism, the change in austenite lattice parameter cannot be interpreted as a change in its chemical composition. The observed changes in a_{γ} would thus

result of the internal stresses induced by the martensite formation. For low volume fraction of martensite formed, it can be highly suspected that austenite is under pressure and, from a critical volume fraction of martensite, austenite becomes under compression. This has already been reported by several authors [166][167][168][169][170][171].

At the exit of the QT step

At the end of the QT step, the microstructure consists of austenite islands embedded in a martensitic matrix. As the martensite's CTE is lower than that of austenite, the latter will not expand freely with temperature. As a consequence, an apparent CTE (i.e. eq.(III.4)) must be used in order to take into account the effects of internal stresses on the thermal expansion of the lattice. The model developed by S. Allain was used [172]. It is mainly based on Mori-Tanaka mean field assumption and predicts the apparent CTE of an austenite/martensite composite from the elastic constant and the CTE of phases. The assumption of spherical austenite islands embedded in a martensitic matrix was made. As austenite is under compression (since the volume fraction of martensite formed is relatively high), the apparent CTE of austenite becomes lower as martensite forms. Consequently, the apparent CTE of austenite is given by the following relation [172] :

$$\alpha_{\gamma}^{app.}(T) = \alpha_{\gamma}(T) + (1 - f_{\gamma}) \left(\frac{20\nu^{\alpha'} - 10}{15(1 - \nu^{\alpha'})} \right) (\alpha_{\gamma}(T) - \alpha_{\alpha'}(T)) \quad (III.4)$$

where f_{γ} is the volume fraction of austenite, $\nu^{\alpha'}$ is the poisson ratio of martensite (taken as 0.33 as for austenite), $\alpha_{\gamma}(T)$ is the stress-free CTE of austenite as presented in (III.2) and $\alpha_{\alpha'}(T)$ is the stress-free CTE of martensite taken from the work of Van Bohemen and equal to [165]:

$$\alpha_{\alpha'}(T) = B_{\alpha'} \left[1 - \exp\left(-\frac{T}{\theta_{\alpha'}}\right) \right] \quad (III.5)$$

where $B_{\alpha'}$ is the CTE of austenite at high temperature ($1.83 \times 10^{-5} \text{ K}^{-1}$) and $\theta_{\alpha'}$ is a critical temperature of 320K.

Figure III-13 presents the temperature evolution of the stress-free CTE of austenite and martensite together with the evolution of apparent CTE of austenite. As soon as martensite starts to form, the austenite apparent CTE lowers until the martensite fraction is stable (around QT), for the rest of the treatment, as the martensite fraction is relatively unchanged (except at the final quench when a very low amount of fresh martensite forms), the apparent CTE follows the same trend as the stress-free CTE of austenite.

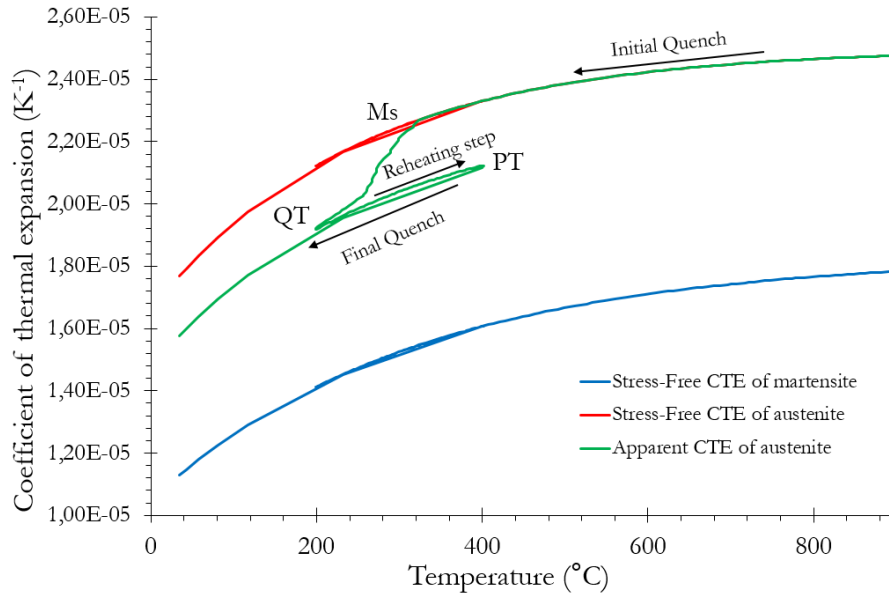


Figure III-13 - Temperature evolution of the different CTE model for austenite and martensite (QT200 PT/ $t=400^{\circ}\text{C}/200\text{s}$).

Figure III-14 shows the time evolution of the change in austenite lattice parameter once the thermal effect is deduced with the apparent CTE modeling. As from 900°C to M_s no other phenomenon apart from pure thermal contraction occurs, the change in austenite lattice parameter was artificially set to zero in order to facilitate the reading of the graph.

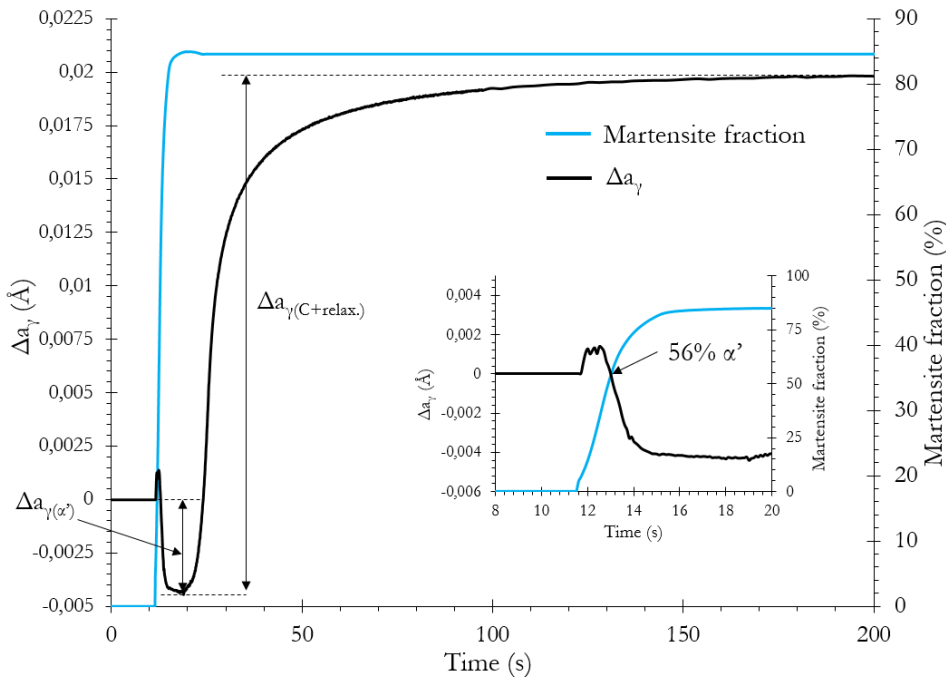


Figure III-14 –Change in austenite lattice parameter with time during the Q&P process when thermal contribution is subtracted ($t=0\text{s}$ taken at 900°C at the beginning of the initial quench step) (QT200 PT/ $t=400^{\circ}\text{C}/200\text{s}$).

The first variations in austenite lattice parameter within 19s was attributed to a mechanical effect induced by martensite formation. It appears clearly that austenite is first under tension for $\Delta a_{\gamma(\alpha')} > 0$ and becomes under compression for a critical volume fraction of martensite of 56% (see the

insert on Figure III-14). The total increase of austenite parameter, noted $\Delta a_{\gamma(C+\text{relax.})}$ on Figure III-14, can be attributed to both a chemical and a mechanical effect, making it difficult the determination of carbon content evolution in austenite.

III.3.3 Carbon composition of austenite

No change in carbon content is expected to happen during the initial cooling from the austenitic domain, neither during martensite formation. However, during the reheating and partitioning steps, some carbon can diffuse towards austenite from martensite or bainite, leading to an expansion of the austenite lattice. As discussed previously, any change in austenite lattice parameter after QT can be attributed to a carbon enrichment of austenite or a change in the stress state of austenite or both. Indeed, from a critical volume fraction of martensite of about 50%, it was shown that austenite is under compression. A stress relaxation phenomenon can however be expected during first heating and soaking at PT (Nakada et al.) [169]. The origins of the latter can be attributed to many mechanisms such as tempering, diffusion of carbon from martensite into austenite and the time-evolution of mechanical properties of both martensite and austenite since their properties depend strongly on carbon. Furthermore, the presence of bainite can impact the stress state in austenite due to its larger specific volume. However, all these mechanical contributions to the austenite lattice parameter variation are very difficult to decouple. In order to overcome this difficulty, it was proposed to define the two boundaries for carbon evolution by considering two limit cases. The first is to suppose that no stress relaxation occurs during reheating and soaking at PT. In other words, the stress relaxation phenomena are neglected and all the increase in a_{γ} occurring after QT (Δa_{γ} positive) was assigned to the chemical contribution; the latter being thus overestimated in that case. The second is to suppose that internal stresses in austenite are immediately and totally relaxed. In that specific case, the quantity $\Delta a_{\gamma(\alpha')}$ on Figure III-14 was subtracted to the total change in a_{γ} measured ($\Delta a_{\gamma(C+\text{relax.})}$ on Figure III-14). Thus, the evolution of a_{γ} obtained that underestimates the chemical contribution, gives an overview of the maximum effect of stress relaxation on the austenite lattice parameter i.e on the carbon enrichment into austenite. Finally, the real chemical contribution in the increase of the austenite lattice parameter is expected to evolve very likely between these two boundaries represented Figure III-15.

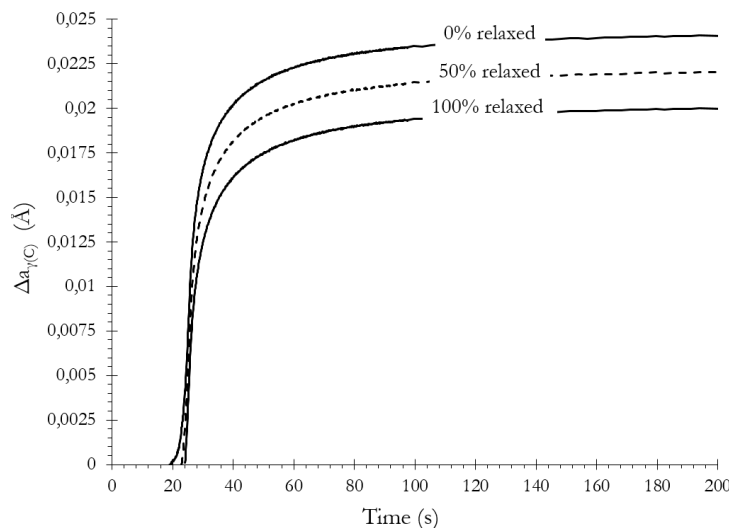


Figure III-15 - Evolution of the change in austenite lattice parameter due to the chemical contribution depending on the amount of stress relaxed immediately at QT200 (QT200 PT/ $t=400^{\circ}\text{C}/200\text{s}$).

Then, the change in austenite lattice parameter was translated into a change in carbon content using the relation by Toji et al. [49]. They used a combination of the equations of Ruhl et al. and

Dyson et al. in order to link the austenite lattice parameter to its alloying element content, giving[60][150] :

$$a_{\gamma} = 3.572 + 0.033C_{\gamma} + 0.0012Mn_{\gamma} - 0.00157Si_{\gamma} \quad (III.6)$$

Where a_{γ} is the experimental austenite lattice parameter (in Å) and C_{γ} , Mn_{γ} and Si_{γ} the concentration of alloying elements (in wt.%).

The partitioning of substitutional elements (Mn and Si) during the Q&P treatment was supposed to be negligible. In that case, the chemical variation in a_{γ} is only linked to the variation in carbon content. As in-situ HEXRD allows the monitoring of time resolved change in austenite lattice parameter, eq.(III.6) can be used in its integrated form:

$$da_{\gamma} = 0.033dC_{\gamma} \quad (III.7)$$

Where da_{γ} is the variation in austenite lattice parameter (in Å) and dC_{γ} is the variation in carbon content of austenite (in wt.%). The error made on the lattice parameter measurements was about ± 0.005 Å after Fullprof analysis, thus the relative error made by estimating carbon using this method is estimated as 0.14%.

III.4 Effects of QT on the evolution of microstructures during quenching and partitioning

The three different Q&P conditions (QT = 200°C, 230°C, 260°C) were treated as presented in the methodology section. This section aims at presenting the results and main conclusions of the HEXRD experiments concerning the chemical composition and phase fraction evolutions of austenite, martensite and bainite.

III.4.1 Evolution of the volume fraction of phases

The thermal path together with the phase fraction evolutions of austenite, martensite and bainite are given for the three QT on Figure III-16. The reference time (t=0s) is taken at the beginning of the initial quench from 900°C.

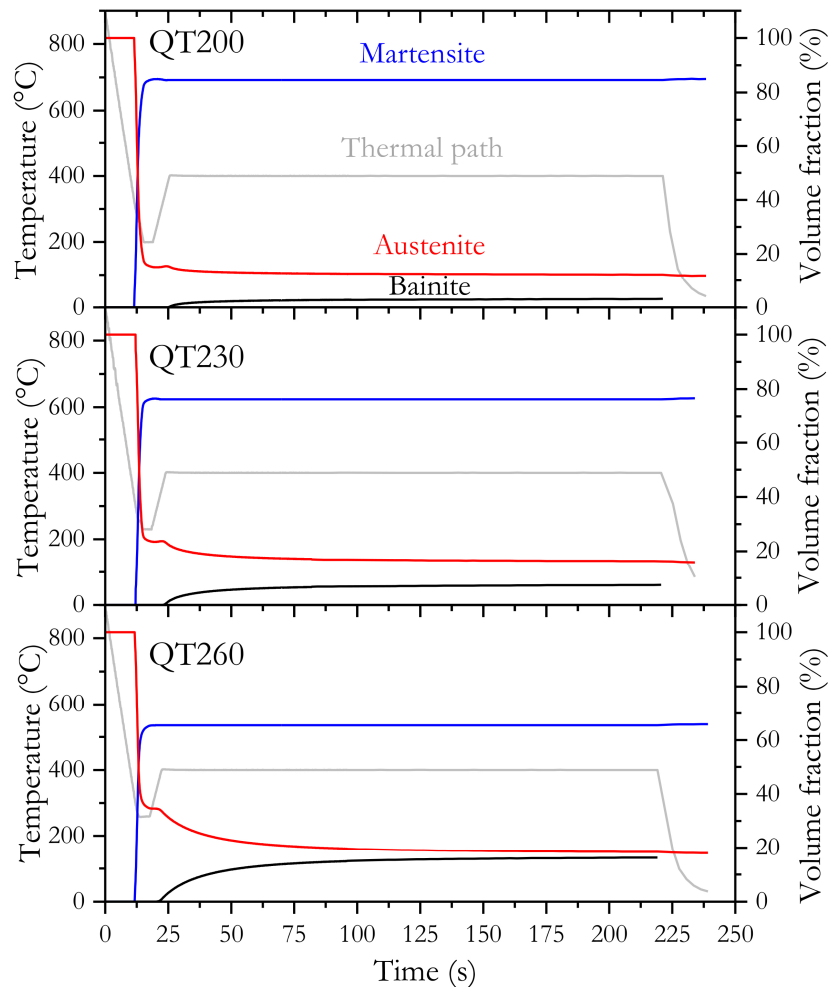


Figure III-16 - Evolution of the phase fraction during the Q&P treatment for the three QT studied.

Martensite starts to form during the initial quench to QT at 324°C, 301°C and 315°C for respectively QT200, QT230 and QT260. The Ms value spreads are similar to those already presented in chapter 2 with dilatometry experiments (approx. $\sigma=12^\circ\text{C}$). However Ms is detected sooner via HEXRD. Indeed, a delay exists between the very first martensite laths formed detected via HEXRD and the measurement of a change of length via dilatometry, explaining the lower Ms values measured via dilatometry.

At the end of the QT step, once the temperature of the sample is homogenized, the initial volume fraction of martensite depends on QT: 85% at QT200, 76% at QT230 and 65% at QT260. Figure III-17 shows the comparison between the two models already studied in chapter

II for the kinetics of martensite transformation and the HEXRD values. The M_s value used in the two models is an average of the three M_s measured i.e 314°C . Contrary to the dilatometry study from chapter 2, the HEXRD results tends to validate Van Bohemen modeling of the martensite transformation as LVT model overestimates the martensite fraction, especially for low QTs.

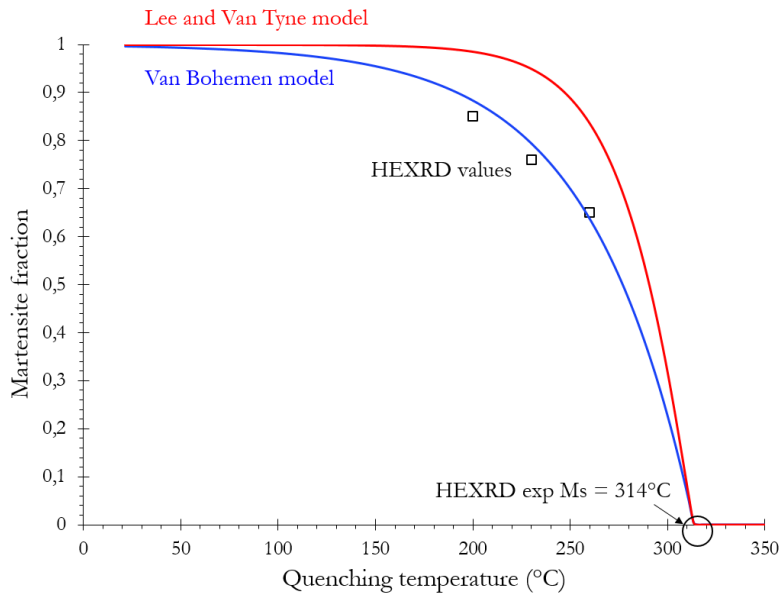


Figure III-17 - Comparison between the calculated volume fraction of martensite using LVT and Van Bohemen models and measured ones by HEXRD.

It is clearly shown that the total volume fraction of bainite formed depend strongly on QT. A decrease of QT leads to a decrease of the total volume fraction of bainite. In order to go further, both the kinetics of bainite fraction and the amount of austenite transformed into bainite (i.e. the transformation rate) were given on Figure III-18 as a function of QT.

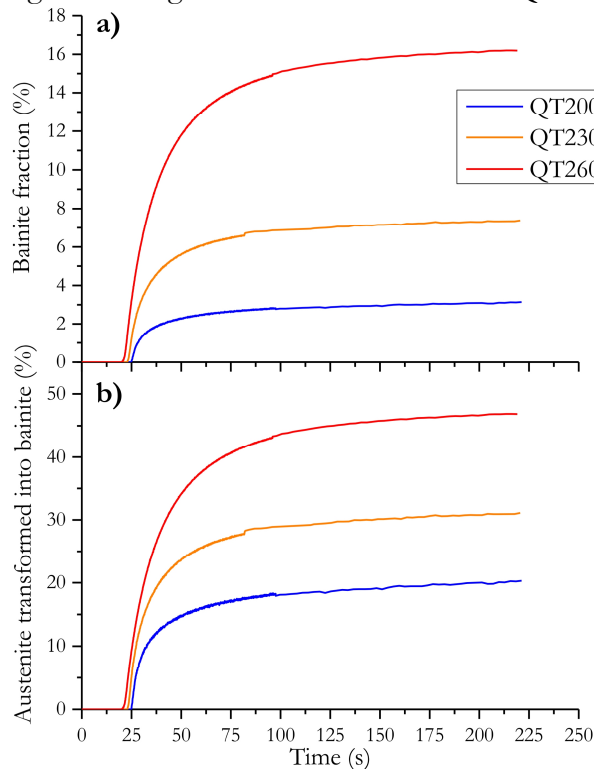


Figure III-18 – Evolution of a) bainite fraction and b) amount of austenite transformed into bainite for the three QT studied.

It is worth noting that bainite starts to form during reheating for the three QT and the lower the QT, the higher the temperature for bainite formation is. The bainite start temperatures measured for the three QT are given in Table III-1. The transformation rate, which is a better indicator than the intrinsic volume fraction, depends on QT. It is shown to decrease with decreasing QT, from 45% at QT=260°C to 20% at QT=200°C. For the three QT studied, the major part of bainite is formed within a very short time: 75% of bainite is formed within 28.2s, 24.6 and 30s for respectively QT200, QT230 and QT260.

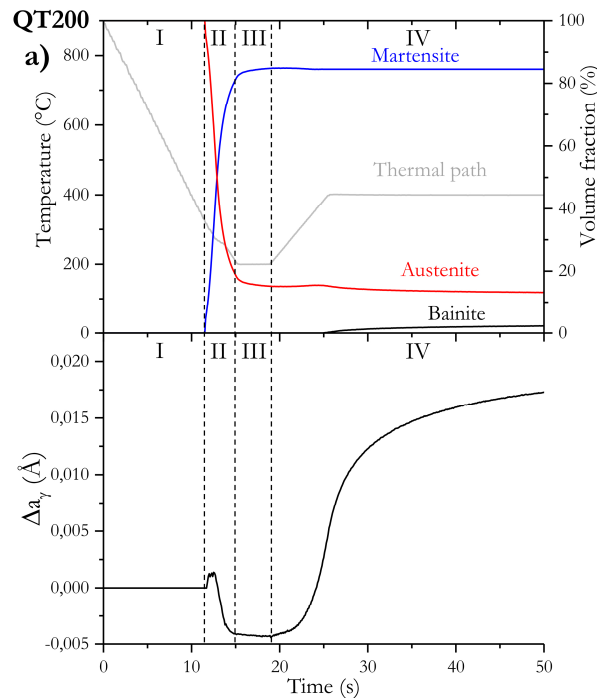
Table III-1 - Bainite starting temperature for the three QT conditions

	Bainite start temperature
QT200	381°C
QT230	369°C
QT260	335°C

III.4.2 Kinetics of carbon enrichment in austenite

III.4.2.1 Evolution of austenite lattice parameter with QT

In order to describe the evolution of the microstructure during the Q&P treatment and in a similar manner than done in section III.3.1 with phase fractions, the evolution of austenite lattice parameter was decomposed into four stages. Figure III-19 a) b) c) present the time evolution of the thermal path, phase volume fractions, change in austenite lattice parameter for the first 50s following the quench from the austenitic domain for the three QT.



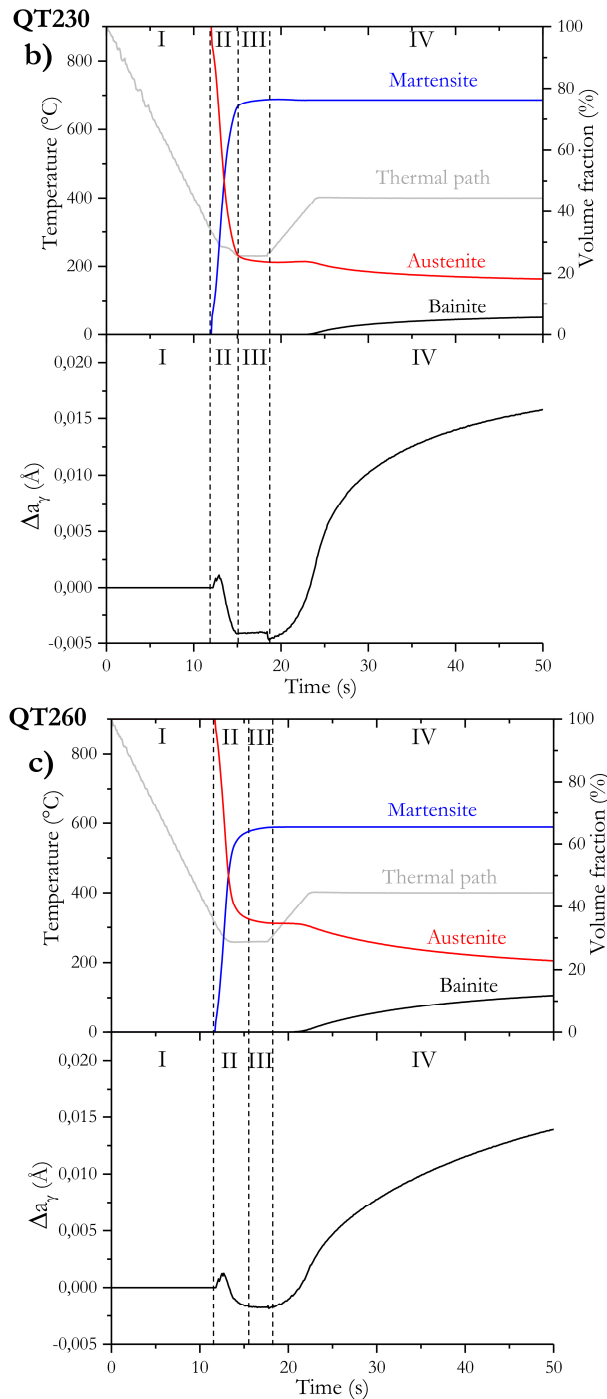


Figure III-19 – Time evolution of the changes in austenite lattice parameter correlated to the changes in phase fractions for a) QT200 b) QT230 and c) QT260.

The four stages of austenite lattice parameter evolution are given below:

- **Stage I: Quenching to Ms**

For the first stage of the evolution of Δa_γ , no change is noticeable. Indeed, this corresponds to the quench from the fully austenitic domain to Ms. No change in phase fraction is observed.

- **Stage II: Martensite formation**

Once Ms is reached and as previously explained, the austenite lattice parameter is subjected to a sequence of tensile and compression state induced by the formation of martensite as shown on Figure III-19 a, b and c.

The critical volume fractions of martensite for the transition of austenite from tensile to

compression state were determined for the three QT. It was measured to be 56, 44 and 52% for QT200, QT230 and QT260, respectively. From a qualitative point of view, these observations agree with the theoretical works of Eshelby for very low volume fraction of martensite, Mori-Tanaka and Scherer for higher volume fractions of martensite when the elastic effects interact [173][174][175]. It is worth noting that both martensite and austenite were assumed to be isotropically elastic, and free boundary conditions were applied (an opposite result could be obtained for constant volume conditions: martensite and austenite would have been under tensile and compression respectively for low volume fraction of martensite). Regarding the critical volume fractions of martensite for the transition from tensile to compression state, it can be expected to depend on elastic properties of phases but also on both the morphologies of phases and the topology of microstructure. Since these elements do not differ significantly with QT, it is thus not surprising that the critical volume fraction for transition does not evolve substantially with QT.

A significant fraction of austenite is transformed into martensite until QT is reached. Finally, the change in austenite lattice parameter induced by martensite (or $\Delta a_{\gamma}(\alpha')$ on Figure III-14) increases as QT lowers. In other words and not surprisingly, a larger martensite fractions induces a larger compression effect on austenite.

- **Stage III: Stagnant stage**

The third stage is defined as a stagnant stage. Indeed, no significant phase fraction evolution occurs during the holding at QT and for the beginning of the reheating step.

- **Stage IV: Increase in austenite lattice parameter**

During this last stage, the austenite lattice parameter undergoes a continuous increase which can be due to both carbon enrichment and relaxation of stresses in austenite. This increase occurs during the reheating step from QT towards PT at 221°C, 255°C and 287°C for respectively QT200, QT230 and QT260. During this stage, bainite starts to form just before reaching PT (cf Table III-1) and continuously develops at the expense of austenite during the whole partitioning step.

Regarding the stage II, the level of stress induced by the martensite can be evaluated. It was shown that for a critical volume fraction of martensite formed, the surrounding austenite is put into compression. For the QT200 condition, at the end of the QT step, the measured austenite lattice parameter is $4.1 \times 10^{-3} \text{ \AA}$, lower than predicted by the stress-free Van Bohemen CTE model. This translates into a relative lattice volume change of -0.34%. By considering that the change in volume results from a hydrostatic pressure of the surrounding martensite, the pressure exerted on austenite can be calculated as [176]:

$$P = B\varepsilon \tag{III.8}$$

$$= \left(\frac{2\mu^{\gamma}(1 + \nu^{\gamma})}{3 \times (1 - 2\nu^{\gamma})} \right) \frac{(V_{\gamma}^{exp} - V_{\gamma}^{calc})}{V_{\gamma}^{calc}}$$

where B is the bulk modulus of austenite (in MPa), ε is the relative deformation (or strain), μ^{γ} is the shear modulus of austenite (MPa), ν^{γ} is the poisson ratio of austenite, V_{γ}^{exp} is the austenite lattice volume measured by HEXRD, V_{γ}^{calc} is the austenite lattice volume calculated with VB model eq.(III.3).

Ghosh and Olson developed a temperature and composition sensitive model to obtain the isotropic shear modulus of austenite and martensite [177]. Accordingly, μ^{γ} is calculated as follow:

$$\mu^{\gamma} = \left[9.2648 + \sum x_j \left(\frac{d\mu}{dx_j} \right) \right] \times [1 - 7.9921 \times 10^{-7}T^2 + 3.317 \times 10^{-10}T^3] \quad (\text{III.9})$$

$$= 74.24 \text{ MPa (at } 200^{\circ}\text{C)}$$

where 9.2648 is the shear modulus of paramagnetic austenite at 0K (in $\times 10^{10}$ N.m⁻²), x_j is the atomic fraction of the alloying element j, $\left(\frac{d\mu}{dx_j} \right)$ is the rate of change of shear modulus with alloying element j concentration, T is the temperature (in K).

The Poisson ratio of austenite is taken as 0.33. Therefore, the pressure calculated with eq.(III.8) into austenite is equal to -658MPa for the QT200 condition. Therefore, before the reheating step, austenite is under a relative important compressive state. Table III-2 presents the calculated stress state of austenite at the end of the QT step for the three QT conditions. As the change in austenite lattice parameter ($\Delta a_{\gamma(\alpha')}$) decreases as the fraction of martensite formed decreases, the pressure on austenite calculated with eq.(III.8) is QT dependent (higher pressure for lowest QT). Comparatively, the value obtained for QT260 seems to be low and may be explained by the total volume fraction of martensite formed. Indeed, only 65.3 % is formed at QT260 while the pressure/compression transition is measured to be 52% at QT260. The difference between these two values is relatively low to have a high level of compression stress in austenite.

Table III-2 - Stress state of austenite calculated after martensite formation for the three QT conditions.

	Internal stresses induced by α' formation
QT200	-658 MPa
QT230	-641 MPa
QT260	-264 MPa

III.4.2.2 Evolution of carbon content in austenite with QT

The increases of the change of austenite lattice parameter (Figure III-19) result from both chemical and mechanical contributions which are very difficult to decouple. To overcome this difficulty, it was proposed in III.3.3 to define two boundaries for the evolution of the change of austenite lattice parameter i. e. for the evolution of carbon content in austenite. They correspond to the following limit cases: no stress relaxation occurs into austenite and internal stresses into austenite are totally and immediately relaxed during reheating and soaking at PT. The carbon evolution is thus expected to evolve within these two boundaries. Following the approach described in III.3.3, the evolutions of carbon content in austenite for the three QT were determined (Figure III-20). The dashed lines correspond to the case where 50% of the internal stresses are relaxed immediately into austenite.

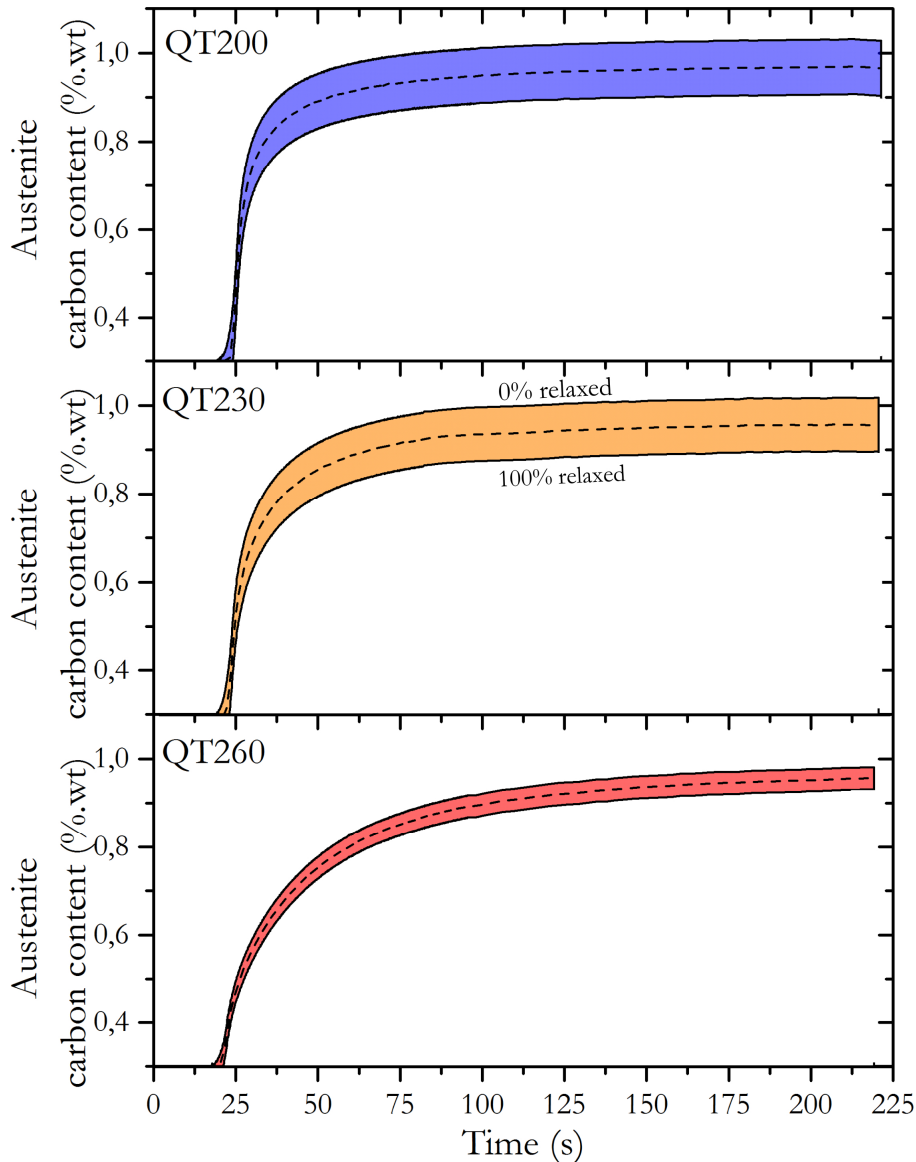


Figure III-20 - Evolution of the austenite carbon content for the three QT. The upper limit and lower limit correspond to two limit cases: no stress relaxation occurs into austenite and internal stresses into austenite are totally and immediately relaxed during reheating and soaking at PT

The first conclusion is that the influence of stress relaxation on the estimated evolution of carbon content into austenite is not very significant. At most, it corresponds to a decrease of carbon content of about 0.10wt% over a total carbon enrichment in austenite of about 0.70wt% for QT200. As expected, the influence of stress relaxation in austenite depends on QT i.e. on the initial volume fraction of martensite at QT. The lowest impact was obtained for QT260 (it is in the order of 0.05wt% over a total carbon enrichment into austenite of about 0.70wt%). The reason for this is simple: the lower the volume fraction of martensite at QT is, the lower the internal stresses into austenite induced by martensite formation are (see Table III-2). It is worth noticing that the lowest boundary for C evolution into austenite is restrictive since, in reality, the internal stresses into austenite cannot be fully relaxed due to the incompatibility of deformation between martensite and austenite. This remains valid if martensite becomes completely carbon depleted because the martensite (ferrite in that case) specific volume is still higher than the one of austenite.

Table III-3 gathers the enrichment start temperature for the 3 QT, that is, the temperature during the reheating from QT to PT where a significant deviation from simple thermal dilatation occurs. For the three QT conditions, the enrichment starts roughly 20°C above QT (221°C, 255°C and 287°C for respectively QT200, QT230, QT260) i.e. after a period of latency nearly identical. The total enrichment and final austenite carbon content are also given.

Table III-3 - Start temperatures of carbon enrichment and final carbon content of austenite for the 3 QT conditions (the two values correspond respectively to 0% and 100% of stresses relaxed)*

	% α' at end of QT	T° start enrichment (*)	Enrichment of austenite during reheating	Enrichment of austenite during partitioning	Total enrichment	%C γ _{FINAL}
QT200	85%	221-353°C	0.23 ± 0.06 wt.%	0.44 ± 0.06 wt.%	0.67 ± 0.06 wt.%	0.97 ± 0.06 wt.%
QT230	76%	255-369°C	0.16 ± 0.07 wt.%	0.50 ± 0.07 wt.%	0.66 ± 0.07 wt.%	0.96 ± 0.07 wt.%
QT260	65%	287-359°C	0.09 ± 0.03 wt.%	0.57 ± 0.03 wt.%	0.66 ± 0.03 wt.%	0.96 ± 0.03 wt.%

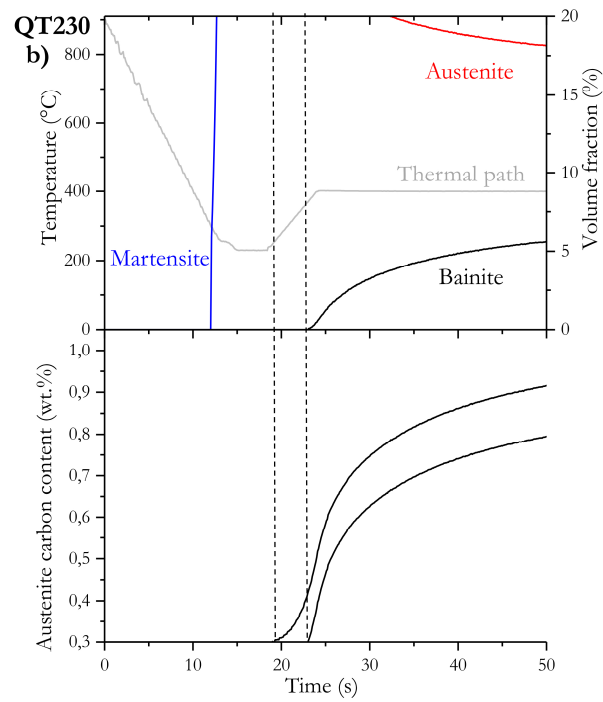
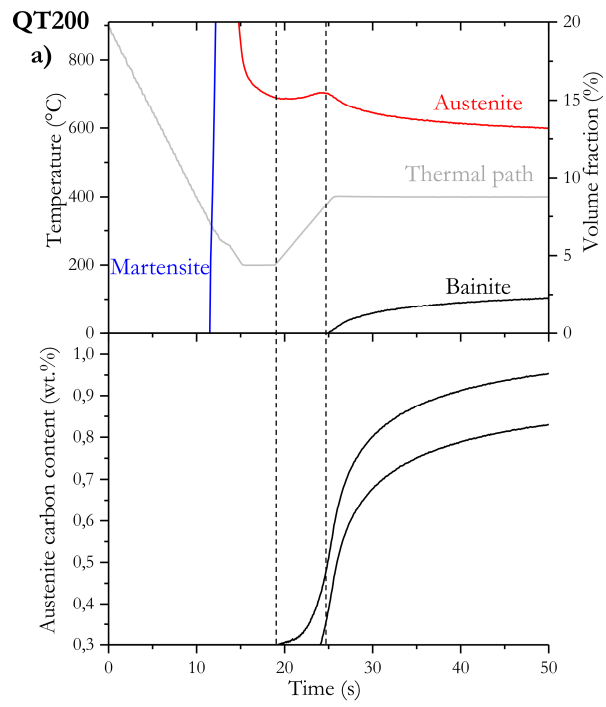
The most significant highlight is that the total carbon enrichment in austenite does not depend on QT. A priori, there is no obvious reasons for such a behavior. For instance, we could expect a higher carbon enrichment in austenite at lower QT since the volume fraction of martensite, and thus the carbon reservoir, are larger. This point of interest will be discussed more deeply in Chapter 4.

III.4.2.3 Origins of the C enrichment in austenite

The change in austenite lattice parameter observed during the reheating and partitioning step was attributed to stress relaxation and carbon enrichment (see Figure III-20). The origins of the carbon enrichment in austenite remain still not very clear. It could be due to carbon partitioning from martensite and/or bainite formation.

Figure III-21 presents the evolution of austenite carbon content and the evolution of phase fractions for the three QT. On Figure III-21 a), i.e. at QT200, a carbon enrichment of austenite was highlighted while bainite transformation has not yet taken place within a certain timeframe during reheating (see dash black box Figure III-21 a)). As a consequence, the increase in carbon content into austenite can be attributed to carbon partitioning from martensite solely. For longer times, it is not possible to decouple the contributions of both partitioning from martensite and bainite formation in the increase of carbon content in austenite from the experimental data. Interestingly, it becomes more and more difficult to decouple these contributions with increasing QT since they increasingly overlap with QT (see Figure III-21 a) and b)). Indeed, the timeframe where only carbon partitioning operates decreases with QT.

In the most favorable case i.e. at QT 200 and at 0% of stress relaxed into austenite, the contribution of partitioning into the carbon enrichment in austenite represents approximately at least 30% of the maximum. In view of the above data, and as expected, this contribution decreases with increasing QT.



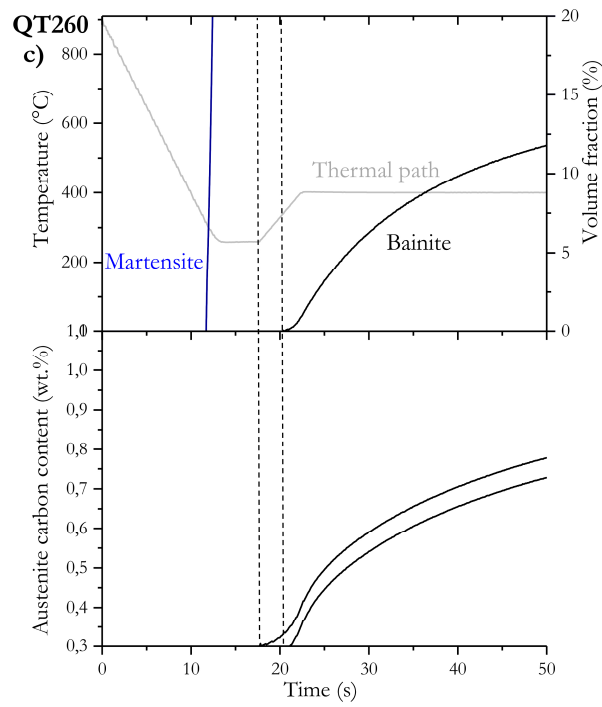


Figure III-21 – Kinetics of austenite carbon enrichment and evolution of the phase fractions during $Q\&P$ process for a) QT200, b) QT230 and c) QT260.

III.5 Partial conclusion

The use of in-situ High Energy X-Ray Diffraction allowed us to have access to ultra-fast time-resolved quantitative information on the quenching and partitioning process. Three Q&P treatment with different QT (200, 230 and 260°C) were studied. From a general manner, the evolution of phase transformations can be decomposed into four main stages:

- (1) a quenching from the fully austenitic domain (900°C) to a temperature that corresponds to Ms during which no phase transformation occurs,
- (2) a temperature decrease from Ms to QT during which a significant increase in martensite at the expense of austenite occurs. The rate of this transformation is very fast in the first stages and becomes more sluggish at the final stage. The final volume fractions of martensite were measured and were shown to depend on QT (85% at QT200, 76% at QT230 and 65% at QT260),
- (3) a stagnant stage during reheating from 230°C to a given temperature in which the microstructural state remains globally unchanged,
- (4) a significant and slow increase in a new-BCT phase fraction at the expense of austenite occurs during both reheating and the partitioning step. This new-BCT phase was analyzed as bainite. The transformation rate, which is a better indicator than the intrinsic volume fraction of bainite, was shown to decrease with decreasing QT, from 45% at QT=260°C to 20% at QT=200°C. For the three QT studied, the major part of bainite is formed within a very short time: 75% of bainite is formed within 28.2s, 24.6 and 30s for respectively QT200, QT230 and QT260.

The analysis of the austenite lattice parameter evolution was made difficult since it is the result of thermal, chemical and mechanical contributions. A theoretical attempt was made to decouple all these contributions and the internal stresses into austenite at QT were determined. A significant result is that austenite is subjected to a sequence of tensile and compression induced by the formation of martensite. The critical volume fractions of martensite for the transition of austenite from pressure to compression state were determined for the three QT. It was measured to be 56, 44 and 52% for QT200, QT230 and QT260, respectively. From a qualitative point of view, these observations agree with the theoretical works available in the literature.

Furthermore, it was shown that any change in austenite lattice parameter after QT can be attributed either to a carbon enrichment of austenite or a stress relaxation phenomenon in austenite, or both. However, all these mechanical contributions to the austenite lattice parameter variation are very difficult to be decoupled. In order to overcome this difficulty, it was proposed to define two boundaries for C evolution by considering two limit cases. The first is to suppose that no stress relaxation occurs during reheating and soaking at PT. In other words, the stress relaxation phenomena are neglected and all the increase in a_γ occurring after QT was assigned to the chemical contribution; the latter being thus overestimated in that case. The second is to suppose that internal stresses in austenite are immediately and totally relaxed. Following this approach, the evolutions of carbon content into austenite for the three QT were determined. The first conclusion is that the influence of stress relaxation on the evolution of carbon content into austenite is not very significant. As expected, the influence of stress relaxation into austenite depends on QT i.e. on the initial volume fraction of martensite at QT. The reason for this is simple: lower the volume fraction of martensite at QT is, lower the internal stresses into austenite induced by martensite formation are. In this part, the most significant highlights are that the total carbon enrichment into austenite does not depend on QT and that the increase of carbon content into austenite results from both carbon partitioning and bainite contributions which appears difficult to be decoupled from an experimental point of view.

Chapter IV : EFFECTS OF COMPETITIVE REACTIONS ON C ENRICHMENT IN AUSTENITE DURING QUENCHING AND PARTITIONING AT 400°C

Table of contents

IV.1 INDIVIDUAL KINETICS MODELS	137
IV.1.1 CARBON PARTITIONING FROM MARTENSITE TO AUSTENITE	137
<i>IV.1.1.1 General equations</i>	<i>137</i>
<i>IV.1.1.2 Numerical method</i>	<i>138</i>
IV.1.2 CARBIDE PRECIPITATION IN MARTENSITE	139
<i>IV.1.2.1 Nucleation rate</i>	<i>139</i>
<i>IV.1.2.2 Growth rate</i>	<i>139</i>
IV.1.3 BAINITE TRANSFORMATION	140
<i>IV.1.3.1 Nucleation of bainite</i>	<i>141</i>
<i>IV.1.3.2 Growth process</i>	<i>141</i>
IV.2 THERMODYNAMICS ASPECTS, REPRESENTATIVE VOLUME ELEMENT AND MODEL COUPLING	142
IV.2.1 DETERMINATION OF THE CHEMICAL POTENTIALS	142
IV.2.2 REPRESENTATIVE VOLUME ELEMENT	143
IV.2.3 COUPLING	144
IV.3 RESULTS AND DISCUSSIONS	145
IV.3.1 KINETICS OF PHYSICAL PHENOMENA	145
IV.3.2 CARBON ENRICHMENT IN AUSTENITE	149
IV.3.3 CRITICAL CARBON CONTENT INTO AUSTENITE AT THE END OF PARTITIONING STEP	152
IV.3.4 AVENUES FOR INCREASING C ENRICHMENT IN AUSTENITE	154
IV.3.5 COMPLEMENTARY INVESTIGATION: MN PARTITIONING AT THE α'/γ INTERFACE	155
IV.4 PARTIAL CONCLUSION	160

The benefits of Quenching & Partitioning depends strongly on the austenite stability, and thus on level carbon enrichment in austenite during the partitioning step at 400°C. In the previous part, it was demonstrated that the latter results from both bainite transformation and carbon rejection from martensite. It was also highlighted that carbide precipitation and carbon segregation on defects take place in martensite even if the alloy studied contains a relatively high amount of silicon. As a consequence, the potential of carbon enrichment is expected to be strongly reduced since a large part of carbon is trapped into martensite. In general, our experimental data show unambiguously that the total carbon enrichment in austenite is lower than both the value predicted under the CCE conditions and the carbon level in retained austenite of TRIP-assisted steels. Taking into consideration the experimental errors, the measured maximum carbon enrichment was surprisingly shown to be independent on the quenching temperature (QT), i.e, on initial volume fraction of martensite. This is even more counterintuitive that the respective contribution of bainite transformation and carbon partitioning from martensite itself should both depend on QT. It is thus clear that a better view of how the competitive reactions affect the carbon enrichment in austenite during the Q&P process is necessary, as it strongly influences the final properties of the material.

IV.1 Individual kinetics models

IV.1.1 Carbon partitioning from martensite to austenite

IV.1.1.1 General equations

In order to describe carbon partitioning process, a Constrained Carbon Equilibrium (CCE) model was proposed [7][110][111]. It relies on the two main following hypotheses: the mobility of iron and substitutional elements is neglected, the α' -martensite/ γ -austenite interface is immobile or stationary. In that case, only carbon equilibrates its chemical potential and the time-evolution of the carbon profile in both α' and γ can be calculated from the Fick's laws, and the appropriate mass balance at the α'/γ interface, which takes into account the assumption of a stationary interface:

$$\begin{cases} \frac{\partial X_C^{\alpha'}}{\partial t} = -D_C^{\alpha'} \Delta X_C^{\alpha'} & (a) \\ \frac{\partial X_C^{\gamma}}{\partial t} = -D_C^{\gamma} \nabla X_C^{\gamma} & (b) \\ -D_C^{\alpha'} \nabla X_C^{\alpha'} = -D_C^{\gamma} \nabla X_C^{\gamma} & (c) \end{cases} \quad (IV.1)$$

where Δ and ∇ are respectively the Laplace operator and the divergence operator, γ and α' represent austenite and martensite respectively, $D_C^{\alpha'}$ and D_C^{γ} are, respectively, the effective diffusion coefficients of carbon in austenite and in martensite.

Regarding the contact conditions, a local equilibrium for C is supposed at the α'/γ interface while the substitutional elements such as Mn and Si are supposed to be uniformly distributed through the immobile interface. This implies that the interfacial chemical potential of carbon has to vary continuously during the diffusion process in order to maintain mass balance. At any time, the carbon concentrations on both sides of the α'/γ interface, $X_C^{\alpha'/\gamma}$ and $X_C^{\gamma/\alpha'}$, were determined from the following relation:

$$\mu_C^{\alpha'}(X_C^{\alpha'/\gamma}, u_{Mn}^0, u_{Si}^0) = \mu_C^{\gamma}(X_C^{\gamma/\alpha'}, u_{Mn}^0, u_{Si}^0) \quad (IV.2)$$

where u_{Mn}^0 and u_{Si}^0 are the nominal u-fractions of Mn and Si. The sub-lattice models were used to derivate the chemical potentials of carbon in both phases γ and α' . For the sake of simplicity, the thermodynamic properties of martensite were assimilated to those of ferrite. We invite the reader to refer to section IV.2 for more details.

IV.1.1.2 Numerical method

In order to solve the differential equations (IV.1) a) and (IV.1) b) for mass conservation in the transient regime and in one dimension, the finite volume method was employed [178]. The equations of diffusion (IV.1) a) and (IV.1) b) were integrated over both a control volume (Figure IV-1) and a time interval from t to $t+\Delta t$. For instance, equations (IV.1) a) and (IV.2) a) lead to the following relations:

$$\int_w^e \int_t^{t+\Delta t} \frac{\partial X_C^\varphi}{\partial t} dt dx = \int_t^{t+\Delta t} \int_w^e \frac{\partial}{\partial x} \left(D_C^\varphi \frac{\partial X_C^\varphi}{\partial x} \right) dx dt$$

and,

$$\int_w^e \left[(X_C^\varphi)_{t+\Delta t} - (X_C^\varphi)_t \right] dx = \int_t^{t+\Delta t} \left[D_C^\varphi \frac{(X_C^\varphi)_E - (X_C^\varphi)_P}{\Delta x} - D_C^\varphi \frac{(X_C^\varphi)_P - (X_C^\varphi)_W}{\Delta x} \right] dt$$

with an implicit scheme, it is found that :

$$\left[(X_C^\varphi)_P^{t+\Delta t} - (X_C^\varphi)_P^{t+\Delta t} \right] \frac{\Delta x}{\Delta t} = \frac{D_C^\varphi}{\Delta x} \left[(X_C^\varphi)_E^{t+\Delta t} - 2(X_C^\varphi)_P^{t+\Delta t} + (X_C^\varphi)_W^{t+\Delta t} \right]$$

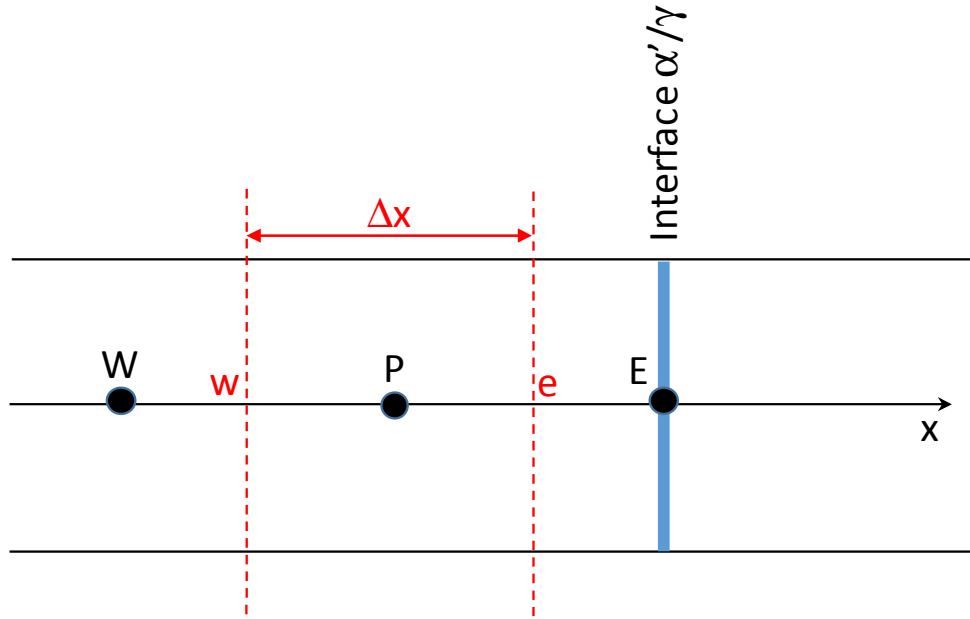


Figure IV-1 - Control volume at the martensite/austenite interface. The control volume is centered on the grid point P, which has the grid point E and W as its neighbors (E denotes the positive x direction and W the negative x direction). e and w denote the location of the limits of the control volume.

A set of n -coupled ordinary differential equations is applied to finite volume obtained by dividing the space and time axes into n and T cells of dimensions Δx and Δt . At each point of the grid, the concentration is determined by the following equation:

$$[A]_n \{C\} = \{b\}$$

where $[A]_n$ is a tridiagonal matrix and $\{b\}$ a column matrix whose coefficients are given in [179]. This equation was solved using the TriDiagonal Matrix Algorithm (TDMA) [178].

IV.1.2 Carbide precipitation in martensite

It was shown that a tempering process takes place in martensite during quenching and partitioning at PT=400°C. The formation of Fe_{2.4}C occurs very early in the thermal treatment (at QT) and continues at PT=400°C. According to the observations, carbides nucleate uniformly throughout the martensite matrix, and the kinetics of formation seems to be relatively fast. The model proposed here aims to describe the precipitation process from the supersaturated solid solution (martensite) for isothermal conditions (at PT) and, more particularly, the evolution of volume fraction of carbides with time. For sake of simplicity, only the nucleation and growth steps were considered. The coarsening process, which is neglected here, is expected to not affect significantly the volume fraction of carbides since it is expected to occur close to the equilibrium state.

The main assumptions of the model are: the supersaturated martensite is a dilute solid solution, local equilibrium holds at the precipitate/matrix interface, a Laplacian concentration field is assumed around the precipitates, carbides have a spherical shape and, finally, the elastic effects are neglected.

IV.1.2.1 Nucleation rate

The model proposed is based on the approach of Deschamps and Bréchet in which the nucleation and growth steps are coupled [180].

On the basis of the classic nucleation theory and by neglecting the incubation time, the nucleation rate can be expressed as [181]:

$$\frac{dN}{dt} = (N_{tot} - N_{act})Z\beta \exp\left(-\frac{\Delta G^*}{kT}\right) \quad (IV.3)$$

where N_{tot} is the total number of nucleation sites per unit volume, N_{act} is the number of nuclei formed, k is the Boltzmann's constant and T is the absolute temperature. Z is the Zeldovitch factor and β is the attachment rate of the atoms surrounding the critical nucleus. The product of Z and β can be obtained by the following approximation:

$$Z\beta = \frac{D_C^{\alpha'} X_C^{\alpha'}}{a^2}$$

where $D_C^{\alpha'}$ and $X_C^{\alpha'}$ are the diffusion coefficient and the carbon molar solute fraction in the matrix respectively and a the lattice parameter of the matrix taken equal to that one of ferrite.

For spherical precipitates, the critical nucleus radius R^* and the energy barrier ΔG^* can be calculated by the classical following equations [180]:

$$R^* = \frac{-2\sigma}{\Delta G_v}$$

$$\Delta G^* = \frac{16\pi\sigma^3}{3(\Delta G_v)^2}$$

where σ is the interfacial energy which is supposed to be isotropic, ΔG_v is the nucleation driving force. For both a binary Fe-C and a dilute solution, the nucleation driving force can be written:

$$\Delta G_v = \frac{RT}{V_p} \left[X_C^p \ln\left(\frac{X_C^e}{\overline{X_C^{\alpha'}}}\right) + (1 - X_C^p) \ln\left(\frac{1 - X_C^e}{1 - \overline{X_C^{\alpha'}}}\right) \right] \quad (IV.4)$$

where V_p is the molar volume of precipitates, R is the perfect gas constant, X_C^p is the carbon molar fraction in the precipitates, $\overline{X_C^{\alpha'}}$ is the average carbon molar fraction in the matrix, and X_C^e is the equilibrium carbon molar fraction at the precipitate/matrix interface.

IV.1.2.2 Growth rate

The growth of carbides was described by the steady-state Zener equation, assuming that the solute flux is proportional to the gradient of the solute mole fraction. Considering the Gibbs-Thomson effect, the average growth rate can be expressed as [180] [182]:

$$\frac{dR}{dt} = \frac{D_C^{\alpha'}}{R} \left[\frac{\bar{X}_C^{\alpha'} - X_C^e \exp\left(\frac{2\sigma V_p}{R_g T R}\right)}{X_C^p - X_C^e \exp\left(\frac{2\sigma V_p}{R_g T R}\right)} \right] + \frac{1}{N} \frac{dN}{dt} (\alpha R^* - R) \quad (IV.5)$$

The first term in equation (IV.5) corresponds to the growth of existing carbides and the second term to the appearance of the new nuclei. The numerical factor α , equal to 1.03, takes into account the fact that new carbides only grow if their size is slightly larger than the critical radius.

One point that should be emphasised is that the mean composition in the matrix $\bar{X}_C^{\alpha'}$ cannot be obtained by a simple mass balance in martensite since simultaneous carbon rejection from martensite into austenite is highly likely. It is similar to considering that carbides precipitation into martensite occurs in an open system. This issue is returned to below.

At any time, the volume fraction of precipitates f_v^p was calculated using the following simple equation:

$$f_v^p = \frac{4}{3} \pi N(t) R(t)^3 \quad (IV.6)$$

IV.1.3 Bainite transformation

Our observations show clearly that a new BCT phase, identified as bainite, was formed during reheating and close to Ms temperature. This situation is common even if isothermal transformation below and just above the Ms temperature during reheating was reported for a long time [176][183][184][185][186][187]. The nature of the transformation product and the transformation mechanism of bainite transformation are still widely debated in literature [188][189][190][191][192]. There are two schools of thought. According to the first, bainite growth is considered to be displacive and/or diffusionless and the overall kinetics is mainly controlled by the nucleation rate. The bainite laths grow to a limited size and the further progress of the transformation requires the nucleation of new laths. The excess carbon into ferritic bainite is thus expected to partition into the residual austenite or precipitate as cementite. In that case, the mechanism of bainite nucleation is consistent with that of isothermal martensite and, as a result, the activation energy for nucleation is taken as a linear function of the chemical Gibbs energy changed for the nucleus formation [121][193][194]. According to the second, bainite growth is considered to be diffusive. The classical theory for ferrite nucleation is commonly used. The energy barrier for bainite nucleation is considered to be inversely proportional to the square of the driving force for nucleation and the growth is mainly controlled by carbon diffusion in both bainite and austenite [195][196]. The arguments used to confirm or overturn any mechanisms should be put into perspective. For instance, the displacive mechanism which is peculiar to the crystallographic transformation of the FCC lattice into the BCC lattice does not necessarily rule out the diffusion of carbon during bainite transformation. In the same way and contrary to what is often alleged, the fact that the nucleation rate of bainitic ferrite decreases with temperature does not constitute formal proof of its diffusive nature. The works of Van Bohemen and Bhadeshia based on the displacive approach show clearly that the nucleation rate of bainite can decrease below a critical temperature T_h [121][197]. It is logical since their approaches are mainly based on the models developed for isothermal martensite. In this particular case, the seminal works of Kurjumov and Maskimova, Magee, and Mihajlovic give some complementary clarifications [194][198][199]. Their works confirm a potential decrease of both kinetics of transformation and nucleation rate below a critical temperature. The reason for this is that the activation energy for isothermal nucleation is linearly related to the transformation free energy change. This evolution can be interpreted in terms of rate-control by interfacial dislocations motion. As the transformation free energy change is also expected to depend on temperature, a C-curve kinetic behaviour such as diffusion-controlled transformation can be obtained. In other words, the decrease of the nucleation rate with temperature is not a sufficient criterion to discriminate both the diffusive and displacive approaches for bainite formation. Anyway, based

on their own assumptions, both schools have proposed different models that predict satisfactory the bainite transformation kinetics [121][195][196][200].

The aim of this work is actually not to enter this controversy but to develop a model able to describe the time-evolution of bainite formation at a given temperature. Our model that couples both the diffusive and diffusionless approaches draws upon the work of Azuma et al. [201]. The precipitation of carbides in both bainite and austenite was neglected since the alloy studied contain a relatively high amount of silicon that prevents any formation of carbides in both phases.

IV.1.3.1 Nucleation of bainite

The first stage consists in nucleation of laths of bainite in the form of arrays of sub-units. It is assumed that nucleation occurs by both carbon diffusion and autocatalysis phenomenon. According to [202], the nucleation rate I_B is then given by :

$$I_B = \frac{dN_B}{dt} = (1 + \beta f_B) I_0 \quad (IV.7)$$

where β is the autocatalysis constant, f_B is the volume fraction of bainite formed. The initial nucleation rate I_0 can be calculated by drawing upon the classic nucleation theory [201]:

$$I_0 = N_0 \frac{k_B T}{h} \exp\left(-\frac{Q_C^Y}{RT}\right) \exp\left(-\frac{\Delta G_B^*}{RT}\right) \quad (IV.8)$$

where N_0 is the number density of potential nucleation sites that should physically depend on the effective nucleation area of the austenite grain boundary per unit volume i. e. on the prior austenite grain size after martensite formation and thus on QT. k_B and h are Boltzmann and Planck constants respectively, T is the absolute temperature in K, Q_C^Y is the activation energy for carbon diffusion in austenite and ΔG_B^* is the energy activation for bainite nucleation which is supposed to depend on the critical nucleation energy for ferrite as:

$$\Delta G_B^* = \frac{9}{4} \pi \frac{\sigma_F^3}{(\Delta G_m^B)^2} = \frac{4(4\eta + 2)}{27\eta^2} \frac{\sigma_F^3}{(\Delta G_v^\alpha - G_N)^2} \quad (IV.9)$$

where ΔG_v^α is the driving force for ferrite nucleation under paraequilibrium conditions, σ_F is the interfacial energy per unit area, η is the aspect ratio of bainite, the term $\frac{4(4\eta+2)}{27\eta^2}$ reflects the fact that the nuclei have a parallelepiped shape with a square cross-section and G_N is the so-called *universal nucleation function* [121]. It infers that the driving force for nucleation needs to exceed a certain value to allow the growth of the nucleus. This quantity that can also be seen as the minimum driving force necessary to achieve a perceptible nucleation rate for bainite, depends on temperature as follow:

$$G_N = 3.637(T - T_0) - 2540 \quad (IV.10)$$

where $T_0 = 273K$

IV.1.3.2 Growth process

In the approach used, the growth process is, by nature, diffusionless and thus controlled by the nucleation process.

The time-evolution of bainite volume V_B can be described from the following equation:

$$\frac{dV_B}{dt} = V_B(t) I_B + \frac{dV_B}{dt} N_B(t) \quad (IV.11)$$

where $V_B(t)$ and $N_B(t)$ are the volume and the number density of bainite at a given time and I_B is the nucleation rate of bainite.

The number density of bainite, $N_B(t)$, was obtained directly from the integration of the nucleation rate I_B . To be as rigorous as possible, the volume of bainite $V_B(t)$ is an unknown quantity that should be calculated by a 3D model. For sake of simplicity, the thickness of bainite sub-unit W_B which is formed at a given time was estimated using the neural network model proposed by Singh and Bhadeshia [203]. It was shown to depend on the yield strength of austenite σ_γ , the transformation temperature T , and the chemical free energy change (driving force) for nucleation ΔG_m^B as :

$$W_B(\mu m) = a + b \times T_r(K) + c \times V_m^B(m^3 \cdot mol^{-1}) \times \Delta G_m^B(J \cdot m^{-3}) - d \times \sigma_\gamma(MPa) \quad (IV.12)$$

where a, b, c and d are constants taken equal to 0.478, 1.2×10^{-4} , 1.25×10^{-4} and 2.2×10^{-3} respectively [201] and $T_r = (T - 298)$, and V_m^B is the molar volume of bainite.

The strength of austenite, that depends on both temperature and composition, is expressed as follows [204]:

$$\sigma_\gamma = (1 - 0.26 \times 10^{-2}T_r + 0.47 \times 10^{-5}(T_r)^2 - 0.326 \times 10^{-8} \times (T_r)^3 \times 15.4(4.4 + 23w_C + 1.3w_{Si} + 0.65 w_{Mn}) \quad (IV.13)$$

where w_i are the austenite compositions in weight %.

It appears that stronger austenite and/or larger driving force result in finer bainite, the former because there is a larger resistance to interface motion and the latter because an increased nucleation rate leads to microstructural refinement.

Each bainite sub-unit is assumed to have a parallelepipedic shape with a square cross-section equal to $(W_B)^2$ and a length equal to ηW_B , η being the aspect ratio of bainite sub-units. The aspect ratio was measured to be 6 by Azuma and mainly between 4 and 40 by Wang et al. [205]. If the aspect ratio is kept unchanged, the extended volume fraction of bainite $f_B^e(t)$ can be written as:

$$f_B^e(t) = N_B(t)\eta(W_B(t))^3 \quad (IV.14)$$

It is worth noting that the volume of bainite $V_B(t)$ is expected to evolve with time since it depends on both the driving force for nucleation and the carbon content into austenite.

A method based on Avrami's extended volume correction was used to account for impingement of developing sub-units [206]. The total volume fraction of bainite in the microstructure is thus given by:

$$f_B(t) = f_M^0(1 - \exp(-f_B^e(t))) \quad (IV.15)$$

IV.2 Thermodynamics aspects, representative volume element and model coupling

IV.2.1 Determination of the chemical potentials

Both α -BCC and γ -FCC were described with a two sub-lattice model $(Fe, Mn, Si)_a(C, Va)_b$. For the γ phase, $a = b = 1$, and for the α phase, $a = 1$, $b=3$. The elements Fe, Mn and Si can substitute to each other on the metal sub-lattice and carbon, and vacancies on the interstitial sub-lattice. The free energy of the ϕ - $(Fe, Mn, Si)_a(C, Va)_b$ phase can be expressed as [207][208]:

$$G_m^\phi = \sum_{i=Fe, Mn, Si} y_i y_C G_{i:C}^\phi + \sum_{i=Fe, Mn, Si} y_i y_{Va} G_{i:Va}^\phi + RT \left(a \sum_{i=Fe, Mn, Si} y_i \ln y_i + b \sum_{i=C, Va} y_i \ln y_i \right) + {}^E G_m^\phi + {}^{magn} G_m^\phi \quad (IV.16)$$

The symbols y_i represent mole fractions evaluated for each sub-lattice separately and can be determined from atomic fractions [209]. $G_{i:Va}^\phi$ is the Gibbs energy of component i in an hypothetical nonmagnetic state and $G_{i:C}^\phi$ is the Gibbs energy of a hypothetical state where all the sites are filled with carbon. ${}^E G_m^\phi$ is the non magnetic excess term that depends on several

interaction terms [209]. All the data used for calculations can be found in [210][211][212][213][214].

The chemical potentials of substitutional elements S (S=Mn, Si) and C can thus be derived from the following relations according to [209][215]:

$$\begin{cases} \mu_S^\varphi = G_m^\varphi + \frac{\partial G_m^\varphi}{\partial y_S} + \frac{\partial G_m^\varphi}{\partial y_{Va}} - \sum_{i=Fe, Mn, Si, C, Va} y_i \frac{\partial G_m^\varphi}{\partial y_i} \\ \mu_C^\varphi = \frac{\partial G_m^\varphi}{\partial y_C} - \frac{\partial G_m^\varphi}{\partial y_{Va}} \end{cases} \quad (IV.17)$$

The contact conditions that apply at the α'/γ interface during carbon partitioning can be determined from equation (IV.2). A routine was developed in order to determine the operative tie-line, i.e. the carbon concentrations on both sides of the α'/γ interface ($X_C^{\alpha'/\gamma}$ and $X_C^{\gamma/\alpha'}$) that fulfil equation (IV.2). It is worth noting that the condition (IV.2) is equivalent to a paraequilibrium condition. However, at a given temperature, $X_C^{\alpha'/\gamma}$ and $X_C^{\gamma/\alpha'}$ are expected to evolve with time, to maintain the mass balance at the immobile interface. Therefore, and contrary to the classical paraequilibrium condition, the operative tie-line is time dependent and cannot be determined simply based upon thermodynamic considerations. Also, it is supposed that the substitutional elements do not equilibrate their chemical potentials during carbon rejection from martensite.

IV.2.2 Representative volume element

One-dimensional systems including α' -martensite, γ -austenite and α_B -bainite in cartesian coordinates were used for modelling. According to the microstructural features, the representative volume element (RVE) for calculation is a cell that consists of martensite, austenite and bainite from right to left as shown in Figure IV-2. The characteristic length L_0 was taken equal to the half-distance between austenite films at the beginning of the partitioning step. This length was estimated to be roughly 1 μm . The size of martensite L_M , austenite L_G and bainite L_B was determined from the volume fraction of phases as :

$$f_M = \frac{L_M}{L_0}; f_\gamma = \frac{L_G}{L_0}; f_B = \frac{L_B}{L_0}$$

Both, the kinetics of carbon partitioning and bainite formation were calculated by considering the RVE and by stating that the polycrystalline sample follows the same overall kinetics. Regarding the carbide precipitation into martensite, the RVE has an indirect effect since it affects the average carbon molar fraction in martensite $\bar{X}_C^{\alpha'}$.

It is worth noting that martensite will behave as a carbon reservoir; a part of carbon will be rejected into austenite and a part of carbon will be trapped into martensite as precipitates or in solid solution.

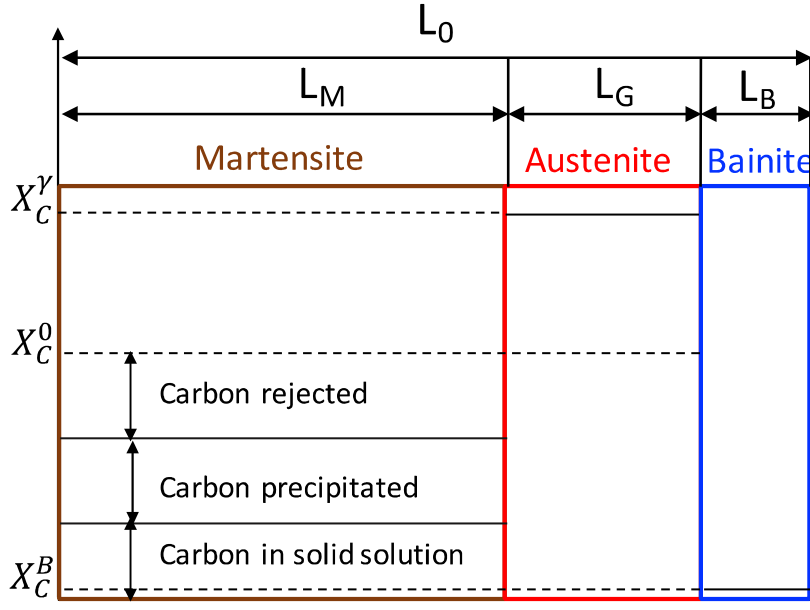


Figure IV-2 - Representative volume element. L_0 is the characteristic length, L_M , L_G and L_B are the size of martensite, austenite and bainite respectively. X_C^0 , X_C^Y and X_C^B are the nominal carbon content, the carbon content in austenite and bainite respectively.

IV.2.3 Coupling

At each time step, the method of calculation is divided into six parts:

1. calculation of carbon partitioning from martensite to austenite. A carbon profile is thus established in both martensite and austenite,
2. an homogenization step to determine the average carbon composition remaining in solid solution in both martensite and austenite,
3. calculation of carbide precipitation state in martensite,
4. carbon mass balance in martensite to determine the remaining carbon content in solid solution in this phase,
5. calculation of bainite formation by considering the average value of carbon content into austenite,
6. carbon mass balance in austenite.

At last, the coupling between carbon partitioning, carbide precipitation and bainite formation is made through the following carbon mass balance in austenite:

$$X_C^0 + \bar{X}_C^R \frac{f_M^0}{f_Y^0} = X_C^Y \frac{f_Y^0}{f_Y^0} + X_C^B \frac{f_B^0}{f_Y^0}$$

where f_M^0 and f_Y^0 are the initial volume fractions (i.e fractions at QT) of martensite and austenite respectively.

If it is assumed that the carbon content in bainite X_C^B is relatively small, the carbon into austenite is given by:

$$X_C^Y = X_C^0 \frac{f_Y^0}{(f_Y^0 - f_B)} + \bar{X}_C^R \frac{f_M^0}{(f_Y^0 - f_B)} \quad (IV.18)$$

The increase of carbon content in austenite depends on the carbon rejected from martensite into austenite \bar{X}_C^R , which, in-turn, is affected by the carbide precipitation process in martensite. For instance, one can imagine a situation where the precipitation process is very fast with respect to carbon partitioning from martensite. In that particular case, the carbon rejected from martensite \bar{X}_C^R is expected to be reduced. In the opposite case, \bar{X}_C^R is expected to be much larger. It is important to note that the contribution of both carbon rejection from martensite and bainite

formation in the increase of carbon content into austenite cannot be obtained directly from equation (IV.18). In order to decouple both, one can define the contribution of carbon rejected from martensite as the total number of carbon atoms rejected from martensite into the initial volume of austenite, i.e. in the absence of any formation of bainite. Accordingly, this contribution does not correspond to the quantity $\bar{X}_C^R \frac{f_M^0}{(f_Y^0 - f_B)}$ in the equation (IV.18) but to the following one:

$$\Delta X_C^{R,\gamma} = \bar{X}_C^R \frac{f_M^0}{f_Y^0} \quad (IV.19)$$

All of which concurs to the reduction of austenite volume corresponds to the bainite contribution. The latter can thus be obtained simply by:

$$\Delta X_C^{B,\gamma} = X_C^\gamma - X_C^0 - \bar{X}_C^R \frac{f_M^0}{f_Y^0} = f_B \left[\frac{X_C^0}{f_Y^0 - f_B} + \frac{f_M^0 \bar{X}_C^R}{f_Y^0 (f_Y^0 - f_B)} \right] \quad (IV.20)$$

Last, but not least, the following global carbon mass balance throughout the system is verified at each time step:

$$\begin{cases} X_C^0 = X_C^{\alpha'} f_M^0 + X_C^p f_p + X_C^\gamma (f_Y^0 - f_B) \\ f_M^0 + f_p + f_Y + f_B = 1 \end{cases}$$

IV.3 Results and discussions

IV.3.1 Kinetics of physical phenomena

The data used for calculations are given in Table IV-1:

Table IV-1- Data used for calculations

$D_C^{\alpha'} = 4 \times 10^{-8} \exp\left(\frac{-84100}{RT}\right)$	Carbon diffusivity in martensite ($\text{m}^2 \cdot \text{s}^{-1}$)	This work
$D_C^\gamma = 1.23 \times 10^{-6} \exp\left(\frac{-125532}{RT}\right)$	Carbon diffusivity in austenite ($\text{m}^2 \cdot \text{s}^{-1}$)	[216]
$N_{tot} = 10^{29}$	Total number of nucleation sites per unit volume ($/\text{m}^3$)	This work
$a = 2.886 \times 10^{-10}$	Lattice parameter of ferrite (m)	
$\sigma = 0.205$	Carbide/matrix interfacial energy (J/m^2)	This work
$V_p = 1.75 \times 10^{-5}$	Molar volume of carbides (m^3/mole)	[217]
$X_C^p = 0.30$	Carbon molar fraction in the carbides	This work
$X_C^e = 0.026 \exp\left(\frac{-28424}{RT}\right)$	Equilibrium carbon molar fraction at the carbide/matrix interface	[218]
$\beta = 400$	Autocatalysis constant	[202]
$\sigma_F = 5.5570 \times 10^{-2}$	Bainite/austenite interfacial energy (J/m^2)	This work

$N_0 = \begin{cases} 1.5 \times 10^{16} \text{ at } QT = 200^\circ\text{C} \\ 1.25 \times 10^{16} \text{ at } QT = 230^\circ\text{C} \\ 4 \times 10^{15} \text{ at } QT = 260^\circ\text{C} \end{cases}$	number density of potential nucleation sites in austenite	This work
$V_m^B = 7.02 \times 10^{-6}$	Molar volume of bainite (m ³ /mole)	
$\eta = 4$	Aspect ratio of bainite sub-units	This work

Figure IV-3 shows that the model developed describes very well both the measured kinetics of bainite transformation and carbon enrichment in austenite at PT=400°C and for the three QT considered (QT=260, 230 and 200°C).

It is clearly shown that kinetics of carbon enrichment into austenite is all the more rapid that QT is low, i.e. the initial volume fraction of martensite is higher. The relative contribution of both bainite transformation and partitioning from martensite in the increase of carbon content into austenite are given in Figure IV-3 d, e and f. The partitioning contribution becomes larger with decreasing QT. It goes from 28% at QT=260°C to 69% at QT=200°C. Such a behaviour can be explained from the interaction between carbon rejected from martensite and bainite transformation. Both the amount and carbon rejection rate are higher with decreasing QT since the carbon reservoir (i.e martensite) is more important and austenite islands size are smaller. This has the effect to impede bainite formation and explain why the kinetics of carbon enrichment is faster at lower QT.

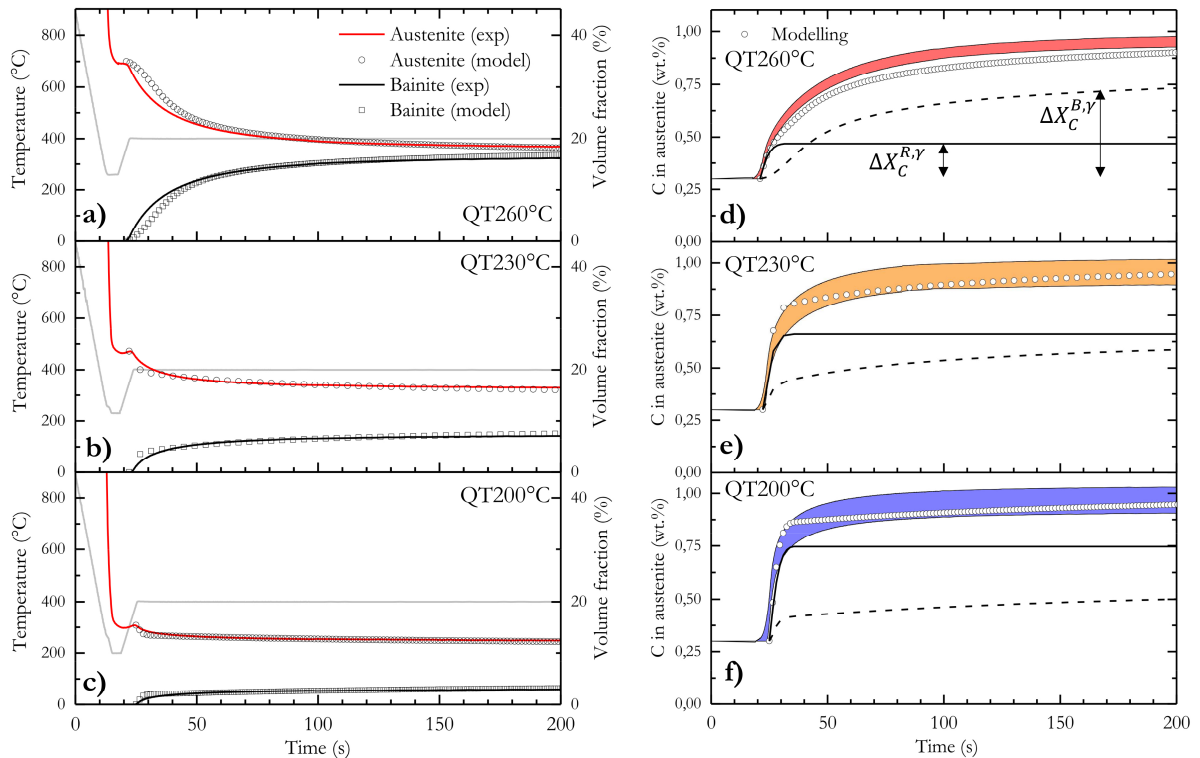


Figure IV-3 - Comparison between calculations and synchrotron experimental data (HEXRD). a), b) and c) give the evolution of thermal path, austenite and bainite fractions at QT=260, 230 and 200°C. d), e) and f) give the time-evolution of carbon content in austenite (the color bands represents the experimental carbon concentration bands taking into account the two limit case of stress relaxation see Figure III-20) . The contribution of both carbon rejected from martensite $\Delta X_C^{R,Y}$ and due to bainite formation $\Delta X_C^{B,Y}$ in the increase of carbon content in austenite were determined from the model developed.

To push further the discussion, the rate of carbon increase in austenite induced by both partitioning and bainite formation were plotted for the three QT considered (Figure IV-4). The partitioning process appears to be very rapid. Carbon is transferred from martensite to austenite approximately within 15s and almost independent of QT. This kinetics effect can be explained by the fine-grained microstructure that affects the carbon diffusion length. It is also shown that the increase of partitioning with decreasing QT is accompanied by a sharp slow down of the carbon increase induced by bainite formation.

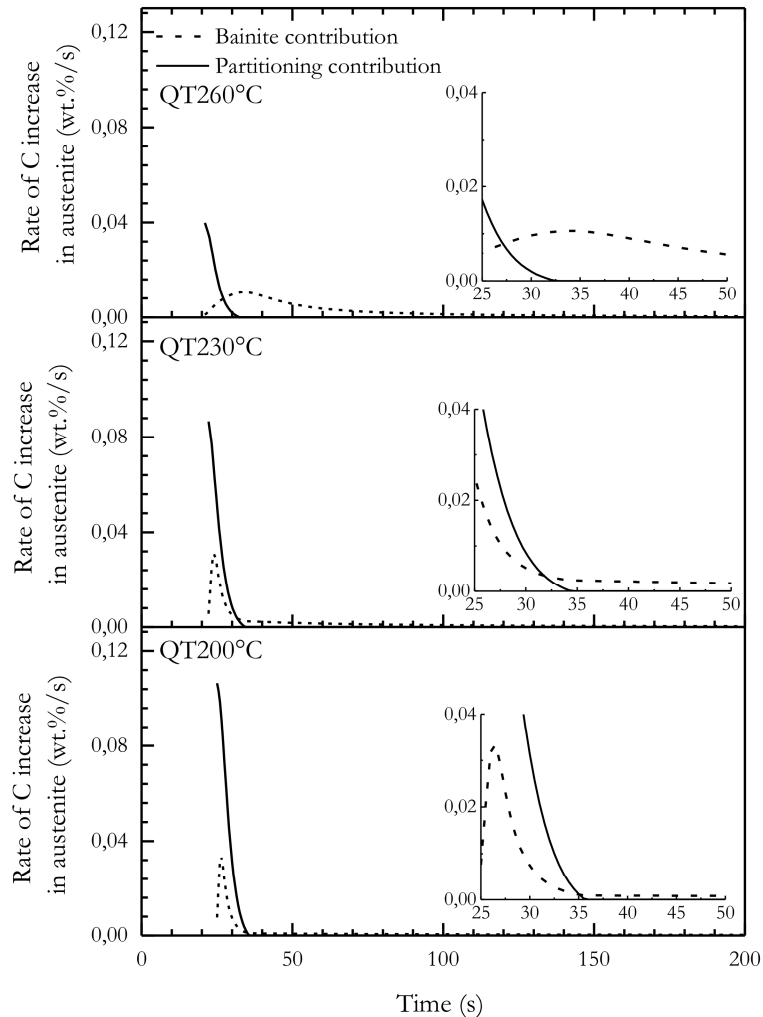


Figure IV-4 - Rate of carbon increase into austenite induced by both partitioning and bainite formation at QT= 260, 230 and 200°C. The inserts correspond to a magnification of the area between 25 and 50s.

In order to better illustrate the effect of carbon rejection from martensite on bainite transformation, the kinetics of carbon enrichment for QT=260°C were plotted for two different conditions; with and without considering carbon partitioning from martensite (Figure IV-5). It is clearly evidenced that carbon rejection from martensite affects strongly both the kinetics of bainitic transformation and the total amount of bainite which is formed (Figure IV-5 a)). Conversely, the kinetics of carbon enrichment, and the maximum carbon content in austenite are not significantly affected by carbon rejected from martensite. We shall return to this key point later.

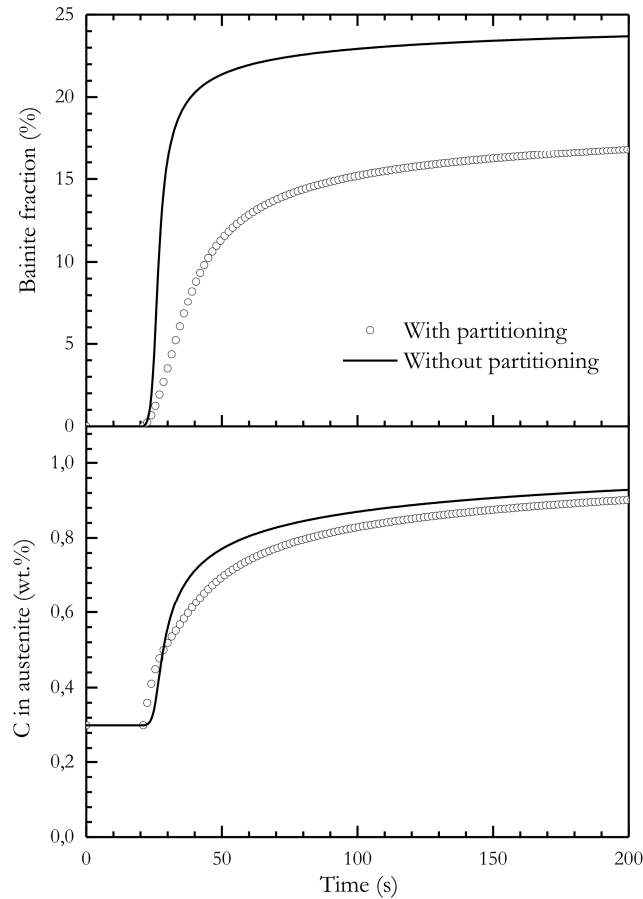


Figure IV-5 - Influence of carbon partitioning on both kinetics of bainite formation and carbon enrichment in austenite at $QT=260^{\circ}C$.

For the same period of time, the evolutions of carbide precipitation states for the three QT are given in Figure IV-6. It is worth noting that the mean radius calculated are in the same order of magnitude than those measured experimentally. Surprisingly, the precipitation state, and more particularly the volume fraction of carbides which are formed, does not depend significantly and monotonously on QT. This point is counterintuitive and will be discussed more deeply. It is obvious that carbide precipitation in martensite is expected to influence the amount of carbon rejected from martensite to austenite. Indeed, one can image a situation in which the amount of carbon trapped in martensite within a very short time is such that carbon rejected from martensite becomes extremely low.

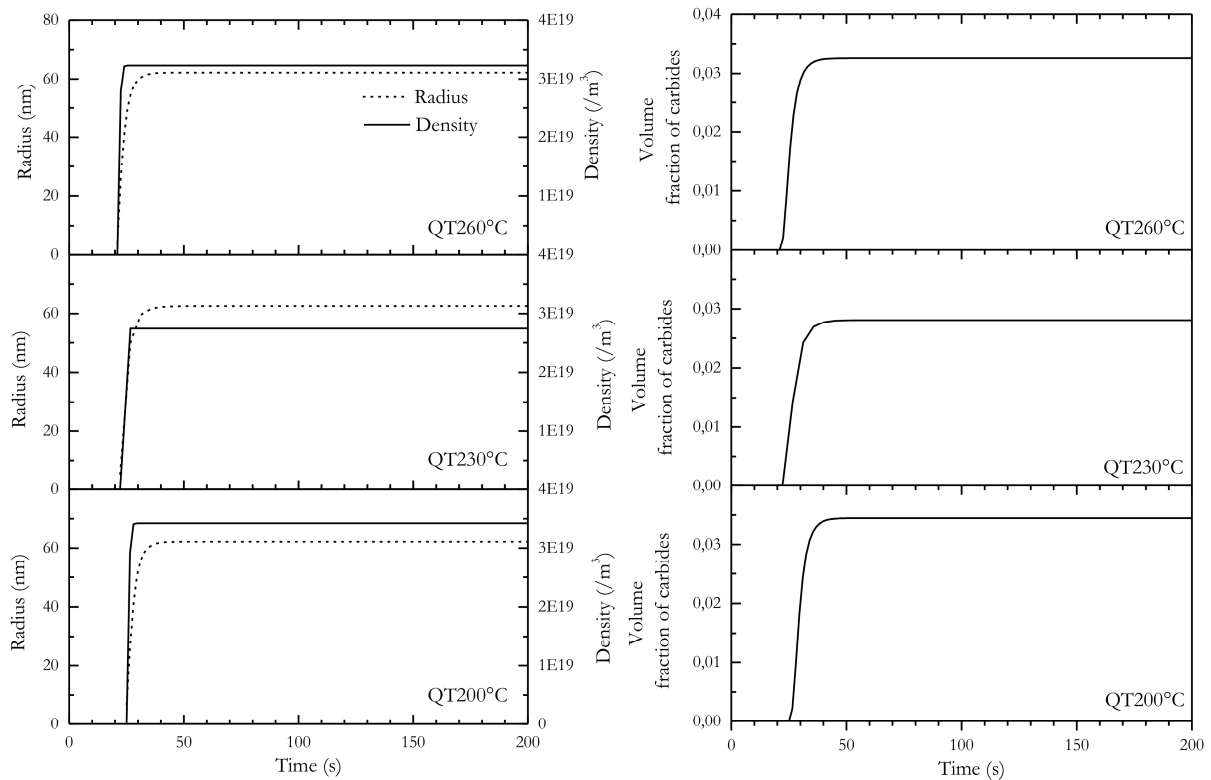


Figure IV-6 - Time evolution of carbides precipitation state (mean radius and volume fraction) in martensite for $QT=260, 230$ and 200°C .

IV.3.2 Carbon enrichment in austenite

The mechanical properties depend on the carbon content in retained austenite and thus on the carbon content at the end of the partitioning at PT. The latter corresponds to the maximum carbon content in austenite. Surprisingly, both the experimental data and calculations show that it does not evolve significantly with QT at PT=400°C (see Figure IV-3). More surprisingly, it is highlighted that the maximum carbon content is not significantly influenced by the carbon rejected from martensite for QT=260°C (Figure IV-5). In order to understand this unexpected behaviour, it was decided to focus on the evolution of the maximum carbon content in austenite as a function of QT, i.e as a function of the initial volume fraction of martensite. Using the model developed, it is relatively straightforward to decouple the contribution of the competitive reactions to the increase of carbon content in austenite. Four types of calculations were performed. In the first, only carbon partitioning from martensite was considered (Figure IV-7 a). In the second, both carbon partitioning from martensite and carbide precipitation in martensite were examined (Figure IV-7 b). In the third, both carbon partitioning and bainite formation were taken into consideration (Figure IV-7 c). Finally, all the contributions were taken into account (Figure IV-7 d). The measured carbon content in austenite at the end of partitioning step by HEXRD and after final cooling at room temperature by XRD are given in Figure IV-7. The carbon measured in retained austenite appears to be slightly higher than those at the end of partitioning step. The reason for this is simple: the lowest carbon austenite islands transform into martensite during final cooling. Therefore, the average measured carbon content in austenite is higher than the average austenite carbon content measured by HEXRD at the end of the partitioning step.

As a reference, the carbon content under CCE conditions was plotted in dashed line in Figure IV-7. It corresponds approximately to a situation in which all the carbon present in martensite is rejected into the initial austenite and, therefore, could be seen as an upper limit of carbon enrichment in austenite. It is thus very interesting to point out that the measured carbon content

in austenite is located above the CCE line for an initial volume fraction of 65%, i. e. for QT=260°C.

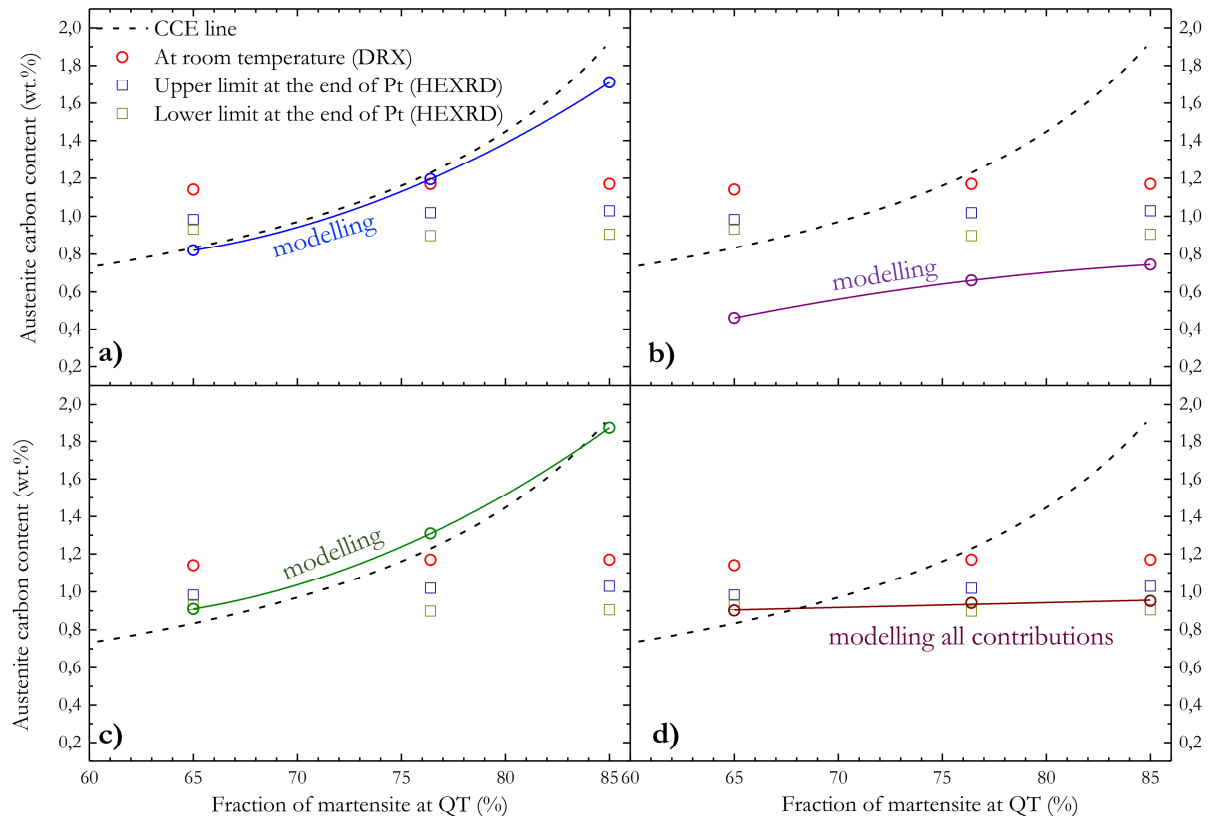


Figure IV-7 - Evolution of maximum carbon content in austenite at the end of PT as a function of initial volume fraction of martensite. For comparison, the measured carbon content at the end of PT by HEXRD, after final cooling at room temperature by XRD and the CCE limit were given. For calculations, four types of interactions were examined: a) only carbon partitioning from martensite b) carbon partitioning from martensite versus carbides precipitation in martensite c) carbon partitioning from martensite versus bainite formation d) carbon partitioning from martensite versus all the contributions.

When only carbon partitioning is considered (Figure IV-7 a), the calculated maximum carbon content in austenite follows the CCE line, except for the higher volume fraction of martensite. This is in fact a distortion introduced by the mean field approach, and more particularly by the carbon homogenization process into austenite. Indeed, when the carbon rejected becomes too important, the carbon gradient at the α'/γ interface is reduced and, in turn, slows down the carbon enrichment in austenite. This effect will apply mainly after a certain amount of time.

When both carbon partitioning and carbides precipitation are coupled (Figure IV-7 b), the maximum carbon content in austenite is systematically located below both the CCE line and the experimental measurements. In that case, the carbides precipitation limits the total amount of carbon rejected from martensite.

When both carbon partitioning and bainite formation are coupled (Figure IV-7 c), the maximum carbon content in austenite is mainly located above the CCE line. This shows clearly that the CCE line cannot be considered as an upper limit in presence of bainite. Another way of saying it is that a carbon content above the CCE line is necessarily an evidence of the presence of bainite. This phenomenon can be attributed to a geometrical effect. The increase of carbon content in austenite is further exacerbated by the austenite volume reduction induced by the presence of bainite.

When all the contributions are taken into account (Figure IV-7 d), it is shown that the maximum carbon content in austenite does barely depends on the initial volume fraction of martensite and

is in very good agreement with the experimental data. It is a very interesting point that deserves further consideration. The comparison between Figure IV-7 c and Figure IV-7 d allows an assessment of the impact of carbides precipitation on the total carbon enrichment in austenite. For instance, it is worth noting that carbide precipitation does not affect the maximum carbon content in austenite at $QT=260^\circ\text{C}$ (initial volume fraction of martensite of 65%). In order to better understand such an evolution, the kinetics of carbon enrichment was plotted for two different conditions at $QT=260^\circ\text{C}$; with and without taking into account carbides precipitation in martensite (Figure IV-8).

In that particular case, the results obtained show that the total carbon enrichment in austenite is the same, for the reason that the lack of carbon rejection induced by carbides precipitation in martensite is exactly balanced by the increase of carbon content induced by bainite formation. The bainite formation is favoured in that case, since the carbon rejected from martensite is reduced.

The situation is however different for the others QT , where the effects of carbide precipitation is more pronounced (Figure IV-7 c) vs Figure IV-7 d)). With decreasing QT , the carbon rejected from martensite is relatively high and impedes bainite formation (Figure IV-3 and Figure IV-4). In that case, the increase of carbon induced by bainite formation can no longer compensate the lack of carbon partitioning induced by carbide precipitation.

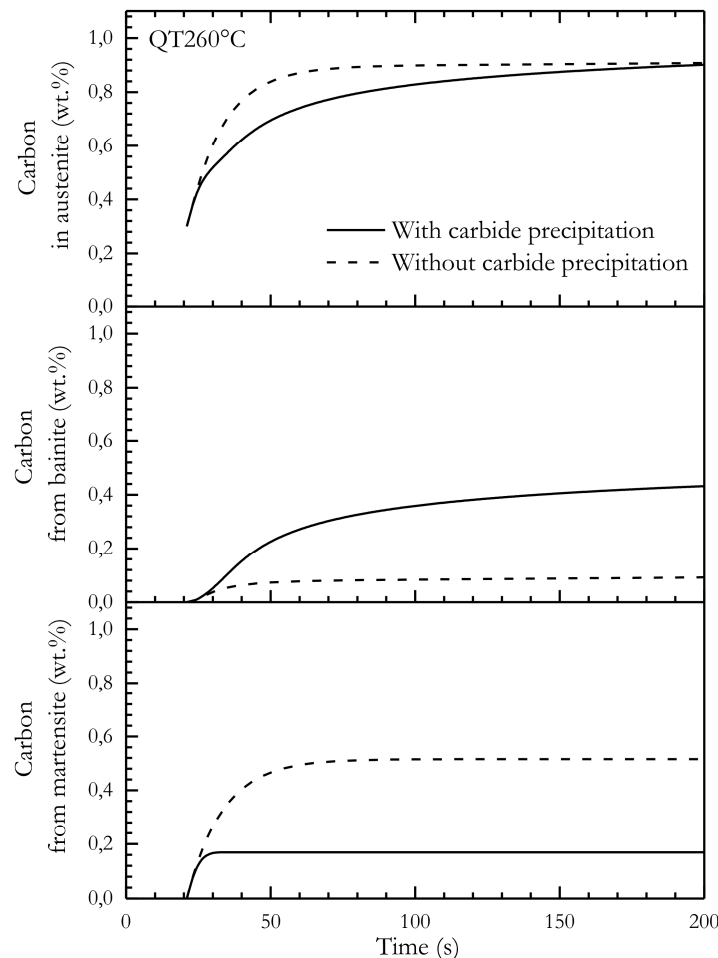


Figure IV-8 - Time-evolution of a) carbon enrichment in austenite b) carbon increase in austenite induced by bainite formation c) carbon increase in austenite induced by partitioning at $QT=260^\circ\text{C}$ for two conditions of calculation: with and without taking into account carbides precipitation in martensite.

Also, a part of carbon is trapped into carbides and limits the carbon partitioning from martensite. This effect is very marked since the process of carbide precipitation and carbon partitioning are

concomitant and their kinetics are similar. This is demonstrated by the calculations of the decrease of carbon in solid solution in martensite induced by both carbide precipitation and carbon partitioning from martensite at $QT=200^{\circ}C$ (Figure IV-9).

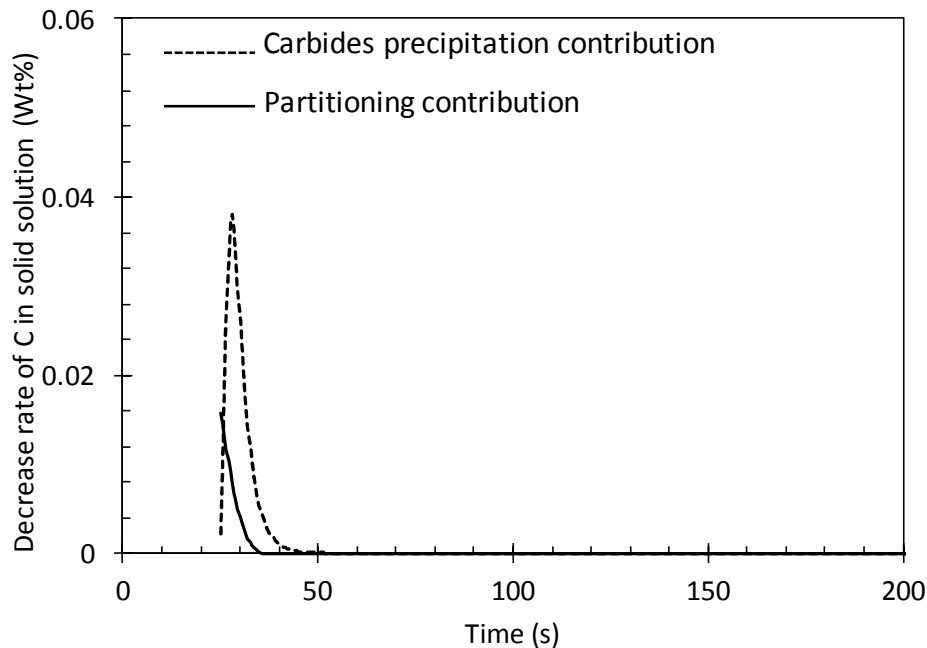


Figure IV-9 - Time-evolution of the decrease of carbon in solid solution into martensite induced by both carbides precipitation and carbon partitioning at $QT=200^{\circ}C$.

IV.3.3 Critical carbon content into austenite at the end of partitioning step

There is however a fundamental issue: why the maximum carbon enrichment does not depend on QT (i.e. on the initial volume fraction of martensite)? To answer this question, it is prime of necessity to remark that carbon partitioning from martensite is a very fast process that takes place within 15s, almost independently of QT (Figure IV-3 and Figure IV-4). For all cases studied, bainite transformation continues while carbon partitioning process is completed, well before the end of partitioning step. This is clearly illustrated in both Figure IV-3 and the inserts given in Figure IV-4. This is a key point since, during isothermal transformation, a limit is expected to be reached beyond which austenite will no longer transform to bainite. The reaction is said to be “incomplete” since bainite transformation stops before achievement of equilibrium state. In that case, bainite transformation is expected to stop as soon as the carbon content in austenite reaches a critical value known as the stasis. It is in this context that the concepts of T_0 and T'_0 were primarily introduced by Zener and Le Houillier [219][220]. The T_0 curve is the locus of all points, on a temperature versus carbon concentration plot, where austenite and ferrite of the same chemical composition have the same free energy. The T'_0 curve is defined similarly but takes into account the stored energy of the bainite (400 J/mole) due to the displacive mechanism of the transformation [221]. For the composition and the partitioning temperature studied, T_0 and T'_0 were calculated equal to 0.72 and 0.48 wt% respectively. These values are much lower than the maximum carbon content measured at the end of PT (see Figure IV-3).

An alternative interpretation is based on a mechanical effect. As pointed out by [222] and based on their calculations, the incomplete reaction phenomenon is due to a mechanical effect rather than a chemical one. At a given time, it becomes thermodynamically unfavourable to form a new subunit because of the additional stress induced, and not because the average carbon content of the austenite has reached the T_0 or T'_0 line. In the same vein, it was also proposed that bainite can no longer grow as a consequence of the Gibbs energy dissipation by plastic deformation either

bainite cannot nucleate in a too hard austenite [223]. These mechanical effects are indirectly taken into account in our model by the size of bainite, which depends on the yield strength of austenite. At a given temperature, the latter is expected to evolve with time since it depends on carbon content in austenite (see equation (IV.13)). At a certain moment, the yield strength of austenite is so high that the size of sub-unit which is formed becomes extremely small. This is the main reason which explains that the calculated kinetics for bainite transformation were also incomplete (see Figure IV-3 and Figure IV-5).

In order to investigate this issue more deeply, a carbide free bainite (CFB) treatment was performed. It consists of heating in the austenitic domain at 900°C for 5min, followed by a cooling at 50°C/s and by a soaking for 2000s at 400°C that corresponds to the partitioning temperature (Figure IV-10).

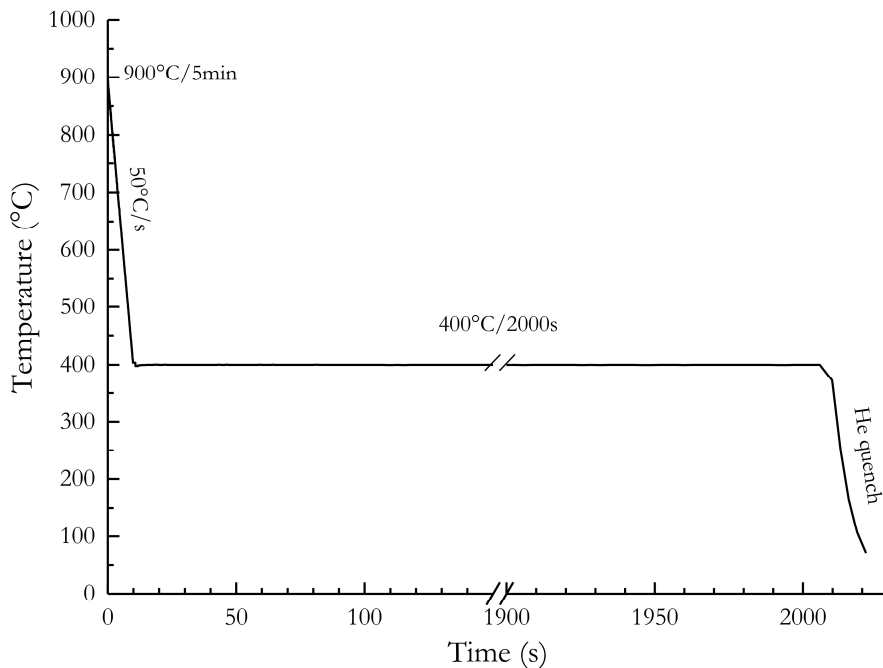


Figure IV-10 - Carbide free bainite thermal treatment.

Both bainite transformation and carbon enrichment in austenite were analysed by in-situ synchrotron HEXRD. The procedure used is the same as previously described for Q&P treatments, except for the lattice parameter one. For the sake of simplicity, the mechanical contribution was not taken into account. After accounting for the thermal contribution on the austenite dilatation, the latter was converted into austenite carbon content. The results obtained are presented in Figure IV-11 ($t=0s$ corresponds to the beginning of first cooling step). Very rapidly, after 12s, austenite transforms into bainite without any significant evolution of carbon content in austenite. After about 50s at 400°C, the increase of carbon content in austenite is observed, concomitant to the bainite transformation. Both the kinetics of bainite and carbon enrichment in austenite are much slower than those observed at 400°C for the Q&P treatments (see Figure IV-3). The reasons for this are very simple: the initial austenite grain size is much bigger (around 50 μm vs less than 1 μm) and there is no prior martensite which can accelerate bainite transformation [224]. The most interesting point is that the maximum carbon content in austenite is 0.85 wt% and the carbon content into retained austenite after final cooling was measured by XRD to be 1.08 wt%. The comparisons done in Figure IV-7 and Figure IV-11 show that these values are pretty close to those observed for the Q&P conditions. These are strong indications that bainite transformation controls the maximum carbon enrichment into austenite at 400°C. It is the most likely reasons that explains that carbon enrichment does not depend on QT at 400°C.

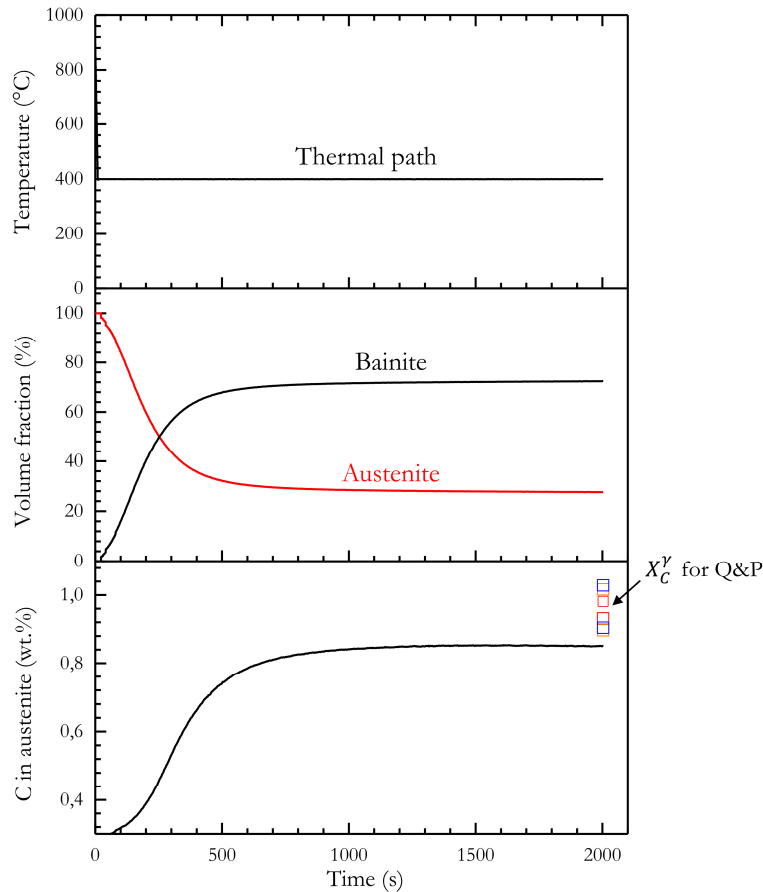


Figure IV-11 - Time-evolution of a) thermal path b) volume fraction of both austenite and bainite c) carbon enrichment in austenite and data corresponding to the lower and upper limits for maximum carbon content in austenite at $QT=260$ (red square), 230 (orange square) and 200°C (blue square). All these data were obtained by *in-situ* synchrotron HEXRD.

IV.3.4 Avenues for increasing C enrichment in austenite

For all cases studied, bainite transformation continues while partitioning process is completed. In that case, the increase of carbon content in austenite due to bainite transformation was then shown to be the limiting process: the reaction was shown to be incomplete since transformation stops as soon as the carbon content in austenite reaches a critical value that corresponds to the maximum carbon enrichment in austenite. In order to increase carbon enrichment in austenite, it is prime necessary to make the carbon partitioning from martensite the limiting process. In our conditions, that requires rejecting higher amount of carbon from martensite. There are two ways to achieve this objective. The first is to reduce the precipitation rate of carbides into austenite, and the second is to speed up the carbon rejection from martensite by refining the microstructure. These two avenues for increasing C enrichment in austenite were tested numerically using the model developed (Figure IV-12 a) and b)). In Figure IV-12 a), the effects of different precipitation rates V_p were studied, from V_{or} corresponding to the original precipitation rate down to $V_p=0$. From a practical point of view, calculations were successively performed by dividing the volume fraction of carbides formed at each time step by 10, 100 and, finally, by considering that no carbides were formed ($V_p=0$). It appears clearly that the effect of carbide precipitation rate in martensite is more pronounced when the initial volume fraction of martensite at QT is high, i.e. when QT is low. For a volume fraction of martensite at QT of 65% (which corresponds to $QT=260^{\circ}\text{C}$), the carbides precipitation rate has little to no effect on maximum carbon enrichment in austenite. This important point, already discussed in the

previous section, is mainly due to the fact that bainite transformation is always the limiting process whatever the carbides precipitation rate. In that case, the carbon reservoir (i.e. martensite volume fraction) is not large enough to affect bainite transformation. For higher volume fraction of martensite, the carbide precipitation rate is shown to have a significant role on the maximum carbon content in austenite. In these cases, the carbon reservoir is large enough to affect bainite formation, and to make carbon partitioning the limiting process. Obviously, this effect is much more pronounced at lower QT; i.e. for higher initial volume fractions of martensite. A similar behaviour was highlighted for the effect of the size of the system L_0 (cf Figure IV-2) on the maximum carbon enrichment of austenite (Figure IV-12 b). This is based on the same explanation. The reduction of the size of the system leads to an acceleration of the C rejection for the main reason that carbon diffusion length is shortened. The carbon rejection rate becomes much faster than the precipitation one, amplified by the fact that the kinetics of carbides precipitation is slowed down by carbon partitioning. Indeed, the driving force for carbide precipitation is reduced by rapid carbon depletion into martensite. Finally, the carbon released into austenite is large enough to affect bainite transformation and to make carbon partitioning the limiting process.

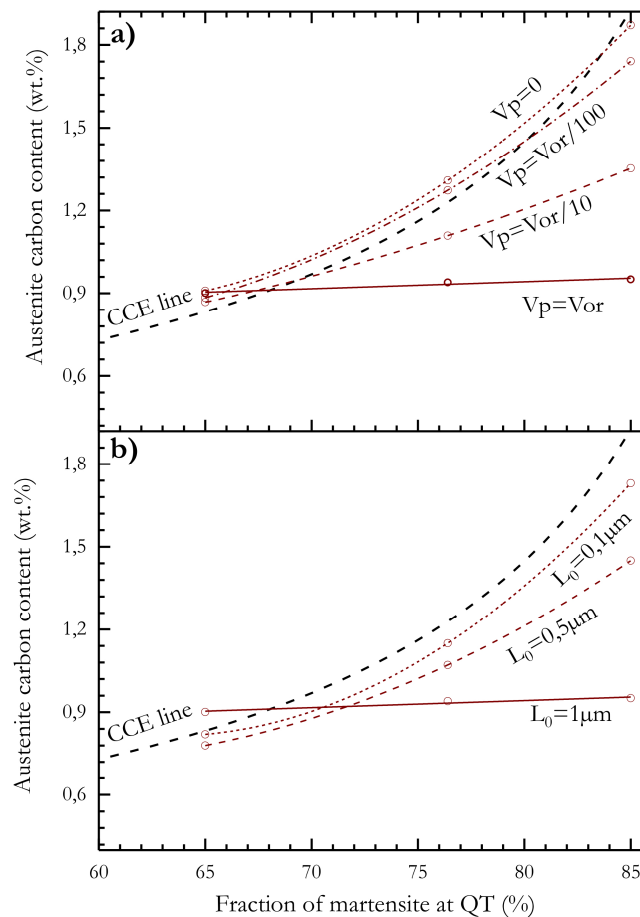


Figure IV-12 - Evolution of maximum carbon content in austenite at the end of PT as a function of the initial volume fraction of martensite. a) for different precipitation rate V_p in martensite b) for different size of the system L_0 . For comparison, the CCE lines were plotted in both figures.

IV.3.5 Complementary investigation: Mn partitioning at the α'/γ interface

In order to describe carbon partitioning process, the Constrained Carbon Equilibrium (CCE) condition was used and the martensite/austenite interface was considered as immobile or stationary. In that case, only carbon equilibrates its chemical potential and not the substitutional

elements such as Mn and Si. In other words, the Mn and Si atoms were supposed to be homogeneously distributed through the α'/γ interface. The actual distribution of these elements is an important point for many reasons. First, it raises the question of the CCE condition, which ignores the partitioning of iron and substitutional alloying elements during the partitioning stage. Second, it could be the marker of the motion of the α'/γ interface, since it is well known that Mn can interact with a moving interface in steels [115].

The immobile character of the interface is still discussed in the literature. Several recent experimental studies suggest that α'/γ interfaces are mobile during Q&P process [116] [139][225]. Last, but not least, interfacial partitioning of substitutional elements is expected to play a key role on both the kinetics and the total carbon enrichment in austenite by modifying local thermodynamic conditions.

In the following, we will focus on the thermal treatment corresponding to QT=200°C since the contribution of bainite in the carbon enrichment into austenite at PT=400°C is the lowest. This contribution was shown to be 31% at QT=200°C and the maximum volume fraction of bainite formed was measured to be around 3% in terms of absolute value.

Two conditions of interest were then selected. One corresponding to time t_p^0 ; i.e. the beginning of partitioning time, and the second corresponding to time t_p^f ; i.e. the end of partitioning time.

At t_p^0 , the carbon enrichment can be mainly attributed to carbon partitioning from martensite while the interface is very likely immobile, as no change in volume fraction of BCT-phases was observed during reheating. Between t_p^0 and t_p^f , it was clearly shown that the carbon enrichment in austenite results from both bainite and carbon partitioning contributions. From an experimental point of view, it is very difficult to ensure the immobile character of the α'/γ interface, since its motion can be “hidden” by the growth bainite, as martensite and bainite have the same BCT structure.

Due to its proven ability to map both interstitial and substitutional elements distribution at the subnanometre scale, atom probe tomography (APT) was used to investigate the carbon, manganese and silicon redistribution through the α'/γ interface, together with their evolution in both austenite and martensite at times t_p^0 and t_p^f .

Figure IV-13 shows a three-dimensional reconstruction of carbon, manganese and silicon for times t_p^0 and t_p^f . At t_p^0 , two distinct regions can be identified based on their different carbon contents (Figure IV-13 a). A depleted carbon region in the left bottom part on the reconstruction corresponds to martensite, the rest being austenite. In addition, a carbon gradient is clearly visible which extends over several nanometres from the α'/γ interface to the austenite (see solid white arrows in Figure IV-13 a).

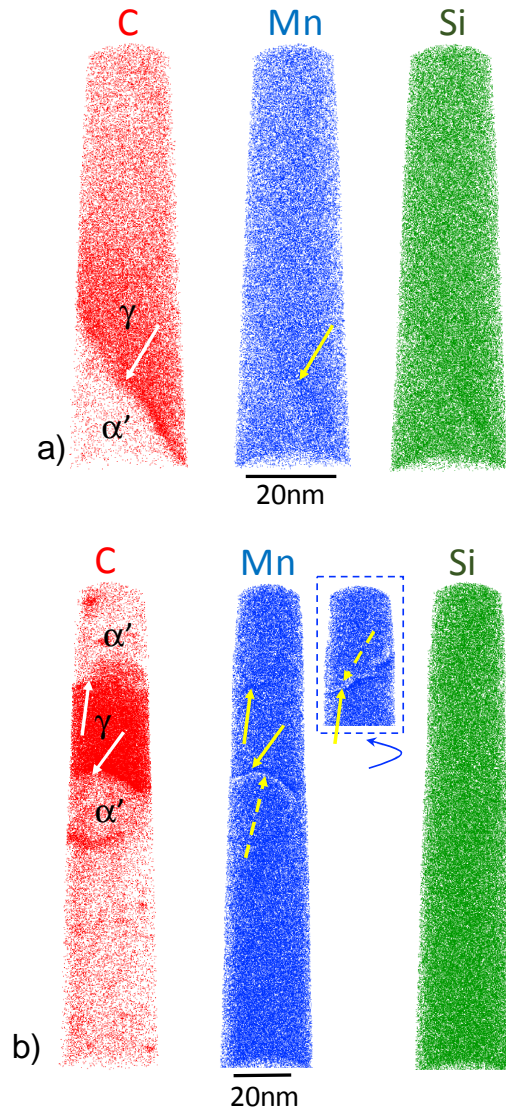


Figure IV-13 - 3D atom probe reconstruction at a) t_p^0 and b) t_p^f . The carbon, manganese and silicon atoms are represented in red, blue and green respectively. The solid and dashed arrows indicate enriched and depleted zones close to the α'/γ interfaces.

On the contrary, both Mn and Si look homogeneously distributed in the volume analysed, the thin Mn and Si enrichment at the interface being the result of local magnification effect [226], and not an actual segregation, as confirmed by the proxygrams shown in Figure IV-14. At t_p^f , three distinct regions can be identified based on the same criteria (Figure IV-13 b). The two depleted carbon regions in both the top and the bottom part on the reconstruction correspond to martensite, while the intermediate region corresponds to a thin austenite layer, about 40 nm thick. In that sample, two different α'/γ interfaces were thus intercepted. It is important to note that Mn distribution shows both a depleted and an enriched zone of few nanometres thick, whereas Si is homogeneously distributed (see solid and dashed yellow arrows in Figure IV-13 b). This is more visible in the bottom interface but it becomes visible in the top interface when viewed in a different orientation (see the insert at top right).

Carbon, manganese and silicon proxygrams across the 2 at.% carbon isoconcentration surface at t_p^0 are shown in Figure IV-14 a). At t_p^f , two separate proxygrams across the 3 at.% carbon

isoconcentration surfaces were plotted separately and then combined to obtain a continuous and accurate concentration evolution across the austenite film as shown in Figure IV-14 b). These results confirm the conclusions drawn from the 3D reconstructions.

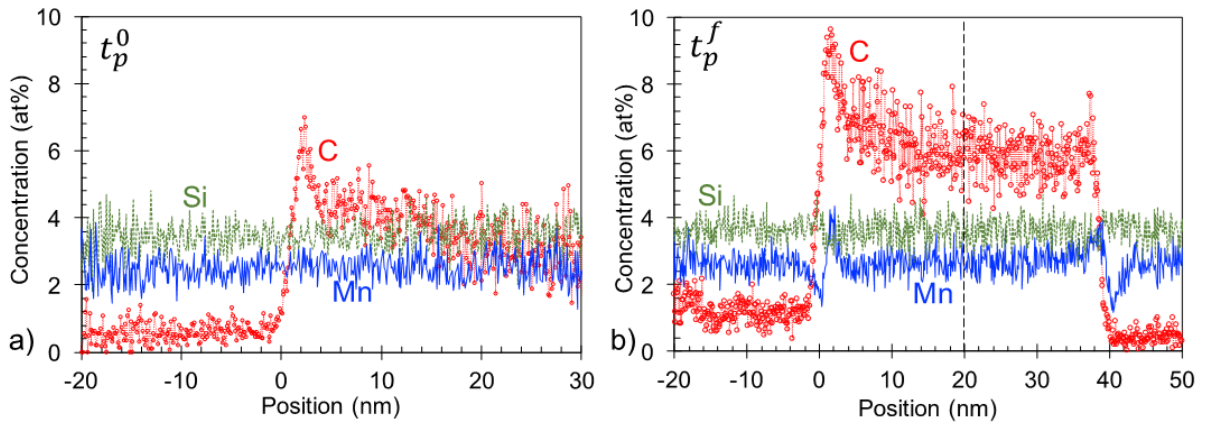


Figure IV-14 - Proxigrams across α'/γ interfaces showing carbon, manganese and silicon concentration profiles at a) t_p^0 and b) t_p^f (dashed line : merging point of the two interfaces proxigrams)

At t_p^0 , the C content of the martensite and austenite close to the α'/γ interface are, respectively, lower and higher than the bulk. The mean carbon content in austenite integrated over 30 nm is about 0.7 wt%. This value is very consistent with that one measured by HEXRD at t_p^0 (0.7wt% vs. 0.5 wt% see Figure IV-3 c). It is important to note that a carbon profile is established in the austenite while both manganese and silicon are homogeneously distributed through the interface (Figure IV-14 a). At t_p^0 , all these observations are consistent with the Constrain Carbon Equilibrium conditions. At t_p^f , the mean carbon content in austenite, integrated over 40 nm in austenite, is about 1.10 wt%. This value, consistent with that one measured by HEXRD and calculated at t_p^f (1.10 vs. 0.95 vs. 0.91 wt%), confirms the carbon enrichment in austenite between t_p^0 and t_p^f . As confirmed by our analysis in the previous part, carbon partitioning from martensite to austenite is the preponderant mechanism for carbon enrichment in the austenite islands for QT=200°C. The most remarkable fact is the Mn depleted and enriched zones which extend over 5 nm in both martensite and austenite respectively, while Si is homogeneously distributed in both phases. The origin of this Mn partitioning is clearly questionable at such low temperature (400°C) and short tempering time (200s). In order to go further, we propose, from the measured profiles of C, Mn and Si and the sub-lattice models, to determine the chemical potential evolution of both C and Mn into austenite at the vicinity of the α'/γ interface at t_p^0 and t_p^f .

From the concentration values measured in austenite (Figure IV-14) and from relations (IV.17), the chemical potential of C, Mn were plotted at the vicinity of α'/γ interface in austenite at 400°C for t_p^0 and t_p^f . For sake of clarity, only the left α'/γ interface were analysed at t_p^f . The results obtained are given in Figure IV-15. At t_p^0 , it is shown that the gradient of chemical potential of both carbon and manganese within austenite at the vicinity of α'/γ interface are of opposite signs, the negative value for carbon evidences its diffusion from martensite to austenite at t_p^0 . The manganese behaviour results from both the Mn and Si concentration profile homogeneity in austenite (see Figure IV-14) and the C profile in austenite. It is worth noting that the thermodynamic interactions between C and Mn are attractive. The system is thus in a metastable state at t_p^0 since the highest carbon and manganese concentration regions (at the vicinity of the interface) correspond respectively to the highest C chemical potential and to the lowest Mn chemical potential. These observations are completely consistent with both the paraequilibrium

and CCE conditions. The carbon chemical potential within austenite is much higher, and its gradient less pronounced at t_p^f . This is the consequence of the carbon enrichment in austenite and the decrease of the driving force for carbon partitioning between t_p^0 and t_p^f . The manganese chemical potential decreases at t_p^f , due to the increase of carbon enrichment into austenite while Si remains homogeneously distributed in austenite. The sign of the manganese chemical potential gradient changes at the α'/γ interface and extends over a distance of about 5 nm. This is an evidence of Mn diffusion from martensite to austenite due to a chemical potential difference. As a consequence, this analysis indicates that both carbon and manganese equilibrate their chemical potential during quenching and partitioning at 400°C. This conclusion is reinforced by the recent simulations of the Mn partitioning during partitioning stage in the absence of interface migration [227], where the Mn profiles calculated in both martensite and austenite are in perfect agreement with those measured in this study. Finally, although the diffusion distance of Mn was only a few nanometres, its influence on the stability of retained austenite (and then on resulting properties) may be significant, because the retained austenite has a thin film morphology. In this study, the Mn gradient extends over 5 nm while the half thickness of retained austenite is about 20 nm (see Figure IV-14 b). Obviously, the effect of Mn partitioning is expected to be all the more pronounced if partitioning time and temperature are respectively longer and higher and the austenite film thinner.

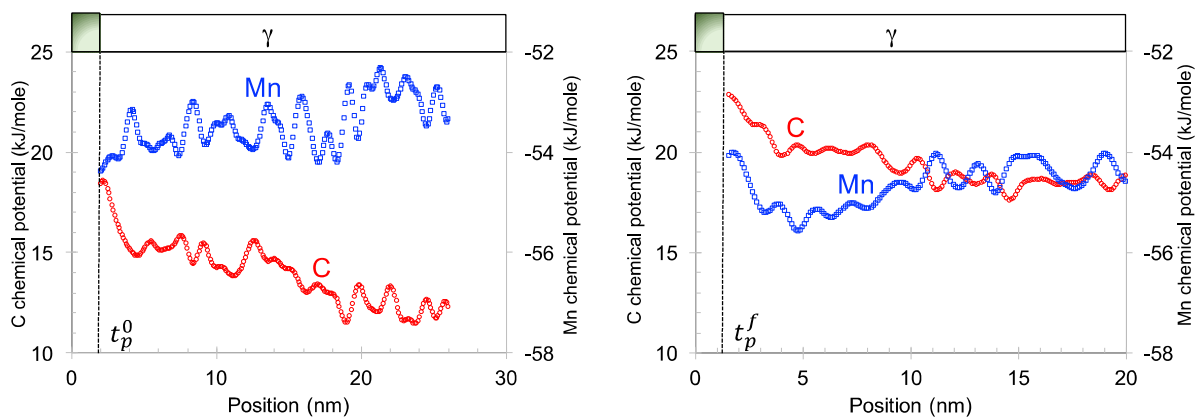


Figure IV-15 - Evolution of chemical potential of both C and Mn at a) t_p^0 and b) t_p^f within austenite at the vicinity of α'/γ interface.

IV.4 Partial conclusion

An original theoretical approach was developed to rationalize the in situ High Energy X-Ray Diffraction experimental data. The results obtained and the analysis conducted give some clarifications regarding the mechanisms of carbon enrichment into austenite during Q&P treatments. Unambiguously, it was shown that the carbon enrichment results from both carbon partitioning from martensite and bainite transformation. Their contribution was determined as a function of QT and that of partitioning was demonstrated to be larger with decreasing QT. This behaviour can be explained by a domino effect: the amount and carbon rejection rate are shown to be higher with decreasing QT and this, in turn, has the effect to impede bainite transformation. Very interestingly, it was shown that the carbon content into austenite at end of the partitioning step can be located above the CCE line in presence of bainite. This phenomenon was attributed to a geometrical effect: the increase of carbon content in austenite is further exacerbated by the austenite volume reduction induced by the presence of bainite.

Very surprisingly and counter-intuitively, the maximum carbon enrichment into austenite was shown to not depend on QT. This was explained by bainite transformation that controls the maximum carbon enrichment into austenite at 400°C. Indeed, for all cases studied, it was evidenced that bainite transformation continues while partitioning process is completed. In that case, bainite transformation was shown to be the limiting process since the maximum carbon content into austenite corresponds to the stasis, i. e. to the critical carbon content at which bainite transformation stops.

In order to increase carbon enrichment in austenite, it is prime necessary to make the carbon partitioning from martensite the limiting process. In our conditions, that requires rejecting higher amount of carbon from martensite. There are two ways to achieve this objective. The first is to reduce the precipitation rate of carbides into austenite, and the second is to speed up the carbon rejection from martensite by refining the microstructure. The carbides precipitation rate into martensite with respect to the carbon rejection rate from martensite is thus a key parameter to be controlled.

The alloying elements partitioning from martensite to austenite during quenching and partitioning was analysed by coupling in situ High Energy X-Ray Diffraction experiments and 3D atom probe tomography. A rapid and significant carbon partitioning from martensite to austenite without any partitioning of both Mn and Si was highlighted while the interface was immobile. After a relatively short time at 400°C, a clear Mn partitioning occurs at the vicinity of the α'/γ interface. The analysis conducted indicates that manganese equilibrates its chemical potential during partitioning and raises the issue of the Constrained Carbon Equilibrium model applicability throughout the partitioning process.

Finally, this study conducted in this chapter shows clearly the effects of complex interactions between carbides precipitation into martensite, carbon partitioning and bainite transformation involved on carbon enrichment in austenite during Quenching and Partitioning at 400°C.

GENERAL CONCLUSION

The need to improve fuel efficiency and safety has led to a high and growing demand for high-strength steels in the automotive industry. In that context, Quenching and Partitioning (Q&P) steels have received much attention, and can be considered as one of the 3rd generation of advanced high strength steels (AHSS) for automotive applications. Their development relies on a processing route that involves quenching below the martensite start temperature (M_s) followed by a rapid heating and ageing above the initial quench temperature. The ageing step, usually performed between 300°C and 500°C, is also termed “partitioning step” since carbon enrichment in austenite is expected to occur during this stage. The benefits of such a treatment in terms of improved mechanical properties depends strongly on the austenite stability and thus on the level of carbon enrichment in austenite during the partitioning step. The work conducted in this thesis give some clarifications regarding both the microstructure evolution and the mechanisms of carbon enrichment into austenite during Q&P treatment of a model Fe-0.3 C-2.5Mn-1.5Si steel.

The optimum quenching and partitioning parameters were determined by the combination of dilatometry and XRD technics. The dilatometry study highlighted an expansion that can be induced by bainite formation. In order to confirm this assumption, an image analysis study was conducted on both Q&P treatments and a CFB reference sample. The prior chemical etching of the samples allowed to discriminate the carbon rich (retained austenite and MA Islands) and poor phases (tempered martensite and bainite). Austenite was present as small and fine long laths as well as in the periphery of the MA islands. Tempered martensite was easily recognizable due to the large presence of intra-lath carbides. The analysis conducted showed that bainite can be characterized by carbide free laths. The phase fraction evolution of these features was studied by a manual counting method on samples that were quenched at various time during the partitioning step. A continuous increase in bainite fraction was observed by image analysis accordingly to the expansion observed by dilatometry. This trend is also observed when the QT varies: as observed in dilatometry, the more austenite is present for partitioning, the more bainite is observed by image analysis. This confirms that the morphological criterion for bainite (small laths with no carbides) is relevant. The presence of bainite was also confirmed by in situ High Energy X-Ray Diffraction experiments. Indeed, a significant and slow increase in a new-BCT phase fraction at the expense of austenite occurs during both reheating and the partitioning step. The volume fractions measured are in agreement with those measured by image analysis. Furthermore, it was shown that the maximum carbon content into austenite can be located above the CCE line that could be seen as an upper limit of carbon enrichment in austenite. This was attributed to a geometrical effect induced by the presence of bainite. As a consequence, there is thus no question about the bainite formation.

Contrary to bainite, tempered martensite laths present a large amount of carbides. The carbon composition of these carbides, measured by Atom Probe Tomography (APT), ranges from 20.0 at.% to 27.7 at.%C. Based on these measurements, it was difficult to rule out on the nature of those carbides that is either transitional (ϵ or η) or equilibrium carbide (θ). The complementary TEM microdiffraction experiments have ruled out the presence of cementite while the distinction between ϵ and η carbides turned out to be more tedious. The thin plate and the spherical shape carbides were analysed as η carbides and ϵ -carbides respectively.

A large amount of carbon was also trapped on defects in martensite and, more specifically on laths boundaries, and, surprisingly not on dislocations. The excess concentration of carbon at the lath boundaries measured by APT suggest that carbon segregates first and, subsequently, a desegregation phenomenon takes place.

The use of in-situ High Energy X-Ray Diffraction allowed us to have access to ultra-fast time-resolved quantitative information on the quenching and partitioning process. Three Q&P treatment with different QT (200, 230 and 260°C) were studied. From a general point of view, the evolution of phase transformations can be decomposed into four main stages:

- (5) a quenching from the fully austenitic domain (900°C) to a temperature that corresponds to Ms during which no phase transformation occurs,
- (6) a temperature decrease from Ms to QT during which a significant increase in martensite at the expense of austenite occurs. The rate of this transformation is very fast in the first stage and becomes more sluggish at the final stage. The final volume fractions of martensite were measured and were shown to depend on QT (85% at QT200, 76% at QT230 and 65% at QT260).
- (7) A stagnant stage during reheating from QT to a given temperature in which the microstructural state remains globally unchanged,
- (8) A significant and slow increase in a new-BCT phase at the expense of austenite occurs during both reheating and partitioning step. This new-BCT phase was identified as bainite. The transformation rate, which is a better indicator than the intrinsic volume fraction of bainite, was shown to decrease with decreasing QT, from 45% at QT=260°C to 20% at QT=200°C. For the three QT studied, the major part of bainite is formed within a very short time: 75% of total bainite is formed within 28.2s, 24.6 and 30s for respectively QT200, QT230 and QT260.

The analysis of the austenite lattice parameter evolution was made difficult since it is the result of thermal, chemical and mechanical contributions. An attempt was made to decouple all these contributions and the internal stresses into austenite at QT were determined. A significant result is that austenite is subject to a sequence of tensile and compression state induced by the formation of martensite. The critical volume fractions of martensite for the transition of austenite from tensile to compression state were determined for the three QT. It was measured to be 56, 44 and 52% for QT200, QT230 and QT260, respectively. From a qualitative point of view, these observations agree with the theoretical works of Eshelby, Mori-Tanaka and Scherer.

Furthermore, it was shown that any change in austenite lattice parameter after QT can be attributed either to a carbon enrichment of austenite or a stress relaxation phenomenon in austenite, or both. However, all these mechanical contributions to the austenite lattice parameter variation are very difficult to be decoupled. In order to overcome this difficulty, it was proposed to define two boundaries for C concentration evolution by considering two limit cases. The first is to suppose that no stress relaxation occurs during reheating and soaking at PT. In other words, the stress relaxation phenomena are neglected, and all the increase in a_γ occurring after QT was assigned to the chemical contribution; the latter being thus overestimated in that case. The second is to suppose that internal stresses in austenite are immediately and totally relaxed. The real chemical contribution in the increase of the austenite lattice parameter is expected to evolve very likely between these two boundaries. Following this approach, the evolutions of carbon content into austenite for the three QT were determined. The first conclusion is that the influence of stress relaxation on the evolution of carbon content into austenite is not very significant. At most, it corresponds to a decrease of carbon content of about 0.10wt% over a total carbon enrichment into austenite of about 0.7wt% for QT200. As expected, the influence of stress relaxation in austenite depends on QT, i.e. on the initial volume fraction of martensite at QT. The lowest impact was obtained for QT260 (it is in the order of 0.05wt% over a total carbon enrichment into austenite of about 0.7wt%). The reason for this is simple: the lower the volume fraction of martensite at QT is, the lower the internal stresses in austenite induced by martensite formation are. In this part, the most significant highlights are that the total carbon enrichment in austenite does not depend on QT, and that the increase of carbon content into austenite results from both carbon partitioning and bainite contributions which appears difficult to be decoupled

from an experimental point of view.

To answer these questions of interest and to rationalize the in situ High Energy X-Ray Diffraction experimental data, an original theoretical approach was developed. The results obtained, and the analysis conducted, give some clarifications regarding the mechanisms of carbon enrichment in austenite during Q&P treatments. Unambiguously, it was shown that the carbon enrichment results from both carbon partitioning from martensite and bainite transformation. Their contributions were determined as a function of QT, and that of partitioning was demonstrated to be larger with decreasing QT. This behaviour can be explained by a domino effect: the amount and carbon rejection rate are shown to be higher with decreasing QT and this, in turn, has the effect to impede bainite transformation

Very interestingly, it was shown that the carbon content in austenite at end of the partitioning step can be located above the CCE line in presence of bainite. This phenomenon was attributed to a geometrical effect: the increase of carbon content in austenite is further exacerbated by the austenite volume reduction induced by the presence of bainite.

Very surprisingly and counter-intuitively, the maximum carbon enrichment into austenite was shown to not depend on QT. This was explained by bainite transformation that controls the maximum carbon enrichment into austenite at 400°C. Indeed, for all cases studied, it was evidenced that bainite transformation continues while partitioning process is completed. In that case, bainite transformation was shown to be the limiting process since the maximum carbon content in austenite corresponds to the stasis, i.e. to the critical carbon content at which bainite transformation stops.

In order to increase carbon enrichment in austenite, it is first necessary to make the carbon partitioning from martensite the limiting process. In our conditions, that requires rejecting higher amount of carbon from martensite. There are two ways to achieve this objective. The first is to reduce the precipitation rate of carbides in martensite, and the second is to speed up the carbon rejection from martensite by refining the microstructure. The carbide precipitation rate in martensite with respect to the carbon rejection rate from martensite is thus a key parameter to be controlled.

The alloying element partitioning from martensite to austenite during quenching and partitioning was analysed by coupling in situ High Energy X-Ray Diffraction experiments and atom probe tomography. A rapid and significant carbon partitioning from martensite to austenite without any partitioning of both Mn and Si was highlighted while the interface was immobile. After a relatively short time at 400°C, a clear Mn partitioning occurs at the vicinity of the α'/γ interface. The analysis conducted indicates that manganese equilibrates its chemical potential during partitioning and raises the issue of the Constrained Carbon Equilibrium model applicability throughout the partitioning process.

To conclude, the study conducted in this work shows clearly the effects of complex interactions between carbide precipitation in martensite, carbon partitioning from martensite to austenite and bainite formation on carbon enrichment in austenite during Quenching and Partitioning at 400°C. There are however two key points which were not addressed in this work. The first is the influence of carbon segregation in martensite on carbon enrichment in austenite. A priori, it could be considered as a limiting process for the carbon enrichment in austenite. The calculations we performed very recently give a reverse trend: carbon segregation favours the partitioning from martensite to austenite since it slows down the carbide precipitation in martensite. From our knowledge, this type of interaction has never been reported in the literature. The second concerns the thermodynamic properties of martensite. In this work, martensite was considered to behave as ferrite. In the absence of carbides, the potential of carbon enrichment due to partitioning seems to be overestimated in that case since the chemical potential of C in martensite is expected to be lower than in ferrite. It is therefore not certain that the absence of carbide precipitation in martensite would lead to an increase of carbon enrichment into austenite.

BIBLIOGRAPHY

- [1] WorldAutoSteel, “Advanced high-strength steels application guidelines,” 2016.
- [2] T. B. Hilditch, T. de Souza, and P. D. Hodgson, “Properties and automotive applications of advanced high-strength steels (AHSS),” in *Welding and Joining of Advanced High Strength Steels (AHSS)*, Elsevier Ltd, 2015, pp. 9–28.
- [3] J. Galán, L. Samek, P. Verleysen, K. Verbeken, and Y. Houbaert, “Advanced high strength steels for automotive industry,” *Revista de Metalurgia*, vol. 48, no. 2, pp. 118–131, 2012.
- [4] J. H. Schmitt and T. Iung, “New developments of advanced high-strength steels for automotive applications,” *Comptes Rendus Physique*, vol. 19, no. 8, pp. 641–656, 2018.
- [5] Chatterjee and Debasish, “Behind the Development of Advanced High Strength Steel (AHSS) Including Stainless Steel for Automotive and Structural Applications -An Overview,” *Materials Science and Metallurgy Engineering*, vol. 4, no. 1, pp. 1–15, 2017.
- [6] Arcelor Mittal, “Sustainability,” 2019. [Online]. Available: <https://automotive.arcelormittal.com/sustainability>. [Accessed: 22-Aug-2019].
- [7] J. Speer, D. K. Matlock, B. C. De Cooman, and J. G. Schroth, “Carbon partitioning into austenite after martensite transformation,” *Acta Materialia*, vol. 51, no. 9, pp. 2611–2622, 2003.
- [8] T. L. Burnett and P. J. Withers, “Completing the picture through correlative characterization,” *Nature Materials*, 2019.
- [9] O. Matsumura, Y. Sakuma, and H. Takechi, “Enhancement of Elongation by Retained Austenite in Steel,” *Transactions of the Iron and Steel Institute*, vol. 27, no. 570, pp. 570–579, 1987.
- [10] D. P. Koistinen and R. E. Marburger, “A general equation prescribing the extent of the austenite-martensite transformation in pure iron-carbon alloys and plain carbon steels,” *Acta Metallurgica*, vol. 7, no. 1, pp. 59–60, 1959.
- [11] S. M. C. van Bohemen, “Bainite and martensite start temperature calculated with exponential carbon dependence,” *Materials Science and Technology*, vol. 28, no. 4, pp. 487–495, 2012.
- [12] K. W. Andrews, “Empirical formulae for the calculations of some transformation temperatures,” *Journal of the Iron and Steel Institute*, vol. 203, pp. 721–727, 1965.
- [13] D. Barbier, “Extension of the martensite transformation temperature relation to larger alloying elements and contents,” *Advanced Engineering Materials*, vol. 16, no. 1, pp. 122–127, 2014.
- [14] S. M. C. van Bohemen and J. Sietsma, “Effect of composition on kinetics of athermal martensite formation in plain carbon steels,” *Materials Science and Technology*, vol. 25, no. 8, pp. 1009–1012, 2009.
- [15] S. M. C. Van Bohemen and J. Sietsma, “Martensite formation in partially and fully austenitic plain carbon steels,” *Metallurgical and Materials Transactions A*, vol. 40, no. 5, pp. 1059–1068, 2009.
- [16] J. G. Speer, A. M. Streicher, D. K. Matlock, F. C. Rizzo, and G. Krauss, “Quenching and partitioning: a fundamentally new process to create high strength TRIP sheet microstructures,” in *Austenite formation and decomposition*, E. B. Damm and M. Merwin, Eds. Wiley-TMS, 2003, pp. 505–522.
- [17] J. Sun and H. Yu, “Microstructure development and mechanical properties of quenching and partitioning (Q&P) steel and an incorporation of hot-dipping galvanization during Q&P process,” *Materials Science and Engineering: A*, vol. 586, pp. 100–107, 2013.
- [18] E. J. Seo, L. Cho, Y. Estrin, and B. C. De Cooman, “Microstructure-mechanical properties relationships for quenching and partitioning (Q&P) processed steel,” *Acta Materialia*, vol. 113, pp. 124–139, 2016.
- [19] M. J. Santofimia, L. Zhao, R. Petrov, C. Kwakernaak, W. G. Sloof, and J. Sietsma, “Microstructural development during the quenching and partitioning process in a newly designed low-carbon steel,” *Acta Materialia*, vol. 59, no. 15, pp. 6059–6068, 2011.
- [20] Y. Toji, G. Miyamoto, and D. Raabe, “Carbon partitioning during quenching and partitioning heat treatment accompanied by carbide precipitation,” *Acta Materialia*, vol. 86, pp. 137–147, 2015.
- [21] L. Liu, B. B. He, G. J. Cheng, H. W. Yen, and M. X. Huang, “Optimum properties of quenching and partitioning steels achieved by balancing fraction and stability of retained austenite,” *Scripta Materialia*, vol. 150, pp. 1–6, 2018.
- [22] D. T. Pierce, D. R. Coughlin, D. L. Williamson, J. Kähkönen, A. J. Clarke, K. D. Clarke, J. G. Speer, and E. De Moor, “Quantitative investigation into the influence of temperature on carbide and austenite evolution during partitioning of a quenched and partitioned steel,” *Scripta Materialia*,

- vol. 121, pp. 5–9, 2016.
- [23] A. J. Clarke, J. G. Speer, M. K. Miller, R. E. Hackenberg, D. V. Edmonds, D. K. Matlock, F. C. Rizzo, K. D. Clarke, and E. De Moor, “Carbon partitioning to austenite from martensite or bainite during the quench and partition (Q&P) process: A critical assessment,” *Acta Materialia*, vol. 56, no. 1, pp. 16–22, 2008.
- [24] D. V. Edmonds, K. He, F. C. Rizzo, B. C. De Cooman, D. K. Matlock, and J. G. Speer, “Quenching and partitioning martensite—A novel steel heat treatment,” *Materials Science and Engineering: A*, vol. 438–440, pp. 25–34, 2006.
- [25] M. J. Santofimia, L. Zhao, R. Petrov, and J. Sietsma, “Characterization of the microstructure obtained by the quenching and partitioning process in a low-carbon steel,” *Materials Characterization*, vol. 59, no. 12, pp. 1758–1764, 2008.
- [26] F. Hajyakbary, J. Sietsma, G. Miyamoto, T. Furuhashi, and M. J. Santofimia, “Interaction of carbon partitioning, carbide precipitation and bainite formation during the Q&P process in a low C steel,” *Acta Materialia*, vol. 104, pp. 72–83, 2016.
- [27] I. de Diego-Calderon, I. Sabirov, J. M. Molina-Aldareguia, C. Föjer, R. Thiessen, and R. H. Petrov, “Microstructural design in quenched and partitioned Q&P steels to improve their fracture properties,” *Materials Science and Engineering: A*, vol. 657, pp. 136–146, 2016.
- [28] A. Arlazarov, M. Ollat, J. P. Masse, and M. Bouzat, “Influence of partitioning on mechanical behavior of Q&P steels,” *Materials Science and Engineering: A*, vol. 661, pp. 79–86, 2016.
- [29] S. Takaki, K. Fukunaga, J. Syarif, and T. Tsuchiyama, “Effect of grain refinement on thermal stability of metastable austenitic steel,” *Materials Transactions*, vol. 45, no. 7, pp. 2245–2251, 2004.
- [30] X. C. Xiong, B. Chen, M. X. Huang, J. F. Wang, and L. Wang, “The effect of morphology on the stability of retained austenite in a quenched and partitioned steel,” *Scripta Materialia*, no. 68, pp. 321–324, 2012.
- [31] G. R. Speich and W. C. Leslie, “Tempering of steel,” *Metallurgical Transactions*, vol. 3, no. 5, pp. 1043–1054, 1972.
- [32] D. McLean, “Grain Boundaries in Metals,” in *Grain Boundaries in Metals*, Oxford University Press, 1957, pp. 116–149.
- [33] A. H. Cottrell and B. A. Bilby, “Dislocation theory of yielding and strain ageing of iron,” *Proceedings of the Physical Society. Section A*, vol. 62, no. 1, pp. 49–62, 1949.
- [34] A. W. Cochardt, G. Schoek, and H. Wiedersich, “Interaction between dislocations and interstitial atoms in body-centered cubic metals,” *Acta Metallurgica*, vol. 3, no. 6, pp. 533–537, 1955.
- [35] M. Wellen, “2. Point Defect Relaxations,” *Materials Science Forum*, vol. 366–368, pp. 95–140, 2001.
- [36] J. P. Hirth and J. Lothe, *Theory of dislocation*, 2nd Ed. 1982.
- [37] D. Kandaskalov and P. Maugis, “A first-principle study of the structural, elastic, lattice dynamical and thermodynamic properties of α -Fe₁₆C₂ and α -Fe₁₆N₂ phases,” *Computational Materials Science*, vol. 128, pp. 278–286, 2017.
- [38] S. Chentouf, S. Cazottes, F. Danoix, M. Gouné, H. Zapolsky, and P. Maugis, “Effect of interstitial carbon distribution and nickel substitution on the tetragonality of martensite: A first-principles study,” *Intermetallics*, vol. 89, pp. 92–99, 2017.
- [39] L. Cheng, A. Böttger, T. H. de Keijser, and E. J. Mittemeijer, “Lattice parameters of iron-carbon and iron-nitrogen martensites and austenites,” *Scripta Metallurgica et Materialia*, vol. 24, no. 3, pp. 509–514, 1990.
- [40] S. Ren and S. Wang, “A theoretical analysis of the spinodal decomposition in Fe- C martensite during aging stage of tempering,” *Metallurgical and Materials Transactions A*, vol. 19, no. 10, pp. 2427–2432, 1988.
- [41] E. Clouet, S. Garruchet, H. Nguyen, M. Perez, and C. S. Becquart, “Dislocation interaction with C in α -Fe: A comparison between atomic simulations and elasticity theory,” *Acta Materialia*, vol. 56, no. 14, pp. 3450–3460, 2008.
- [42] R. M. Douthwaite and J. T. Evans, “Interaction between a tetragonal distortion and a $\langle 111 \rangle$ screw dislocation in an anisotropic cubic crystal,” *Scripta Metallurgica*, vol. 7, pp. 1019–1026, 1973.
- [43] D. J. Bacon, “On the carbon dislocation interaction in iron,” *Scripta Metallurgica*, vol. 3, no. 10, pp. 735–740, 1969.
- [44] A. H. Cottrell, *Dislocations and plastic flow in crystals*. Oxford University Press, 1953.
- [45] N. F. Mott, “Mechanical Strength and Creep in Metals,” in *Imperfections in nearly perfect crystals*, 1952, pp. 173–196.

- [46] D. Kalish and M. Cohen, "Structural changes and strengthening in the strain tempering of martensite," *Materials Science and Engineering*, vol. 6, no. 3, pp. 156–166, 1970.
- [47] D. Kalish and E. M. Roberts, "On the distribution of carbon in martensite," *Metallurgical Transactions*, vol. 2, no. 10, pp. 2783–2790, 1971.
- [48] G. A. Thomas, F. Danoix, J. G. Speer, S. W. Thompson, and F. Cuvilly, "Carbon atom redistribution during Quenching and Partitioning," *ISIJ International*, vol. 54, no. 12, pp. 2900–2906, 2014.
- [49] Y. Toji, H. Matsuda, M. Herbig, P.-P. Choi, and D. Raabe, "Atomic-scale analysis of carbon partitioning between martensite and austenite by atom probe tomography and correlative transmission electron microscopy," *Acta Materialia*, vol. 65, pp. 215–228, 2014.
- [50] J. Wilde, A. Cerezo, and G. D. W. Smith, "Three-dimensional atomic-scale mapping of a Cottrell atmosphere around a dislocation in iron," *Scripta Materialia*, vol. 43, no. 1, pp. 39–48, 2000.
- [51] S. Nagakura, Y. Hirotsu, M. Kusunoki, T. Suzuki, and Y. Nakamura, "Crystallographic study of the tempering of martensitic carbon steel by electron microscopy and diffraction," *Metallurgical Transactions A*, vol. 14, no. 5, pp. 1025–1031, 1983.
- [52] M. Kusunoki and S. Nagakura, "Modulated structure of iron-carbon martensite studied by electron microscopy and diffraction," *Journal of Applied Crystallography*, vol. 14, pp. 329–336, 1981.
- [53] K. A. Taylor, G. B. Olson, M. Cohen, and J. B. Vander Sande, "Carbide precipitation during stage I tempering of Fe-Ni-C martensites," *Metallurgical Transactions A*, vol. 20, no. 12, pp. 2749–2765, 1989.
- [54] K. A. Taylor, L. Chang, G. B. Olson, G. D. W. Smith, M. Cohen, and J. B. V. Sande, "Spinodal decomposition during aging of Fe-Ni-C martensites," *Metallurgical Transactions A*, vol. 20, no. 12, pp. 2717–2737, 1989.
- [55] A. Vieweg, E. Povoden-Karadeniz, G. Ressel, P. Prevedel, T. Wojcik, F. Mendez-Martin, A. Stark, J. Keckes, and E. Kozeschnik, "Phase evolution and carbon redistribution during continuous tempering of martensite studied with high resolution techniques," *Materials and Design Design*, vol. 136, pp. 214–222, 2017.
- [56] A. J. Clarke, M. K. Miller, R. D. Field, D. R. Coughlin, P. J. Gibbs, K. D. Clarke, D. J. Alexander, K. A. Powers, P. A. Papin, and G. Krauss, "Atomic and nanoscale chemical and structural changes in quenched and tempered 4340 steel," *Acta Materialia*, vol. 77, pp. 17–27, 2014.
- [57] D. T. Pierce, D. R. Coughlin, K. D. Clarke, E. De Moor, J. Poplawsky, D. L. Williamson, B. Mazumder, J. G. Speer, A. Hood, and A. J. Clarke, "Microstructural evolution during quenching and partitioning of 0.2C–1.5Mn–1.3Si steels with Cr or Ni additions," *Acta Materialia*, vol. 151, pp. 454–469, 2018.
- [58] K. H. Jack, "Results of further X-ray structural investigations of the iron-carbon and iron-nitrogen systems and of related interstitial alloys," *Acta Crystallographica*, no. 3, pp. 392–394, 1950.
- [59] S. Nagakura, "Study of Metallic Carbides by Electron Diffraction Part {III}. Iron Carbides," *Journal of the Physical Society of Japan*, vol. 14, no. 2, pp. 186–195, 1959.
- [60] R. C. Ruhl and M. Cohen, "Splat quenching of iron-carbon alloys," *Trans. TMS-AIME*, vol. 245, pp. 241–251, 1969.
- [61] D. H. Jack and K. H. Jack, "Invited review: Carbides and nitrides in steel," *Materials Science and Engineering*, vol. 11, no. 1, pp. 1–27, 1973.
- [62] Y. Hirotsu and S. Nagakura, "Crystal structure and morphology of the carbide precipitated from martensitic high carbon steel during the first stage of tempering," *Acta Metallurgica*, vol. 20, no. 4, pp. 645–655, 1972.
- [63] J.-M. R. Génin, "The clustering and coarsening of carbon multiplets during the aging of martensite from mössbauer spectroscopy: The preprecipitation stage of epsilon carbide," *Metallurgical Transactions A*, vol. 18, pp. 1371–1388, 1987.
- [64] J.-M. R. Génin, "On the morphology of the modulated precipitation of extended multiplets and Fe₉C₄ epsilon or eta carbide obtained by aging and tempering in Fe-C martensite," *Metallurgical Transactions A*, vol. 19, no. 12, pp. 2901–2909, 1988.
- [65] W. Lu, M. Herbig, C. H. Liebscher, L. Morsdorf, R. K. W. Marceau, G. Dehm, and D. Raabe, "Formation of eta carbide in ferrous martensite by room temperature aging," *Acta Materialia*, vol. 158, pp. 297–312, 2018.
- [66] S. W. Thompson, "Structural characteristics of transition-iron-carbide precipitates formed during the first stage of tempering in 4340 steel," *Materials Characterization*, vol. 106, pp. 452–462, 2015.

- [67] S. S. Nayak, R. Anumolu, R. D. K. Misra, K. H. Kim, and D. L. Lee, "Microstructure-hardness relationship in quenched and partitioned medium-carbon and high-carbon steels containing silicon," *Materials Science and Engineering A*, vol. 498, no. 1–2, pp. 442–456, 2008.
- [68] D. T. Pierce, D. R. Coughlin, D. L. Williamson, K. D. Clarke, A. J. Clarke, J. G. Speer, and E. De Moor, "Characterization of transition carbides in quench and partitioned steel microstructures by Mössbauer spectroscopy and complementary techniques," *Acta Materialia*, vol. 90, pp. 417–430, 2015.
- [69] Y. A. Bargaryastsky, "Bargaryastsky, Y.A.," *Dokl. Akad. Nauk SSSR*, vol. 73, pp. 1161–1164, 1950.
- [70] S. Y. Lu, K. F. Yao, Y. B. Chen, M. H. Wang, N. Chen, and X. Y. Ge, "Effect of quenching and partitioning on the microstructure evolution and electrochemical properties of a martensitic stainless steel," *Corrosion Science*, vol. 103, pp. 95–104, 2016.
- [71] B. Kim, J. Sietsma, and M. J. Santofimia, "The role of silicon in carbon partitioning processes in martensite/austenite microstructures," *Materials and Design*, vol. 127, pp. 336–345, 2017.
- [72] E. A. Ariza, J. Poplawsky, W. Guo, K. Unocic, A. J. Ramirez, A. P. Tschiptschin, and S. S. Babu, "Evaluation of carbon partitioning in new generation of Quench and Partitioning (Q&P) steels," *Metallurgical and Materials Transactions A*, vol. 49, no. 10, pp. 4809–4823, 2018.
- [73] P. Jacques, E. Girault, T. Catlin, N. Geerlofs, T. Kop, S. van der Zwaag, and F. Delannay, "Bainite transformation of low carbon Mn–Si TRIP-assisted multiphase steels: influence of silicon content on cementite precipitation and austenite retention," *Materials Science and Engineering: A*, vol. 273–275, pp. 475–479, 1999.
- [74] M. J. Santofimia, T. Nguyen-Minh, L. Zhao, R. Petrov, I. Sabirov, and J. Sietsma, "New low carbon Q&P steels containing film-like intercritical ferrite," *Materials Science and Engineering: A*, vol. 527, no. 23, pp. 6429–6439, 2010.
- [75] F. G. Caballero, M. K. Miller, C. Garcia-Mateo, C. Capdevila, and S. S. Babu, "Redistribution of alloying elements during tempering of a nanocrystalline steel," *Acta Materialia*, vol. 56, no. 2, pp. 188–199, Jan. 2008.
- [76] B. Kim, C. Celada, D. S. Martín, T. Sourmail, and P. E. J. Rivera-Díaz-del-Castillo, "The effect of silicon on the nanoprecipitation of cementite," *Acta Materialia*, vol. 61, no. 18, pp. 6983–6992, Oct. 2013.
- [77] E. Kozeschnik and H. K. D. H. Bhadeshia, "Influence of silicon on cementite precipitation in steels," *Materials Science and Technology*, vol. 24, no. 3, pp. 343–347, 2008.
- [78] G. Miyamoto, J. C. Oh, K. Hono, T. Furuhashi, and T. Maki, "Effect of partitioning of Mn and Si on the growth kinetics of cementite in tempered Fe-0.6 mass% C martensite," *Acta Materialia*, vol. 55, no. 15, pp. 5027–5038, 2007.
- [79] W. S. Owen, "No Title," *Trans. ASM*, vol. 46, pp. 812–829, 1954.
- [80] R. Rementeria, J. D. Poplawsky, M. M. Aranda, W. Guo, J. A. Jimenez, C. Garcia-Mateo, and F. G. Caballero, "Carbon concentration measurements by atom probe tomography in the ferritic phase of high-silicon steels," *Acta Materialia*, vol. 125, pp. 359–368, 2017.
- [81] W. L. Fink and E. D. Campbell, "Influence of heat treatment and carbon content on the structure of pure iron-carbon alloys," *Trans. Am. Soc. Steel Treat.*, vol. 9, pp. 717–754, 1926.
- [82] N. Seljakow, J. Kurdjmov, and N. Goodtzov, "Tetragonal Structure of Carbon Steel," *Nature*, no. 119, p. 494, 1927.
- [83] E. C. Bain, "The nature of martensite," *Trans. AIME*, vol. 70, pp. 25–35, 1924.
- [84] C. Zener, "Theory of strain interaction of solute atoms," *Physical Review*, vol. 74, no. 6, pp. 639–647, 1948.
- [85] P. Maugis, F. Danoix, H. Zapolsky, S. Cazottes, and M. Gouné, "Temperature hysteresis of the order-disorder transition in carbon-supersaturated α -Fe," *Physical Review B*, vol. 96, no. 21, p. 214104, 2017.
- [86] X. Liu, F. Zhong, J. Zhang, M. Zhang, M. Kang, and Z. Guo, "Lattice-parameter variation with carbon content of martensite. I. X-ray-diffraction experimental study," *Physical Review B*, vol. 52, no. 14, pp. 9970–9978, 1995.
- [87] V. A. Lobodyuk, Y. Y. Meshkov, and E. V. Pereloma, "On Tetragonality of the Martensite Crystal Lattice in Steels," *Metallurgical and Materials Transactions A*, pp. 1–7, 2018.
- [88] C. S. Roberts, "No Title," *Trans. AIME*, vol. 197, no. 203, 1953.
- [89] A. G. Khachaturyan and G. A. Shatalov, "On the theory of the ordering of carbon atoms in a martensite crystal," *Fiz. Met. Met.*, vol. 32, pp. 1–9, 1971.

- [90] O. D. Sherby, J. Wadsworth, D. R. Lesuer, and C. K. Syn, "The c/a Ratio in Quenched Fe-C and Fe-N Steels - A Heuristic Story," *Materials Science Forum*, vol. 539–543, pp. 215–222, 2009.
- [91] Y. Lu, H. Yu, and R. D. Sisson, "The effect of carbon content on the c/a ratio of as-quenched martensite in Fe-C alloys," *Materials Science and Engineering A*, vol. 700, pp. 592–597, 2017.
- [92] K. Honda and Z. Nishiyama, "No Title," *Sci. Rep. Toboku Imp. Univ. Ser. 1*, vol. 21, p. 299, 1932.
- [93] G. . Kurdjumov and A. G. Khachaturyan, "Nature of axial ratio anomalies of the martensite lattice and mechanism of diffusionless $\gamma \rightarrow \alpha$ transformation," *Acta Metallurgica*, vol. 23, no. 9, pp. 1077–1088, 1975.
- [94] A. Udyansky, J. Von Pezold, A. Dick, and J. Neugebauer, "Orientational ordering of interstitial atoms and martensite formation in dilute Fe-based solid solutions," *Physical Review B - Condensed Matter and Materials Physics*, vol. 83, no. 18, pp. 1–11, 2011.
- [95] P. V. Chirkov, A. A. Mirzoev, and D. A. Mirzaev, "Tetragonality and the distribution of carbon atoms in the Fe–C martensite: Molecular-dynamics simulation," *The Physics of Metals and Metallography*, vol. 117, no. 1, pp. 34–41, 2016.
- [96] P. Maugis, "Ferrite, martensite and supercritical iron: A coherent elastochemical theory of stress-induced carbon ordering in steel," *Acta Materialia*, vol. 158, pp. 454–465, 2018.
- [97] C. S. Becquart, J. M. Raulot, G. Bencteux, C. Domain, M. Perez, S. Garruchet, and H. Nguyen, "Atomistic modeling of an Fe system with a small concentration of C," *Computational Materials Science*, vol. 40, pp. 119–129, 2007.
- [98] Y. Lu, H. Yu, X. Cai, Y. Rong, and R. D. Sisson, "Martensite lattice parameter measured by modern X-ray diffraction in Fe-C alloy," in *23rd International Federation of Heat Treatment and Surface Engineering Congress 2016, IFHTSE 2016*, 2016, no. April.
- [99] D. Kim, S.-J. Lee, and B. C. De Cooman, "Microstructure of low C steel isothermally transformed in the M_s to M_F ," *Metallurgical and Materials Transactions A*, vol. 43A, pp. 4967–83, 2012.
- [100] A. Navarro-Lopez, J. Sietsma, and M. J. Santofimia, "Effect of prior athermal martensite on the isothermal transformation kinetics below M_s in a low-C high-Si Steel," *Metallurgical and Materials Transactions A*, vol. 47, no. 3, pp. 1028–1039, 2015.
- [101] A. Navarro-Lopez, J. Hidalgo, J. Sietsma, and M. J. Santofimia, "Characterization of bainitic/martensitic structures formed in isothermal treatments below the M_s temperature," *Materials Characterization*, vol. 128, pp. 248–256, 2017.
- [102] B. P. J. Sandvik and H. P. Nevalainen, "Structure-property relationships in commercial low-alloy bainitic-austenitic steel with high strength, ductility, and toughness," *Metals Technology*, vol. 8, no. 1, pp. 213–220, 1981.
- [103] Y. Toji, H. Matsuda, and D. Raabe, "Effect of Si on the acceleration of bainite transformation by pre-existing martensite," *Acta Materialia*, vol. 116, pp. 250–262, 2016.
- [104] W. Gong, Y. Tomota, S. Harjo, Y. H. Su, and K. Aizawa, "Effect of prior martensite on bainite transformation in nanobainite steel," *Acta Materialia*, vol. 85, pp. 243–249, 2015.
- [105] S. Samanta, P. Biswas, S. Giri, S. B. Singh, and S. Kundu, "Formation of bainite below the M_s temperature: Kinetics and crystallography," *Acta Materialia*, vol. 105, pp. 390–403, 2016.
- [106] M. C. Somani, D. A. Porter, L. P. Karjalainen, and R. D. K. Misra, "On various aspects of decomposition of austenite in a high-silicon steel during Quenching and Partitioning," *Metallurgical and Materials Transactions A*, vol. 45, no. 3, pp. 1247–1257, 2013.
- [107] F. Hu and K. M. Wu, "Nanostructured high-carbon dual-phase steels," *Scripta Materialia*, vol. 65, no. 4, pp. 351–354, 2011.
- [108] M. Gouné, F. Danoix, S. Allain, and O. Bouaziz, "Unambiguous carbon partitioning from martensite to austenite in Fe-C-Ni alloys during quenching and partitioning," *Scripta Materialia*, vol. 68, no. 12, pp. 1004–1007, 2013.
- [109] S. Y. P. Allain, G. Geandier, J. C. Hell, M. Soler, F. Danoix, and M. Gouné, "In-situ investigation of quenching and partitioning by High Energy X-Ray Diffraction experiments," *Scripta Materialia*, vol. 131, pp. 15–18, 2017.
- [110] J. G. Speer, D. V. Edmonds, F. C. Rizzo, and D. K. Matlock, "Partitioning of carbon from supersaturated plates of ferrite, with application to steel processing and fundamentals of the bainite transformation," *Current Opinion in Solid State and Materials Science*, vol. 8, no. 3–4, pp. 219–237, 2004.
- [111] J. G. Speer, D. K. Matlock, B. C. Decooman, and J. G. Schroth, "Comments on "On the definitions of paraequilibrium and orthoequilibrium" by M. Hillert and J. Ågren," *Scripta Materialia*,

- 50, 697–9 (2004),” *Scripta Materialia*, vol. 52, pp. 83–85, 2005.
- [112] M. Hillert and J. Ågren, “On the definitions of paraequilibrium and orthoequilibrium,” *Scripta Materialia*, vol. 50, no. 5, pp. 697–699, 2004.
- [113] A. Hultgren, “Isothermal transformation of Austenite,” *Trans. ASM*, vol. 39, pp. 915–989, 1947.
- [114] H. Jiang, B. Zhuang, X. Duan, Y. Wu, and Z. Cai, “Element distribution and diffusion behavior in Q&P steel during partitioning,” *International Journal of Minerals, Metallurgy, and Materials*, vol. 20, no. 11, pp. 1050–1059, 2013.
- [115] M. Gouné, F. Danoix, J. Ågren, Y. Bréchet, C. R. Hutchinson, M. Militzer, G. Purdy, S. van der Zwaag, and H. Zurob, “Overview of the current issues in austenite to ferrite transformation and the role of migrating interfaces therein for low alloyed steels,” *Materials Science and Engineering: R: Reports*, vol. 92, pp. 1–38, 2015.
- [116] N. Zhong, X. Wang, Y. Rong, and L. Wang, “Interface migration between martensite and austenite during Quenching and Partitioning (Q&P) process,” *Journal of Materials Sciences and Technology*, vol. 22, no. 06, p. 751, 2006.
- [117] G. A. Thomas and J. G. Speer, “Interface migration during partitioning of Q&P steel,” *Materials Science and Technology*, vol. 30, no. 9, pp. 998–1007, 2014.
- [118] D. De Knijf, M. J. Santofimia, H. Shi, V. Bliznuk, C. Föjer, R. Petrov, and W. Xu, “In situ austenite–martensite interface mobility study during annealing,” *Acta Materialia*, vol. 90, pp. 161–168, 2015.
- [119] Z. Dai, X. Wang, J. He, Z. Yang, C. Zhang, and H. Chen, “Elucidating the effect of Mn partitioning on interface migration and carbon partitioning during Quenching and Partitioning of the Fe-C-Mn-Si steels: Modeling and experiments,” *Acta Materialia*, vol. 144, pp. 666–678, 2018.
- [120] Z. Dai, X. Wang, J. He, Z. Yang, C. Zhang, and H. Chen, “Effect of interfacial Mn partitioning on carbon partitioning and interface migration during the Quenching and Partitioning process,” *Metallurgical and Materials Transactions A*, vol. 48, no. 7, pp. 3168–3174, 2017.
- [121] H. K. D. H. Bhadeshia, *Bainite in steels: transformations, microstructure and properties*, 2001st ed. IOM Communicataions Ltd, 2001.
- [122] G. P. Krielaart, J. Sietsma, and S. Van Der Zwaag, “Ferrite formation in Fe-C alloys during austenite decomposition under non-equilibrium interface conditions,” *Materials Science and Engineering*, vol. 237, pp. 216–223, 1997.
- [123] J. Sietsma and S. Van Der Zwaag, “A concise model for mixed-mode phase transformations in the solid state,” *Acta Materialia*, vol. 52, no. 14, pp. 4143–4152, 2004.
- [124] C. Bos and J. Sietsma, “A mixed-mode model for partitioning phase transformations,” *Scripta Materialia*, vol. 57, no. 12, pp. 1085–1088, 2007.
- [125] J. G. Speer, R. E. Hackenberg, B. C. Decooman, and D. K. Matlock, “Influence of interface migration during annealing of martensite/austenite mixtures,” *Philosophical Magazine Letters*, vol. 87, no. 6, pp. 379–382, 2007.
- [126] M. J. Santofimia, L. Zhao, and J. Sietsma, “Model for the interaction between interface migration and carbon diffusion during annealing of martensite/austenite microstructures in steels,” *Scripta Materialia*, vol. 59, no. 2, pp. 159–162, 2008.
- [127] M. J. Santofimia, J. G. Speer, A. J. Clarke, L. Zhao, and J. Sietsma, “Influence of interface mobility on the evolution of austenite–martensite grain assemblies during annealing,” *Acta Materialia*, vol. 57, no. 15, pp. 4548–4557, 2009.
- [128] Y. Takahama, M. J. Santofimia, M. G. Mecozzi, L. Zhao, and J. Sietsma, “Phase field simulation of the carbon redistribution during the quenching and partitioning process in a low-carbon steel,” *Acta Materialia*, vol. 60, no. 6–7, pp. 2916–2926, 2012.
- [129] M. G. Mecozzi, J. Eiken, M. J. Santofimia, and J. Sietsma, “Phase field modelling of microstructural evolution during the quenching and partitioning treatment in low-alloy steels,” *Computational Materials Science*, vol. 112, pp. 245–256, 2016.
- [130] M. Militzer, “Phase field modeling of microstructure evolution in steels,” *Current Opinion in Solid State and Materials Science*, vol. 15, no. 3, pp. 106–115, 2011.
- [131] R. S. Qin and H. K. Bhadeshia, “Phase field method,” *Materials Science and Technology*, vol. 26, no. 7, pp. 803–811, 2010.
- [132] S. M. Allen and J. W. Cahn, “A microscopic theory for antiphase boundary motion and its application to antiphase domain coarsening,” *Acta Metallurgica*, vol. 27, no. 6, pp. 1085–1095, 1979.
- [133] A. S. Nishikawa, M. J. Santofimia, and J. Sietsma, “Influence of bainite reaction on the kinetics of

- carbon redistribution during the Quenching and Partitioning process,” *Acta Materialia*, vol. 142, pp. 142–151, 2018.
- [134] M. Hillert, L. Höglund, and J. Ågren, “Role of carbon and alloying elements in the formation of bainitic ferrite,” *Metallurgical and Materials Transactions A*, vol. 35A, pp. 3693–3700, 2004.
- [135] P. Gustafson, “A thermodynamic evaluation of the Fe-C system,” *Scand. J. Metall.*, vol. 14, no. 5, pp. 259–267, 1985.
- [136] L. A. Carapella, “Computing A’ or Ms from analysis,” *Metal. Progress*, vol. 46, pp. 108–118, 1944.
- [137] S.-J. Lee and C. J. Van Tyne, “A Kinetics Model for Martensite Transformation in Plain Carbon and Low-Alloyed Steels,” *Metallurgical and Materials Transactions A*, vol. 43, no. 2, pp. 422–427, Sep. 2011.
- [138] A. J. Clarke, J. G. Speer, D. K. Matlock, F. C. Rizzo, D. V Edmonds, and M. J. Santofimia, “Influence of carbon partitioning kinetics on final austenite fraction during quenching and partitioning,” *Scripta Materialia*, vol. 61, no. 2, pp. 149–152, 2009.
- [139] D. De Knijf, M. J. Santofimia, H. Shi, V. Bliznuk, C. Föjer, R. Petrov, and W. Xu, “In situ austenite-martensite interface mobility study during annealing,” *Acta Materialia*, vol. 90, pp. 161–168, 2015.
- [140] M. J. Santofimia, L. Zhao, and J. Sietsma, “Volume Change Associated to Carbon Partitioning from Martensite to Austenite,” *Materials Science Forum*, vol. 706–709, pp. 2290–2295, Jan. 2012.
- [141] K. S. Choi, Z. Zhu, X. Sun, E. De Moor, M. D. Taylor, J. G. Speer, and D. K. Matlock, “Determination of carbon distributions in quenched and partitioned microstructures using nanoscale secondary ion mass spectroscopy,” *Scripta Materialia*, vol. 104, pp. 79–82, 2015.
- [142] ASTM E975-13, *Practice for X-Ray Determination of Retained Austenite in Steel with Near Random Crystallographic Orientation*. ASTM International, 2013.
- [143] C. F. Jaczak, “Retained Austenite and Its Measurement by X-Ray Diffraction,” in *1980 Automotive Engineering Congress and Exposition*, 1980, no. 800426.
- [144] R. L. Banerjee, “X-ray determination of retained austenite,” *Journal of Heat Treating*, vol. 2, no. 2, pp. 147–150, 1981.
- [145] P. J. Jacques, B. M. Hance, M. Radu, S. E. Kruger, A. Iza-Mendia, A.-F. Gourgues, S. Allain, O. Bouaziz, J. Huang, A. De, L. Zhao, S. van der Zwaag, L. Samek, Y. Houbaert, and J. Speer, “On measurement of retained austenite in multiphase TRIP steels — results of blind round robin test involving six different techniques,” *Materials Science and Technology*, vol. 25, no. 5, pp. 567–574, 2008.
- [146] T. Gnäupel-Herold and A. Creuziger, “Diffraction study of the retained austenite content in TRIP steels,” *Materials Science and Engineering A* 528, 2011.
- [147] D. H. Kim, J. G. Speer, H. S. Kim, and B. C. De Cooman, “Observation of an Isothermal Transformation during Quenching and Partitioning Processing,” *Metallurgical and Materials Transactions A*, vol. 40A, pp. 2048–60, 2009.
- [148] M. Takahashi and H. K. D. H. Bhadeshia, “The interpretation of dilatometric data for transformations in steels,” *J Mater Sci Lett*, vol. 8, no. 4, pp. 477–478, 1989.
- [149] S. S. Babu, E. D. Specht, S. a. David, E. Karapetrova, P. Zschack, M. Peet, and H. K. D. H. Bhadeshia, “In-situ observations of lattice parameter fluctuations in austenite and transformation to bainite,” *Metallurgical and Materials Transactions A*, vol. 36, no. 12, pp. 3281–3289, 2005.
- [150] D. J. Dyson and B. Holmes, “Effect of alloying additions on lattice parameter of austenite,” *J. Iron Steel Inst*, vol. 208, pp. 469–474, 1970.
- [151] C. GarcíadeAndrés, F. G. Caballero, C. Capdevila, and L. F. Álvarez, “Application of dilatometric analysis to the study of solid–solid phase transformations in steels,” *Materials Characterization*, vol. 48, no. 1, pp. 101–111, 2002.
- [152] ASTM E562-02, *Standard Test Method for Determining Volume Fraction by Systematic Manual Point Count*. ASTM International, 2002.
- [153] I. G. Wood, L. Vočadlo, K. S. Knight, D. P. Dobson, W. G. Marshall, G. D. Price, and J. Brodholt, “Thermal expansion and crystal structure of cementite, Fe₃C, between 4 and 600 K determined by time-of-flight neutron powder diffraction,” *Journal of Applied Crystallography*, vol. 37, no. 1, pp. 82–90, 2004.
- [154] D. J. Larson, T. J. Prosa, R. M. Ulfig, B. P. Geiser, and T. F. Kelly, *Local Electrode Atom Probe Tomography*. New York, NY: Springer New York, 2013.
- [155] B. Gault, M. P. Moody, J. M. Cairney, and S. P. Ringer, *Atom Probe Microscopy*, vol. 160. New York, NY: Springer New York, 2012.

- [156] G. Badinier, “Effect of Carbon Segregation and Carbide Precipitation on the Mechanical Response of Martensite,” The University Of British Columbia, 2013.
- [157] B. Hutchinson, J. Hagström, O. Karlsson, D. Lindell, M. Tornberg, F. Lindberg, and M. Thuvander, “Microstructures and hardness of as-quenched martensites (0.1-0.5%C),” *Acta Materialia*, vol. 59, no. 14, pp. 5845–5858, 2011.
- [158] Y. Xiao, W. Li, H. S. Zhao, X. W. Lu, and X. J. Jin, “Investigation of carbon segregation during low temperature tempering in a medium carbon steel,” *Materials Characterization*, vol. 117, pp. 84–90, 2016.
- [159] P. Maugis and K. Hoummada, “A methodology for the measurement of the interfacial excess of solute at a grain boundary,” *Scripta Materialia*, vol. 120, pp. 90–93, 2016.
- [160] B. W. Krakauer and D. N. Seidman, “Absolute atomic-scale measurements of the Gibbsian interfacial excess of solute at internal interfaces,” *Physical Review B*, vol. 48, no. 9, pp. 6724–6727, 1993.
- [161] G. Da Rosa, “Mécanismes et conséquences de la ségrégation du bore aux joints de grains austénitiques dans les aciers à très haute résistance.,” 2018.
- [162] J. H. Jang, H. K. D. H. Bhadeshia, and D. W. Suh, “Solubility of carbon in tetragonal ferrite in equilibrium with austenite,” *Scripta Materialia*, vol. 68, no. 3–4, pp. 195–198, 2013.
- [163] H. M. Rietveld, “A profile refinement method for nuclear and magnetic structures,” *Journal of Applied Crystallography*, vol. 2, no. 2, pp. 65–71, 1969.
- [164] R. A. Young, “Introduction to the Rietveld method,” in *The Rietveld Method*, R. A. Young, Ed. Oxford University Press, 1993, pp. 1–38.
- [165] S. M. C. Van Bohemen, “The nonlinear lattice expansion of iron alloys in the range 100-1600 K,” *Scripta Materialia*, vol. 69, no. 4, pp. 315–318, 2013.
- [166] F. Bruneseaux, “Apport de la diffraction des rayons X à haute énergie sur les transformations de phases , application aux alliages de titanes,” 2008.
- [167] Y. Tanaka and K. Shimizu, “Anomalous changes in austenite and martensite lattice parameters of Fe-Mn-C alloys,” vol. 21, no. 9, 1980.
- [168] M. Villa, F. Niessen, and M. A. J. Somers, “In Situ Investigation of the Evolution of Lattice Strain and Stresses in Austenite and Martensite During Quenching and Tempering of Steel,” *Metallurgical and Materials Transactions A*, 2017.
- [169] N. Nakada, Y. Ishibashi, T. Tsuchiyama, and S. Takaki, “Self-stabilization of untransformed austenite by hydrostatic pressure via martensitic transformation,” *Acta Materialia*, vol. 110, pp. 95–102, 2016.
- [170] M. Villa, K. Pantleon, and M. A. J. Somers, “In situ investigation of the martensitic transformation in Fe – 12 wt .% Ni – 0 . 6 wt .% C steel at subzero temperatures,” *Journal of Alloys and Compounds*, vol. 577, pp. S543–S548, 2013.
- [171] M. Villa, F. B. Grumsen, K. Pantleon, and M. A. J. Somers, “Martensitic transformation and stress partitioning in a high-carbon steel,” *Scripta Materialia*, vol. 67, no. 6, pp. 621–624, 2012.
- [172] G. Badinier, C. W. Sinclair, S. Allain, F. Danoix, and M. Gouné, “The Mechanisms of Transformation and Mechanical Behavior of Ferrous Martensite,” in *Reference Module in Materials Science and Materials Engineering*, Elsevier {BV}, 2017.
- [173] J. D. Eshelby, “The elastic interaction of point defects,” *Acta Metallurgica*, vol. 3, pp. 487–490, 1955.
- [174] T. Mori and K. Tanaka, “Average stress in matrix and average elastic energy of materials with misfitting inclusions,” *Acta Metallurgica*, vol. 21, no. 5, pp. 571–574, 1973.
- [175] G. W. Sherer, *Relaxation in glass and composites*. John Wiley & Sons, 1986.
- [176] S. Allain, G. Geandier, J.-C. Hell, M. Soler, F. Danoix, and M. Gouné, “Effects of Q&P Processing Conditions on Austenite Carbon Enrichment Studied by In Situ High-Energy X-ray Diffraction Experiments,” *Metals*, vol. 7, no. 7, p. 232, 2017.
- [177] G. Ghosh and G. B. Olson, “The isotropic shear modulus of multicomponent Fe-base solid solutions,” vol. 50, pp. 2655–2675, 2002.
- [178] S. V. Patankar, *Numerical heat transfer and fluid flow*. New York, NY: CRC Press, 1980.
- [179] T. Belmonte, M. Gouné, and H. Michel, “Numerical modeling of interstitial diffusion in binary systems. Application to iron nitriding,” *Materials Science and Engineering: A*, vol. 302, no. 2, pp. 246–257, 2001.
- [180] A. Deschamps and Y. Brechet, “Influence of predeformation and ageing of an Al–Zn–Mg alloy—II. Modeling of precipitation kinetics and yield stress,” vol. 47, no. 1, 1999.

- [181] Y. Wang, S. Denis, B. Appolaire, and P. Archambault, “Modelling of precipitation of carbides during tempering of martensite,” *Journal de Physique IV*, vol. 120, pp. 103–110, 2004.
- [182] M. Perez and A. Deschamps, “Microscopic modelling of simultaneous two-phase precipitation: application to carbide precipitation in low-carbon steels,” *Materials Science and Engineering: A*, vol. 360, no. 1–2, pp. 214–219, 2003.
- [183] S. V. Radcliffe and E. C. Rollason, “The kinetics of the formation of bainite in high-purity iron-carbon alloy,” *Journal of the Iron and Steel Institute*, vol. 191, pp. 56–65, 1959.
- [184] H. Okamoto and M. Oka, “Lower bainite with midrib in hypereutectoid steels,” *Metallurgical Transactions A*, vol. 17, no. 7, pp. 1113–1120, 1986.
- [185] S. M. C. van Bohemen, M. J. Santofimia, and J. Sietsma, “Experimental evidence for bainite formation below Ms in Fe-0.66C,” *Scripta Materialia*, vol. 58, no. 6, pp. 488–491, 2008.
- [186] P. Kolmskog, A. Borgenstam, M. Hillert, P. Hedström, S. S. Babu, H. Terasaki, and Y.-I. Komizo, “Direct observation that bainite can grow below Ms,” *Metallurgical and Materials Transactions A*, vol. 43, no. 13, pp. 4984–4988, 2012.
- [187] P. Huyghe, M. Caruso, J.-L. Collet, S. Dépinoy, and S. Godet, “In Situ Quantitative Assessment of the Role of Silicon During the Quenching and Partitioning of a 0.2C Steel,” *Metallurgical and Materials Transactions A*, vol. 50, no. 8, pp. 3486–3494, 2019.
- [188] R. F. Hehemann, K. R. Kinsman, and H. I. Aaronson, “A debate on the bainite reaction,” *Metallurgical Transactions*, vol. 3, no. 5, pp. 1077–1094, 1972.
- [189] J. W. Christian and D. V. Edmonds, “Phase Transformations in Ferrous Alloys,” in *Phase Transformations in Ferrous Alloys*, 1984, p. 293.
- [190] M. Hillert, “Diffusion in growth of bainite,” *Metallurgical and Materials Transactions A*, vol. 25, no. 9, pp. 1957–1966, 1994.
- [191] H. K. D. H. Bhadeshia and J. W. Christian, “Bainite in steels,” *Metallurgical Transactions A*, vol. 21A, pp. 767–797, 1990.
- [192] A. Borgenstam, M. Hillert, and J. Ågren, “Metallographic evidence of carbon diffusion in the growth of bainite,” *Acta Materialia*, vol. 57, no. 11, pp. 3242–3252, 2009.
- [193] G. B. Olson and M. Cohen, “Stress-assisted isothermal martensitic transformation: Application to TRIP steels,” *Metallurgical Transactions A*, vol. 13, no. 11, pp. 1907–1914, 1982.
- [194] A. Mihajlović, “Activation energy of isothermal martensitic $\beta\text{-}\alpha'$ transformation,” *Journal of Materials Science*, vol. 5, no. 11, pp. 955–959, 1970.
- [195] D. Quidort and Y. J. M. Brechet, “A Model of Isothermal and Non Isothermal Transformation Kinetics of Bainite in 0.5% C Steels,” *ISIJ International*, vol. 42, no. 9, pp. 1010–1017, 2002.
- [196] N. V. Luzginova, L. Zhao, and J. Sietsma, “Bainite formation kinetics in high carbon alloyed steel,” *Materials Science and Engineering: A*, vol. 481–482, pp. 766–769, 2008.
- [197] S. M. C. Van Bohemen, “Modeling Start Curves of Bainite Formation,” *Metallurgical and Materials Transactions A*, vol. 41, no. 2, pp. 285–296, 2010.
- [198] G. V. Kurdyumov and O. P. Maksimova, “Kinetics of the transformation of austenite into martensite at low temperatures,” *Doklady Akademii Nauk SSSR*, vol. 61, p. 83, 1948.
- [199] C. L. Magee, “The nucleation of martensite,” in *Phase Transformations*, H. I. Aaronson and V. F. Zackay, Eds. Metals Park, OH: American Society of Materials, 1970, pp. 115–156.
- [200] S. M. C. van Bohemen and J. Sietsma, “Modeling of isothermal bainite formation based on the nucleation kinetics,” *International Journal of Materials Research*, vol. 99, no. 7, pp. 739–747, 2008.
- [201] M. Azuma, N. Fujita, M. Takahashi, and T. Iung, “Modelling Upper and Lower Bainite Transformation in Steels,” *ISIJ International*, vol. 45, no. 2, pp. 221–228, 2005.
- [202] G. I. Rees and H. K. D. H. Bhadeshia, “Bainite transformation Part 1 Modified model,” vol. 8, no. November, pp. 985–993, 1992.
- [203] S. . Singh and H. K. D. H. Bhadeshia, “Estimation of bainite plate-thickness in low-alloy steels,” *Materials Science and Engineering: A*, vol. 245, no. 1, pp. 72–79, 1998.
- [204] C. H. Young and H. K. D. H. Bhadeshia, “Strength of mixtures of bainite and martensite,” *Materials Science and Technology*, vol. 10, no. 3, pp. 209–214, 1994.
- [205] J. Wang, S. van der Zwaag, Z. Yang, and H.-S. Fang, “Aspect ratio of bainite in steels,” *Materials Letters*, vol. 45, no. 3–4, pp. 228–234, 2000.
- [206] J. W. Christian, *Theory of Transformations in Metals and Alloys, Part I*. Oxford: Pergamon Press, 1975.
- [207] M. Hillert and L.-I. Staffansson, “The Regular Solution Model for Stoichiometric Phases and Ionic Melts,” *Acta Chemica Scandinavica*, vol. 24, pp. 3618–3626, 1970.

- [208] B. Sundman and J. Ågren, "A regular solution model for phases with several components and sublattices, suitable for computer applications," *Journal of Physics and Chemistry of Solids*, vol. 42, no. 4, pp. 297–301, 1981.
- [209] M. Hillert, *Phase Equilibria, Phase Diagrams and Phase Transformations*. Cambridge University Press, 1998.
- [210] J. Miettinen, "Reassessed thermodynamic solution phase data for ternary Fe-Si-C system," *Calphad*, vol. 22, no. 2, pp. 231–256, 1998.
- [211] J. Lacaze and B. Sundman, "An assessment of the Fe-C-Si system," *Metallurgical Transactions A*, vol. 22, no. 10, pp. 2211–2223, 1991.
- [212] W. Huang, "A thermodynamic assessment of the Fe-Mn-C system," *Metallurgical Transactions A*, vol. 21, no. 8, pp. 2115–2123, 1990.
- [213] W. Zheng, X. Lu, Y. He, and L. Li, "Thermodynamic modeling of Fe-C-Mn-Si alloys," *Journal of Iron and Steel Research International*, vol. 24, no. 2, pp. 190–197, 2017.
- [214] Y. Van Leeuwen, "Moving Interface in Low-carbon Steel," Technische Universiteit Delft, 2001.
- [215] J. C. Dalton, "Thermodynamics of paraequilibrium carburization and nitridation of stainless steels," Case Western Reserve University, 2014.
- [216] P. Thibaux, A. Métenier, and C. Xhoffer, "Carbon Diffusion Measurement in Austenite in the Temperature Range 500 °C to 900 °C," *Metallurgical and Materials Transactions A*, vol. 38, no. 6, pp. 1169–1176, 2007.
- [217] Y. Wang, "Etude et modélisation de l'effet du revenu sur les évolutions des microstructures, du comportement thermomécanique et des contraintes résiduelles de trempe," Institut National Polytechnique de Lorraine, 2006.
- [218] J. F. Butler, "Kinetics of the two-stage precipitation of carbon from ferrite," *Journal of the Iron and Steel Institute*, pp. 127–133, 1966.
- [219] C. Zener, "Kinetics of the decomposition of austenite," *Trans. Am. Inst. Min. Metall. Engng.*, vol. 167, p. 550, 1946.
- [220] R. Houillier, G. Bégin, and A. Dubé, "A study of the peculiarities of austenite during the formation of bainite," *Metallurgical Transactions*, vol. 2, no. 9, pp. 2645–2653, 1971.
- [221] H. K. D. H. Bhadeshia, "A rationalisation of shear transformations in steels," *Acta Metallurgica*, vol. 29, no. 6, pp. 1117–1130, 1981.
- [222] D. Van Dooren, "Theoretical Modeling of the Carbide-Free Bainite Transformation," Université de Gent, 2006.
- [223] O. Bouaziz, P. Maugis, and J. D. Embury, "Bainite tip radius prediction by analogy with indentation," *Scripta Materialia*, vol. 54, no. 8, pp. 1527–1529, 2006.
- [224] H. Guo, X. Feng, A. Zhao, Q. Li, and J. Ma, "Influence of Prior Martensite on Bainite Transformation, Microstructures, and Mechanical Properties in Ultra-Fine Bainitic Steel," *Materials*, vol. 12, no. 3, p. 527, 2019.
- [225] M. J. Santofimia, L. Zhao, R. Petrov, C. Kwakernaak, W. G. Sloof, and J. Sietsma, "Microstructural development during the quenching and partitioning process in a newly designed low-carbon steel," *Acta Materialia*, vol. 59, no. 15, pp. 6059–6068, 2011.
- [226] M. K. Miller, *Atom Probe Microanalysis: Principles and Applications to Materials Problems*. Materials Research Society, 1989.
- [227] E. J. Seo, L. Cho, and B. C. De Cooman, "Kinetics of the partitioning of carbon and substitutional alloying elements during quenching and partitioning Q&P processing of medium Mn steel," *Acta Materialia*, vol. 107, pp. 354–365, 2016.

Résumé

Étude des mécanismes d'enrichissement en carbone de l'austénite dans les aciers duplex Q&P à très haute résistance

L'allègement dans le secteur de l'automobile revête un enjeu important du fait de normes d'émission de CO₂ de plus en plus drastiques, de la nécessité de réduire la consommation en carburant des véhicules et d'une aspiration sociétale à une économie « plus verte ». Pour répondre à ces défis et dans un souci de sécurité et de contrôle des coûts, l'industrie automobile étudie actuellement la possibilité de développer et de produire une 3^{ème} génération d'aciers à très haute résistance. Ils résultent de traitements thermomécaniques généralement innovants, possèdent des microstructures complexes et des propriétés mécaniques améliorées. Le procédé de Quenching and Partitioning (Q&P) est le traitement le plus prometteur, il consiste en une trempe sous la température de début de transformation martensitique Ms, puis, d'un réchauffage et d'un maintien au-dessus de la température initiale de trempe (QT). L'étape de maintien est appelée "étape de partition", car un enrichissement en carbone de l'austénite est attendu. Les propriétés mécaniques exceptionnelles des aciers Q&P sont dues à leur microstructure duplexe complexe : de très fins îlots d'austénite résiduelle imbriqués dans une matrice martensitique revenue et/ou fraîche. Bien que les mécanismes d'enrichissement en carbone de l'austénite résiduelle lors de l'étape de partition soient encore débattus dans la littérature, il existe des preuves tangibles qui attestent d'un phénomène de partition du carbone de la martensite vers l'austénite. Cependant, la formation de bainite et de carbures dans la martensite soulève la question de l'influence de ces réactions et de leurs interactions sur les mécanismes et les cinétiques d'enrichissement en carbone de l'austénite. Il s'agit clairement d'un sujet d'intérêt puisque les propriétés mécaniques de ces aciers reposent principalement sur la teneur en carbone des îlots d'austénite.

Cette thèse qui repose sur une approche expérimentale multi-échelle couplée à une approche théorique en champ moyen, a pour ambition d'apporter des éléments de réponse aux mécanismes d'enrichissement en carbone de l'austénite dans un aciers duplex Q&P à très haute résistance de composition Fe-0,3 C-2,5Mn-1,5Si. Après avoir déterminé les paramètres Q&P optimaux à l'aide de mesures dilatométriques et en diffraction des rayons X, l'acier en question a été soumis à un traitement Q&P avec trois QT différents (260, 230 et 200°C) et à une température de partition de 400°C. Les données dilatométriques combinées à une étude d'analyse d'images MEB mettent en évidence la formation de bainite durant l'étape de partition. La présence de bainite a également été confirmée par DRX à Haute Energie (DRXHE). Alors que la bainite se présente sous forme de lattes sans carbures, la martensite revenue révèle un état avancé de précipitation intra-lattes. L'analyse des données obtenues en sonde atomique tomographique (APT) et en MET a montré que ces carbures sont transitoires (η et ϵ). Leur teneur en carbone est comprise entre 20,0 et 27,7 %at. Les mesures APT ont également mis en évidence la ségrégation de carbone sur les défauts de la martensite lors de la trempe initiale et le calcul de l'évolution de la grandeur d'excès en carbone sur les joints de lattes suggère qu'un phénomène de déségrégation du carbone se produit au cours du traitement. La DRXHE in-situ a permis de suivre l'évolution des paramètres de maille de l'austénite. Il a été démontré que l'austénite est soumise à des contraintes de traction pour de faibles fractions volumiques de martensite et de compression à partir d'une fraction volumique de martensite critique quasiment indépendante de QT. Un modèle de coefficient de dilatation thermique de l'austénite tenant compte de son état de contrainte a été développé avec succès. Une méthodologie a été proposée afin de découpler les effets chimiques et mécaniques. Ainsi, l'évolution de la teneur en carbone de l'austénite a été déterminée pour les trois QT. Il a été montré que l'enrichissement en carbone de l'austénite résulte de la partition du carbone de la martensite et de la transformation bainitique mais, de manière surprenante, ne dépend pas de QT. Enfin, une approche théorique originale a été développée. Elle décrit les effets des réactions compétitives (partition, transformation bainitique et précipitation de carbures) sur l'enrichissement en carbone de l'austénite et répond aux nombreuses questions soulevées par nos mesures expérimentales. Elle donne des voies à explorer afin d'augmenter l'enrichissement en carbone de l'austénite, donc, d'améliorer les propriétés mécaniques et d'allègement des aciers Q&P.

Mots clés : Quenching & Partitioning, métallurgie, transformation de phases, diffusion du carbone

Abstract

Study of the mechanisms of carbon enrichment in austenite in Q&P steels

The need to reduce the fuel consumption of vehicles while increasing safety led the automotive industry to develop a 3rd generation of Advanced High Strength Steels. Such steels combine innovative processing routes, complex microstructures, improved mechanical properties and are a possible response in vehicle lightweighting. The Quenching and Partitioning (Q&P) process is the most promising route and involves quenching below the martensite start temperature followed by a reheating and ageing above the initial quench temperature (QT). The ageing step is termed “partitioning step” since carbon enrichment in austenite is expected to occur during this stage. The exceptional mechanical properties of Q&P steels come from their complex duplex microstructure: very fine austenite island retained at room temperature embedded in both recovered and fresh martensite. Although the mechanisms of carbon enrichment in retained austenite during the partitioning step are still debated, strong evidences of carbon partitioning from martensite to austenite exist. However, both the formation of bainite and carbides into martensite raise the question of the effects of competitive reactions on the carbon enrichment in austenite. It is clearly a topic of interest since the benefits of such a treatment in terms of improved mechanical properties depends strongly on the austenite stability and thus on the level of carbon enrichment in austenite during the partitioning step.

This thesis aims at combining an innovative multiscale experimental methodology with an original theoretical approach providing a unique opportunity to give some clarifications regarding the microstructure evolution and the mechanisms of carbon enrichment into austenite. After having determined the optimum Q&P parameters using dilatometric and XRD measurements, a Q&P treatment at three different QT (260, 230 and 200°C) and at a partitioning temperature of 400°C was applied to a model Fe-0.3 C-2.5Mn-1.5Si steel. The dilatometric data combined with an SEM image analysis study showed that bainite forms during the partitioning step. The presence of bainite was also confirmed by in-situ High Energy X-Ray Diffraction. While bainite was shown to appear as carbide free laths, tempered martensite showed an advanced state of intra-lath precipitation. The combination of atom probe tomography (APT) and TEM technics showed that these carbides are transitional and both η and ϵ carbides were observed. Their carbon content ranged from 20.0 to 27.7 at.%. APT measurements also highlighted carbon segregation on martensite defects during the initial quench and calculation of the evolution of the carbon excess concentration on laths boundaries suggest that desegregation occurs along the Q&P treatment. In-situ HEXRD permitted to follow the austenite lattice parameter evolution and it was shown that austenite is subjected to a sequence of tensile and compression state induced by the formation of martensite. A model for the coefficient of thermal expansion of austenite taking into account its stress state was successfully developed. The evolutions of carbon content into austenite for the three QT were determined. Surprisingly the carbon enrichment into austenite was shown not to depend on QT. It was also shown that the increase of carbon content in austenite results from both carbon partitioning and bainite contributions. Lastly, an original theoretical approach was developed. It was evidenced that bainite continues to form while partitioning process is rapidly completed, thus bainite transformation controls the maximum austenite carbon enrichment at 400°C, independently of QT. The contribution of partitioning from martensite was shown to be larger with decreasing QT. The developed model successfully described the experimentally observed phase transformations and austenite carbon enrichment by taking into account the interactions between carbon partitioning, bainite transformation and carbide precipitation.

Keywords : Quenching & Partitioning, metallurgy, phase transformation ; carbon diffusion

Unité de recherche

Institut de Chimie de la Matière Condensée de Bordeaux (ICMCB), UMR 5026
87 Avenue du Docteur Albert Schweitzer, 33600 Pessac